Resolving the timing of events around the Cretaceous-Paleogene Boundary

By

Courtney Jean Sprain

A dissertation submitted in partial satisfaction of the

requirements for the degree of

Doctor of Philosophy

in

Earth and Planetary Science

in the

Graduate Division

of the

University of California, Berkeley

Committee in charge:

Professor Paul R. Renne, Chair
Professor Mark A. Richards
Professor William A. Clemens

Spring 2017

Resolving the timing of events around the Cretaceous-Paleogene Boundary

Abstract

Resolving the timing of events around the Cretaceous-Paleogene Boundary

by

Courtney Jean Sprain

Doctor of Philosophy in Earth and Planetary Science

University of California, Berkeley

Professor Paul R. Renne, Chair

Despite decades of study, the exact cause of the Cretaceous-Paleogene boundary (KPB) mass extinction remains contentious. Hypothesized scenarios center around two main environmental perturbations: voluminous (>10^6 km^3) volcanic eruptions from the Deccan Traps in modern-day India, and the large impact recorded by the Chicxulub crater. The impact hypothesis has gained broad support, bolstered by the discoveries of iridium anomalies, shocked quartz, and spherules at the KPB worldwide, which are contemporaneous with the Chicxulub impact structure. However, evidence for protracted extinctions, particularly in non-marine settings, and paleoenvironmental change associated with climatic swings before the KPB, challenge the notion that the impact was the sole cause of the KPB mass extinction. Despite forty years of study, the relative importance of each of these events is unclear, and one key inhibitor is insufficient resolution of existing geochronology.

In this dissertation, I present work developing a high-precision global chronologic framework for the KPB that outlines the temporal sequence of biotic changes (both within the terrestrial and marine realms), climatic changes, and proposed perturbations (i.e. impact, volcanic eruptions) using $^{40}Ar/^{39}Ar$ geochronology and paleomagnetism. This work is focused on two major areas of study: 1) refining the timing and tempo of terrestrial ecosystem change around the KPB, and 2) calibrating the geomagnetic polarity timescale, and particularly the timing and duration of magnetic polarity chron C29r (the KPB falls about halfway into C29r).

First I develop a high-precision chronostratigraphic framework for fluvial sediments within the Hell Creek region, in NE Montana, which is one of the best-studied terrestrial KPB sections worldwide. For this work I dated 15 tephra deposits with ± 30 ka precision using $^{40}Ar/^{39}Ar$ geochronology, ranging in time from ~300 ka before the KPB to 1 Ma after. By tying these results to paleontological records, this work is able to constrain the timing of terrestrial faunal decline and recovery in addition to calibrating late Cretaceous and early Paleocene North American Land Mammal Ages biostratigraphy.

To aid in global correlation, I next sought to calibrate the timing and duration of C29r. However, based on discrepancies noticed between a calculated duration for C29r, from new dates collected as part of this dissertation and previously published magnetostratigraphy for the Hell Creek region, and the duration provided within the Geologic Time Scale 2012, it became

clear that reliability of sediments from the Hell Creek as paleomagnetic recorders was suspect. To test this claim, a complete characterization of the rock magnetic properties of sediments from the Hell Creek region was undertaken. To aid characterization, a new test to determine the presence of intermediate composition titanohematite ($Fe_{2-y}Ti_yO_3$; $0.5 \leq y \leq 0.7$) was developed. Results from rock magnetic characterization show that sediments from the Hell Creek should be reliable paleomagnetic recorders, so long as care is taken to remove goethite (a secondary mineral that previous magnetostratigraphic studies in the Hell Creek did not remove), and to avoid samples that have been heated above ~200ºC.

With the knowledge that sediments from the Hell Creek region are reliable magnetic recorders, I collected 14 new magnetostratigraphic sections, and 18 new high-precision $^{40}Ar/^{39}Ar$ dates which together provide constraints on the timing and duration of chron C29r, at unprecedented precision. This work enables correlation of our record in the Hell Creek to other KPB records around the globe, in addition to providing a test of the Paleocene astrochronologic timescale.

Table of Contents

List of Tables

List of Figures

Dedicated to my loving family and husband

Acknowledgements

I would first like to acknowledge my advisor, Paul Renne, for his mentorship, support, advice, guidance, and most importantly for giving me the opportunity to work on a multitude of amazing projects (only a subset mentioned in this dissertation), that led me around the world. I'd like to thank Paul for introducing me to $^{40}Ar/^{39}Ar$ geochronology, while simultaneously allowing me to keep pursuing my passion for paleomagnetism. I would also like to thank Paul for always including me on opportunities not just for research but on press releases, symposia talks, and workshops. You have always shown a lot of faith in me as a scientist and it has led me to develop a strong faith in myself.

This dissertation work would also not be possible without the help and guidance of Bill Clemens. Bill, your forty years of knowledge about the Hell Creek has been pivotal for my dissertation work. I appreciate all of our long discussions about the Hell Creek, and the KPg boundary, in addition to our meetings in the field. Your kind words, encouragement, and guidance made this dissertation work possible. I also want to thank Bill for helping me interpret paleontological data for many parts of this dissertation.

I'd also like to thank Mark Richards for teaching me more about mantle plumes than I ever thought I'd know and for showing me that big ideas have a place in science. Your enthusiasm for the Deccan is unending, and I want to thank you and Paul for letting me be a part of the Deccan project. I'd also like to acknowledge other members of the Deccan project including Steve Self, Loyc Vanderkluysen, Tushar Mittal, Kanchan Pande, Isabel Fendley, Michael Manga, and Walter Alvarez.

I would further like to thank Nick Swanson-Hysell and his group for letting me be an honorary Swanson-Hysell group member. You gave me an outlet to pursue my passion for paleomagnetism and I am a much better paleomagnetist thanks to your knowledge and guidance. For that I am grateful.

I'd next like to thank Greg Wilson, for field support, guidance, and mentorship. Our field campaigns in the Hell Creek would not have been possible without your support, and I thank you for letting the Berkeley crew become a part of the UW clan. I'd also like to thank my many field assistants including Andy Tholt, Jessica Banaszak, Ryan Ickert, Elizabeth Niespolo, Isabel Fendley, and Gabriella Quaresma, for agreeing to live in a tent for a up to a month, for camping through hail storms, for working in extreme weather conditions, and for digging in the dirt for me. Your positive attitudes and hard work made these field campaigns possible. I'd also like to thank members of the Wilson crew including Stephanie Smith, Brody Hovatter, Dave Demar, Luke Weaver, Alex Brannick, and honorary member Tom Tobin, for including us within your clan, for making field campaigns fun, and for your general support and guidance. I will never forget our games of waffle/kick ball or the baculites booze cruise. This work would also not have been possible without the kind hospitality of local ranchers including the Engdahl's, Tharp's, McKeever's, and Thomas', and to Becca, whose coffee shop kept me going through difficult field seasons.

I would not have gotten through these last five years without the support of my friends and fellow colleagues at the BGC. I'd like to specifically thank Lisa Smeenk, Abed Jaouni, Tim Becker, Francoise Spaulding-Keller, Tania Borostyan, and Gary Scott for their support and guidance. I also want to thank my fellow jets both past and present including Bill Mitchell, Ryan Ickert, Elizabeth Niespolo, Isabel Fendley, Daniel Rutte, and C. Brenhin Keller in addition to the shoestars including Marissa Tremblay, Chelsea Willett, Matt Fox, Alka Tripathy, Sonia Tikoo-Schantz, Becky Reverman, and Nick Fylstra. I also want to acknowledge my fellow fifth years,

and Ben Nault.

I would also like to thank my parents for always supporting me, even when my decision was to move halfway across the country for grad school. You both taught me how to be a hard worker and your support has pushed me to pursue my dreams. I particularly want to thank you both for not discouraging me from picking up rocks and taking them home as a kid. I would not be where I am today without you. I also want to thank my sister, whose love and support has pushed me along my way.

I can't get through these acknowledgments without thanking my loving husband. You moved across the country with me, have picked me up when I have fallen down, and have constantly been there to lean on when I needed support. I could not have done this without you. I also want to thank your parents, who let me take their son across the country and who have welcomed me into their family.

Lastly, I'd like to acknowledge the sources of funding for this work including the National Science Foundation who awarded me a graduate student research fellowship, the Geological Society of America/ExxonMobil and the Paleontological Society, whose research grants helped fund field campaigns, and the Institute for Rock Magnetism, particularly Josh Feinberg, Mike Jackson, and Bruce Moskowitz, for always welcoming me with open arms and for giving me a visiting fellowship without which I would not have been able to complete the third chapter of this dissertation

Chapter 1. Introduction

The mass extinction at the Cretaceous-Paleogene boundary (KPB) marks one of the most important biotic turnover events in Earth history, resulting in the collapse of dinosaur-dominated ecosystems and the initiation of a new phase of mammalian radiation (Wilson, 2013, 2014). While the event at the KPB is not the most severe mass extinction in Earth history, it is important to study for several reasons. First, more than 350 KPB sites exist worldwide, making the KPB one of the best-recorded mass extinction events in Earth history (Schulte et al., 2010). These sites are found on all seven continents, are recorded in the Pacific and Atlantic oceans, and include both marine and terrestrial localities (Schulte et al., 2010). Second, the KPB mass extinction event has significant implications for our understanding of the effects of abrupt climate change and volcanic hazards. This event also has important implications for our understanding of evolution, specifically mammalian diversification. The first million years of the Paleogene (Pal.) witnessed rapid mammalian evolutionary change, including increases in average body size, morphological disparity, and taxonomic richness (Alroy, 1999; Halliday and Goswami, 2015; Wilson 2014). Further, many orders of modern mammals appear to diverge within this period, including early primates, making the earliest Paleogene important for the study of both ancient and modern faunas (Meredith et al., 2011). Lastly, the Cretaceous-Paleogene mass extinction is one of the few geologic events that captures the public imagination, providing Earth scientists with the opportunity to teach the general public about phenomena such as extinction, evolution, and climate change, which are important to understanding ongoing anthropogenic environmental crises.

1.1 Impact vs. Volcanism: Brief history and current state of research

The KPB mass extinction event has been intensely studied for many decades, however the relative importance of potential causes of the mass extinction events and environmental change, such as voluminous ($>10^6$ km^3) volcanic eruptions of the Deccan Traps (DT, in modern-day India) and the large impact recorded by the Chicxulub crater (~180 km in diameter), remains contentious (Schulte et al., 2010; Archibald et al., 2010; Courtillot and Fluteau, 2010; Keller et al., 2010). The impact hypothesis first gained support nearly forty years ago with the discovery of an iridium anomaly, along with other platinum group elements, within a claystone layer at the KPB in Gubbio, Italy, Stevns Klint, Denmark, and Caravaca, Spain (Alvarez et al., 1980; Smit and Herogen, 1980). The Ir-peak has since been found at other KPB sites around the world and is shown to co-occur with impact-indicative ejecta such as spherules, shocked minerals, and Ni-spinels (e.g. Montanari et al. 1983, Bohor et al., 1990). The impact hypothesis was further bolstered by the discovery of the Chicxulub crater in the Yucatan peninsula, Mexico (Hildebrand and Boynton, 1990), which coincides in age with the KPB (Swisher et al., 1992; Renne et al., 2013). Impact models suggest that Chicxulub would have induced earthquakes (magnitude M≈11) and tsunamis, in addition to releasing large amounts of dust and climate altering gases (such as carbon dioxide and sulfate aerosols) into the atmosphere. Modeled environmental effects of the impact include global cooling, extended darkness (together forming an "impact winter" scenario), acid rain, and global wild fires (Toon et al., 1997; Pierazzo et al., 2003; Kring et al., 2007; Ivanov et al., 2005; Artemieva and Morgan, 2009; Goldin and Melosh, 2009). Physical evidence for many of these environmental effects is lacking, particularly for global wildfires (Harvey et al., 2008) and acid rain (Sheehan et al., 2006). However, recent studies

using TEX_{86} paleothermometry at KPB sections in Brazos River, Texas and New Jersey have found evidence for an abrupt cooling phase immediately after the KPB consistent with an "impact winter" scenario (Vellekoop et al., 2014, 2016).

Many have argued that the result of environmental effects brought on by the Chicxulub impact would be a geologically abrupt mass extinction (e.g. Robertson et al., 2004; Fastovsky and Sheehan, 2005; Goldin and Melosh, 2009; Schulte et al., 2010). Records of marine planktonic microfossils and terrestrial pollen and spores, are consistent with this hypothesis (e.g. Smit, 1990; Sweet et al., 2001; Bown, 2005; MacLeod et al., 2007; Nichols and Johnson, 2008; Vajda et al., 2001). However, records of protracted extinctions dominantly in non-marine settings and climate change in the Late Cretaceous challenge the notion that the impact was the sole cause of the KPB. In the terrestrial realm, evidence for ecological instability in the last ~400 ka of the Cretaceous has been observed in mammalian and amphibian faunas, which temporally correlate with other observed ecological changes such as turnover in paleoflora and palynoflora (Wilson 2005, 2014; Wilson et al., 2014; Wilf et al., 2003; Wilf and Johnson, 2004; Sweet and Braman, 2001). Records of dinosaur faunas show evidence of a diversity decline in the last 10 Ma of the Cretaceous (Archibald, 2014; Barrett et al., 2011), and additional evidence suggests that in the last ~ 2 Ma of the Cretaceous there was a decline in relative abundance of dinosaurs (Horner et al., 2011). It is difficult to observe changes in dinosaur abundance closer to the KPB due to poor preservation caused by small population size. To characterize potential environmental perturbations in the Late Cretaceous that affected terrestrial communities it is best to examine better-preserved and more abundant terrestrial faunas, e.g. mammals rather than dinosaurs (Archibald, 2014; Wilson et al., 2014), as there is a better chance of being able to detect faunal responses to ecological perturbations with a larger sample size. In the marine realm, changes in species richness, relative abundance, and geographic range of planktonic foraminifera, in addition to protracted extinctions of mollusks are also observed in the Late Cretaceous (Kucera and Malmgren, 1998; Tobin et al., 2012). In general, these trends observed within Late Cretaceous communities temporally correlate with changes in climate. Records of oxygen isotope composition of planktonic foraminifera and marine macrofauna, leaf margin analysis of paleofloras, and clumped carbonate isotope and TEX_{86} paleothermometry show evidence for a warming event (about 5–6ºC) approximately 500–600 ka before the KPB followed by a cooling event (about 8 ºC), approximately 100 ka before the KPB (Li and Keller, 1998; Wilf et al., 2003; MacLeod et al., 2005; Tobin et al., 2012; Petersen et al., 2016; Vellekoop et al., 2014, 2016). Taken together, this evidence suggests that ecological changes were happening prior to the impact, and that it therefore may not have been the only event contributing to the KPB mass extinction.

In addition to the Chicxulub impact, the Deccan Traps in western India have long been cited as a potential cause of the KPB mass extinction (McLean, 1979, 1980, 1985; Courtillot et al., 1986). The Deccan hypothesis was first bolstered by Dewey McLean (1979, 1980, 1985) who suggested that greenhouse gases emitted from the Deccan Traps could have caused the mass extinction. However, this hypothesis did not gain traction until Vincent Courtillot and colleagues demonstrated the first convincing evidence that the majority of the Deccan Traps erupted around the KPB, dominantly within the short, < 1 Ma, span of magnetic polarity chron C29r (Courtillot et al., 1986, 1988; Duncan and Pyle, 1988; Vandamme and Courtillot, 1992). The Deccan Traps were later suggested to have erupted in three pulses: the first pulse starting ~ 2 Ma before the KPB and ending well before it, the second starting around the C30n/C29r transition and extending until the KPB, and the third beginning around the C29r/C29n transition and extending

into C29n (Chenet el al., 2007, 2008, 2009; Keller et al., 2008). The second pulse of magmatism was cited to encompass over 80% of the Deccan Traps volume and is often called upon as the source of the late Maastrichtian warming and cooling events described above (Li and Keller, 1998; MacLeod et al., 2005; Nordt et al., 2003; Tobin et al., 2012, 2014; Wilf et al., 2003; Thibault and Husson, 2016; Chenet et al., 2009). The evidence for these pulses was based on imprecise K/Ar ages (Chenet et al., 2007) and what we know now to be improper placement of the KPB within the Deccan lava pile (Renne et al., 2015). Two recent high-precision geochronologic studies performed in the Western Ghats region of western India, one utilizing the U/Pb zircon dating technique (Schoene et al., 2015) and the other using $^{40}Ar/^{39}Ar$ geochronology (Renne et al., 2015), have now shown that the Deccan Traps volcanism in the Western Ghats did not erupt in pulses as described in Chenet et al. (2007), but instead erupted relatively continuously starting at the C30n/C29r transition, extending into C29n (Schoene et al., 2015; Renne et al., 2015; note that the KPB falls approximately halfway into C29r). New work also suggests that most of the known volume of Deccan lava (with an unknown volume existing offshore) erupted after the KPB (Richards et al., 2015; Renne et al. 2015), potentially triggered by seismic energy associated with the Chicxulub impact (Richards et al., 2015). It has been suggested that the voluminous flows erupting after the KPB may have delayed ecosystem recovery from the mass extinction (Renne et al., 2015). Hypothesized environmental effects associated with the eruption of the Deccan Traps include global warming, cooling, ocean acidification, and acid rain due to the input of magmatic gases, such as CO_2 and sulfate aerosols, into the atmosphere (Wignall, 2001; Self et al., 2014; Ernst and Youbi, 2017). However, the actual mechanisms by which volcanic gases perturb global environments are not well understood and modeled outcomes are largely dependent upon variables such as the amount of and specific species of gas released and the tempo of eruptions, which are not well constrained (Self et al., 2014).

With the combination of existing evidence of ecological stress, climate change, and the eruption of the Deccan Traps in the Late Cretaceous, it is hard to believe that the Chicxulub impact was the only contributing factor to the KPB mass extinction. As such, many authors have argued for a scenario involving multiple perturbations that ultimately led to a global-scale mass extinction event (Wilson, 2014, Wilson et al., 2014; Archibald et al., 2010; Richards et al., 2015; Renne et al., 2016). A common model for this multiple cause extinction event is press-pulse (White and Saunders, 2005; Arens and West, 2008), in which press mechanisms occurring over long time intervals ~ 100 ka (Deccan Traps), cause ecological stress and leave ecosystems more susceptible to pulse mechanisms (Chicxulub impact, large pulse of magmatism) which occur on shorter timescales (< 10 ka). This model has gained support from recent ecological studies which suggest that ecosystems may respond to a gradual accumulation of environmental perturbations in a nonlinear fashion, suggestive of an "ecological threshold" above which sudden, largescale, biotic changes may occur (e.g. Scheffer et al., 2001; Scheffer and Carpenter, 2003; Huggett, 2005). Records of changes observed in terrestrial faunas including salamanders and mammals (Wilson, 2014; Wilson et al., 2014), are consistent with expected results predicted from press-pulse models, but key features such as the robustness of biotic patterns, relationship between the Late Cretaceous ecological decline and the more severe extinctions seen at the KPB, scale of Late Cretaceous environmental perturbations, and most basically temporal correlations among these events require further investigation before this model can be adequately tested (Wilson et al., 2014).

In summary, the last four decades of research have amassed an immense amount of data

that has not made the impact vs. volcanism debate any clearer. What is seen are two events that are both temporally linked to the mass extinction, with similar predicted environmental consequences (albeit acting on different time scales), that may have ultimately worked in tandem. With this knowledge in hand, we can now move beyond the impact vs. volcanism debate and begin to form hypotheses about extinction mechanisms that can be tested in the geologic record. However, before we can begin to test extinction mechanism hypotheses, a high-precision global chronologic framework that outlines the temporal sequence of biotic changes (both within the terrestrial and marine realms), climatic changes, and proposed perturbations (i.e. impact, volcanic eruptions) is needed.

1.2 Developing a global chronostratigraphic framework

In this dissertation, I present work developing this high-precision global chronologic framework using $^{40}Ar/^{39}Ar$ geochronology and paleomagnetism focusing on two major areas of study: 1) refining the timing and tempo of terrestrial ecosystem change around the KPB, and 2) calibrating the geomagnetic polarity timescale (GPTS), and particularly the timing and duration of magnetic polarity chron C29r.

1) Understanding the timing and tempo of terrestrial ecosystem change is important for several reasons. First, few studies have quantified high-resolution temporal patterns of extinction and recovery for terrestrial biota, despite the fact that the ecological result of the KPB event in the terrestrial realm is one of the most dramatic examples of ecosystem collapse and replacement in Earth history (Sereno, 1999; Pearson et al. 1999; McGhee et al., 2004). Secondly, the first million years of the Paleogene saw rapid mammalian evolutionary change and it is suggested that many orders of modern mammals diverged around the KPB, making it important for the study of both ancient and modern faunas (Meredith et al., 2011, O'Leary et al., 2013). Lastly, to understand the role Deccan Traps volcanism played in the end Cretaceous mass extinction event and subsequent recovery (and to test the Chicxulub triggering hypothesis e.g. Richards et al. 2015), it is first important to constrain the tempo and timing of Late Cretaceous ecological decline in addition to post-extinction recovery, particularly for the terrestrial realm, which may have experienced effects of Deccan volcanism (particularly cooling) more drastically than marine environments (Wignall, 2001).

2) The GPTS, if calibrated using high-precision chronology, has the capacity to greatly improve our understanding of the events around the KPB. Presently, the GPTS is used for age control in numerous KPB studies including the timing of volcanism in the Deccan Traps, a majority of studies based on marine sections, and studies on climate and ecological change across the KPB (Chenet et al., 2009; Li and Keller, 1999; Tobin et al., 2014; Wilson, 2014; Wilson et al., 2014). The current calibration of the GPTS for circum-KPB polarity chrons (30n-28n) draws heavily on astronomical tuning (Ogg, 2012), using Swisher et al.'s (1993) $^{40}Ar/^{39}Ar$ age for the KPB as a calibration point. Problems with this calibration include: the KPB age from Swisher et al. (1993) has been shown to be ~200 ka too old per reanalysis (Renne et al., 2013), astronomical records for the KPB fail to account for the possible biasing effects of climate signals other than those due to orbital forcing (e.g. Deccan Traps and Chicxulub impact), and complex sedimentation has been recorded in marine sections immediately following the KPB, which can obscure orbital signals and complicate cyclostratigraphic interpretation (e.g., Westerhold et al., 2008). Further, polarity reversal ages given in the GPTS do not include uncertainty estimates, making them unsuitable for high-resolution studies (Ogg, 2012). A precisely calibrated GPTS would provide absolute age constraints for sections without dateable

tephras, would provide a means of comparing results between marine and terrestrial sections at a high-level, would test the accuracy of astronomically tuned chronologies (which are primarily used in marine sections for age control), and would provide a means for correlating biotic changes with observed climatic changes, and proposed perturbations at high-precision.

The field study for this dissertation is within the Hell Creek region of NE Montana, USA. The Hell Creek region is an ideal location for this work because:

(1) It is one of few KPB sites globally where high-resolution geochronology is possible (Renne et al., 2013).

(2) It is among the most thoroughly sampled terrestrial records of paleontological, geochemical, and geological data across the KPB (Clemens, 2002).

(3) It contains suitable lithologies for paleomagnetic sampling (Archibald et al., 1982; Swisher et al., 1993; LeCain et al., 2014).

Over 60 thin (~1mm–10 cm) silicic tephras have been identified in the Hell Creek region, ranging over 70 m of stratigraphy. Every tephra examined to date contains suitable material (K-feldspar) for high-precision $^{40}Ar/^{39}Ar$ dating and chemical analysis, and past studies have yielded resolutions as precise as ±10 ka and absolute accuracy in the range of ±40 ka, for ~ 66 Ma deposits (Renne et al., 2013). Material utilized in other high precision dating techniques (such as U/Pb) is also present, but has been shown to be hindered by inheritance (Mitchell, 2014). The Hell Creek is one of the only locations that preserves mammalian fossil localities from late Cretaceous–early Paleogene in stratigraphic superposition (comprising Lancian [La], Puercan [Pu], and earliest Torrejonian [To] North American Land Mammal Ages [NALMA]; Clemens, 2002) and intensive sampling of vertebrate faunas over ~50 years has yielded over 150,000 vertebrate microfossils (over 12,000 of which are mammal), from > 500 localities (Wilson, 2014).

1.3 Dissertation Outline

In chapter two (modified from Sprain et al., 2015) I develop a high-precision chronostratigraphic framework for fluvial sediments within the Hell Creek region, MT, using high-precision $^{40}Ar/^{39}Ar$ geochronology. Sanidine from 15 tephra samples was analyzed in 1,649 total fusion experiments (1,597 on single crystals) and 12 incremental heating analyses of multigrain aliquots. Ages were determined for 13 distinct tephras, with ±30 ka precision, ranging in time from ~300 ka before the KPB to 1 Ma after it (Sprain et al., 2015). By tying these results to paleontological records, this work is able to constrain the timing of faunal decline and recovery in addition to calibrating late Cretaceous and early Paleocene North American Land Mammal Ages biostratigraphy (Sprain et al., 2015). Results show that pre-KPB ecological decline occurred within the last 200 ka of the Cretaceous, depauperate basal Paleogene Puercan1 disaster fauna are constrained to the first 70 ka of the Paleogene, and that faunal recovery transpired less than ~925 ka after the KPB (Sprain et al., 2015). Application of the new results to previous magnetostratigraphic data from the Hell Creek indicate an appreciably compressed duration for chron C29r, with a minimum estimate of 345 ± 38 ka compared to the 710 ka estimate from the Geologic Time Scale 2012 (Ogg, 2012). This short estimate for the duration C29r suggests one of two things. First, it may suggest that all previous estimates of the duration of C29r are off by a factor of two, which further would imply that the astronomically tuned chronologies used to determine the previous ~710 ka estimate are erroneous by as many as four 100 ka eccentricity cycles. This new result may also suggest that the past placement of either the

C30n/C29r transition, the C29r/C29n transition, or both in the Hell Creek region was incorrect. In order to investigate these results, a complete rock magnetic characterization of sediments from the Hell Creek region was undertaken. The work from this chapter served as the framework for chemical and isotopic analyses performed by Ickert et al. (2015).

The magnetic properties of a rock are a function of the concentration of magnetic materials, the composition of magnetic minerals, and the particle size of magnetic materials. Many magnetic parameters can be sensitive to one, two, or all three of these variables. By characterizing these magnetic parameters using the appropriate rock magnetic techniques, it is possible to infer the mineralogy, concentration, and grain size of the magnetic particles that are within a geologic sample. In chapter 3 (modified from Sprain et al., 2016), I use rock magnetic techniques to assess the reliability of Hell Creek sediments as magnetic recorders by answering these three questions:

1) What magnetic mineralogy is present in these sediments, and what is holding the remanence?
2) What is the grain size of the magnetic particles holding the remanence in these deposits?
3) Based on mineralogy and grain size, what is the likelihood that these sediments could or have acquired secondary magnetizations?

Results from extensive rock magnetic analyses suggest that sediments from the Hell Creek region in Montana are composed of three principal magnetic minerals in various proportions: goethite (FeOOH), compositionally intermediate titanohematite ($Fe_{2-y}Ti_yO_3$; $0.5 \leq y \leq 0.7$), and magnetite/titanomagnetite ($Fe_{3-y}Ti_yO_4$). The dominant ferrimagnetic mineral by mass is intermediate composition titanohematite with compositions ranging from y = 0.53–0.63 (see above). The dominant magnetic remanence carrier, however, is probably magnetite and titanomagnetite. Intermediate titanohematite has similar properties to intermediate titanomagnetite, except for its unique self-reversing property whereby under certain conditions during cooling through its Curie temperature, the mineral acquires a magnetic direction antiparallel to the applied field. When this mineral is a part of detrital remanent magnetizations (DRM) held in sedimentary deposits, this self-reversing property is masked making identification difficult using traditional rock magnetic techniques. To ease the identification of this mineral, I developed the self-reversal test, which provides a unique identifier of intermediate titanohematite, while simultaneously assessing how much remanence is held by this phase. Both intermediate titanohematite and intermediate titanomagnetite are likely to carry primary magnetic remanence representative of the Late Cretaceous and Early Paleogene magnetic field. Goethite, on the other hand, is almost certainly secondary, meaning that it formed after the deposition of the Hell Creek sediments and it does not record magnetic directions representative of KPg time. Overall, these results show that sediments from the Hell Creek region are likely to be reliable paleomagnetic recorders, given that they have not been reheated above 200ºC and that care is taken to remove any remanence held by goethite (which cannot be removed by traditional alternating field demagnetization techniques). Considering that all past magnetostratigraphic studies performed in the Hell Creek region utilized alternating field demagnetization techniques, we conclude that the most likely scenario for the short duration of C29r calculated in Chapter 2 is misplacement of reversal boundaries, necessitating new magnetostratigraphy. The work from Chapter 3 further suggests that intermediate titanohematite is most likely present in other sedimentary basins in central North America, and that it may be a more important carrier of DRM than previously thought.

In chapter four, I provide constraints on the timing and duration of the most important

circum-KPB chron, C29r, using high-precision $^{40}Ar/^{39}Ar$ geochronology and magnetostratigraphy for fluvial sediments from the Hell Creek region. In this chapter I show results for 14 new magnetostratigraphic sections, representing 285 paleomagnetic specimens, and 18 new high-precision $^{40}Ar/^{39}Ar$ dates, comprising 1,148 single crystal total fusion analyses. Combined, these results provide six independent constraints on the age of the C29r/C29n reversal, with a weighted mean age of 65.726 ± 0.013/0.044 Ma, and two constraints on the C30n/C29r reversal, with a weighted mean age of 66.314 ± 0.052/0.068 Ma. Together, these results show that the duration of C29r was ~588 ka and that the placement of both the C29r/C29n and the C30n/C29r transition in a few of the past magnetostratigraphic sections is incorrect. These errors are most probably due to unremoved normal overprints, likely held by goethite, which cannot be removed by only alternating field demagnetization techniques. This result calls into question other magnetostratigraphic frameworks developed in central North American basins that were determined using only alternating field demagnetization techniques (e.g. the San Juan basin). Our new duration for C29r is generally consistent with the GTS2012 estimate of 710 ka (Ogg, 2012), and additionally is consistent with astronomically tuned chronologies (e.g. Thibault and Husson, 2016). The results from this chapter support the placement of Puercan1 disaster faunas within C29r, and recovered Puercan3 faunas within C29n, which is generally consistent with results from other North American basins. We further present new geochronologic data for the KPB yielding the most precise date yet, of 66.047 ± 0.008/0043 Ma.

Using this new high-precision chronologic framework developed in this dissertation, we can begin to tie records of ecological and environmental change, from both terrestrial and marine sections, together with records of Deccan volcanism and the Chicxulub impact, at high-precision. Upon first analysis, it appears that records of pre-KPB ecological stress, coincide with Late Maastrichtian climate change and Deccan Traps volcanism. However, using the estimated placement of the KPB with the Deccan lava pile presented in Renne et al. (2015), and Deccan volume estimates presented in Richards et al. (2015), it appears that 70% of the Deccan volume erupted after the KPB. This result calls into question whether the observed correlation between Late Maastrichtian climate change and Deccan volcanism is a cause and effect scenario, and if so, why larger climatic variations are not seen post-KPB.

Chapter 2: High-resolution chronostratigraphy of the terrestrial Cretaceous-Paleogene transition and recovery interval in the Hell Creek region, Montana

Adapted from Sprain, C.J., Renne, P.R., Wilson, G.P., and Clemens, W.A., Geological Society of America, Bulletin, v. 127, p. 393–409, 2015, doi:10.1130/B31076.1. An edited version of this paper was published by GSA.

Abstract Detailed understanding of ecosystem decline and recovery attending the Cretaceous-Paleogene Boundary (KPB) mass extinctions is hindered by limited constraints on the pace and tempo of environmental events near the boundary. To mitigate this shortcoming, high-resolution $^{40}Ar/^{39}Ar$ geochronology was performed on tephras intercalated between fossiliferous terrestrial sediments of the upper Hell Creek and lower Fort Union formations, in the western Williston Basin of northeastern Montana (USA). Tephra samples were collected from 10 stratigraphic sections spanning an area of ~5000 km^2. Several distinctive tephras can be correlated between sections separated spatially by as much as ~60 km. The tephras are thin distal deposits generally preserved only in lignite beds, which are interbedded with clastic deposits yielding vertebrate faunas of Lancian (late Maastrichtian) to Torrejonian (early Danian) North American Land Mammal Ages. Sanidine from 15 tephra samples was analyzed in 1,649 total fusion experiments (1,597 on single crystals) and 12 incremental heating analyses of multigrain aliquots. Ages were determined for 13 distinct tephras, ranging from 66.289 ± 0.051 to 64.866 ± 0.023 Ma, including only analytical uncertainties. This level of precision is sufficient to resolve the ages of all the coal beds that have served as a basis for a regional stratigraphic framework. The data confirm that the Hell Creek-Fort Union formational contact is diachronous, and further support the age of the KPB impact layer at 66.043 ± 0.010 Ma, or ± 0.043 Ma considering systematic uncertainties. Application of the new results to previous magnetostratigraphic data indicate an appreciably compressed time interval between the base of chron C29r and the top of chron C28r, with a maximum duration estimate of 1.421 ± 0.066 Ma. Most notable is the implied brevity of chron C29r with a maximum estimate of 457 ± 54 ka, possibly as brief as 345 ± 38 ka, compared to the 710 ka estimate from the Geologic Time Scale 2012 (GTS2012). Further, application of new results to terrestrial biostratigraphy adds higher precision to the timing and tempo of biotic change before and after the KPB. Our results indicate that the timing of pre-KPB ecological decline is constrained to the last ca. 200 ka of the Cretaceous, adding further support to the press-pulse extinction hypothesis. Additionally, the duration of the depauperate basal Paleogene Puercan1 disaster fauna is confined to a 70 ka interval. Faunal recovery in this region, indicated by the appearance of primitive members of the placental mammal radiation and the restoration of taxonomic richness and evenness, occurred within ca. 900 ka after the KPB. These results show that biotic recovery after the mass extinction in the terrestrial realm was more rapid than in the marine.

2.1 Introduction

The cause(s) of the Cretaceous-Paleogene (K/Pg) mass extinction remain contentious despite decades of intense scrutiny (Schulte et al., 2010; Archibald et al., 2010; Courtillot and Fluteau, 2010; Keller et al., 2010). The impact hypothesis (Alvarez et al., 1980) has gained broad support, bolstered by the discoveries of Ir anomalies, shocked quartz, and spherules at Cretaceous-Paleogene boundary (KPB) sites worldwide and of the Chicxulub impact structure (Schulte et al., 2010 and references therein). However, evidence of pre-KPB originations and

extinctions as well as paleoenvironmental change (Chenet et al., 2009; Archibald et al., 2010; Wilson, 2005, 2014; Wilson et al., 2014b) involving large climate swings before the KPB (Li and Keller, 1999; Stüben et al., 2003; Wilf et al., 2003; Tobin et al., 2012, 2014) challenge the notion that the impact was the sole cause of the KPB extinctions. The evidence for abrupt extinctions consistent with an impact killing mechanism comes mainly from marine records (D'Hondt, 2005), whereas records of terrestrial vertebrate animals show evidence of more prolonged ecological decline (Wilson, 2005, 2014; Wilson et al., 2014b) starting in the latest Cretaceous. Terrestrial and marine records also yield disparate results for the tempo of ecosystem recovery, e.g., the restoration of atmospheric $\delta^{13}C$ to pre-impact values appears to have occurred orders of magnitude more rapidly than in the oceans (Renne et al., 2013).

In this paper, we present a new high-precision $^{40}Ar/^{39}Ar$ geochronology that constrains the ages of faunal and floral assemblages in a key region of North America. These data delimit the rates and nature of terrestrial ecosystem recovery at a local scale, and begin to enable comparisons at larger, more regional scales with high temporal resolution. Such comparisons will ultimately clarify whether or not terrestrial biotic transitions were regionally diachronous, which can illuminate the specific ecological mechanisms for the terrestrial KPB extinctions and subsequent biotic recovery. In addition, applying our results to existing magnetostratigraphy allows us to test currently accepted calibrations of the Geomagnetic Polarity Time Scale (GPTS) in relevant parts of the time scale (i.e. chrons C30n through C28n). An improved calibration for the GPTS will allow for a detailed comparison between KPB events in marine and terrestrial realms, which is currently hindered by a lack of high-precision age control, especially in the former. The main source of age control in marine records comes from magnetostratigraphy, whose accuracy depends on both calibration of the geomagnetic polarity time scale (GPTS) and correlation to the GPTS. Orbital tuning offers higher age resolution but also depends on correlation to provide an anchor.

2.2 Western Williston Basin

The Williston Basin located primarily in NW United States is among the most thoroughly sampled sources of geological, paleontological, and paleoecological data used to study changes within the terrestrial realm across the Cretaceous-Paleogene boundary (KPB) (e.g., Hartman et al., 2002; Wilson et al., 2014a, and references therein). Within the Williston Basin, two formations span the KPB: the Hell Creek Formation (mostly Cretaceous), and Tullock Member of the Fort Union Formation in the western part of the basin and the Ludlow Member of the Fort Union Formation (mostly Paleogene) in the eastern part of the basin. In Canada, the Frenchman Formation is broadly correlative to the Hell Creek Formation, and the Ravenscrag Formation is broadly correlative to the Fort Union Formation (Hartman, 2002). These formations were deposited in predominantly fluvial systems and comprise siltstones, shales, and lignites, representative of flood plain deposits, and sandstones, mainly representative of channel deposits (Gill and Cobban, 1973; Cherven and Jacob, 1985; Fastovsky, 1987).

In the western Williston Basin, south and east of Fort Peck Reservoir (Hell Creek region, Montana), the Tullock Member and (to a lesser extent) the Hell Creek Formation, contain numerous sanidine-bearing silicic tephras, which have been radioisotopically analyzed to produce a generalized chronostratigraphy (Swisher et al., 1993, fig. 2.4) wherein occurrences of fossils are dated by bracketing tephras. The tephras are almost exclusively found within lignite beds, probably due to preservational bias. Lignites are rare in the Hell Creek Formation and become more numerous in the Fort Union Formation, suggesting increased hydraulic flux and a

rise in water table (Fastovsky, 1987). The contact between the Hell Creek and Fort Union formations (and the historical placement of the KPB) is placed at the first laterally continuous lignite above the stratigraphically highest occurrence of the unreworked remains of non-avian dinosaurs (Calvert, 1912; Brown, 1952; Clemens and Hartman, 2014; Moore et al., 2014; Hartman et al., 2014). In our study area in NE Montana, the lignite that defines the contact between the Hell Creek and Fort Union formations is named the Z coal, with successive lignite units in the Tullock Member receiving successive letter designations up through U (Collier and Knechtel, 1939). We will use the term "coal" when referring to named lignite deposits for consistency with usage by Collier and Knechtel (1939) and subsequent workers.

Early definitions of the Z coal clearly state that it is probably not a single continuous unit, but rather a sequence of lignite lenses at approximately the same stratigraphic position (Collier and Knechtel, 1939). Subsequent workers have modified the term Z coal to specify occurrences of subunits in particular areas, for example, IrZ and MCZ. Our field observations indicate that many of the other named lignites are similarly laterally discontinuous, and this is further substantiated by our $^{40}Ar/^{39}Ar$ results.

Currently, the KPB is recognized in this region (Clemens and Hartman, 2014; Moore et al., 2014; Hartman et al., 2014) above the highest stratigraphic appearance of *in situ* fossils of non-avian dinosaurs, below the lowest occurrence of unreworked Paleocene pollen (Bercovici et al., 2009), locally by the presence of a clay horizon containing an iridium anomaly, shocked quartz, and spherules that is interpreted as an impact debris horizon, and by a -1.5 ‰ to -2.8 ‰ carbon isotope anomaly which has allowed the recognition of the KPB in locations where the impact horizon is not preserved (Arens and Jahren, 2000, 2002; Arens et al., 2014). The KPB thus defined is not always coincident with the Hell Creek-Fort Union formational contact (Johnson, 1992; Pearson et al., 2001; Nichols and Johnson, 2002; Arens and Jahren, 2002; Clemens and Hartman, 2014) and can be either above or below the contact depending on location.

Over forty distinct tephra deposits have been identified in our field area, mainly within lignite beds, spanning approximately 70 m of section from the upper Hell Creek Formation through the Tullock Member of the Fort Union Formation. Every one of these tephras examined to date contains sanidine, many of sufficient size to permit high-precision dating of single crystals. Thus, the Hell Creek region provides an opportunity to establish a chronostratigraphic framework of unprecedentedly high resolution for study of the evolution of terrestrial ecosystems from just before the KPB through the recovery from this remarkable event in Earth history. In particular, this work serves to calibrate the ages of mammalian faunas that have been assigned to North American Land Mammal Ages (NALMA) by previous studies (Archibald, 1982; Lofgren, 1995; Clemens, 2002; Wilson, 2005, 2013, 2014; Clemens and Wilson, 2009).

2.3 Sampling

Sampling for this work was conducted in 2010–2012, at locations shown in Figure 2.1. Stratigraphic sections at these locations either (1) coincide with sections characterized in previous studies, or (2) were measured and described in the course of our work. Sampled sections are somewhat bimodally distributed geographically, hence we group them into eastern and western areas.

Western Area

The western portion of our field area is primarily within northern Garfield County. The

first radioisotopic age determinations of tephras in the area were made at a site we identify as the Lerbekmo Site (47°30'57.66"N/106°56'11.64"W, LB in Figure 2.1) (Folinsbee et al., 1963). All locations herein are based on the WGS84 datum. Outcrops of the Z coal at this location are present in low buttes ~150 m east of the road (Garfield County Route 543) linking the town of Jordan with the Hell Creek State Recreation Area. Here the Z coal is ~160 cm thick and the impact claystone is present at the base of the coal (Renne et al., 2013 and references therein). Tephras from the Z coal have been sampled by a number of workers at this site, which in the literature has been referred to by several other names (e.g., Divide Knob, Hell Creek Marina Road) (Folinsbee et al. 1963; Shafiqullah et al., 1964; Baadsgaard and Lerbekmo, 1980, 1983; Baadsgaard et al., 1988; Renne et al., 2013; Hartman et al., 2014). The most recent age determinations, using high precision $^{40}Ar/^{39}Ar$ dating, for two tephras found within the Z coal were presented by Renne et al. (2013) and are referred to in this study (Fig. 2.4A).

In a map compiled in 1977 and modified in 1980, Archibald (1982) mapped the complex of Z coals from the region between Brownie Butte (bb) and Hell Hollow (HH), a distance of ~12 km. In this area, the Z coal is subdivided by beds of mudstones and siltstones up to a thickness of 13.7 m (Archibald, 1982). This complexity was recognized by distinguishing an upper and a lower Z coal. Brownie Butte is ~6 km west of the Lerbekmo Site (see Appendix A.3). As a result of erosion of the intervening valley of Hart Creek and ground cover, the exact stratigraphic relationships of the Z coal at the Lerbekmo Site and the upper and lower Z coals in the vicinity of Brownie Butte have yet to be determined.

The westernmost extent of Archibald's mapping is Hell Hollow (HH). From 1977 into the early 1980s prospecting and mapping were extended southwestward into an area the field parties dubbed Hauso Flats (HF). At an isolated butte in the flats, now called Iridium Hill, both the upper and lower Z coals are exposed and separated by ~18 m of mudstones and siltstones (Swisher et al., 1993; Renne et al., 2013). In the summer of 1980 the impact claystone was discovered within what had been mapped as the lower Z coal (Alvarez et al., 1983; Clemens and Hartman, 2014) and has subsequently been shown to temporally correlate with the Chicxulub bolide impact and the KPB (Renne et al., 2013). Swisher et al. (1993) renamed the lower Z coal of Archibald the Iridium Z (IrZ) coal and the upper Z coal the Hauso Flats Z (HFZ) coal. We follow the usage of Swisher et al. (1993). As noted in Figure 2.4A (Hauso Flats section), tephras in both the IrZ and HFZ have previously yielded radioisotopic age determinations (Renne et al., 2013). In the western research area, we collected additional samples from tephras of IrZ and HFZ coal sites as well from the Y, W, V, and U coals.

Hell Hollow. The Hell Hollow (HH) locality is approximately 3 km NE of Hauso Flats. At this location both the IrZ and HFZ coals recognized at Hauso Flats have been mapped (Archibald, 1982). The IrZ at Hell Hollow is in places incised by the Hell Hollow Channel sandstone, which contains vertebrate fossils assigned to the early Puercan (Pu1) NALMA (Swisher et al., 1993) (University of California Museum of Paleontology locality (UCMP loc. V74111). The Hell Hollow Channel sandstone is capped by the HFZ. Tephras from both coals, correlated in the field with those dated by Renne et al. (2013) at Hauso Flats, were sampled for dating.

The IrZ coal at this locality (47°32'3.60"N/107°10'22.14"W) is ~10 cm thick and contains a ~1- to 4-mm-thick, pink (Munsell color, 5 R 8/2), sanidine-bearing tephra. The thickness of the tephra is highly variable and it is absent from some outcrops, possibly as a result of erosion by the Hell Hollow Channel, which locally cuts down into or through the IrZ coal.

The HFZ in this location (47°32'23.16"N/107°10'16.62"W) is 2–3 m thick and contains at least two tephras. One tephra is ~0.5–1.0 cm thick and occurs roughly 1 m above the base of the

coal. This tephra is red (10 R 5/4) in color and contains sanidine. Coarse pseudomorphs of cuspate glass shards are apparent. A second ~5-cm-thick tephra occurs roughly in the middle of the coal, ~12 cm above the first deposit. This tephra is red (10 R 5/4) in color and contains very fresh, coarsely crystalline, euhedral sanidine crystals and biotite. The upper tephra was sampled for dating.

Nirvana. An additional IrZ coal tephra was sampled at a locality (47°31'37.14"N/107°11'10.98"W) informally known as "Nirvana" (NV) ~1 km SW from our Hell Hollow locality. In this location, the IrZ coal is ~15 cm thick and a 1- to 3-mm-thick, pink (5 R 8/2) tephra appears roughly 1 cm from the top of the coal. The tephra contains abundant sanidine crystals that were used for $^{40}Ar/^{39}Ar$ dating. A channel filling 1.6–6.3 m below the base of the IrZ coal has yielded a Lancian vertebrate fauna (UCMP loc. V77130).

Garbani Hill. The Garbani Hill (GH) locality (47°30'57.60"N/107°4'6.06"W) is ~8 km SE from the Hell Hollow area. The Garbani Quarry is in an exposure of the Garbani Channel filling on the SW slope of Garbani Hill. It is not included in the Garbani Hill section (Fig. 2.4A). The fossiliferous strata in the quarry have been divided into a series of sublocalities. Of these, the most productive is UCMP loc. V73080. The quarry has yielded a local fauna probably of Pu3 age (Clemens, 2013).

In this area the Y coal occurs as a doublet. Locally the Garbani Channel can be shown to have cut down through the X coal to the level of the Y coal. To the south in the Biscuit Butte (BB) area the W coal caps the channel filling.

At Garbani Hill, we collected tephras from the Y coal doublet. The lower Y coal in the doublet at Garbani Hill is ~50 cm thick, with roughly 1 m of shale separating the lower coal from the 1-m-thick upper Y coal. In the lower coal a 1- to 3-cm-thick pink-grey (5 YR 8/1) tephra occurs ~2 cm below the top of the coal. This tephra contains abundant sanidine and was collected for dating.

Within the upper Y coal two tephras were identified. Approximately 50 cm from the base of the coal a massive grey (10 R 8/2) tephra is located. This tephra is 20–30 cm thick, and contains abundant sanidine crystals. Ten cm above this deposit the second tephra is located. This tephra is roughly 2 cm below the top of the upper coal and is ~1–2 cm thick with a distinctive pink (5 R 8/2) color. In this location, the tephra is unconsolidated and laterally discontinuous. The lower massive tephra was selected for dating due to the coarser grain size of sanidine crystals.

The X coal as mapped by Archibald (1982) also crops out at this locality, but no tephra deposits could be identified within the coal here.

Saddle Section. Approximately 1 km SW from Garbani Hill the W coal occurs as a doublet at the informally named "Saddle Section" (SS) locality (47°30'34.80"N/107° 4'54.90"W). Each coal of the doublet is ~1 m thick with ~2 m of sediment between the two. The lower coal contains at least six tephra layers varying in thickness from 1 to 40 mm. All tephras have apparent sanidine crystals and are either pink (5 R 8/2) or grey (5 YR 7/2).

The upper coal of the doublet contains at least eight distinct tephra layers that vary in thickness from a few mm to 4 cm and again are pink (5 R 8/2) or grey (5 YR 7/2). A ~4-cm-thick grey (5 YR 7/2) tephra with conspicuously coarse sanidine crystals occurs ~6 cm below the top of the coal. This is the second tephra counting down from the top of the coal, and was used for

dating.

Biscuit Butte. Approximately 2.5 km to the south of the Saddle Section the W, V, and U coals crop out on the side of the basin just to the north of Biscuit Butte (BB). At this location, we collected tephra samples from the U (47°29'13.08"N/107° 4'7.64"W) and V (47°29'21.84"N /107° 4'23.82"W) coals. The W coal at Biscuit Butte, as at the Saddle Section and elsewhere in the region, is also a doublet with abundant tephra deposits (six or more in each coal). Due to stratigraphic position and distinctive grain size, we were able to identify the tephra we collected and dated from the top of the upper unit at the Saddle Section and are confident based on the distinctive number of tephras in each coal and stratigraphic position that this W coal outcrop at Biscuit Butte is time-stratigraphically correlative.

The V coal is located approximately 6 m above the top of the upper W coal, as shown (but not named) by LeCain et al. (2014). It is ~30 cm thick and contains one tephra, a ~0.5- to 1.0-cm-thick pink (5 YR 8/1) tephra found 7–10 cm below the top of the coal. This tephra was used for dating.

Thirteen meters above the V coal is the U coal, the base of which marks the contact between the Tullock Member and the overlying Lebo Member of the Fort Union Formation. At this location, the U coal is approximately 2.5 m thick and contains multiple sanidine-bearing tephras. Approximately 85 cm above the base of the coal, an 18-cm-thick grey-pink (5 YR 8/1) tephra occurs that we collected for dating. This tephra is almost certainly the same one analyzed by Swisher et al. (1993) based on the tephra's diagnostic thickness.

Horsethief Canyon. The Horsethief Canyon (HTC) locality is roughly 35 km south from Hell Hollow on the Bliss Ranch. Two coals were identified at this location, one crops out at the base of a channel sandstone deposit, and the other crops out at the top of that channel deposit. The channel deposit contains the Horsethief Canyon vertebrate fossil localities (UCMP locs. V73094 and V73095), which are earliest Torrejonian (To1) in age (Archibald et al., 1982; Clemens and Wilson, 2009). The coal at the base of the sandstone was tentatively identified as a coal termed UW coal by W. Rohrer of the USGS (Archibald, 1982). This coal (47°11'55.68"N/107°23'7.26"W) was sampled. The coal here is 1.45 m thick and contains over 18 distinct tephra deposits. Tephra deposits range in thickness from a few mm to a few cm. Most deposits are pink in color (5 R 8/2), and all appear to contain sanidine. Approximately 10 cm below the top of the coal we collected a coarsely crystalline 2- to 4-cm-thick tephra for dating. The tephra is grey (N7) in color and contains abundant sanidine crystals. Based on coal descriptions, particularly the great number of tephras, we believe this deposit correlates to the upper unit of the W coal, cropping out at our Saddle Section and Biscuit Butte localities.

Capping the channel sandstone deposit is a coal tentatively designated by Archibald (1982) as the U. The coal deposit sampled (47°11'37.74"N/107°24'6.06"W) is ~1 m thick and contains at least four tephra layers. A reddish-brown (10R 5/4) tephra roughly 4 cm thick located in the middle of the coal was sampled for dating. This tephra contains coarse crystals of euhedral sanidine.

Eastern Area

In the eastern part of our field area, primarily in McCone County, the base of the Tullock Member is exposed in the area between the valley of Bug Creek and, to the south, the valley of McGuire Creek. For over a century the valley of Bug Creek has been a focus of paleontological

and later, beginning in the 1960s, geological research (Clemens and Hartman, 2014). Recognizing differences in their geology, exposures of the Hell Creek Formation and Tullock Member in the valley of Bug Creek have been separated into two areas (see for example Fastovsky and Dott, 1986; Smit et al., 1987). To the east is the complex stratigraphic section exposed in Russell Basin. The western area includes the Bug Creek Anthills fossil locality (UCMP loc. V65127 and sub-localities). With the exception of the palynological study by Arens et al. (2014), the research reported here is based on outcrops in the western area.

In the valley of Bug Creek we followed a section measured by Archibald et al. (1982) from the Null coal in the Hell Creek Formation through the basal lignite of the Tullock Member exposed on the southern slope of the ridge overlooking the Bug Creek Anthills locality. Samples of tephra were taken from the basal lignite of the Tullock Member, which has been identified by a variety of names: Z coal of Sloan and Van Valen (1965), the unnamed coal of Smit and van der Kaars (1984, fig. 2.4); Coal with Marker, Facies D, of Fastovsky and Dott (1986); upper Z coal of Smit et al. (1987); and formational or upper Z coal of Rigby and Rigby (1990). Primarily based on palynological data this lignite and the sandstone on which it rests have been shown to be of earliest Paleocene age (Rigby et al., 1987).

To the south, the geology of the strata exposed in the valley of McGuire Creek and Black Spring Coulee was studied in detail by Lofgren (1995) who dubbed the basal lignite of the Tullock Member the McGuire Creek Z coal (MCZ). Two sections in this area were studied and tephras were collected from the included lignites. In both sections the MCZ was deposited on strata of earliest Paleocene age.

The MCZ coal in this area varies in thickness between ~0.5 m and 2 m, and has been found to contain between zero and four distinct tephras. The most distinctive tephra contains abundant biotite, is ~8 cm thick, and is typically grey-green (5GY 5/2) in color. This tephra has been used as a criterion for identification of the basal coal of the Tullock Member (Z coal) across McCone County and into eastern portions of Garfield County (Swisher et al., 1993). As noted below, on the basis of color, texture, thickness, stratigraphic position, and mineralogy, the two tephras sampled in the MCZ are correlative with the basal two tephras sampled in the valley of Bug Creek and tephras in the Z coals in our Haxby road (HX) and Lerbekmo (LB) localities in Garfield County. To the best of our knowledge, concentrations of iridium large enough to indicate the presence of an impact claystone have yet to be discovered in the eastern area.

Bug Creek. Five km north of McGuire Creek (47°40'52.50"N/106°11'44.04"W), we collected from the basal lignite of the Tullock Member above the Bug Creek Anthills vertebrate fossil locality (Sloan and Van Valen, 1965; UCMP loc. V65127 and sub-localities). The lignite in this section (BC) is ~1 m thick and contains three tephras. The lowermost of these, 31 cm above the base of the lignite, is 2 cm thick, pink (10 R 8/2), and contains abundant sanidine. The second tephra is 23 cm above the lowermost tephra, is ~6 cm thick, grey-green (5 GY 5/2), contains abundant biotite and underlies a ~1-cm-thick, pink (10 R 8/2) sanidine and altered biotite-bearing tephra 37 cm above. These tephras were collected for chemical analysis, but were not dated.

Below the Hell Creek-Fort Union formational contact (47°40'48.60"N/106°12'49.56"W) we collected a tephra in the Null coal mapped by Rigby and Rigby (1990), which is correlative with the Tonstein Lignite, based on stratigraphic position and presence of tephra, mapped several km to the south by Lofgren (1995). Possible correlatives of this coal, with one or two superficially similar tephras, are also present on the western side of the Big Dry Arm (Lofgren, 1995). The Null coal is the only known coal in the Cretaceous strata of the Hell Creek Formation

within this region that includes a tephra deposit. This coal lies ~50 m below the basal lignite of the Tullock Member at Bug Creek and is ~20 m below the Bug Creek Channel deposit at the Bug Creek Anthills locality. The coal is 17 cm thick, with a pink (5 R 8/2) 2-cm-thick tephra ~10 cm from the bottom of the coal. The tephra is fine grained, and small sanidine crystals were used for dating.

Z-line. The Z-line locality (ZL) is located ~1 km south of the McGuire Creek Bay, off of the eastern side of the Big Dry Arm of the Fort Peck Reservoir in McCone County (47°36'37.26"N/106°12'37.74"W). Here the MCZ coal is ~85 cm thick and contains two distinct tephras. A 2.0- to 2.5-cm-thick pink (10 R 8/2) tephra was located ~22 cm above the base of the coal and roughly 30 cm below a ~7-cm-thick, biotite-bearing grey (5 GY 5/2) tephra. The lower tephra does not contain biotite but does contain abundant euhedral sanidine crystals that were used for $^{40}Ar/^{39}Ar$ dating. The MCZ here caps the Z-line Channel of Lofgren (1995) that contains a Pu1 vertebrate fauna (UCMP loc. V84194). The two tephras correlate to the lower two tephras present in basal lignite of the Tullock Member at our Bug Creek locality based on color, thickness, texture, stratigraphic order, and mineralogy, particularly the appearance of biotite found in the upper tephra.

McGuire Creek. A second locality (MC) approximately 2 km NE of McGuire Creek was also sampled. The section here (47°37'47.50"N/106°10'12.40"W) corresponds to section sB of Lofgren (1995) that is the northeastern most section included in his cross section Y–Y'. At this locality, the MCZ coal is ~60 cm thick and contains three tephra deposits. The lowest tephra is ~3 cm above the base of the deposit. It is pink (10 R 8/2), 0.5- to 1.0-cm-thick, and contains abundant sanidine crystals. Approximately 11 cm above this tephra a 6- to 7-cm-thick, biotite-bearing grey (5 GY 5/2) tephra is present, ~26 cm below the third tephra deposit. The third tephra is ~7 cm below the top of the deposit. It is 3–5 cm thick, contains abundant sanidine crystals and altered biotite, and is pink (5 R 8/2) in color. The bottom two tephras best correlate with the two tephras identified in the Z-line and Bug Creek localities based on appearance (thickness, color, etc.), mineralogy, and stratigraphic order. Sanidine from the lowermost tephra was used for $^{40}Ar/^{39}Ar$ dating. At this locality, the MCZ overlies strata yielding the "Swamp Local Fauna" of Lofgren (1995, UCMP locs. V85085, V85086, V86093). The absence of dinosaurian remains suggests that this local fauna is of Paleocene age.

In addition to the MCZ coal, tephra in a second coal was identified in Lofgren's (1995) sB section for radioisotopic dating. This coal, which was mapped as the X coal by Rigby and Rigby (1990), is approximately 18 m above the MCZ coal. The lignite deposit here is ~1.8 m thick and the unit contains three distinct tephras. The first tephra is ~20 cm thick and located 25 cm from the bottom of the coal deposit. Roughly 46 cm above this tephra deposit a second tephra is located that is ~0.5 cm thick and contains abundant sanidine crystals. A third overlying tephra is located ~45 cm above the second tephra. It is 0.5 cm thick and is sanidine bearing. All tephra deposits are pink (10 R 8/2) in color. Sanidine from the second tephra was used for radioisotopic dating.

Haxby Road. In addition to locations in McCone County, our study has also identified numerous occurrences of the basal lignite of the Tullock Member in eastern Garfield County. One locality (HX) is just off the Haxby Road (47°38'49.80"N/106°33'37.14"W) ~26 km west of the McGuire Creek locality. At least two tephras have been identified in this 112-cm-thick coal deposit. The

lower of these is ~67 cm from the base of the coal, and is 2 cm thick, pink (10 R 8/2) and sanidine rich. Approximately 20 cm above this tephra there is a second 6- to 10-cm-thick grey (5 GY 5/2), biotite-bearing tephra. These tephras correlate based on color, thickness, texture, mineralogy, and stratigraphic positions with the two present at Z-line and the bottom two present at the McGuire Creek, Bug Creek and Lerbekmo localities. We collected sanidine from the lower tephra for $^{40}Ar/^{39}Ar$ dating.

2.4 $^{40}Ar/^{39}Ar$ Geochronology

The first geochronologic work conducted in the Hell Creek region used K/Ar, U-Pb and Rb/Sr methods to date the diagnostic thick tephra found within the Z coal at the Lerbekmo locality in Garfield County (Folinsbee et al., 1963; Shafiqullah et al., 1964; Baadsgaard and Lerbekmo 1980, 1983; Baadsgaard et al., 1988). Ages (uncorrected for modern constants) reported for this tephra range from 63.5–66.5 Ma with uncertainty estimated at ca. 500 ka. The first study to use a high-precision dating technique was conducted by Swisher et al. (1993) using the $^{40}Ar/^{39}Ar$ method on single crystals of sanidine and plagioclase to date tephras from the IrZ, Z, HFZ, W and U coals. Our study presents 15 high-precision $^{40}Ar/^{39}Ar$ sanidine ages from the Null, IrZ, MCZ, Z, HFZ, Y, X, W, V, U and unknown coals, two refining previous work and 13 from previously undated units, many in previously undescribed stratigraphic sections (Table 2.1). New ages are constrained with a relative precision of ~0.2%, over an order of magnitude better than early determinations and roughly half that of Swisher et al. (1993). The dates reported here represent a small fraction of the more than 40 tephras we have identified in the upper Hell Creek and Fort Union formations. A detailed account of methods utilized is given in Appendix A.1.

Results

Detailed discussion of the results for each sample is given in the Appendix. A summary of these results is given in Table 2.1. Pooled ages are given in Table 2.2. These are computed from two or more locations where appropriate, including data from Renne et al. (2013), as described in Appendix A.2.

2.5 Discussion

Sediment Accumulation Rates

Dated tephras in their stratigraphic contexts, and proposed correlations, are shown in Figures 2.4A–B. A noteworthy feature of our results is the consistency of average implied sediment accumulation rates (SARs), which vary between 5 and 10 cm/ka, within uncertainties, above the level of the HFZ. Below this level, SAR's are 19 ± 4 cm/ka between the Null coal and basal lignite of the Tullock Member at Bug Creek, 21 ± 7 cm/ka at Hell Hollow and 26 ± 8 cm/ka at Hauso Flats, both between the IrZ and HFZ coals. The significance of these higher rates is obscured by the fact that nearly half of the intervening Bug Creek section is poorly exposed. Slope wash in this interval suggests that the underlying strata are dominated by sandstones, which might be expected to record higher accumulation rates than finer-grained deposits that constitute much of the other sections. This hypothesis is supported by previous studies that have shown that the basal lignite of the Tullock Member rests upon a silty sandstone, referred to as the Big Bugger, at other outcrops of the basal lignite within the western part of the valley of Bug Creek (Fastovsky and Dott, 1986; Smit et al., 1987). Similarly, large channel deposits exist between the IrZ and HFZ coals at Hell Hollow and Hauso Flats.

The interval between dated tephra in the W to U coals in the Biscuit Butte section

exemplifies the consistency of SARs. The W–V and V–U intervals indicate similar SARs of 8 ± 4 and 7 ± 1 cm/ka, respectively. This is also seen between different locations for the same stratigraphic interval. The lowest SAR recorded in any section is that for the lower part of the Z coal at the Lerbekmo section. There, we ascribe the pooled age (66.043 ± 0.010 Ma) of the IrZ coal tephra to the iridium anomaly at the base of the Z coal, and the pooled age of 66.013 ± 0.015 Ma for the lower Z coal tephra as discussed in Appendix A.2. This 80-cm interval predominantly comprising lignite thus apparently represents 30 ± 18 ka, corresponding to a mean SAR of 3 ± 2 cm/ka. This rate is indistinguishable from SARs of 3–12 cm/ka estimated for similar-aged lignite in North Dakota (Chin et al., 2013).

Magnetostratigraphy and the Geomagnetic Polarity Time Scale

The relatively uniform SARs for each stratigraphic interval, regardless of location, support the validity of interpolating between dated tephras to constrain the ages of various features in these sections, including geomagnetic polarity reversals. Using polarity sequences from previous magnetostratigraphic studies in the study area (LeCain et al., 2014; Swisher et al., 1993; Archibald et al., 1982) we calculated reversal ages using linear interpolation between dated tephras and reversal boundaries. For this procedure, we placed reversals halfway between the bounding sample sites defining the reversal, and used half the distance between these bounding sites as the uncertainty. This estimate of uncertainty in placement of reversals amounts to the 100% confidence interval, provided that no systematic uncertainties exist in the paleomagnetic data. Uncertainty in the resulting chron boundary ages is dominated by the coarse spacing of samples defining the chron boundaries. With improved chron boundary placement in existing sections, and additional sections to test the applicability of linear SARs, it may be possible to improve calibration of the Geomagnetic Polarity Time Scale.

Base C29r. To calculate an age for the chron 30n/29r reversal we utilized a magnetostratigraphic section reported by Archibald et al. (1982) from the Bug Creek locality. At this locality, the reversal is bounded by two coals, the basal lignite of the Tullock Member ~30 m above the reversal and the Null coal ~21 m below. A distance of ± 1 m was used as a proxy for uncertainty in reversal placement. Using our $^{40}Ar/^{39}Ar$ age for the Null coal and our pooled age for tephras in the Z coal (see Appendix A.2 for the basis for calculation of pooled ages) we calculated a reversal age of 66.177 ± 0.032/0.044 Ma. However, we note that the two sites bracketing the reversal have within-site directional clustering that is reportedly indistinguishable from random (Archibald et al., 1982). Thus, we use the uppermost of six successive normal polarity sites having statistically non-random directional clustering as a maximum age for the base of C29r to calculate a maximum age of 66.195 ± 0.042/0.052 Ma. The most conservative possible constraint our data yield is that the base of C29r is younger than the age of the Null coal tephra dated at 66.289 ± 0.051/0.065 Ma.

Top C29r. The chron 29r/29n reversal age was calculated from the Pearl Lake magnetostratigraphic section reported in LeCain et al. (2014). This section is ~1 km NE from our Garbani Hill locality. LeCain et al. (2014) identified the IrZ coal, HFZ coal, and a Y coal stringer, traced to the Y coal at Garbani Hill, within the Pearl Lake locality. The reversal is bounded ~6 m above by the Y coal and ~10 m below by the HFZ coal. A distance of ± 1 m was used as a conservative proxy for uncertainty in reversal placement. Using our age for GC12-3 (the lower coal in the Y coal doublet from Garbani Hill) and our pooled age for the HFZ coal, a

reversal age of 65.832 ± 0.019/0.036 Ma was estimated. We note that the Y coal as recognized by Archibald et al. (1982) at Purgatory Hill, and by Swisher et al. (1993) at Hauso Flats, occurs less than 2 m above the top of C29r. The discrepancy between these relationships and that reported by LeCain et al. (2014) may reflect variable SARs, diachrony of the Y coal, or ambiguity in identification of the Y coal. In any case, our $^{40}Ar/^{39}Ar$ age is most straightforwardly attributed to the section of LeCain et al. (2014), thus we use this for the present purposes.

Top C29n. An age for the chron 29n/28r boundary was constrained using the Biscuit Butte magnetostratigraphic section reported by LeCain et al. (2014). The reversal at this locality is bounded by the V coal ~3.5 m above, and by the W coal ~4.5 m below. A distance of ± 0.5 m was used as a conservative proxy for uncertainty in reversal placement. Using our ages for the V coal at Biscuit Butte and W coal at the Saddle Section, which is unambiguously traceable to the Biscuit Butte section, we calculate a reversal age of 65.075 ± 0.017/0.035 Ma. The placement of this boundary in the same stratigraphic section is more uncertain using the magnetostratigraphy of Swisher et al. (1993), from which we calculate an age of 65.071 ± 0.055/0.065 Ma for the boundary. The two results are indistinguishable, hence we prefer the more precise age of 65.075 ± 0.017/0.035 Ma derived from the data of LeCain et al. (2014).

Top C28r. To calculate an age for the chron 28r/28n boundary we also used the Biscuit Butte magnetostratigraphic section from LeCain et al. (2014). Bounding the reversal are the U coal (~5.5 m above) and the V coal (~9 m below). A conservative reversal placement uncertainty of ± 6 m was used. A reversal age of 64.931 ± 0.072/0.078 Ma was calculated using our ages for the U and V coals from Biscuit Butte. At the same stratigraphic section, Swisher et al. (1993) constrained the placement of this reversal much more precisely, and from their data we calculate an age of 64.868 ± 0.025/0.048 Ma. The difference between the two ages is insignificant, hence we prefer the age of 64.868 ± 0.025/0.048 Ma derived from the data of Swisher et al. (1993).

Our results indicate a significantly compressed time interval between the base of C29r and the top of C28r (Fig. 2.5) compared with Geologic Time Scale 2012 (GTS2012; Ogg, 2012). The latter indicates a duration of 1.731 Ma for this interval, with no uncertainties stated. The most conservative limit provided by our data uses the abovementioned age of 64.868 ± 0.025/0.048 Ma for the top of C28r and our age (66.289 ± 0.051/0.065 Ma) for the Null coal as a maximum limit on the base of C29r, which yields a maximum interval duration of 1.421 ± 0.066 Ma. If we accept the placement of the base of C29r as located by Archibald et al. (1982), this interval decreases to 1.309 ± 0.053 Ma. The biggest difference between our results and GTS2012 is the duration of C29r. Our results indicate a maximum duration of 0.457 ± 0.054 Ma, and a possible duration as brief as 0.345 ± 0.038 Ma, for this interval corresponding to the two possible placements of the base of C29r used above. The GTS2012 duration estimate for chron 29r is 710 ka (Ogg, 2012), twice the duration (345 ± 38 ka) calculated here using the Archibald et al. (1982) placement, and 1.6 times longer than our inferred maximum duration. Discrepancies involving C29r are not unexpected because GTS2012 draws heavily on the results of Swisher et al. (1993) for the IrZ coal, which has been shown to be ca. 200 ka too old relative to other dated coals in the Tullock Member (Renne et al., 2013).

Estimations for the duration of C29r using precession cycle counting on astronomically tuned sections from ODP holes 1267B (Husson et al., 2011) and 762C (Thibault et al., 2012) and from Zumaia in Spain (Kuiper et al., 2008) suggest a total duration for C29r between 540–677

ka. Results of Westerhold et al. (2008) on sections from Walvis Ridge, Shatsky Rise, and Zumaia sections suggest a longer duration of 713-725 ka. While these values exceed our minimum estimate for the duration of C29r, they overlap with our maximum estimate. Specifically, the duration of 540 ka calculated using Husson et al.'s (2011) estimate for the Cretaceous portion of C29r, which is better-constrained in most marine sections than the Paleogene portion, is within uncertainty of our maximum estimation. We note that none of the orbital tuning results take into account the possible effects of climate signals other than those due to orbital forcing, whereas climate perturbations attending the KPB extinctions might have introduced extra signal that could bias ages based on cycle counting.

The timing and duration of C29r bears special importance to the study of the KPB for several reasons. Accurate and precise calibration of the chron boundaries will facilitate correlation between marine and terrestrial records with improved resolution because the former have few opportunities for direct, high-resolution dating. Moreover, the duration of C29r is relevant to assessment of the potential role of other events to the KPB, such as the Deccan Traps volcanism (Chenet et al., 2007; Keller, 2008; Chenet et al., 2009; Tobin et al., 2012). According to many workers, greater than 80% of Deccan Traps volcanism is constrained to fall within C29r (e.g., Chenet et al, 2007 and references therein). If the majority of the volcanism was confined to C29r, our new estimate suggests a significantly shorter period over which it was most active, implying that the output of climate-modifying magmatic volatiles would have been more concentrated in time than previously believed. Such a short time interval for the majority of Deccan volcanism would favor hypotheses that volcanism may have played a major role in applying stress to ecosystems prior to the Chicxulub impact (Arens et al., 2014), although a foreshortened timescale of Deccan volcanism also implies a shorter time interval for pre-Chicxulub volcanogenic effects on climate. In addition, the temporal proximity between the main surge of volcanism and the impact make it difficult to tease apart the poorly understood biotic effects of the impact from those of the volcanism. That is, an apparently abrupt pattern of extinction in the fossil record may reflect effects of the impact or volcanism or both, depending on the sampling density of the rock record. Accordingly, due to the importance of the age and duration of C29r, we suggest that further work is required to validate the results given here. Improved constraints on the age and tempo of Deccan volcanism are also critically needed to test their possible role in KPB phenomena.

Diachronous Hell Creek-Fort Union contact

The contact between the Hell Creek and Fort Union formations is defined by the first lignite (Z, IrZ, MCZ) above the stratigraphically highest non-avian dinosaur (Calvert, 1912; Brown, 1952; Collier and Knechtel, 1939). This definition is based on the fact that lignite deposits are much more abundant in the Tullock Member of the Fort Union Formation than in the Hell Creek Formation. The Tullock Member also contains more variegated beds than the Hell Creek Formation (Fastovsky, 1987). The paleoenvironmental implications of the lithostratigraphic contact include increased hydraulic flux and a rise in water table around KPB time (Fastovsky, 1987).

Studies of these formations across the Williston Basin (between sections in Montana and North Dakota) show that the lithostratigraphically defined formational contact is not synchronous everywhere. In North Dakota, previous studies showed that the KPB is not coincident with the Hell Creek-Fort Union contact and occurs as much as 2.6 m above the formational contact (Johnson, 1992). In Montana, early studies found an opposite trend, with the

KPB corresponding to the base of the Tullock Member of the Fort Union Formation in locations in north central Garfield County, whereas in eastern Garfield and western McCone counties the KPB appeared to be located below the formational contact (Lofgren, 1995; Clemens, 2002) as early Puercan (Pu1) faunas and floras are found in the uppermost 2–3 m of the Hell Creek Formation.

In the region of the present study (Fig. 2.1), the KPB and the formational contact are coincident in the part of the western area studied so far, and both are coincident with the IrZ coal, with the impact claystone preserved at the base of the coal or immediately below it, where that coal is present. In the eastern area of Figure 2.1, the formational contact lies above the KPB and is coincident with the base of the MCZ coal (*sensu* Lofgren, 1995, or the formational Z *sensu* Rigby and Rigby, 1990). Unfortunately, the stratigraphic relationship between the IrZ and so called Z coals in our eastern study area is obscure because no section has yet been found that contains both of these coals as identified by their distinctive tephras. However, at the Lerbekmo (LB) section of Figure 2.1 the impact layer, and the palynologically defined KPB occur at the base of the of the Z coal, whereas the diagnostically distinct thick tephra deposit identified in outcrops of the Z (MCZ) coal in the eastern area occurs higher in the coal. The thin tephra identified in IrZ coal deposits in the western area is absent from the LB section and has never been reported east of it. In the eastern area of Figure 2.1, impact signals are absent from the defining basal lignite (Z or MCZ coal) at the Hell Creek-Fort Union formational contact. Furthermore, vertebrate localities in the uppermost Hell Creek Formation in eastern Garfield County and western McCone County yield earliest Puercan (Paleocene, Pu1) local faunas (Clemens, 2002). The evidence that the formational boundary is diachronous is quantitatively substantiated by our pooled $^{40}Ar/^{39}Ar$ age determinations for tephras in the Z and IrZ coals, which indicate an age difference of 30 ± 18 ka.

The diachronous nature of the lithostratigraphically defined Hell Creek-Fort Union formational contact in the study area, and more broadly in the greater Williston Basin, may have important implications for the nature of the KPB environmental transition. There was clearly not a regionally synchronous lithofacies change at the KPB. It is possible to infer an eastward migration of coal-forming environments through our study area on the time scale of 30 ± 18 ka, possibly consistent with the effects of a regression in a coastal plain environment, but this trend is reversed farther east in North Dakota where the KPB lies above the lithostratigraphic formational contact (Johnson, 1992). Further mapping and stratigraphic analysis may clarify the paleoenvironmental significance of the diachronous contact, but for now we conclude that the record of lithofacies transition represented by the contact is not obviously consistent with an instantaneous forcing mechanism. Our data and observations support the conclusions of Fastovsky (1987) and Retallack (1994) that paleoenvironmental change across the KPB in the Hell Creek region of northeastern Montana occurred over tens of thousands of years.

Faunal and Floral Turnover

The new radioisotopic dates presented here provide both greater resolution of the tempo of the evolution of the biota in northeastern Montana and more precise correlation of fossil localities distantly separated from our research area. Fossil assemblages from the middle to upper third of the Hell Creek Formation to the KPB document a pattern of declining evenness in both mammalian and amphibian local faunas. This pattern has been interpreted as a sign of increasing ecological instability of local communities (Wilson, 2005, 2014; Wilson et al., 2014b). The new date for the Null coal and the refined estimate for the base of C29r both presented in this paper

help to constrain the timing of this pre-KPB ecological decline to the last ca. 200 ka of the Cretaceous, compared to the last ca. 400–700 ka of previous estimates. The more rapid rate of change further supports the press-pulse hypothesis (Arens and West, 2008) suggesting that local biotic communities would have been particularly vulnerable to collapse from the poorly understood environmental effects of the KPB impact.

Mammalian and amphibian fossil assemblages from the lowermost Tullock Member in our western study area and the uppermost Hell Creek Formation and lowermost Tullock Member in our eastern study area (Fig. 2.1) represent earliest Paleogene (Puercan1) 'disaster' faunas: low taxonomic diversity, low evenness, and an influx of immigrant taxa (Clemens, 2010; Wilson, 2013, 2014; Wilson et al., 2014b). Bracketed by the KPB and the HFZ coal in the western study area or the KPB and the MCZ coal in the eastern study area, these Pu1 faunas are constrained to the first ca. 70 ka of the Paleogene, compared to previous estimates of roughly 390 ka (Swisher et al., 1993), providing insight into the immediate aftermath of K/Pg impact and the rate of colonization by the immigrant taxa.

A >20-m stratigraphic gap in the fossil record separates the Pu1 faunas found below the HFZ from the superjacent Garbani Channel deposits bracketed by the Y and W coals. The new dates indicate that this gap in our sampling represents ca. 232 ka. Sites in our research area yielding local faunas clearly of Pu2 age have yet to be discovered and described. These would hold clues to the nature and tempo of the initial transition from 'disaster' to 'recovery' faunas. Fossil assemblages from the thick Garbani Channel deposits in the middle of the Tullock Member show a recovering mammalian fauna and an early phase of the placental mammal radiation: high taxonomic diversity and local first appearance of some higher-level taxa, such as triisodontids, pantodonts, taeniodonts, and plesiadapiforms (Clemens, 2002, 2011, 2013; Wilson, 2014). Bracketed by the Y and W coals, the new dates imply that this mammalian recovery occurred relatively rapidly, less than ca. 925 ka after the KPB, compared to the 2–3 Ma estimates for marine ecosystems (D'Hondt, 2005).

Fossil assemblages from the Farrand Channel (in the BB section) and the Horsethief Canyon localities (HTC section) occur in the upper third of the Tullock Member and represent the earliest Torrejonian (To1) faunas in North America (Clemens and Wilson, 2009). The Farrand Channel localities are bracketed by the W and V coals, and thus constrain the beginning of the Torrejonian to no later than 1 Ma after the KPB. The Horsethief Canyon localities, ca. 35 km to the southwest, are bracketed by the coals tentatively identified as correlative with the W and U coals in the valleys of Hell Creek and Snow Creek. A V coal has not been identified in this section.

Further application of our new ages to palynological records established by Arens et al. (2014) from this region suggest a shortened interval over which reported angiosperm species richness declined leading up to the KPB. Using our new SAR estimate for the Hell Creek formation from our Bug Creek locality, we calculated an interval of ~18 ka, with a maximum of between 33–48 ka, over which angiosperm species richness declined in the last 3.5 m of the Hell Creek Formation in Russell Basin. This result is significantly shorter than the 78 ka to 110 ka period estimated by Arens et al. (2014), but may be spurious due to aforementioned uncertainty about the anomalously high SAR determined from the Bug Creek section. Using an SAR of 7 cm/ka, typical of the Tullock Fm. in this area, this interval expands to a maximum of 65–80 ka, still marginally briefer than estimated by Arens et al. (2014). However, angiosperm species richness may have begun to decline earlier, as the data of Arens et al. (2014) only extend to 3.5 m below the KPB.

2.6 Conclusions

Our dates for 15 samples representing 13 distinct tephras include at least one tephra from each coal bed in the sequence Null, IrZ, Z, MCZ, HFZ, Y, X, W, V and U, identified by previous workers in the Hell Creek and Fort Union (Tullock Member) formations within the study region. A generalized, composite chronostratigraphic section is shown in Figure 2.6. Distinctive tuffs in the Z and MCZ coals establish the main portions of these coals were deposited isochronously over a region of as least 250 km^2, but it is unclear whether the coal is (or was, prior to erosion) continuous over this area. Similarly, our results indicate that W coal outcrops separated by ~60 km are essentially contemporaneous. It remains to be seen, however, whether other coals assigned the same name in different locations, and by different workers, are time-stratigraphically equivalent. In particular, there are significant uncertainties remaining as to how coals with the same letter designation in the eastern and western areas are correlated. Further work, including tephrochemical studies, will address this issue and is in progress.

Our results confirm conclusions from previous studies that the Hell Creek-Fort Union formational boundary is diachronous, not just between sites within the Williston Basin but also within the Hell Creek region. This point is quantitatively substantiated by our pooled age determinations for tephras in the IrZ and Z (MCZ) coals (both representing the lithostratigraphically-defined formational contact), which show an age difference of 30 ± 18 ka. Our pooled age for the IrZ of 66.043 ± 0.010/0.043 Ma we consider to be the best age available for the KPB due to the occurrence of this tephra within ~1 cm of the impact claystone. As such, the diachronous nature of the Hell Creek-Fort Union formational contact suggests there was not a synchronous lithofacies change at the KPB, which further supports conclusions that the paleoenvironmental change across the KPB in the Hell Creek region was gradual (Fastovsky, 1987; Retallack, 1994).

An additional finding from our study is the consistent average sediment accumulation rates (SARs) calculated for sections with more than one dated horizon, varying between 5–10 cm/ka above the level of the HFZ, and ~20 cm/ka below the HFZ. The relatively uniform SARs for each stratigraphic interval, regardless of location, supports the validity of using linear interpolation between dated tephras to constrain ages for geomagnetic polarity reversals within these sections. As a preliminary test our study used previously collected polarity sequences from magnetostratigraphic studies conducted in our region, to calculate reversal ages and ultimately durations for polarity chrons C29r–C28r. Our results show a significantly compressed time interval from the base of C29r to the top of C28r with a maximum estimate of 1.421 ± 0.066 Ma and minimum estimate of 1.309 ± 0.053 Ma, compared to the estimate of 1.731 Ma presented in GTS2012 (Ogg, 2012). The most notable result is the drastically reduced estimate (roughly half of GTS2012) for the duration of C29r at 345 ± 38 ka. If correct, this estimate significantly shortens the time interval over which the main phase of Deccan volcanism was active, as it has been constrained to have occurred mainly within C29r (Chenet et al., 2007). Such a short interval may favor hypotheses that volcanism played a significant role in the mass extinction. Similarly, marine biostratigraphic and chemostratigraphic records whose time scales are based on the ages of C29r boundaries would tend to be foreshortened. Improved constraints on these reversal ages will likely be obtained by additional magnetostratigraphic studies that are in progress. The dominant contributor to uncertainty in our reversal age estimates was the coarse sampling of previous studies. By improving sampling intervals, chron placement, in addition to providing further tests of the consistency of SARs, our ages can ultimately be used as a calibration for the

GPTS and can be exported to marine records.

Our new radioisotopic dates applied to paleontological records from the Hell Creek region add precision to the record of terrestrial ecosystem evolution from just before the KPB mass extinction through biotic recovery. Our results show that the timing of ecological decline prior to the mass extinction is estimated to begin 200 ka before the KPB compared to previous estimates of 400–700 ka. This new estimate favors the hypothesis that these local biotic communities would have been vulnerable to collapse due to the additional stresses caused by the KPB impact. Additionally, our work further constrains rates of earliest Paleogene (Puercan1) disaster faunas to within the first 70 ka of the Paleogene, with mammalian recovery occurring no less than ca. 925 ka after the mass extinction. We have further been able to constrain the beginning of the Torrejonian NALMA to no later than 1 Ma after the KPB.

Figures

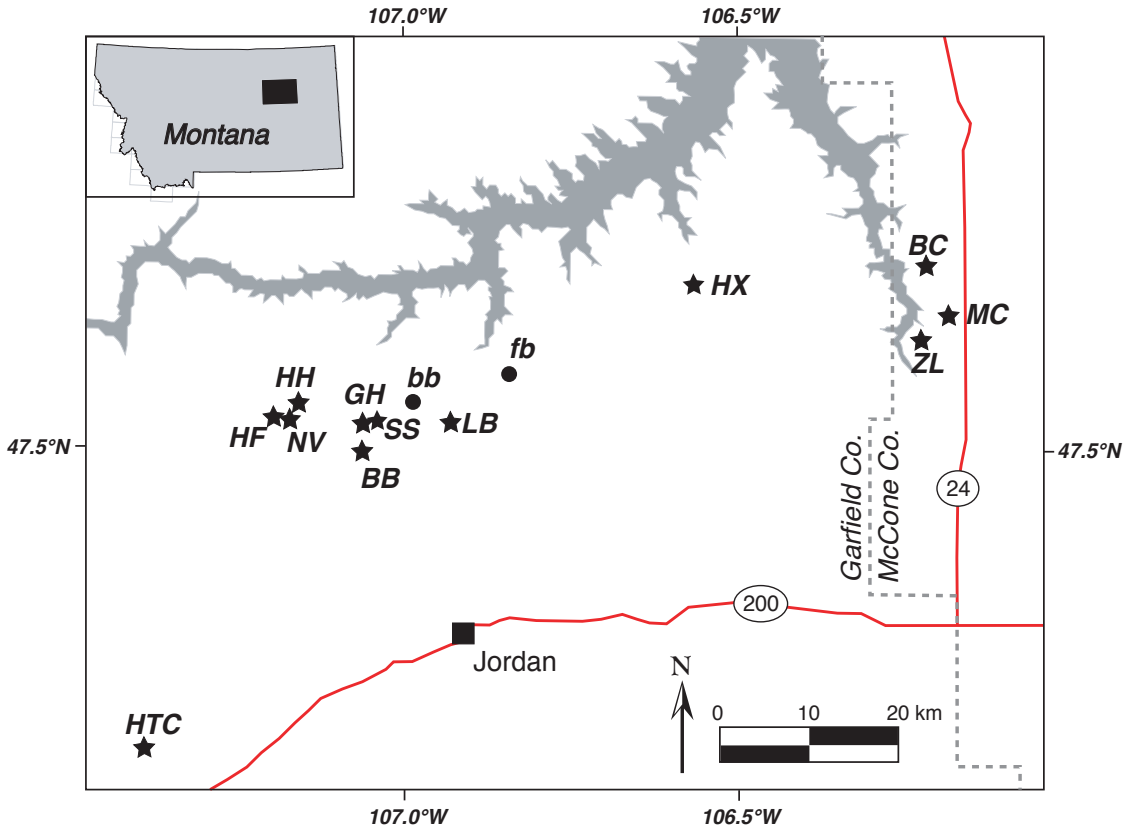

Fig. 1 Sprain et al.

Figure 2.1. Location map showing the study area in the Hell Creek region of northeastern Montana. Fort Peck reservoir is shown in grey. Labeled stars show locations of measured stratigraphic sections where tephras for geochronologic dating were collected. Note bimodal distribution between western and eastern sections. HF: Hauso Flats, HH: Hell Hollow, NV: Nirvana, SS: Saddle Section, BB: Biscuit Butte, GH: Garbani Hill, LB: Lerbekmo, HX: Haxby Road, BC: Bug Creek, MC: McGuire Creek (Lofgren, also shown as LG in Table 2.1 and Table 2.2), ZL: Z-line. Also shown are Brownie Butte (bb) and Flag Butte (fb) locations referred to in text, indicated by filled circles.

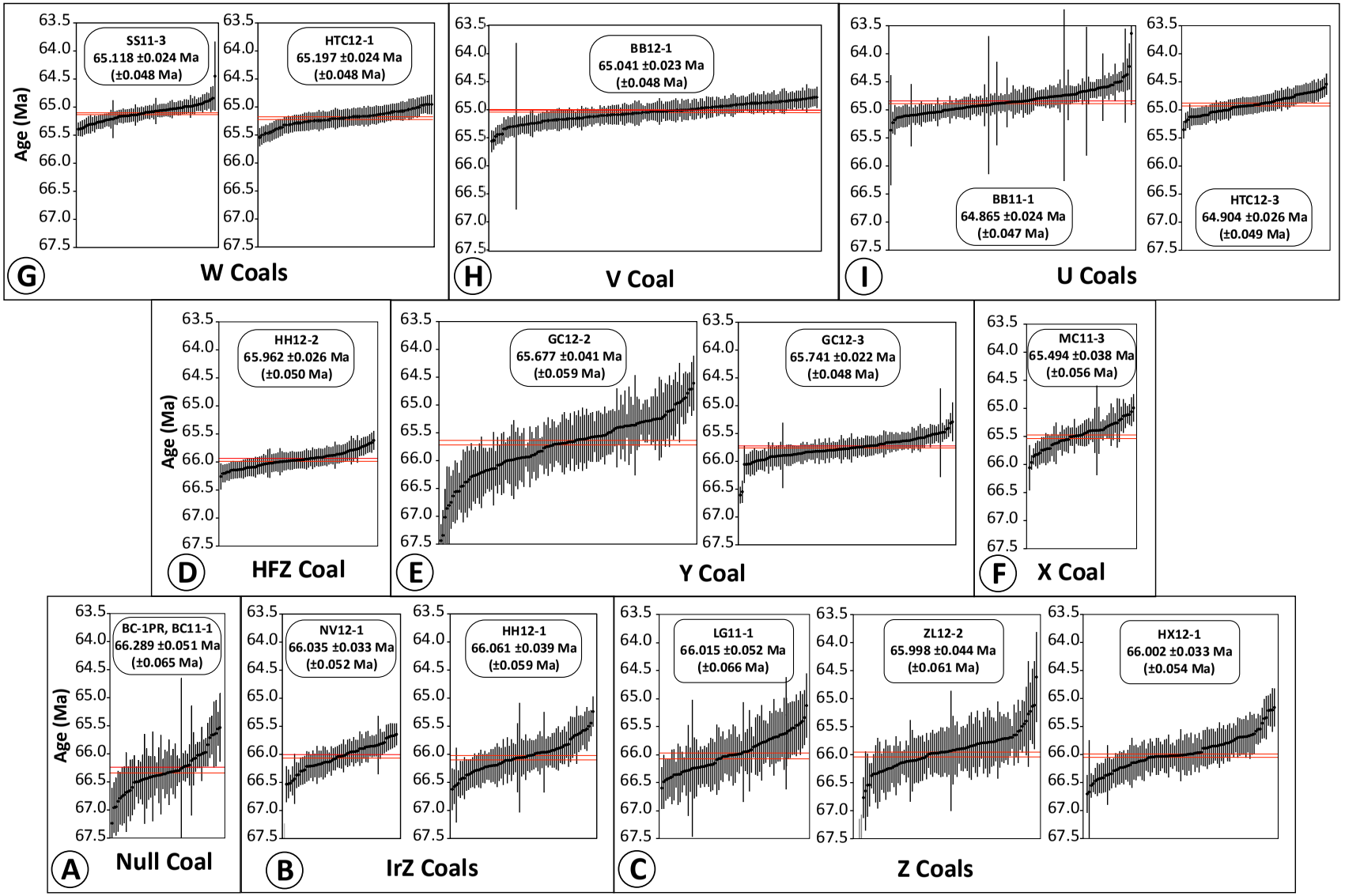

Sprain *et al.* Fig. 2

Figure 2.2. Summary of single-crystal $^{40}Ar/^{39}Ar$ results for tephras. Stratigraphic relationships are described in Figure 2.4. Individual ages are shown in rank order with analytical uncertainty limits of 1σ. Red lines show uncertainty limits for the weighted mean age for each sample. **(A)** Null Coal at the Bug Creek (BC) section. **(B)** The IrZ coal at two locations, Hell Hollow (HH) and Nirvana (NV), yield indistinguishable ages. **(C)** The Z coal at three locations: Z-line (ZL), Haxby Road (HX), and McGuire Creek (MC) yield indistinguishable ages. **(D)** The HFZ Coal at Hell Hollow (HH). **(E)** Two tephras collected from the upper and lower beds of the Y coal doublet at Garbani Hill (GH). Ages are consistent with stratigraphic order and are distinguishable at 1σ. **(F)** The X Coal at the McGuire Creek section (MC). **(G)** Tephras collected at two locations of the W coal, the Saddle Section (SS) and Horsethief Canyon (HTC). Ages are similar but distinguishable at 95% confidence, favoring credence that the same tephra was not collected from each site. **(H)** The V Coal at Biscuit Butte (BB). **(I)** The U Coal at Biscuit Butte (BB) and at Horsethief Canyon (HTC). Although ages are not distinguishable at 95% confidence, based on field evidence and tephra characteristics we do not believe the same tephra was collected at each site.

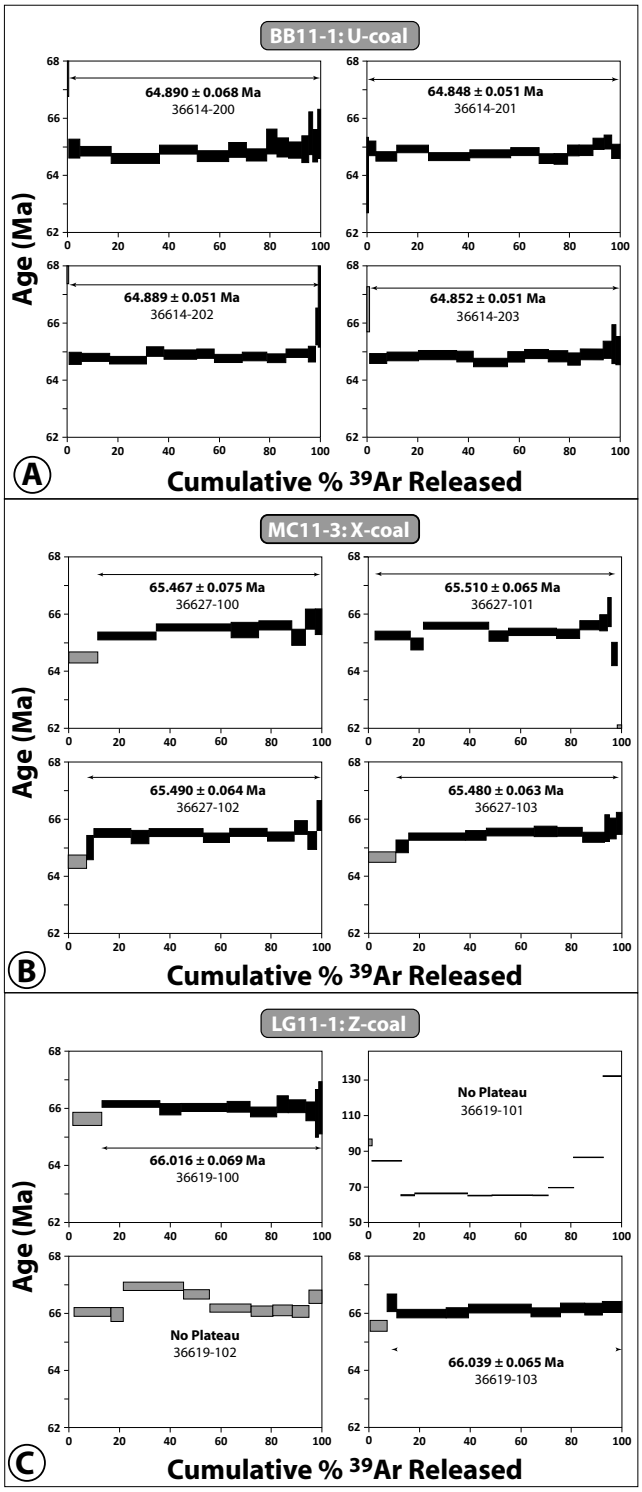

Sprain *et al.* Fig. 3

Figure 2.3. $^{40}Ar/^{39}Ar$ age spectra for multi-grained aliquots of feldspar samples from the U coal **(A)**, X coal **(B)**, and Z (MCZ) coal **(C)**.

Figure 2.4A.

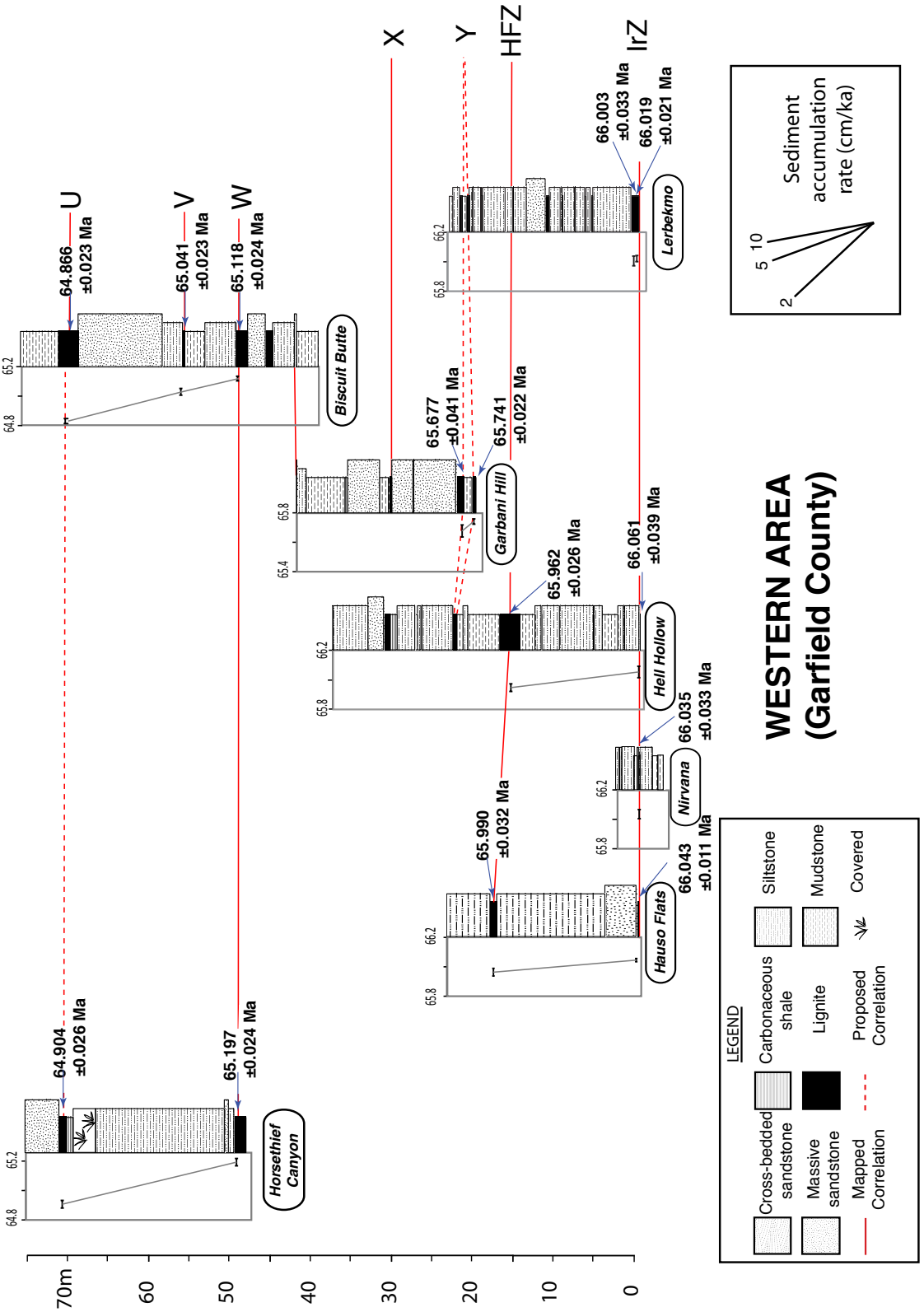

Fig. 4A Sprain et al.

Figure 2.4B.

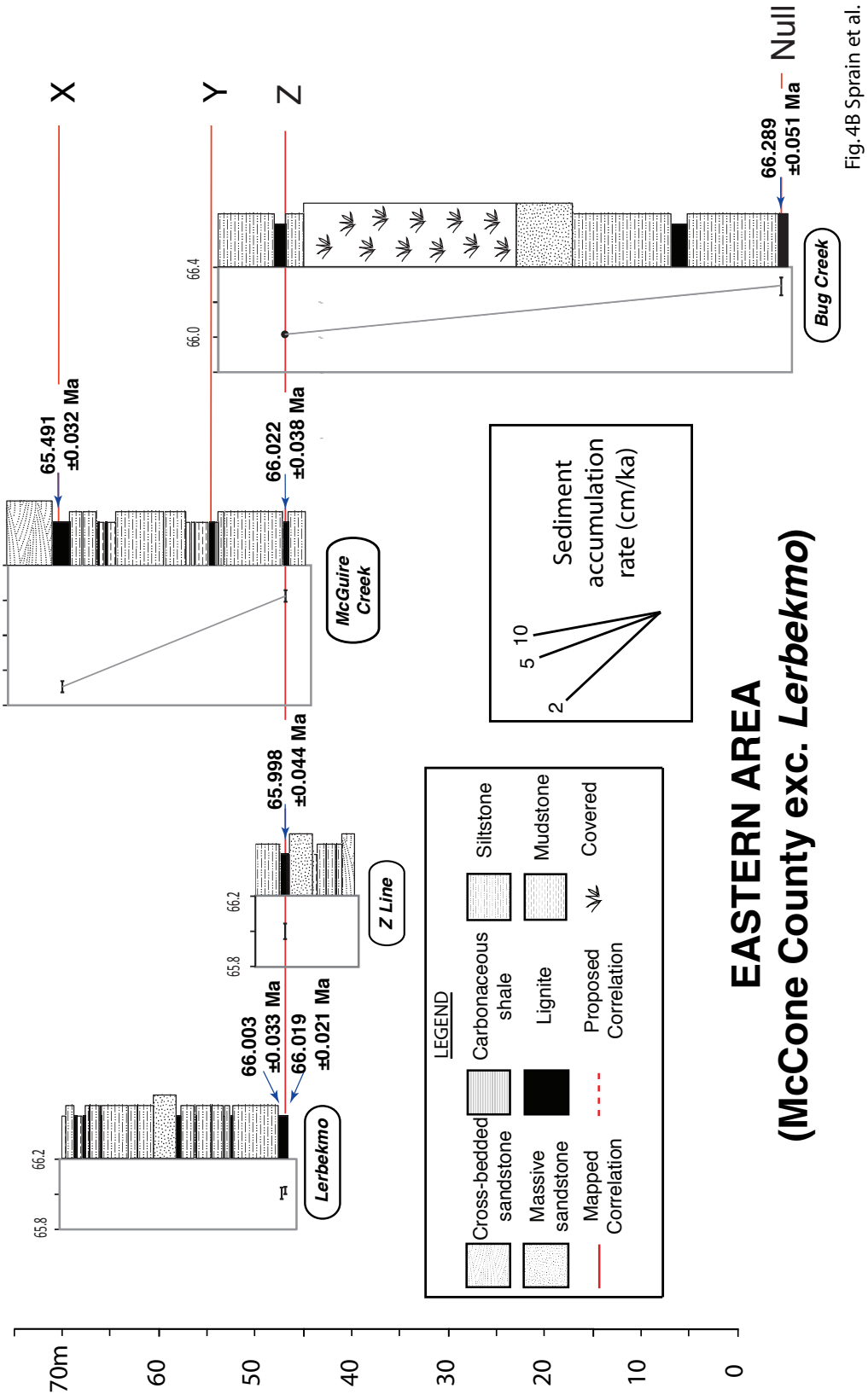

Fig. 4B Sprain et al.

Figure 2.4. Stratigraphy and correlations for sections within Garfield (western) and McCone (eastern) counties. Red lines indicate mapped correlations and dotted red lines indicate proposed correlation. **(A)** Garfield County sections from west to east. Geochronologic data from both the Hauso Flats and Lerbekmo (Hell Creek Marina Road) localities were presented by Renne et al. (2013). Stratigraphic sections were adapted from Archibald (1982: Horsethief Canyon and Hell Hollow IrZ–HFZ), Swisher et al., (1993: Hauso Flats), Turner et al. (2010: Nirvana), LeCain et al. (2014: Garbani Hill and Biscuit Butte), This Study (Lerbekmo and Hell Hollow HFZ–Top). Note, the stratigraphy of the Saddle Section locality is consistent with the basal Biscuit Butte and as such is not included in the figure. **(B)** McCone County localities include: Z-line, McGuire Creek, and Bug Creek. Lerbekmo locality is included for comparison. Stratigraphic sections for Z-line and McGuire Creek are adapted from Lofgren (1995) and Bug Creek was adapted from Archibald et al. (1982). Stratigraphy was not collected from the Haxby Road section. Stratigraphy was plotted using Matstrat (Lewis et al., 2011).

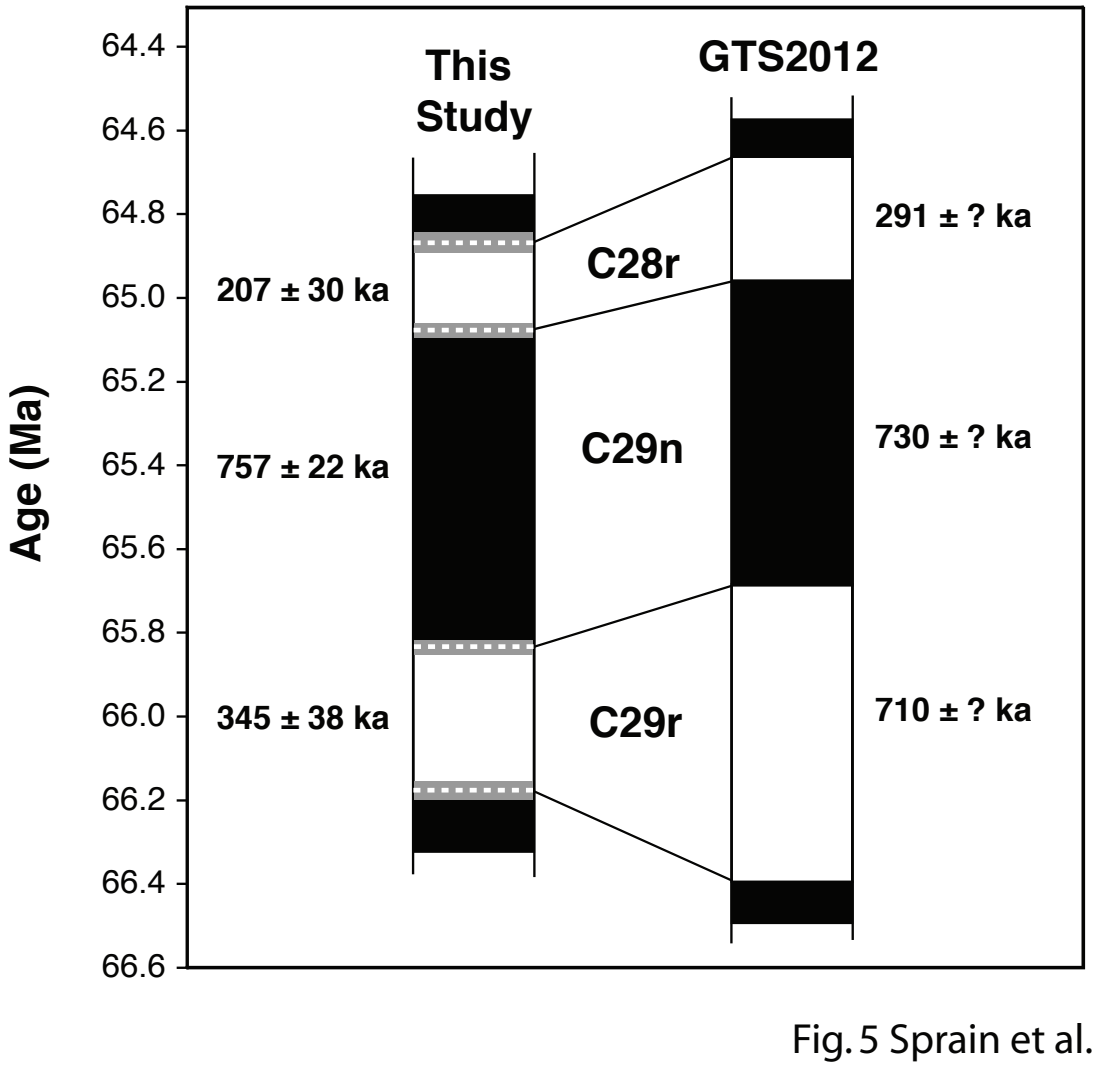

Figure 2.5. Paleomagnetic-reversal age comparison between this study and the Geologic Timescale 2012 (Ogg, 2012). Dashed white lines denote weighted mean age estimates and grey boxes indicate systematic uncertainty estimates at 1σ. GTS2012 did not report uncertainties for these chron boundary ages.

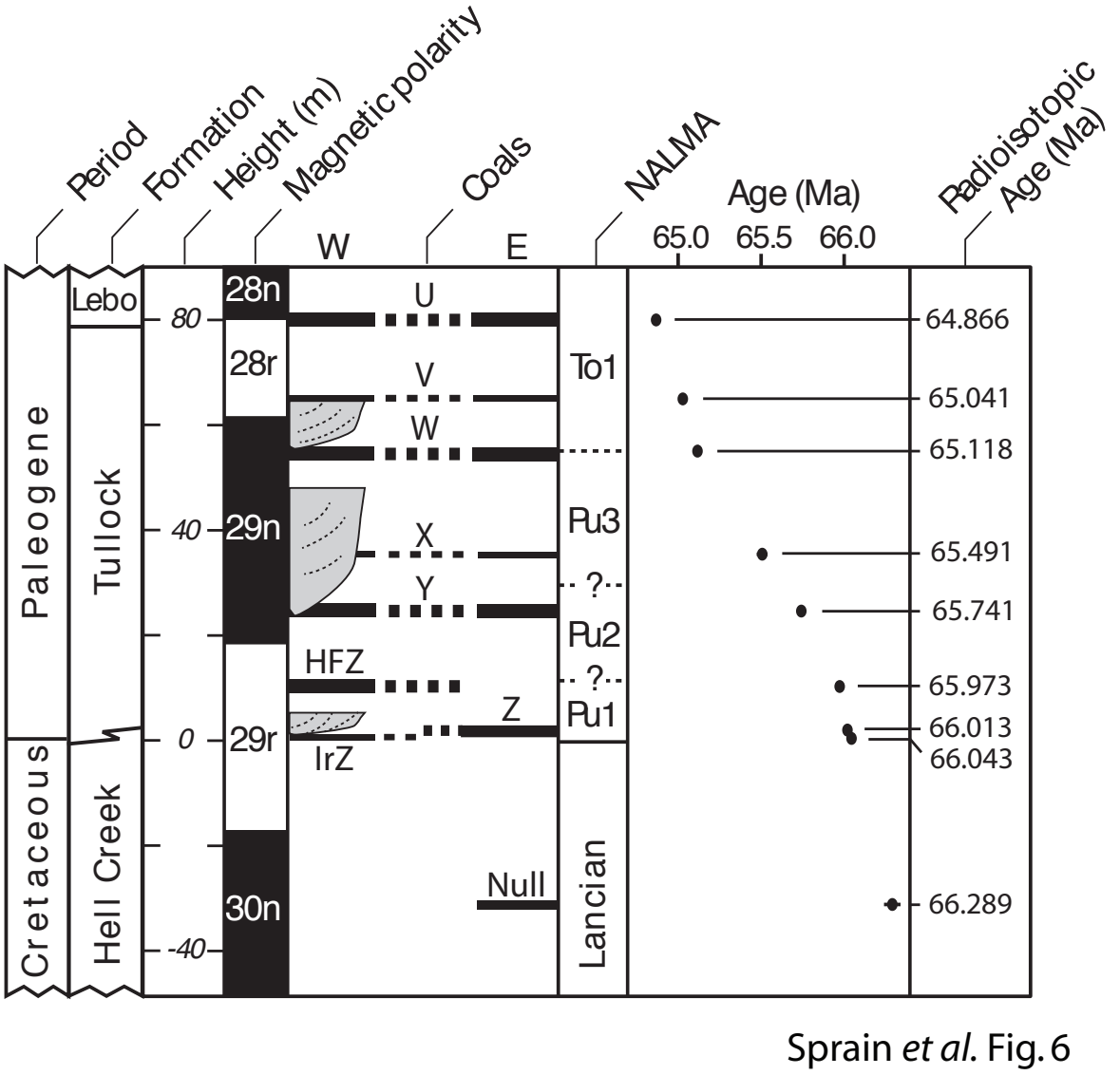

Figure 2.6. Composite chronostratigraphic summary. Dashed lines indicate uncertain chronostratigraphic relationships between the western (W) and eastern (E) portions of the study area. Major channels (Hell Hollow, Garbani and Farrand, in ascending order) are shown schematically and their placement in the diagram is not meant to indicate that they are confined to the western versus eastern areas. Placement of paleomagnetic polarity chrons follows LeCain et al. (2014) except the C28r/C28n boundary, which follows Swisher et al. (1993). Error bars (σ) in the age versus stratigraphic height panel are smaller than the symbols for all units except the Null coal tephra.

Table 2.1. Summary of $^{40}Ar^*/^{39}Ar$ ages

Coal	Sample	Section	Age (Ma)	±σ (Ma)[1]	±σ (Ma)[2]	Method[3]	N/N_0[4]
U	BB11-1	BB	64.865	0.024	0.047	SCTF	119/119
U	BB11-1	BB	64.867	0.031	0.052	SHP	54/57
U	**BB11-1**	**BB**	**64.866**	**0.023**	**0.047**	**Comb**	
U?	**HTC12-3**	**HTC**	**64.904**	**0.026**	**0.049**	**SCTF**	**71/73**
V	**BB12-1**	**BB**	**65.041**	**0.023**	**0.048**	**SCTF**	**175/179**
UW	**HTC12-1**	**HTC**	**65.197**	**0.024**	**0.048**	**SCTF**	**85/93**
W	**SS11-3**	**SS**	**65.118**	**0.024**	**0.048**	**SCTF**	**68/68**
X	MC11-3	LG	65.494	0.038	0.056	SCTF	52/52
X	MC11-3	LG	65.488	0.039	0.057	SHP	35/47
X	**MC11-3**	**LG**	**65.491**	**0.032**	**0.053**	**Comb**	
Y	**GC12-2**	**GH**	**65.677**	**0.041**	**0.059**	**SCTF**	**118/243**
Y	**GC12-3**	**GH**	**65.741**	**0.022**	**0.048**	**SCTF**	**104/106**
HFZ	**HH12-2**	**HH**	**65.962**	**0.026**	**0.050**	**SCTF**	**77/79**
MCZ	LG11-1	LG	66.015	0.052	0.066	SCTF	72/150
MCZ	LG11-1	LG	66.028	0.050	0.065	SHP	18/42
MCZ	**LG11-1**	**LG**	**66.022**	**0.038**	**0.057**	**Comb**	
Z	**HX12-1**	**HX**	**66.002**	**0.033**	**0.054**	**SCTF**	**93/94**
MCZ	**ZL12-2**	**ZL**	**65.998**	**0.044**	**0.061**	**SCTF**	**89/90**
IrZ	**HH12-1**	**HH**	**66.061**	**0.039**	**0.059**	**SCTF**	**70/74**
IrZ	**NV12-1**	**NV**	**66.035**	**0.033**	**0.052**	**SCTF**	**55/56**
Null	**BC11-1** **BC-1PR**	**BC**	**66.289**	**0.051**	**0.065**	**SCTF**	**54/174**

Notes: Coal designations are based on references cited in text. Ages are based on the calibration of Renne et al. (2011). Age uncertainties excluding[1] and including[2] systematic sources are shown. Method[3] refers to single crystal total fusion (SCTF) or step-heating plateau (SHP) ages; where appropriate these are combined (Comb) as the weighted mean. N/N_0[4] refers to the the number of analyses (single crystal fusions or incremental heating steps) used for age calculation relative to the number of ages obtained.

Table 2.1 Summary of $^{40}Ar^*/^{39}Ar$ ages.

Table 2.2. Summary of pooled $^{40}Ar^*/^{39}Ar$ ages

Coal	Samples	Sections	Age (Ma)	±σ $(Ma)^2$	±σ $(Ma)^3$
HFZ	HH12-2	HH	65.962	0.026	0.050
HFZ	HF-3PR	HF[1]	65.990	0.032	0.053
HFZ	**Pooled**		**65.973**	**0.020**	**0.047**
Z (MCZ)	LG11-1	LG	66.022	0.038	0.057
Z	HX12-1	HX	66.002	0.033	0.054
Z (MCZ)	ZL12-2	ZL	65.998	0.044	0.061
Z	HC-2PR	LB[1]	66.019	0.021	0.046
Z	**Pooled**		**66.013**	**0.015**	**0.044**
IrZ	HH12-1	HH	66.061	0.039	0.059
IrZ	NV12-1	NV	66.035	0.033	0.052
IrZ	HF-1PR	HF[1]	66.043	0.011	0.043
IrZ	**Pooled**		**66.043**	**0.010**	**0.043**

Notes: Ages pooled from multiple localities.[1]Denotes data from Renne et al. (2013). Age uncertainties excluding[2] and including[3] systematic sources are shown.

Table 2.2. Summary of pooled $^{40}Ar^*/^{39}Ar$ ages.

Chapter 3. Importance of titanohematite in detrital remanent magnetizations of strata spanning the Cretaceous-Paleogene boundary, Hell Creek region, Montana

Adapted from Sprain, C.J., Feinberg, J.M, Renne, P.R., and Jackson, M., Geochemistry, Geophysics, Geosystems, v. 17, p. 660–678, 2016, doi:10.1002/2015GC006191. An edited version of this paper was published by AGU.

Abstract Intermediate composition titanohematite, $Fe_{2-y}Ti_yO_3$ with $0.5 \leq y \leq 0.7$, is seldom the focus of paleomagnetic study and is commonly believed to be rare in nature. While largely overlooked in magnetostratigraphic studies, intermediate titanohematite has been identified as the dominant ferrimagnetic mineral in an array of Late Mesozoic and Early Cenozoic Laramide clastic deposits throughout the central United States. Intermediate titanohematite is ferrimagnetic and has similar magnetic properties to titanomagnetite, except its unique self-reversing property. Due to these similarities, and with detrital remanent magnetizations masking its self-reversing nature, intermediate titanohematite is often misidentified in sedimentary deposits. Past studies relied upon non-magnetic techniques including X-Ray diffraction and electron microprobe analysis. While these techniques can identify the presence of intermediate titanohematite, they fail to test whether the mineral is the primary recorder. To facilitate the identification of intermediate titanohematite in sedimentary deposits, we characterize this mineral using low-temperature magnetometry and high-temperature susceptibility experiments, and present a new identification technique based on titanohematite's self-reversing property, for sediments that span the Cretaceous-Paleogene boundary (Hell Creek region, Montana). Results from the self-reversal test indicate that the majority of remanence is held by minerals that become magnetized parallel to an applied field, but that intermediate, self-reversing titanohematite ($y = 0.53–0.63$) is an important ancillary carrier of remanence. While earlier literature suggests that intermediate titanohematite is rare in nature, reanalysis using specialized rock magnetic techniques may reveal that it's more abundant in the rock record, particularly within depositional basins adjacent to calc-alkaline volcanics, than previously thought.

3.1 Introduction

Intermediate composition titanohematite is often described as occurring only rarely in nature. Its paragenesis is restricted to limited geologic environments and it has been documented in few paleomagnetic studies, most commonly by the presence of its unique self-reversing property. Intermediate titanohematite received much interest after Nagata et al.'s (1951) discovery of a reversed thermoremanent magnetization (RTRM) in the Haruna dacite tuff from Japan, which complicated early recognition of geomagnetic polarity reversals (Cox et al., 1963; McDougall and Tarling, 1963). Since that time, intermediate titanohematite has been identified only in a handful of other locations, most involving rapidly cooled intermediate calc-alkaline volcanic rocks (Kennedy, 1981; Heller et al., 1986; Lawson et al., 1987; Ozima et al., 1992). Aside from rock magnetic studies of self-reversal mechanisms, intermediate titanohematite is often viewed as a magnetic rarity of negligible importance to most paleomagnetic studies. While this belief prevails, intermediate titanohematite has been identified as the dominant ferrimagnetic mineral in a vast array of late Mesozoic and early Cenozoic clastic sediments deposited across central North America (e.g. Force et al., 2001), suggesting that it may be more abundant and perhaps more important to paleomagnetic records than previously perceived.

Titanohematite was first identified in clastic sediments by Butler and Lindsay (1985) in

the Fruitland and Kirtland Formations, the Ojo Alamo Sandstone, and the Nacimiento Formation, which span the Cretaceous-Paleogene boundary in the San Juan basin, New Mexico. Initial paleomagnetic studies (Taylor and Butler, 1980; Lindsay et al., 1981) from the San Juan basin included limited rock magnetic analyses, which identified magnetite/titanomagnetite as the primary magnetic carriers owing to median destructive fields ≤40 mT. Furthermore, because the remanent magnetization of the sediments was detrital, the titanohematite recorded a direction parallel to the magnetic field, effectively masking its self-reversing property. The first study dedicated to characterizing the magnetic mineralogy of San Juan basin sedimentary rocks (Butler, 1982) found Curie temperatures of ~200ºC, not ~580ºC as had been expected. Holding a similar belief that intermediate titanohematite is rare in the rock record, the author concluded that the primary magnetic mineral was intermediate composition titanomagnetite. It wasn't until Butler and Lindsay (1985) revisited the rock magnetic properties of these sediments that intermediate titanohematite was recognized as the dominant ferrimagnetic mineral. Examination of magnetic separates using strong field thermomagnetic curves, X-ray diffraction (XRD), and electron microprobe analysis (EPMA) allowed Butler and Lindsay (1985) to conclude that the dominant ferrimagnetic mineral was intermediate titanohematite based on Curie temperatures of ~200ºC, rhombohedral crystal structures, and high Ti:Ti+Fe ratios. Since Butler and Lindsay (1985), intermediate titanohematite has been identified using similar techniques in KPg age Laramide clastic deposits across central North America, including the San Juan Basin (Northwest New Mexico; Butler and Lindsay, 1985; Force et al., 2001), the Bighorn basin (South-Central Montana, North-Central Wyoming; Butler et al., 1987; Force et al., 2001), and much of the Williston basin (Western and Central North Dakota and Eastern Montana, USA and Southern Alberta, Saskatchewan, and Manitoba, Canada; Lund et al., 2002; Swisher et al., 1993; Lerbekmo, 1999; Force et al., 2001) (see Fig. 1). We speculate that intermediate titanohematite is present in additional KPg age Laramide deposits, but that it has been misidentified as intermediate titanomagnetite or titanomaghemite due to inadequate rock magnetic analysis (e.g. Peppe et al., 2009, 2011).

To facilitate the identification of intermediate titanohematite in sedimentary deposits, in this study we characterize this mineral using low-temperature magnetometry experiments, high-temperature susceptibility measurements, and newly developed laboratory-based self-reversal experiments for KPg age sediments from the Hell Creek region, Montana. Rock magnetic characterization of intermediate composition titanohematite will help facilitate identification of this mineral in the future; moreover, by more accurately understanding its properties, it will be possible to better analyze sources of error and complexity in paleomagnetic analysis when this mineral is an important carrier of remanence. While intermediate composition titanohematite may only form in limited geologic settings, its abundance and longevity in the rock record may be more extensive than previously understood, as its self-reversing behavior can be masked by detrital remanent magnetizations (DRMs).

3.2 Magnetic Characteristics of Intermediate Titanohematite

Rhombohedral titanohematites ($Fe_{2-y}Ti_yO_3$) are a solid solution series with compositions between hematite (Fe_2O_3) and ilmenite ($FeTiO_3$) end-members (Dunlop and Ozdemir, 1997). While the ionic substitution is exactly the same as in titanomagnetites, with Ti^{4+} substituting for Fe^{3+} and one Fe cation changing valence state from Fe^{3+} to Fe^{2+}, Ti substitution in hematite has a much more profound effect on its magnetic properties. Like hematite, titanohematite also has a corundum structure. Oxygen anions form a hexagonal-close-packed lattice, and Fe and Ti cations

fill in 2/3 of the interstices, lying effectively within the basal plane. Cation distribution is disordered when titanohematite compositions are below $y \leq 0.5$, resulting in Fe^{2+} and Ti^{4+} being distributed equally in all c planes. This creates a magnetization very similar to hematite: antiferromagnetic with weak parasitic ferromagnetism. In this composition range the mineral behaves similarly to hematite. For compositions with $y \geq 0.5$, cation distribution is roughly ordered with Ti^{4+} and Fe^{2+} distributed in alternating cation planes, resulting in ferrimagnetism. Above compositions of $y \sim 0.8$, titanohematites are paramagnetic at room temperature but show ferrimagnetic properties at low temperatures (Burton et al., 2008). The maximum saturation magnetization at room temperature occurs around $y=0.7$, with an $M_s \sim 35$ Am^2/kg (Moskowitz et al., 2015; Fig. 3.2). Néel/Curie temperatures decrease roughly linearly with Ti substitution, with compositions above $y=0.8$ having Curie points below room temperature (Burton et al., 2008; Fig. 3.2).

Single-phase intermediate compositions ($0.5 \leq y \leq 0.7$) can be preserved by rapid chilling of calc-alkaline intermediate to silicic lavas and pyroclastics (Dunlop and Özdemir, 1997). It is within these compositions that a self-reversed thermoremanent magnetization can be acquired (Uyeda, 1958; Heller et al., 1986; Hoffman, 1992), although a more recent compilation of data suggests that self-reversal can occur between $0.45 \leq y \leq 0.75$ (Fabian et al., 2011). In a majority of models for self-reversal in the hematite-ilmenite solid-solution series, reverse thermoremanent magnetization (RTRM) occurs due to an ordered ferrimagnetic phase being magnetized antiparallel to a magnetizing field as result of interactions with an Fe-rich, more disordered phase, i.e. a weakly ferromagnetic phase or intermediate x phase, however the exact cause of the self-reversing process remains enigmatic (for more details see: Nagata and Uyeda, 1959; Nagata, 1961; Uyeda, 1957, 1958; Ishikawa, 1962; Ishikawa and Syono 1962, 1963; Hoffman, 1975; Kennedy and Osborne, 1987; Nord and Lawson, 1989; Haag, 1990a, b, 1993; Hoffmann and Fehr, 1996; Bina et al., 1999; Ozima and Funaki, 2001; Fabian et al., 2011; Robinson et al., 2012a, 2012b, 2014). Studies have shown this self-reversal is not suppressed even in fields of 2T, suggesting that the self-reversal is caused by exchange coupling as only this mechanism can resist such high fields (Dunlop and Özdemir, 1997). The primary control on self-reversal in titanohematite appears to be the coexistence of two phases in the same crystal and their exchange interactions, rather than simple interactions between repeated, highly geometric microstructures. Note that this differs from the situation in partially oxidized titanomagnetites, in which self-reversed remanence components can be produced by magnetostatic interactions, which are stronger due to the higher magnetization intensities in those minerals (Krása et al., 2005). Néel/Curie temperatures within the self-reversing composition range vary from 300ºC to room temperature, with coercivities ranging ~30 mT and below (Nagata and Akimoto, 1956; Nagata, 1961; Fabian et al., 2011; Fig. 3.2). It has also been observed that magnetization increases almost linearly to liquid nitrogen temperatures (Ishikawa and Akimoto, 1957).

While RTRM can occur over compositional ranges of $0.45 \leq y \leq 0.75$, intermediate compositions alone will not guarantee self-reversal. The development of an RTRM is strongly dependent upon thermal history, and grain size (Haag et al., 1993; Ozima et al., 2003; Ishikawa, 1962; Ishikawa and Syono, 1963; Lagroix et al., 2004). Samples that are entirely ordered or disordered will not show the self-reversing behavior (Ozima et al., 2003). This degree of order in titanohematite is dependent upon thermal history. It has been shown that samples that have been quenched from above the ordering temperature and then annealed below the ordering temperature for short periods of time acquire an RTRM that is much stronger than for samples that were strongly annealed (Ishikawa, 1962; Ishikawa and Syono, 1962, 1963; Fabian et al.,

2011). This behavior has been suggested to be due to the growth of ordered domains and the decrease of antiphase boundaries during annealing (Fabian et al., 2011). If the reverse ferrimagnetic phase forms domains, then it will lose its RTRM. When ordered phases are multidomain (MD) the domain boundaries acquire a reversed magnetization, but the interior of the domains respond to the applied field and acquire a magnetization parallel to the applied field and a normal TRM is recorded (Dunlop and Özdemir, 1997).

3.3 Regional Geology

The Hell Creek region of Montana holds one of the best terrestrial records of biotic and abiotic changes leading up to and across the Cretaceous-Paleogene boundary (KPB) and mass extinction. It is located within the Williston sedimentary basin in NE Montana (Fig. 3.1A, B), which has been an active area of deposition since the Ordovician. Throughout the late Cretaceous, the Hell Creek region (and much of the western interior) was covered by a shallow epicontinental sea (Western Interior Seaway) that bisected North America, extending at times from the Gulf of Mexico to the Arctic Ocean. Orogenic pulses loosely ascribed to the Laramide orogeny, coupled with hypothesized eustatic regression in the Late Maastrichtian resulted in major regression of the seaway, marking its last appearance in the Hell Creek region (Gill and Cobban, 1973). The seaway persisted in the northern Western Interior through the end Cretaceous and had a short transgressive period in the early Paleocene, marked by marine formations deposited from the Cannonball Sea in North and South Dakota (Boyd and Lillegraven, 2011). The Hell Creek (mostly Cretaceous) and Tullock Member of the Fort Union Formation (mostly Paleogene) in the Hell Creek region comprise fluvial deposits that formed as a prograding clastic wedge following the eastward advancement of the Sheridan Delta due to the rapid retreat of the Western Interior seaway (Fastovksy, 1987). The Hell Creek/Tullock Mb. formational boundary is roughly coincident with the KPB. These formations are correlative with other fluvial deposits within the Williston basin including the Hell Creek and Ludlow Member of the Fort Union Formation in North Dakota and South Dakota and the Frenchman and Ravenscrag Formations in Canada (Hartman, 2002; Hartman et al., 2014). Rock types included in these deposits include siltstone, mudstone, fine sandstone, and lignite, representative of flood plain deposition, and coarser sandstones, representative of channel deposition.

Thin, distal volcanic tephra layers are preserved within lignite deposits in the Hell Creek region. These layers contain minerals amenable to both high precision $^{40}Ar/^{39}Ar$ dating, and U/Pb dating (Renne et al., 2013; Sprain et. al., 2015), and have yielded precision as good as 40 ka (Renne et al., 2013; Sprain et al., 2015). $^{40}Ar/^{39}Ar$ and U/Pb ages of tephra layers, combined with magnetostratigraphy, form the geochronologic framework for a variety of studies on biotic and abiotic terrestrial processes associated with the mass extinctions. Thus, a well-grounded understanding of the magnetic minerals recording the magnetostratigraphy in this region is essential.

Provenance studies of the Hell Creek Formation and Tullock Member in the Hell Creek region are limited. However, analysis of paleocurrent directions in the early Paleocene suggest that sediment was transported to the east from central Montana and northeast, across the Powder River Basin in southern Montana, into the Williston basin (Cherven and Jacob, 1985; Fig. 3.1). These trends are compatible with sandstone compositions indicating a dominantly volcanic-metamorphic provenance for late Cretaceous sediments, associated with Laramide (*sensu lato*) magmatic arc volcanism to the west (likely western Montana or eastern Idaho), and mixed volcanic and sedimentary detritus for early Paleocene deposition, indicative of the propagation of

retroarc thrust belts and uplift of supracrustal sedimentary rocks like the Bighorn Mountains and Black Hills to the southwest (Cherven and Jacobs, 1985). A suggested source for the volcanic detritus is the Elkhorn Mountains (Cherven and Jacobs, 1985; Gill and Cobban, 1973; Force et al., 2001) in southwestern Montana, which consist of the eroded remnant of a volcanic plateau that comprises calc-alkaline silicic to intermediate lavas and tuffs. This volcanic environment is amenable to the formation of intermediate titanohematite, however RTRMs have not been documented for the Elkhorn rocks (Diehl, 1991). Based on stratigraphic and paleontological data the Elkhorn volcanics have been dated to the early Campanian, ~80 Ma. Due to the abundance of Laramide volcanic centers in the late Cretaceous, it is equally possible that another volcanic center, such as the Idaho Batholith, is the sediment source for the Hell Creek Formation and Tullock Member.

Magnetostratigraphic analysis is actively used in the Hell Creek as a means to correlate paleontological records across the region (Archibald et al., 1982; Swisher et al., 1993; LeCain et al., 2014). Of the multiple magnetostratigraphic studies, only one study completed rock magnetic analysis (Swisher et al., 1993; data published in Force et al., 2001). Magnetic mineralogy was characterized using strong-field thermomagnetic analysis, X-ray diffraction (XRD), electron microprobe analysis (EPMA), and room temperature IRM acquisition (Swisher et al., 1993; Force et al., 2001). Curie temperatures were found to be between 160−200°, with X-ray diffraction and EPMA results indicating an intermediate-composition titanohematite as the dominant ferromagnetic mineral (Swisher et al., 1993). In all Hell Creek paleomagnetic studies coercivity spectra reveal that the characteristic remanent direction is constrained between 20–80 mT (Archibald et al., 1982; Swisher et al., 1993; LeCain et al., 2014; Table 3.1). These results are similar to those observed for other KPg Laramide continental deposits in the San Juan Basin, New Mexico, Big Horn Basin, WY and MT, Powder River Basin, WY and MT, and other parts of the Williston Basin (Southeastern MT, Southern Canada, and Eastern and Central North Dakota; Butler et al., 1981; Lindsay et al., 1981; Butler et al., 1987; Peppe et al., 2009, 2011; Lerbekmo and Coulter, 1984, 1985; Lerbekmo, 1999, Lund et al., 2002). No further rock magnetic analyses have been conducted on rocks from the Hell Creek region since Swisher et al. (1993). The goal of our study is to update the magnetic characterization of rocks from the Hell Creek region using modern equipment and techniques, to test previous results, and to understand the degree to which intermediate titanohematite may influence the fidelity of magnetostratigraphic records in Laramide basins throughout the central United States.

3.4 Methods

Sampling

Oriented block samples for paleomagnetic analysis were collected from siltstones, mudstones, and fine-grained sandstones across both the Hell Creek Fm. and Tullock Mb. of the Fort Union Fm. (Fig. 3.1B, C). For each sampling horizon, three block samples were collected. Two to three 16 cm^3 specimen cubes were cut from each block sample. When an oriented sample was not needed, chips taken from original block samples were used. Oriented cubes were cut and subjected to stepwise thermal and AF demagnetization and remanence measurements at the Berkeley Geochronology Center. Directional results will be published in a future contribution. To obtain magnetic extracts, rock chips were crushed using a rubber mallet and ground to an appropriate size using a mortar and pestle. For samples with abundant magnetic material, extracts were obtained using a Nd-hand magnet with a plastic sleeve. Extracts from samples with sparse magnetic material were collected using either the pump extraction or flask extraction

method described in Strehlau et al. (2014). All extracts were obtained at the Institute for Rock Magnetism at the University of Minnesota.

Rock Magnetic Measurements

Rock magnetic experiments were conducted at the Institute for Rock Magnetism at the University of Minnesota. High temperature, low-field susceptibility experiments were conducted on seven whole rock samples and seven magnetic separates using a Geofyzika KLY-2 KappaBridge AC susceptibility meter with an AC field of 300 Am^{-1} and a frequency of 920 Hz. Heating of whole rock samples was two-cycled, starting at room temperature and going up to 300ºC, cooling to room temperature, and then heating from room temperature to 600ºC, and cooling back to room temperature. Of the seven extracts, four underwent multi-cycled heating with peak temperatures every 100ºC, ending at 400ºC. One additional extract was heated similarly up to 600ºC. The two remaining magnetic extracts were heated without cycling from room temperature up to 600ºC and then back to room temperature. Measurements were collected on warming and cooling. Of the 14 high-temperature susceptibility experiments, two were measured in argon. The other 12 samples were run in air. Néel/Curie temperatures were determined by taking the first derivative of the measured data (Fabian et al., 2013).

Low temperature experiments were run on a Quantum Design Magnetic Properties Measurement System (MPMS-5S). Thirty-five specimens were run on the MPMS, 11 specimens underwent the FC-ZFC-LTSIRM-RTSIRM protocol, and 24 underwent the more abbreviated sweep-cool-warm (or warm-cool) protocol (See Bilardello and Jackson (2013) for more details). The FC-ZFC-LTSIRM-RTSIRM protocol involves first applying a sustained DC field of 2.5 T on a sample as it cools from room-temperature to 20 K (field-cooling, FC). The field is then turned off and the remanence upon warming to 300 K is measured. The sample is then cooled back to 20 K (zero-field cooling, ZFC) and a 2.5 T low temperature saturation isothermal remanent magnetization (LTSIRM) is imparted. Remanence is again measured upon warming to room temperature (and is referred to as the ZFC remanence). Once at room-temperature a 2.5 T SIRM (RTSIRM) is applied and remanence is measured upon cooling to 20 K, and again during warming back to room-temperature. Under the sweep-cool-warm protocol the sample is first given a 2.5 T RTSIRM and then remanence is measured as the sample is cooled to 20 K. At 20 K, a 2.5 T LTSIRM is imparted and the remanence is measured upon warming to 300 K (also known as ZFC). Under the sweep-warm-cool protocol the RTSIRM and ZFC are switched. Measurements were taken for both protocols every 5 K.

Major hysteresis loops and backfield curves for 35 specimens were measured at room temperature using a MicroMag Princeton Measurements vibrating sample magnetometer (VSM) with a nominal sensitivity of 5×10^{-9} Am^2. First order reversal curves (FORCs) were obtained for 4 specimens including two magnetic extracts on both the VSM and the MicroMag Princeton Measurements Alternating Gradient Magnetometer with a sensitivity of 1×10^{-11} Am^2. FORC data were processed using the FORCinel software of Harrison and Feinberg (2008).

To further understand the mineralogy and range of coercivities present in our samples a triaxial-IRM Lowrie test was conducted on 18 oriented cubes (Lowrie, 1990). Three orthogonal IRM's were sequentially imparted on the specimens in fields of 1 T, 300 mT, and 100 mT using an ASC pulse magnetizer. Samples were then step-wise thermally demagnetized up to 550ºC in an ASC Model TD-48SC Thermal Demagnetizer with a TRM field coil. Samples were measured on a 2G Superconducting Magnetometer with nominal sensitivity of 2×10^{-11} Am^2 inside a magnetically shielded room with background fields $\leq$200 nT.

In order to further evaluate the presence of intermediate titanohematite in our samples we developed a self-reversal test. First, the NRM of the sample was measured. Next, we imparted a partial TRM using a 100 μT field with a declination and inclination of 0° and 0°, at a peak temperature of 300°C, for a soak time of 30 minutes in a ASC Model TD-48SC Thermal Demagnetizer with a TRM field coil for 13 oriented cubic specimens. The 300°C peak temperature was chosen to ensure that any self-reversing titanohematite acquired a RTRM, but also to avoid any dramatic mineralogic alteration to the sediment samples. Specimens were then measured and subjected to stepwise alternating field (AF) demagnetization up to fields between 150–170 mT. Measurements and AF demagnetization were conducted using the U-Channel Superconducting Rock Magnetometer (2G Enterprises, Inc. 755, DC-4K Liquid Helium Free SQUID) with inline ARM and offline IRM capabilities. Specimens whose magnetic remanence is dominated by self-reversing titanohematite should show a TRM that is oriented antiparallel to the applied field direction (declination 180°, inclination 0°). Specimens that contain a mixture of magnetic minerals that record a remanence parallel to an applied field (e.g. magnetite, titanomagnetite, goethite, and non-self-reversing titanohematite) and nearly antiparallel to an applied field (self-reversing titanohematite) should show a demagnetization path that falls along a great circle in equal area projection between 0° and 180°. Samples with negligible self-reversing minerals should show no great circle behavior and should instead show circular clustering parallel to the applied field direction. Depending on the relative rates of removal of the parallel and antiparallel components, the total TRM intensity may also show diagnostic patterns of variation during stepwise demagnetization.

Non-Magnetic Analysis

To further constrain mineralogy, X-ray Diffraction (XRD) and electron microprobe analysis (EPMA) were conducted on magnetic extracts at the University of California, Berkeley. XRD patterns were collected for 6 samples using a PANalytical X'Pert Pro diffractometer equipped with a Co-K_α source. Extracts were mixed with acetone and placed on silicon zero background plates, which were then mounted onto the XRD sample stage for pattern acquisition. Collection times were optimized for each sample and ranged from 25 minutes to 3 hours. The X'Pert HighScore PANalytical software was used for analysis accessing the PDF-2 2003 release database.

Sample compositions for three magnetic extracts were measured by electron probe microanalysis (EPMA) with a Cameca SX-51 in the Department of Earth and Planetary Science at the University of California, Berkeley. Analyses were conducted with 15 keV accelerating voltage, 20 nA beam current, and 1 micron beam diameter. Elements were acquired using analyzing crystals LIF for Fe kα, Mn kα, PET for Ti kα, Ca kα, TAP for Mg kα, Al kα, and NICRBN for O kα. On and off peak counting times were 20 seconds for all elements, except O kα, for which the on and off peak count time was 40 seconds.

To inspect the optical properties of our magnetic minerals further, scanning electron microscope (SEM) images using backscattered electrons (BSE) were collected for magnetic extracts. SEM analysis was carried out on a Zeiss EVO Variable Vacuum Instrument -10 SEM at the University of California, Berkeley. Qualitative chemical analysis was performed with an energy-dispersive X-ray detector (EDS) and elemental analysis was performed on the EDAX system with a silicon drift detector and thin windows, which detect down to Boron.

3.5 Results

The determination of Néel/Curie temperatures from high-temperature susceptibility, $\chi(T)$, measurements was unsuccessful for whole rock specimens because response was not reversible between heating and cooling cycles. The irreversibility was likely caused by alteration of Fe-bearing clay minerals to form magnetite during heating, suggested by a susceptibility increase upon cooling. Alteration appears minimally at temperatures below 350ºC, and occurs primarily at temperatures between 350ºC and 600ºC. High-temperature susceptibility experiments on magnetic extracts were much more successful. For all specimens, temperature curves were reversible below 400ºC and show Néel/Curie temperatures ranging from ~100°C to 200°C (Fig. 3.3). These data are consistent with the estimates from Swisher et al. (1993) for rocks from the Hell Creek region, and is in the range of expected Néel/Curie temperatures for intermediate composition titanohematite. Titanohematite compositions were determined from Néel/Curie temperatures using the calibration of Moskowitz et al. (2015) and range from y = 0.53–0.63 (Fig. 3.3). For two specimens, a second Néel/Curie temperature is found around 580ºC (Fig. 3.3). While this temperature is indicative of the presence of magnetite, it is difficult to say from these data alone whether magnetite is a primary mineral found within the sample, or if it was a laboratory-induced by-product of alteration upon heating, potentially from clay minerals in impure magnetic extracts. Fortunately, the low temperature magnetometry data help address this ambiguity. Extracts that were heated beyond 400ºC show irreversibility between heating and cooling curves (Fig. 3.3). Unlike whole rock specimens, cooling curves for extracts show a drop in susceptibility suggesting that irreversibility may be caused by oxidation of a magnetic mineral, potentially titanomaghemite.

The low temperature magnetometry experiments showed signs of magnetite and/or titanomagnetite in 90% of the samples. The Verwey transition occurs at ~120K in stoichiometric magnetite and is a first-order phase transition from cubic to monoclinic crystal symmetry. The Verwey transition does not occur in Ti-substituted forms of magnetite, but a similar low temperature behavior is observed associated with a change in sign of the mineral's magnetocrystalline anisotropy constant at a temperature that depends on Ti content (Moskowitz et al., 1998; Church et al., 2011). When magnetite and titanomagnetite grains become partially oxidized ('maghemitization') these transitions occur over broader temperature ranges and eventually become completely smeared out, making it difficult to determine if a sample contains pure magnetite or titanomagnetite. This latter behavior was expressed by 90% of the samples in this study (Figs. 3.4 and 3.5).

For all specimens (whole rock and magnetic extract) RTSIRM curves show a near two-fold increase in remanence towards lower temperatures (Fig. 3.4). Results from the FC-ZFC-RTSIRM-LTSIRM protocol also show a significant remanence gain on RTSIRM cooling (Fig. 3.4). While at first glance the two-fold increase in remanence on RTSIRM cooling appears diagnostic of goethite (e.g. Lowrie and Heller, 1982; Dekkers, 1989; France and Oldfield, 2000), this feature is also present for magnetic extracts (Fig. 3.5), which likely do not contain goethite, because it is difficult to extract using common magnetic separation techniques. Proof of the absence of goethite in magnetic extracts exists in FC-ZFC measurements as one of goethite's diagnostic features, a wide spread between FC and ZFC remanences, is absent for all specimens except one (Fig. 3.5). A likely explanation for this observed trend is that the increased intensity toward lower temperatures is due to the presence of intermediate-composition titanohematite, not goethite, as it also has a low ordering temperature (~200°C), and therefore spontaneous magnetization increases strongly on cooling.

Hysteresis data are consistent with the presence of a low-coercivity ferromagnetic mineral, indicated by low (<10 mT) bulk coercivities, and backfield curve saturation well below 1T; some samples however have a higher coercivity tail which we suggest is due to the presence of goethite and/or hematite. Paramagnetic minerals make up a large percentage of the magnetic signal consistent with the abundance of clays in our samples. Plotting hysteresis data on a Day plot (Fig. 3.6) with the mixing curves from Dunlop (2002) shows that the dominant mineralogy of our samples is not pure magnetite. While samples appear to plot in a roughly congruent pattern, they show higher Bcr/Bc ratios than magnetite and fall to the right of the Dunlop mixing lines. Looking at the data on a squareness-coercivity plot (Mr/Ms vs. Bc: Fig. 3.7) we see that our data plot in a linear trend, suggesting that our samples have similar mineralogies but varying grain sizes. Plotting the trends for low Ti-magnetite and TM60 (Wang and Van der Voo, 2001) we see that our data plot between the trends, suggesting that our samples are likely oxidized.

FORC data were collected to further assess the distribution of coercivities in both whole-rock samples and magnetic separates. FORC diagrams for both sample types show a strong coercivity peak around 5 mT with strong interaction fields (Hu) extending in both the positive and negative direction to ± 20 mT along the Hu axis (Fig. 3.8). This peak is most likely representative of the pseudo-single-domain grains within our samples and is consistent with the measured bulk coercivities measured from the major hysteresis loops. In addition to the low coercivity peak, considerably higher coercivity grains extend out along the Hu = 0 axis to as far as 70 mT, indicating populations of stable-single domain grains. These high coercivity grains are more apparent in the whole rock samples, suggesting that the magnetic separation techniques used in this study are biased towards the collection of larger sized particles (e.g., PSD and MD), as SD size grains may adhere to clay particles removed during the extraction.

Thermal demagnetization of isothermal remanent magnetizations (IRM) applied along the X, Y, and Z axes of representative samples shows that for the majority of samples the IRM is held by grains whose coercivities fall between 0–300 mT, with a majority of remanence held between 0–100 mT (Fig. 3.9). Very little remanence is held between 300 mT–1 T, however it is evident that the small amount of remanence held in this component is removed around 300ºC, consistent with unblocking temperatures for intermediate titanohematite. Remanence held between 0–100 mT, and 100–300 mT shows an almost continuous drop in remanence between 100–300ºC and a sharper drop between 300–400ºC, consistent with the presence of both intermediate titanohematite (with Tc between 100–200ºC) and titanomagnetite(maghemite) (most evident within the higher 300–400ºC range). Remaining remanence after 400ºC is likely held by magnetite or titanomagnetite(maghemite), observed in both high-T susceptibility experiments (although it might be due to alteration) and low-temperature experiments. For a few samples (e.g., HHA1-3B in Figure 3.9), a large drop in remanence for all coercivities occurs around 100ºC, consistent with the presence of intermediate titanohematite.

Results from the self-reversal test show that all whole-rock samples have a component that acquires thermoremanent magnetization parallel to the applied field. This component could be held by titanomagnetite or maghemite with blocking temperatures below 300ºC, or by titanohematite with disordered domains that have Néel/Curie temperatures higher than the applied temperature (in which case the ordered domains would not acquire an antiparallel direction), or by goethite. Of the thirteen samples run, two show complete reversal from the applied direction after demagnetization to AF steps between 150–170 mT. One such sample, MKA1-3D, is shown in Figure 3.10, where demagnetization data trace a clear great circle path on a stereonet, reaching an orientation nearly orthogonal to the TRM field direction after 50 mT

demagnetization, and continuing to change progressively up to the maximum AF treatment of 130 mT, after which it is very nearly antiparallel to the TRM field direction. The moment of the sample initially decreases strongly, reaching a minimum near 50 mT where the x component (parallel to the TRM field) changes sign, and then increases progressively as the field-parallel TRM is removed more rapidly than the antiparallel RTRM. This behavior is strongly suggestive of the presence of intermediate titanohematite, and is consistent with earlier studies that show self-reversing titanohematite to have slightly more elevated coercivities than magnetite and titanomagnetite (Lawson et al, 1987; Goguitchaichvili and Prévot, 2000). Of the remaining samples, 5 specimens show incomplete trends toward the antiparallel direction during demagnetization, which could be caused by a stronger overlap in coercivity between minerals holding the parallel and antiparallel components. An example of this behavior (HHA3-2D) is shown in Figure 3.10. The acquisition of the antiparallel direction in some of these samples suggests that the intermediate titanohematite present is SD to PSD in grain size because self-reversal is unlikely to occur in MD size intermediate titanohematite grains (Dunlop and Özdemir, 1997).

Four specimens showed little sign of any remanence antiparallel to the applied field direction. These specimens acquired a direction slightly offset from the applied field direction and trended toward the applied field during AF demagnetization. One specimen acquired a direction slightly offset from the applied field and did not show any change with AF demagnetization (HH1-1C in Figure 3.10). While it is possible that these particular samples contain intermediate titanohematite with low coercivity, which would therefore be removed first during AF demagnetization, it is more likely given the elevated coercivities observed in earlier studies, that this specimen does not contain intermediate titanohematite. Instead, the remanence of this sample is held almost entirely by minerals that acquire a thermoremanence parallel to an applied field.

XRD analysis shows that for 4 of the 6 magnetic extracts the diffraction peaks of the Fe-Ti oxides best-align with those of an ilmenite standard, indicating that the oxides have rhombohedral crystal structures consistent with intermediate titanohematite (Fig. 3.11). Titanomagnetite was only identified in one sample in which ilmenite is also identified. However, upon reanalysis using a longer collection time, titanomagnetite no longer appears as a best-match mineral. One sample did not yield good results due to the small size of the extract. Pure end-member magnetite was not identified in any of the six analyses, but this is not surprising given that the detection limit for most XRD systems is 1% by mass. The sensitivity of rock magnetic measurements is much higher by comparison.

Results from EPMA analysis were used to calculate Ti:Ti+Fe ratios for each grain, from which an average and standard deviation for each magnetic extract were calculated. Within an extract, Ti:Ti+Fe ratios are consistent, with standard deviations of no more than 6 percent of the average value. The calculated Ti ratios for the samples ranged from 0.245 to 0.303 and are only consistent with titanomagnetite compositions ($Fe_{3-x}Ti_xO_4$) where $x \geq 0.74$, which would correspond to Curie temperatures $\leq$70°C; this is far too low to explain the behavior observed here. Instead, these Ti ratios are more likely to be intermediate composition titanohematite. Titanium ratios determined from microprobe analysis were accordingly plotted on the titanohematite solid-solution series in Fig. 3.12, which suggest a possible range of titanohematite compositions from y = 0.5–0.6, consistent with observed Néel/Curie temperatures. SEM images using backscattered electrons were collected from the same magnetic extracts used for EPMA analysis to check for potential microstructures within the Fe-Ti oxides. No evidence of

intergrowths or other distinctive microstructural features were discerned and as such we do not include the images here.

3.6 Discussion

Magnetic Mineralogy of Hell Creek sediments

Results from extensive rock magnetic analysis suggest that sediments from the Hell Creek region in Montana are composed of three principal magnetic minerals in various proportions: goethite, intermediate titanohematite, and magnetite/titanomagnetite(maghemite). Based on the results of the self-reversal tests, intermediate titanohematite is never so abundant so as to be the dominant (*sensu* intensity) remanence carrier, but does occur as a significant carrier of remanence (upwards of 25%) in the majority of samples. The identification of the Verwey transition in low temperature magnetometry experiments, persistent remanence above 400°C, and Curie temperatures ~580ºC also support the presence of magnetite and titanomagnetite (or their partially oxidized equivalents) and suggests that these minerals are likely to be the primary holders of remanence. While the XRD results show the presence of titanomagnetite in only one sample, it is important to consider the coarse resolution of this nonmagnetic technique. Goethite is identified in select specimens in low temperature magnetometry experiments, recognized by a large increase in remanence upon cooling and a wide spread between FC and ZFC curves for whole rock samples.

The integration of information from our rock magnetic techniques and non-magnetic techniques (similar to those used in past studies, e.g., Force et al., 2001) lead us to conclude that the dominant magnetic carrier in our samples is magnetite/titanomagnetite(maghemite), while intermediate titanohematite is an important ancillary magnetic carrier phase in most samples. Calculated Néel/Curie temperatures of ~200ºC are consistent with EPMA data and XRD results that suggest that the dominant mineralogy by mass is rhombohedral intermediate composition titanohematite, with compositions ranging from y = 0.53–0.63 (Fig. 3.11). Furthermore, low-T magnetic experiments show a large magnitude increase in magnetization upon cooling for magnetic extracts, not due to goethite, which is suggestive of another mineral phase with low ordering temperature, but most likely intermediate titanohematite. The stronger saturation magnetization of magnetite and titanomagnetite, however, allow these minerals' remanence to overshadow that of titanohematite. Results from the self-reversal tests show evidence for a mineral phase that acquires a direction antiparallel to the applied field direction, consistent with the presence of intermediate titanohematite. These results are further corroborated with the moderate coercivities and saturating fields < 300 mT observed in hysteresis measurements.

These mineralogic results, combined with evidence for SD grain sizes from FORC diagrams and the self-reversal test, suggest that the Hell Creek sediments have the capacity to be reliable paleomagnetic recorders over geologic timescales, provided that they have not been heated above ~200 °C. Reheating of these sediments could result in a RTRM overprint, which would greatly complicate paleomagnetic interpretation. While goethite was likely formed during diagenesis after deposition, the intermediate titanohematite, magnetite, and titanomagnetite are likely primary detrital minerals in sediment derived from Laramide basement uplifts and Cretaceous volcanism to the west. Intermediate titanohematite only forms in limited geological environments (calc-alkaline volcanic centers), which is consistent with those associated with Cordilleran volcanism. This argument is further corroborated by the identification of intermediate titanohematite in upper Cretaceous-lower Paleogene sediments in sedimentary basins throughout the Central U.S. (Table 3.1; Fig. 3.1). Furthermore, intermediate

titanohematite cannot form at near-surface conditions and therefore is unlikely to be due to diagenetic alteration. Thus, sediments from the Hell Creek region are likely to be reliable paleomagnetic recorders, given that the sediments have not been reheated above 200ºC, or struck by lightning, and that care is taken to remove any remanence held by goethite.

Intermediate Titanohematite recognition

We conclude that intermediate titanohematite is best recognized when observations from XRD and EPMA analysis, high-temperature susceptibility experiments, and the self-reversal test can be integrated. XRD and EPMA analysis along with high-temperature susceptibility measurements have been utilized before as means to identify the presence of intermediate titanohematite in the majority of previous studies (Force et al., 2001). While these analyses are a reasonable means for identifying the presence of intermediate titanohematite, none of these experiments adequately tests whether this mineral phase is the primary carrier of remanence. The self-reversal test, developed in this study, is a powerful new technique that not only provides a unique identifier of titanohematite (the presence of an antiparallel direction acquired at temperatures only slightly above blocking temperatures for intermediate titanohematite), but it also provides a good assessment of how much remanence is held by this phase. Furthermore, due to intermediate titanohematite's unique self-reversing property, this technique has the potential to stand on its own, unlike other analyses.

Comparison to Previous studies

Comparing the results of this study to other rock magnetic and paleomagnetic studies on Late Cretaceous and Paleogene age clastic deposits across central North America, it can be seen that these sediments all share similar magnetic properties (Table 3.1). In all paleomagnetic studies a primary signal was obtained between coercivities of 10–80 mT, and temperatures below 400ºC, with calculated Curie temperatures ranging between 150–250ºC. When conducted, XRD and EPMA analysis indicate the presence of intermediate composition titanohematite in all studies.

Of the selected studies shown in Table 3.1, intermediate titanohematite was identified or indicated in ~75% of these deposits extending in age from Late Cretaceous to Early Eocene. It is clear that due to similarities in magnetic properties, sediment source, and age, even in studies where titanohematite was not indicated as a primary magnetic recorder, it likely is present. However, overlaps in coercivity, unblocking temperatures, and Néel/Curie temperatures between intermediate titanohematite and magnetite/titanomagnetite (or their partially oxidized equivalents), along with common beliefs about the relative rarity of titanohematite in nature, create a situation where the potential presence of intermediate titanohematite is rapidly dismissed. Therefore, more advanced rock magnetic and non-magnetic techniques are needed to test the importance of intermediate titanohematite to sedimentary remanence.

Intermediate titanohematite has also been identified in economically important placer deposits that mark Upper Cretaceous shorelines extending from Montana to New Mexico (Houston and Murphy, 1962, 1977; Force, 2000; Force et al., 2001) and in uranium-bearing Mesozoic and Cenozoic sandstones within Central U.S. and south Texas (Force et al., 2001). Looking at the ages and distributions of these deposits in concert with those for the intermediate titanohematite bearing sediments discussed above, Force et al. (2001) suggest that the sources for this unique mineral come from three distinct volcanic centers of different age in three different areas within the U.S. This evidence suggests that geologic environments producing intermediate

titanohematite are not as rare as they are presented in literature, and when these environments are coupled with effective sediment transport mechanisms, like those within the Late Cretaceous North American Cordillera, this mineral can become widespread in detrital deposits far beyond the volcanic source for millions of years. Therefore, it is likely that other sedimentary basins next to calc-alkaline volcanic centers, such as those in the Andes and other convergent margins, also preserve intermediate titanohematite, even if RTRMs are not preserved in outcropping volcanics. Understanding the role intermediate titanohematite plays in sedimentary remanence is imperative for proper paleomagnetic interpretation as intermediate titanohematite, due to its low unblocking temperatures combined with its ability to acquire a RTRM, has the potential to complicate paleomagnetic records. While the current literature suggests that intermediate titanohematite is rare in nature, it appears that more specialized yet straightforward rock magnetic analysis may reveal it to be more abundant in the rock record than previously thought.

3.7 Conclusion

Extensive rock magnetic analyses on sediments that span the Cretaceous-Paleogene boundary in the Hell Creek region, Montana show that the dominant ferrimagnetic mineral by mass is intermediate composition titanohematite with compositions ranging from y = 0.53–0.63. The dominant magnetic remanence carrier, however, is probably magnetite and titanomagnetite(maghemite). Néel/Curie temperature determination and XRD and EPMA analysis are effective techniques for recognizing the presence of intermediate titanohematite. The self-reversal test, a new technique developed in this study for intermediate titanohematite identification, contributes information about how much of a sediment's remanence may (or may not) be held by intermediate titanohematite. Further development, however, is needed to make it into a tool that is capable of detecting a greater range of titanohematite compositions. The similar magnetic properties shared between our sediments and coeval sediments across the central U.S. suggest that titanohematite may carry a greater fraction of natural remanent magnetization than previously recognized, which is important to characterize in order to avoid biased paleomagnetic interpretation. Although geologic environments where intermediate composition titanohematite forms are limited, if they are coupled with efficient sediment transport mechanisms, then this mineral can become widespread in detrital sediment deposits over millions of years of deposition. It is likely that other sedimentary basins sourced from intermediate calc-alkaline volcanic centers also preserve intermediate titanohematite and that this mineral may be more abundant in the rock record than previously perceived.

Figures

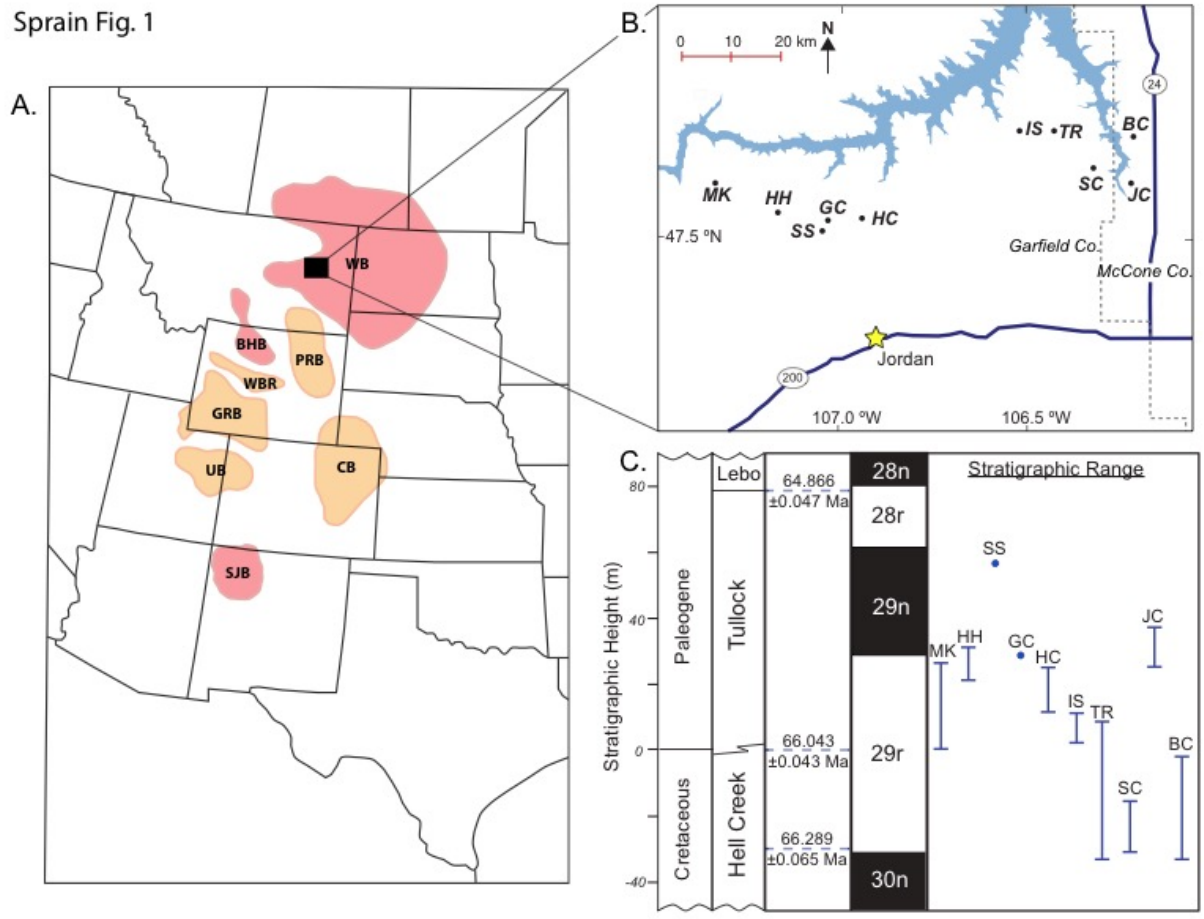

Figure 3.1. A. Major foreland basin systems of the western continental United States that contain upper Cretaceous-lower Paleogene sediments (after Force et al., 2001). Basins in red indicate where intermediate titanohematite has been identified. WB: Williston basin, BHB: Big Horn basin, PRB: Powder River basin, WBR: Wind River basin, GRB: Green River basin, UB: Uinta basin, CB: Denver basin, SJB: San Juan basin. B. Location map of study area in the Hell Creek region of northeastern Montana. Fort Peck reservoir is shown in light blue. Labeled dots indicate locations of paleomagnetic samples used in this study. MK: McKeever Ranch, HH: Hell Hollow, GC: Garbani Channel (Hill), SS: Saddle Section, HC: Hell Creek Marina road (Lerbekmo), IS: Isaac Ranch, TR: Thomas Ranch, SC: Sandy Chicken, BC: Bug Creek, JC: Jack's Channel. C. Stratigraphic column showing magnetic polarity (black = normal, white = reverse) and stratigraphic range of sites shown in B. Ages picked are for the U, IrZ (Cretaceous-Paleogene boundary), and Null coal from Sprain et al. (2015). Figure after Sprain et al. (2015).

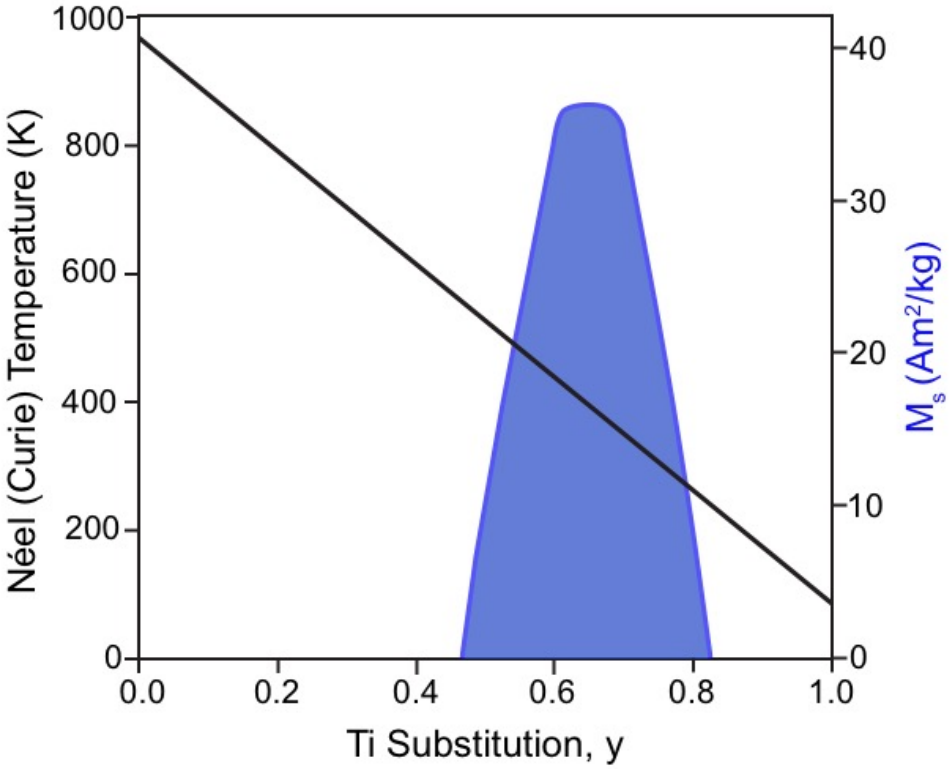

Figure 3.2. Effect of titanium substitution (y) on room-temperature saturation magnetization (Ms, blue) and Néel /Curie temperature (black) for the titanohematite solid-solution series. Blue shaded area represents region where titanohematite behaves ferrimagnetically. Figure after Moskowitz et al. (2015).

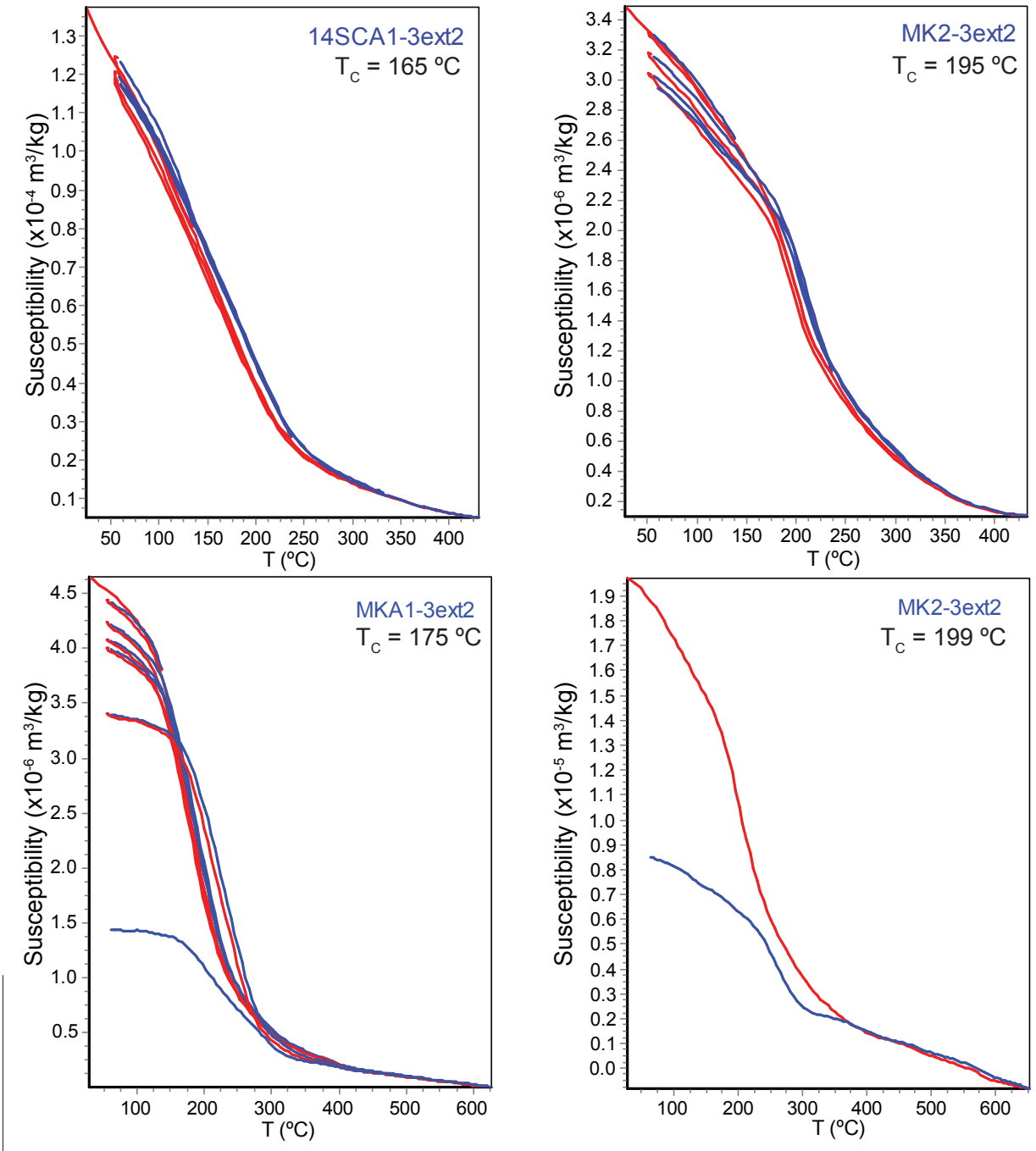

Sprain Figure 3

Figure 3.3. High-temperature heating (red) and cooling curves (blue) of bulk magnetic susceptibility, in air and argon (14SCA1-3ext2 only), for representative magnetic extracts. Néel/Curie temperatures (Tc) are indicated in the upper right of each panel.

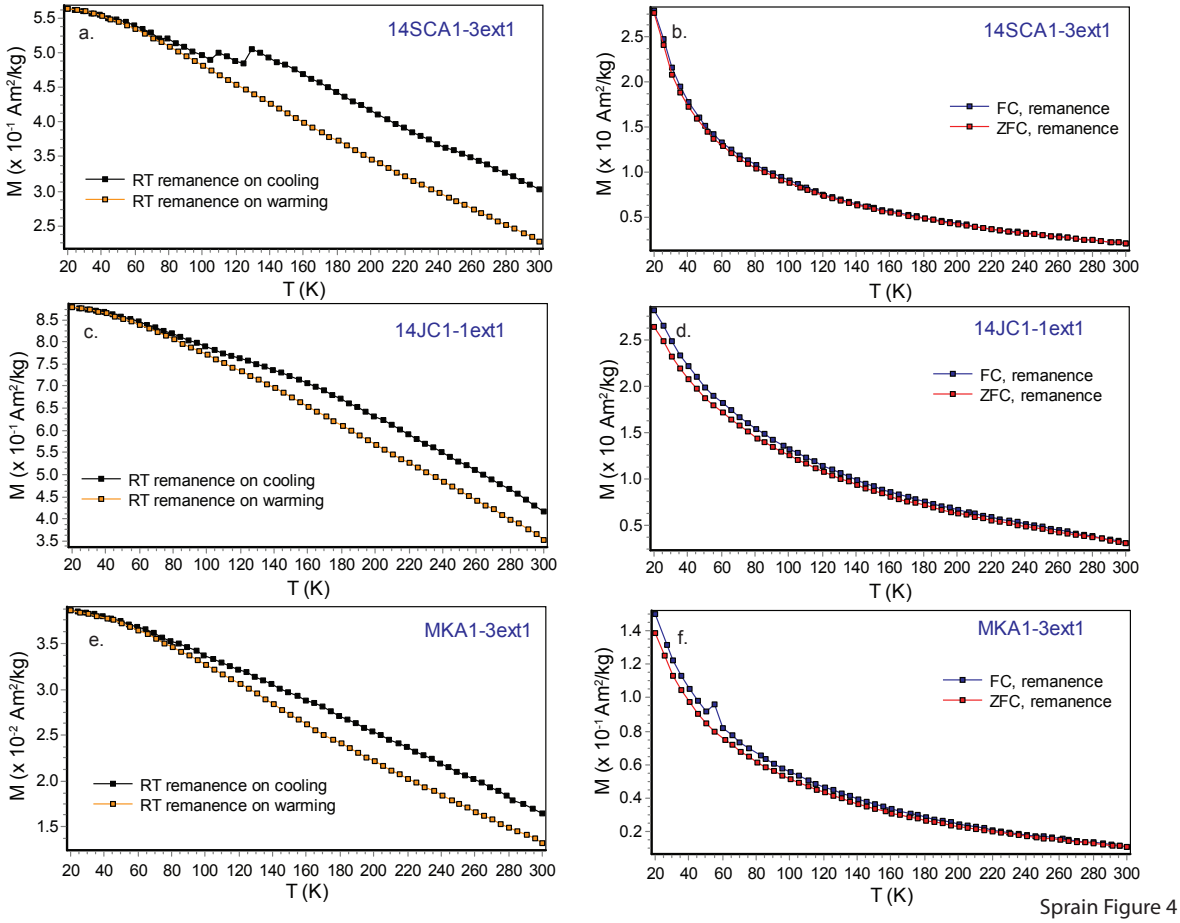

Figure 3.4. Low temperature magnetization curves on magnetic extracts for representative samples. The left panels show measurements of magnetization (M) during cooling (black) and warming (orange) following the application of a saturation isothermal remanent magnetization (SIRM) applied at room temperature (RT). The right panels show measurements of magnetization during warming following a sustained direct current field of 2.5 T during cooling (field-cooled, FC: blue), and measurements of magnetization during warming following a SIRM imparted at low temperature (zero field-cooled, ZFC: red). Note: spikes in magnetization in a. and f. are measurement artifacts.

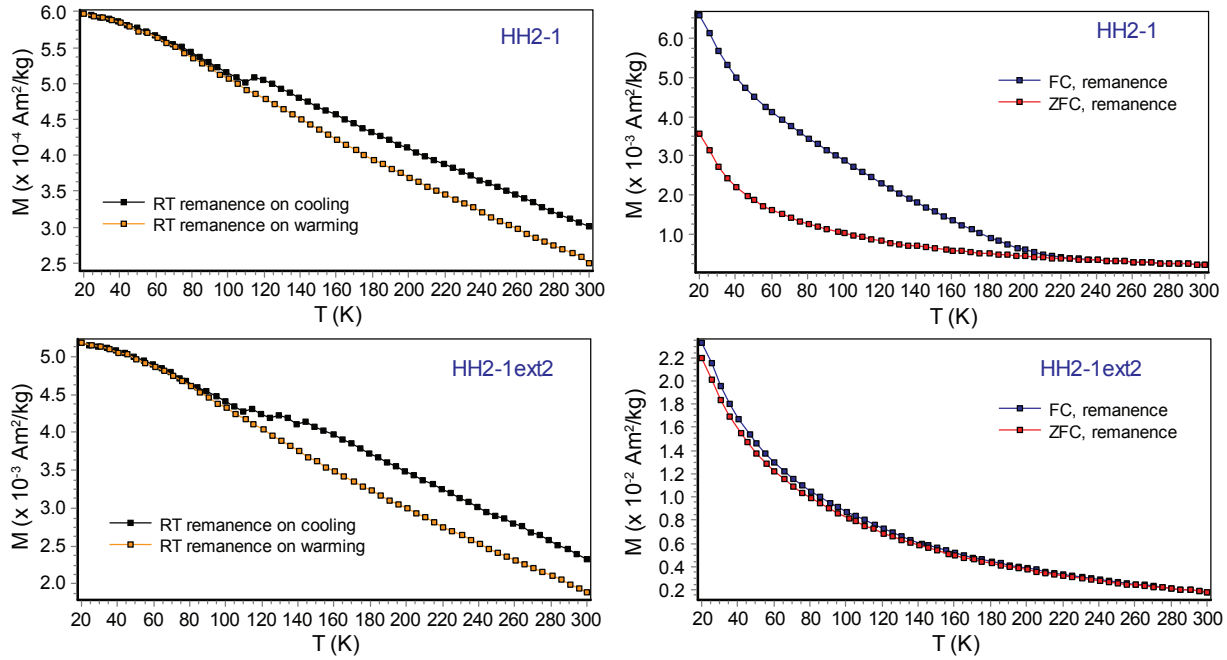

Sprain Figure 5

Figure 3.5. Low-temperature magnetization curves for a whole-rock sample (HH2-1) and a magnetic extract (HH2-1ext2) from the same specimen. Notice the large spread between the field-cooled (FC) and zero field-cooled (ZFC) curves for the whole-rock sample is not present for the magnetic extract but the RTSIRM curves remain similar.

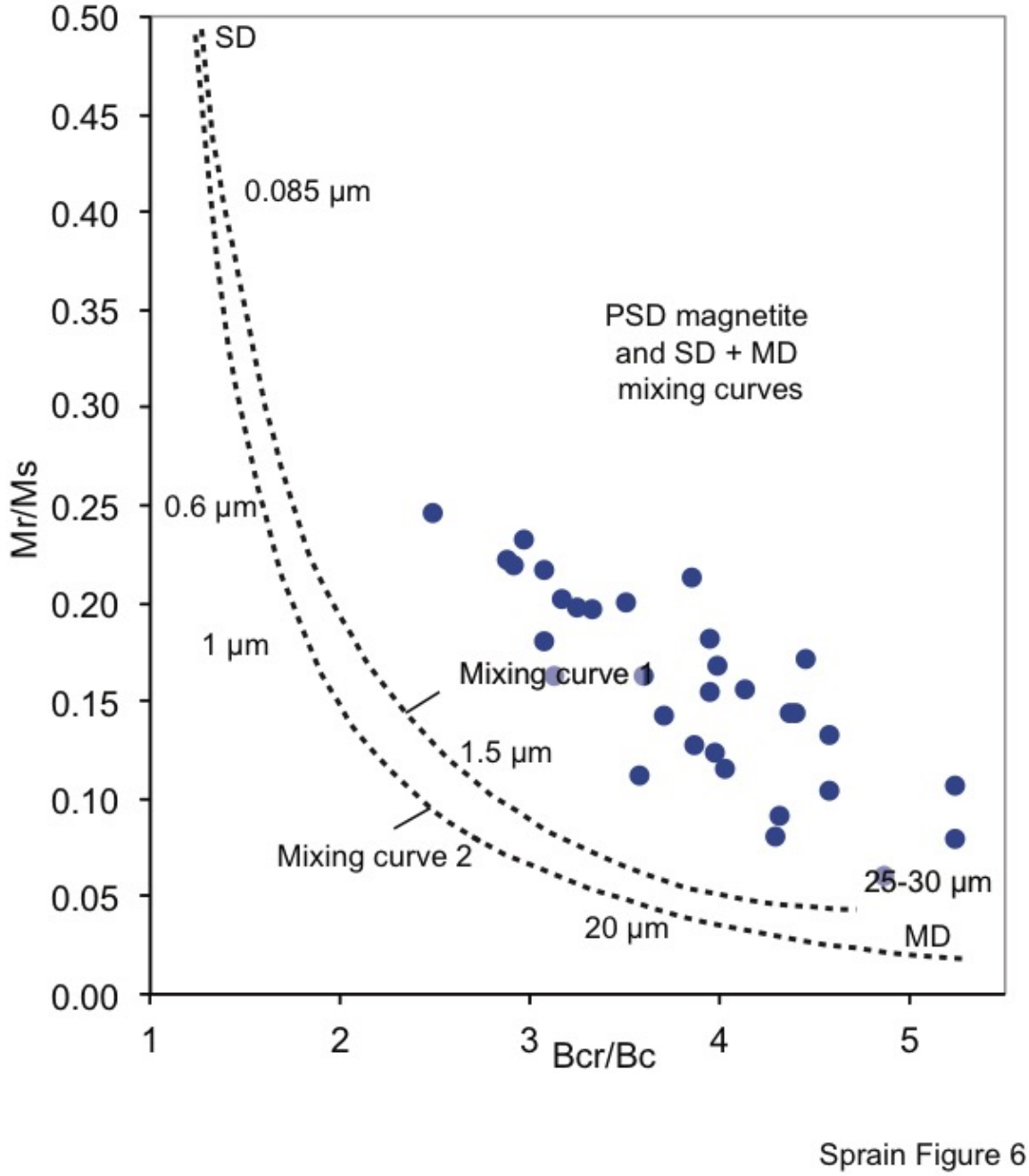

Figure 3.6. Day plot of hysteresis ratios (Mr/Ms vs. Bcr/Bc) for all measured whole-rock specimens (Day et al., 1977). Dotted curves indicate theoretical mixing curves of single domain (SD) and multidomain (MD) magnetite grains after Dunlop (2002). All data fall to the right of the mixing curves, suggesting that magnetite does not control the hysteresis properties of our samples.

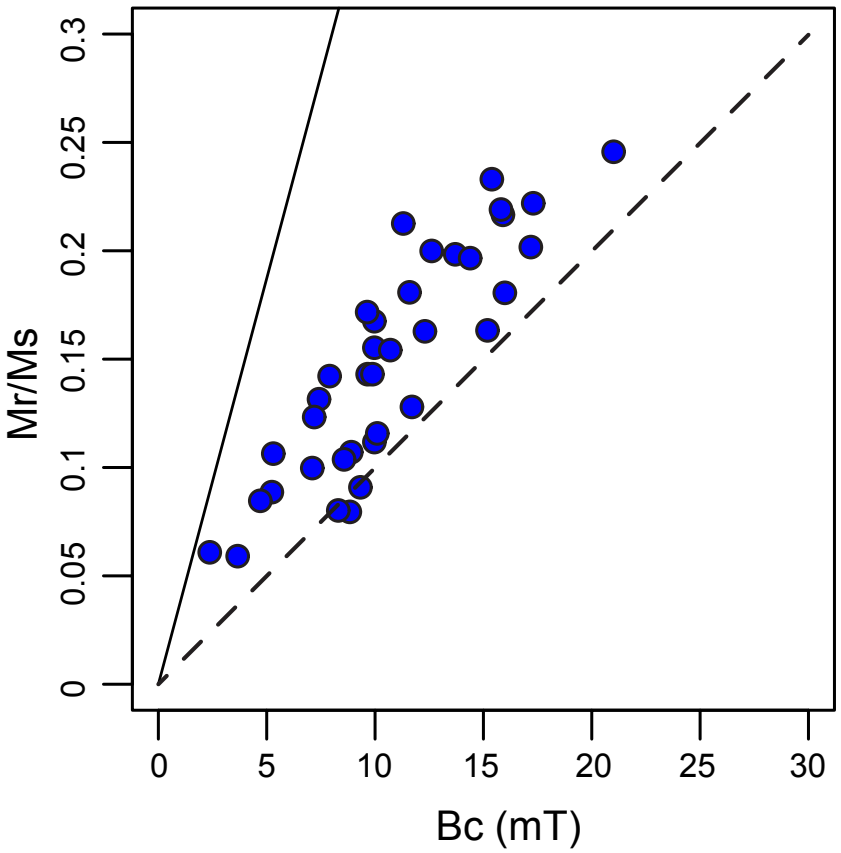

Figure 3.7. Squareness plot (Mr/Ms vs. Bc) for all measured whole-rock specimens. Solid and dotted lines show trends for TM60 and low-Ti magnetite after Wang and Van der Voo (2004). Data form a linear trend falling between the two lines, indicating that our samples share similar mineralogies, which are not solely magnetite or titanomagnetite.

Sprain Figure 8

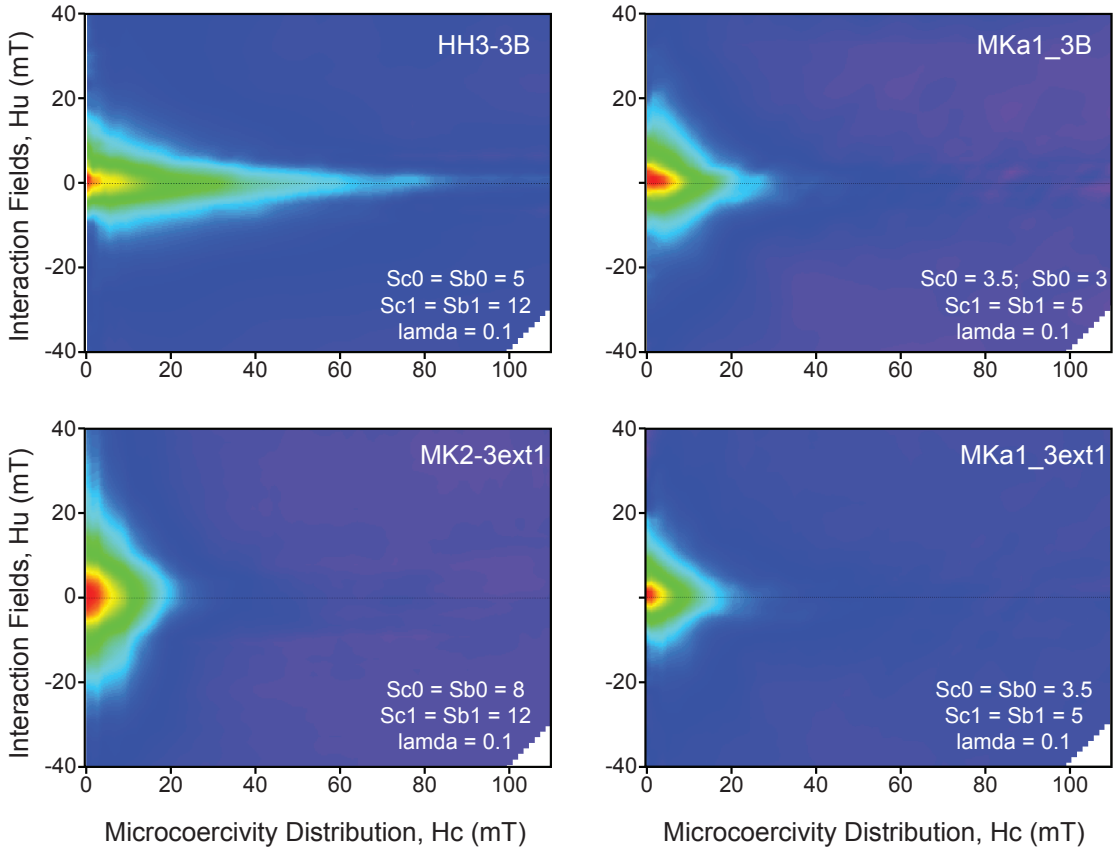

Figure 3.8. FORC distributions for two whole rock samples (HH3-3B and MKa1_3B) and two magnetic extracts (MK2-3ext1 and MKa1_3ext1) from the Hell Creek region. Each specimen shows varying combinations of PSD grains and non-interacting, stable SD grains, however SD populations are smaller in magnetic extracts. Distributions were produced using FORCinel v.2.02 (Harrison and Feinberg, 2008) and the VARIFORC method of Egli (2013). Each FORC distribution was produced after subtracting an averaged lower branch and removing the first point artifact.

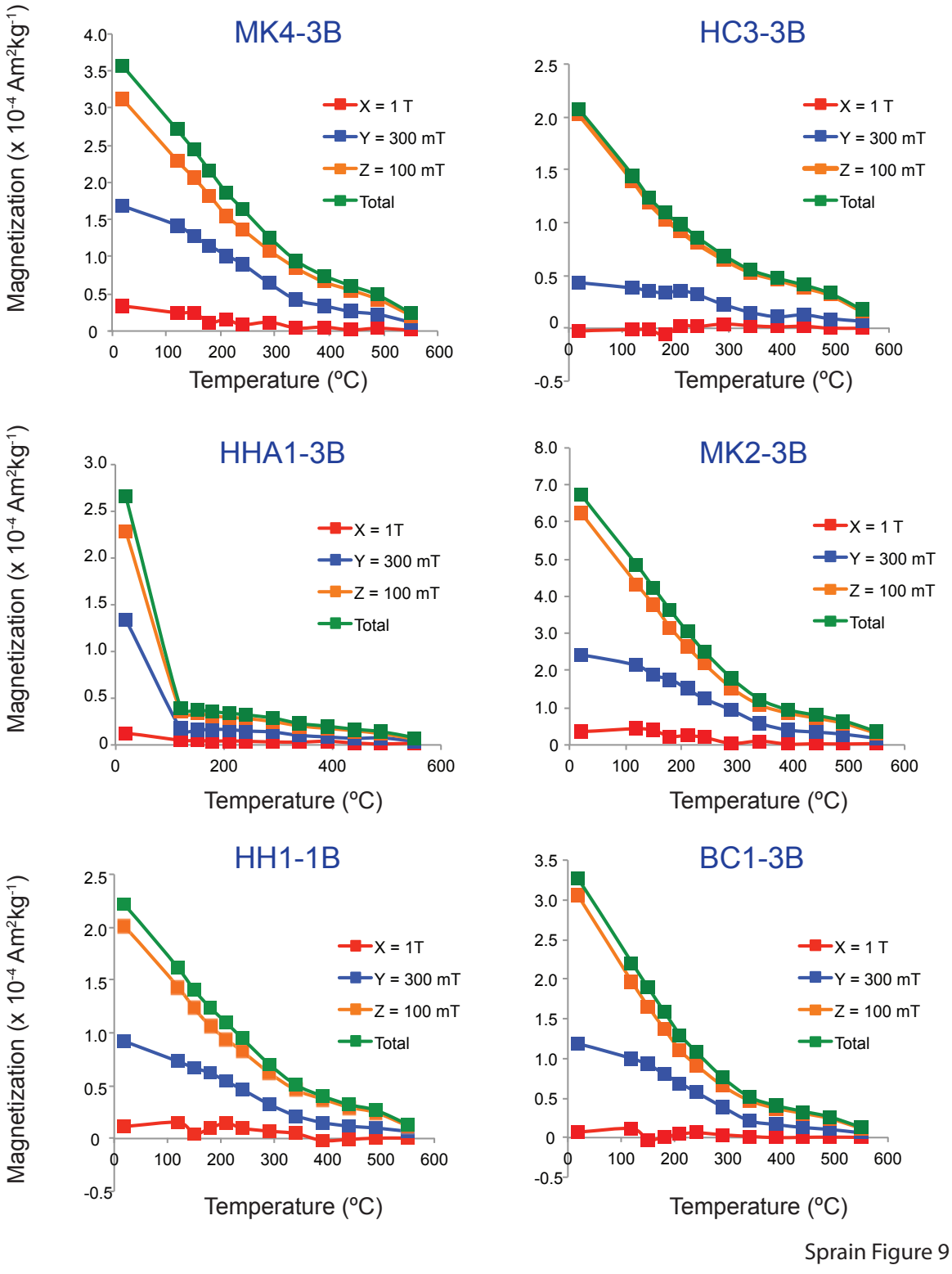

Figure 3.9. Thermal demagnetization of isothermal remanent magnetization (IRM) imparted along orthogonal X, Y, and Z axes for six selected specimens. Peak DC fields for each axis are noted. Approach follows that of Lowrie (1990).

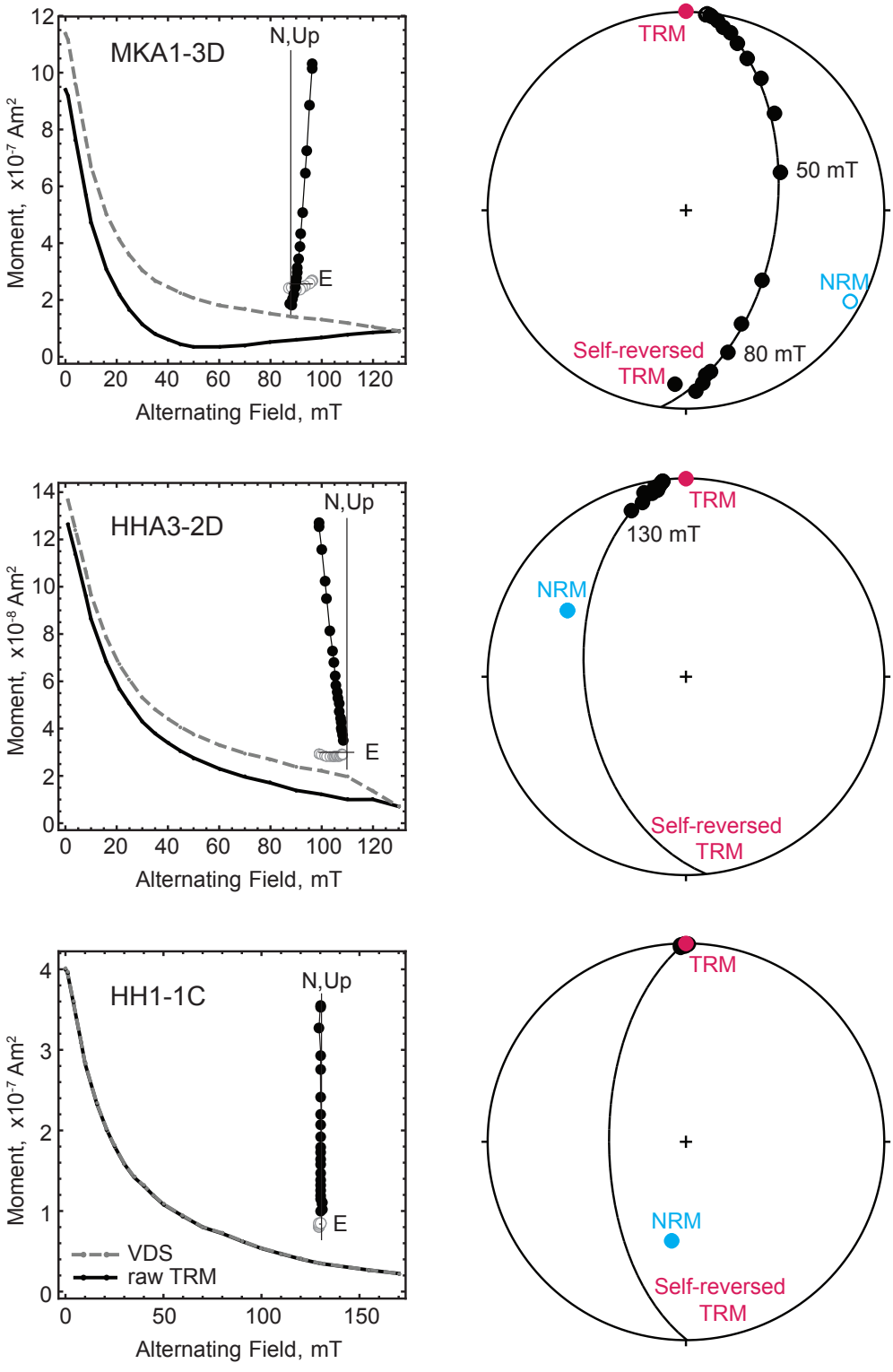

Sprain Figure 10

Figure 3.10. Demagnetization data from self-reversal tests showing three varieties of behavior. Plots on left show the intensity of the TRM during AF demagnetization, with orthogonal vector endpoint diagrams as insets. Gray dashed lines show the vector difference sum (VDS) of the data, while black lines show the uncorrected, raw demagnetization data. Stereonets on the right show the directional evolution of the TRM during AF demagnetization. Natural remanent magnetization (NRM) directions for each specimen are shown in blue. Best-fit great circles are shown for each specimen. Specimen MKA1-3D clearly shows a high coercivity component that is oriented antiparallel to the applied field direction of the TRM. This self-reversed component is much reduced in specimen HHA3-2D, although is still detectable in the stereonet as the remanence direction begins to travel along a great circle containing the antiparallel direction. Specimen HH1-1C demonstrates a sample with no discernable antiparallel component.

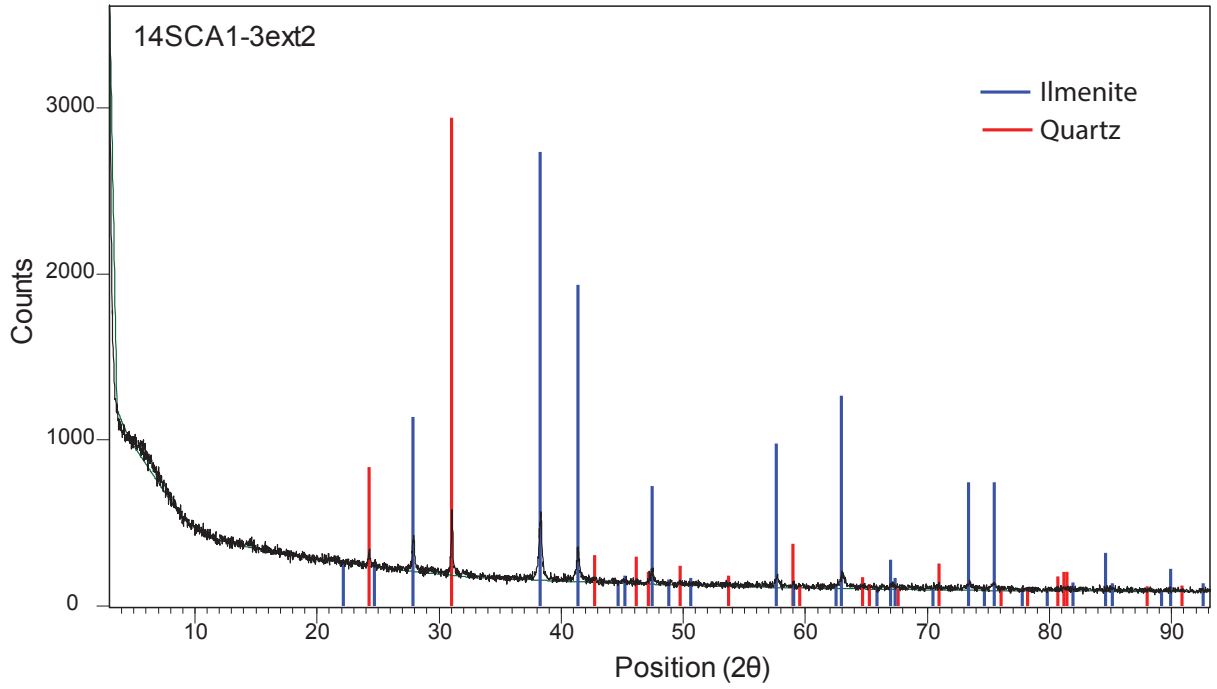

Sprain Figure 11

Figure 3.11. X-Ray diffraction pattern for representative sample (14SCA1-3ext2). Colored lines mark spectra of mineral standards that were selected as best-fits for the measured sample.

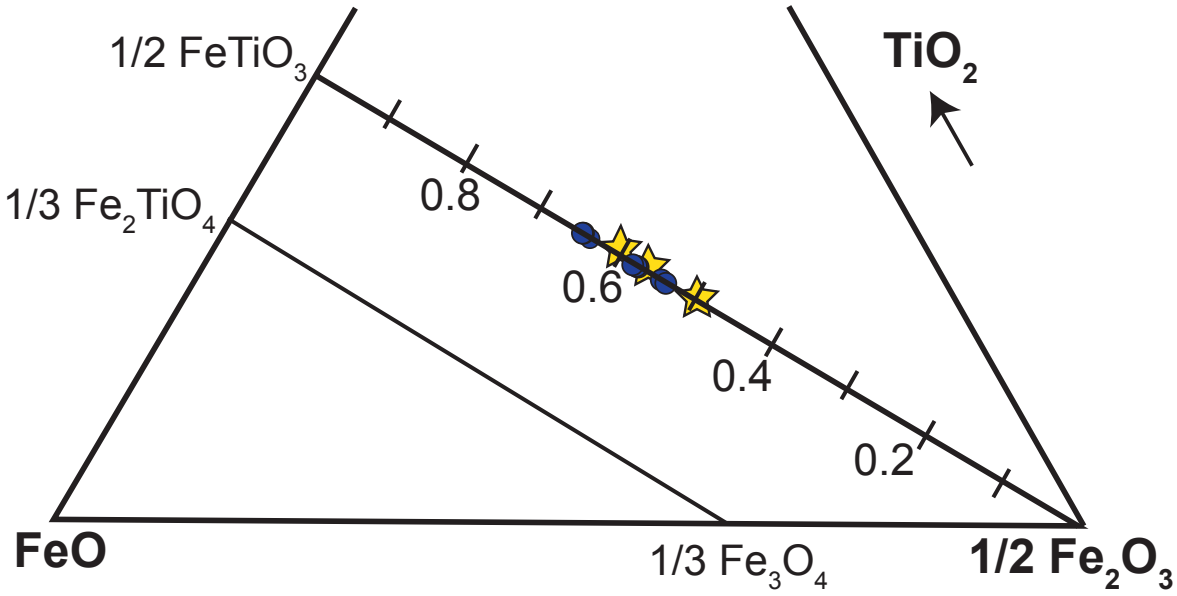

Sprain Figure 12

Figure 3.12. TiO_2-FeO-$1/2Fe_2O_3$ ternary diagram comparing titanohematite compositions determined from Néel/Curie temperatures (blue dots) and microprobe analysis of magnetic extracts (yellow stars). Calculated compositions from Néel/Curie temperature were determined using the calibration in Moskowitz et al. (2015).

Table 3.1: Magnetic properties of Laramide sediments

Location	Curie T Range (ºC)	AF demag range (mT)	Tub (ºC)	Age	Chrons	Mineral ID	IRM acquisition	XRD	EPMA	Paper
BHB, WY	180-250*, 580*	30	N/A	Late Pal.-Eoc.	C27r-C25r	M/TM, TH*	<300 mT	Y*	Y*	Butler et al., 1981*
SJB, NM	180-300*	20-60	N/A	Late Cret.-Pal.	C31n-C25r	M/TM, TH*	N/A	Y*	Y*	Lindsay et al., 1981*
BHB, MT	150-250	10-40	<300	Late Pal.	C27r-C26r	TH	200-300 mT	Y*	Y*	Butler et al., 1987*
WB, MT	160-200	20-80	<300	Late Cret.-Early Pal.	C30n-C28n	TH	<300 mT	Y*	Y*	Swisher et al., 1993
WB, MT	N/A	2.5-50	N/A	Late Cret.-Early Pal.	C30r?-C28n	N/A	N/A	N	N	LeCain et al., 2014
WB, ND	<225	10-50	100-300	Late Cret.-Early Pal.	C30n-C29n	TH	N/A	Y	Y	Lund et al., 2002
WB, MT	200*	20-80	N/A	Late Cret.-Early Pal.	C30n-C29n	M/TM, TH*	<300 mT	Y*	Y*	Archibald et al., 1982*
BHB, WY	~200, 580	N/A	N/A	Late Cret.-Early Pal.	N/A	TH, M	N/A	Y	Y	Force et al., 2001
WB, MT	~200	N/A	N/A	Late Cret.-Early Pal.	N/A	TH	N/A	Y	Y	Force et al., 2001
WB, Canada	N/A	10-30	100	Late Cret.-Early Pal.	C33n-C26r	TM, M, TH	N/A	N/A	N/A	Lerbekmo, 1999
WB, Canada	N/A	10-30	N/A	Late Cret.-Early Pal.	C33n-C29r	TM, M	N/A	N/A	N/A	Lerbekmo and Coulter, 1985
WB, ND	450-580, some 180-200	N/A	250-400	Late Cret.-Early Pal.	C29n-C27r	TMH	>100 mT	N/A	EDS	Peppe et al., 2009
PRB, MT	N/A	N/A	250-400º	Early Pal.	C29n-C26r	TMH	N/A	N/A	N/A	Peppe et al., 2011

*Reanalyzed in Force et al. (2001)

Table 3.1. Magnetic properties of upper Cretaceous-lower Paleogene sediments from Laramide-style basins within the Western U.S. Location indicates major foreland basin and U.S. state, unless conducted outside the U.S. BHB: Big Horn basin, SJB: San Juan basin, WB: Williston basin, and PRB: Powder River basin. AF demag range shows either the alternating field (AF) at which the characteristic remanent magnetization (ChRM) could be constrained, or the range of AFs over which the ChRM was removed. T_{UB} is the unblocking temperature determined from thermal demagnetization experiments. Mineral ID is the magnetic mineral attributed with carrying primary remanence. M: Magnetite, TM: Titanomagnetite, TH: Intermediate titanohematite, TMH: Titanomaghemite. IRM acquisition indicates the field at which saturation was reached. * Reanalyzed in Force et al. (2001).

Chapter 4. Calibration of Chron 29r: New high-precision geochronologic and paleomagnetic constraints from the Hell Creek region, Montana and their implications for the Cretaceous-Paleogene boundary mass extinction

Abstract The mass extinction at the Cretaceous-Paleogene boundary (KPB) marks one of the most important biotic turnover events in Earth history. Yet, despite decades of study the causes of the KPB crises remains in debate. A major inhibitor to consensus is inadequate geochronology, illustrated in the geomagnetic polarity timescale (GPTS). The GPTS, if calibrated using high-precision chronology, has the capacity to greatly improve our understanding of the events around the KPB. The GPTS is used for age control in numerous KPB studies including the timing of Deccan Traps (DT) volcanism, a majority of studies in marine sections, and studies on climate and ecological change across the KPB. The current calibration of the GPTS for circum-KPB polarity chrons (30n-28n) from the Geologic Time Scale 2012 draws heavily on astronomical tuning, and uses an $^{40}Ar/^{39}Ar$ age for the KPB as a tie point which has since been shown to be 200 ka too old. Furthermore, complex sedimentation has been recorded in marine sections immediately following the KPB, which can possibly obscure orbital signals and complicate cyclostratigraphic interpretation. An independent test of the cyclostratigraphy for this time period is imperative for confidence in the astronomical timescale. Further, polarity reversal ages given in the GPTS do not include uncertainty estimates, making them unsuitable for high-precision studies. Recent calibrations have been attempted using U/Pb geochronology on zircons, however U/Pb zircon dates are more likely to be biased by inheritance than ages determined using $^{40}Ar/^{39}Ar$ geochronology on single crystals of sanidine, and have been shown record residence times of ~10's of ka.

In this study, we provide constraints on the timing and duration of the most important circum-KPB chron, C29r, using high-precision $^{40}Ar/^{39}Ar$ geochronology and magnetostratigraphy on fluvial sediments from the Hell Creek region, Montana. Here we show results for 14 new magnetostratigraphic sections, and 18 new high-precision $^{40}Ar/^{39}Ar$ dates which together provide six independent constraints on the age of the C29r/C29n reversal and two constraints on the C30n/C29r reversal. Together, these results show that the duration of C29r was ~588 ka. We further present new geochronologic data for the KPB yielding the most precise date yet, of 66.047 ± 0.008/0043 Ma. Integrating our results into the extensive paleontological framework for this region further provides important constraints on rates of terrestrial faunal change across the KPB.

4.1 Introduction

Inadequate chronology is a key inhibitor to understanding major events in Earth history. An accurate timescale can inform us about rates of natural processes, can be used to correlate rock sequences across distant localities and geological settings, and in turn can be used to help us understand the underlying mechanisms behind these major events. Unfortunately, many major events in Earth history suffer from poor chronology and one such event is the Cretaceous-Paleogene mass extinction. The Cretaceous-Paleogene boundary mass extinction is one of the most important biotic turnover events in Earth history, drastically changing the nature of the biosphere both in the oceans and on land. Despite decades of study, a consensus has not been reached in regard to the cause of this mass extinction event, however most arguments center around the Chicxulub impact (e.g. Schulte et al., 2010), Deccan Traps volcanism (e.g. Keller et al., 2016), or both (e.g. Arens and West, 2008; Richards et al., 2015; Renne et al., 2015). The

Chicxulub impact has been dated at high-precision (Swisher et al., 1992; Renne et al., 2013) and has been shown to correlate in time with a tephra deposit that crops out 1 cm above the impact claystone in the Hell Creek region, northeastern Montana (Renne et al., 2013), which also coincides with a negative carbon isotope anomaly, and is above the highest in-situ dinosaur faunas and below Paleogene pollen. In recent years, the chronology of the Deccan Traps has been greatly improved due to two high-precision geochronologic studies performed in the Western Ghats region of western India, one utilizing the U/Pb zircon dating technique (Schoene et al., 2015) and another using $^{40}Ar/^{39}Ar$ geochronology (Renne et al., 2015). Before these studies, imprecise K/Ar geochronology and improper placement of the KPB within the Deccan sequence were used to argue that the Deccan Traps erupted in three pulses: the first pulse starting ~ 2 Ma before the KPB and ending well before it, the second starting around the C30n/C29r transition and extending until the KPB, and the third beginning around the C29r/C29n transition and extending into C29n (Chenet el al., 2007, 2008, 2009; Keller et al., 2008). The second pulse of magmatism was cited to encompass roughly 80% of Deccan Traps volume and has been called upon as the source of the late Maastrichtian warming event and latest Maastrichtian cooling (Li and Keller, 1998; MacLeod et al., 2005; Nordt et al., 2003; Tobin et al., 2012, 2014; Wilf et al., 2003; Thibault and Husson, 2016; Chenet et al., 2009), and associated ecological stress (Kucera and Malmgren, 1998; Keller et al., 2008; Tobin et al., 2012; Wilson et al., 2014; Thibault and Husson, 2016; Peterson et al., 2016). With more precise geochronology, we now know that the above-cited placement of the KPB within the Deccan Traps is incorrect and that the Deccan Traps volcanism in the Western Ghats did not erupt in pulses as described in Chenet et al. (2007), but instead showed relatively continuous eruption starting at the C30n/C29r transition, extending well into C29n (Schoene et al., 2015; Renne et al., 2015). New work has also shown that most of the volume of Deccan lava within the Western Ghats erupted after the KPB (Richards et al., 2015; Renne et al. 2015), however it is not clear whether the eruption of volcanic gases followed a similar trend. These new results beg for a reassessment of the role Deccan Traps volcanism played in the mass extinction event, calling into question what effect if any, volcanism had on pre-KPB environments and post-KPB recovery.

To understand the role Deccan traps volcanism played in the end Cretaceous mass extinction event and subsequent recovery interval, it is first important to constrain the tempo, timing, and mode of post-extinction faunal recovery in the early Paleogene, in addition to constraints on latest Cretaceous ecological instability, for both marine and terrestrial sections while also providing a means for correlation between these two realms. One way to achieve this would be with a Geomagnetic Polarity timescale calibrated with high-precision chronology for circum-KPB chrons (C30n-C28r; note the KPB is roughly halfway into C29r). Means for direct dating in marine sections are limited and geochronologic constraints are often provided by a combination of magnetostratigraphy and astronomical tuning, which has the power to provide high-resolution chronologies on the order of ~20 ka. However, beyond ~50 Ma, astronomical solutions are difficult to model due to the chaotic behavior of the solar system (Laskar et al., 2004), so astronomical tuning relies upon floating chronologies that must be anchored to an absolutely dated tie point. Current astronomically tuned marine KPB sections use the KPB, identified by an Ir-anomaly and extinction events, as their tie point (Thibault et al., 2016; Dinarés-Turrel et al., 2003, 2007; Westerhold et al., 2008). However, there are complexities using astrochronologic tuning in these sections because events related to the KPB mass extinction, such as climatic changes and disruption of normal sedimentation, could obscure orbital climate signals. Having additional absolutely dated tie points, such as magnetic reversals,

would provide an added constraint on cyclostratigraphic interpretation. In terrestrial sections, chronology is usually determined by a combination of direct dating of tephra deposits (where available), and magnetostratigraphy. Magnetostratigraphy is also used as a means of correlation between sites both within and across basins. A precisely calibrated GPTS would provide absolute age constraints for sections without dateable tephras, and would provide a means of comparing results between marine and terrestrial sections at a high-level. Furthermore, a majority of data looking at climatic changes surrounding the KPB are from marine sections and the few that are from terrestrial records have chronologies that are solely based on magnetostratigraphy (e.g. Wilf et al., 2003 and Tobin et al., 2014). By calibrating the GPTS with high-precision dates, we can further provide a means for correlating faunal changes in the terrestrial realm with observed climatic changes, at high-precision.

The current calibration of circum-KPB GPTS presented with the 2012 Geologic Timescale (Ogg, 2012) utilizes a combined astronomical and radioisotopic age model, employing Hilgen et al.'s (2010) Paleocene timescale of 25, 405 ka eccentricity cycles and Husson et al.'s (2010) and Thibault et al.'s (2012) cyclostratigraphy for the Late Cretaceous, tied to Swisher et al.'s (1993) date for the KPB. This calibration is non-ideal for three reasons: 1) Swisher et al.'s (1993) date for the KPB has been shown to be 200 ka too old based on reanalysis (Renne et al., 2013), 2) due to complexities associated with the KPB that may obscure orbital signals, and 3) uncertainty estimates were not provided making this calibration unsuitable for high-precision analysis. Recently, Clyde et al. (2016) provided data for circum-KPB chrons (C30n-C28r) using U/Pb zircon geochronology on tephras interbedded with fluvial sediments from the Denver basin, dominantly from the Kiowa core. Ages for the C29r/C29n, and C28r/C28n reversals were based on both the core and singular outcrops, while the rest were based solely on the core. For accurate GPTS calibration, ideally reversal ages should be confirmed from more than one (or two) sections, especially for terrestrial sediments that are fluvial in origin. This is because fluvial systems have complex, non-constant laterally variable sedimentation patterns (Kidwell and Holland, 2002). To have confidence in an age model from these types of systems, independent constraints from multiple sections are necessary. This was impossible for the Clyde et al. (2016) study because outcrops of the KPB in the Denver basin are limited. Furthermore, U/Pb zircon dates are more likely to be biased by inheritance than studies utilizing $^{40}Ar/^{39}Ar$ geochronology because zircons crystallizing from a magma can retain their radiogenic Pb for upwards of 10's to 100's of ka prior to eruption (Simon et al., 2008; Wotzlaw et al., 2014). At best, these results provide a maximum constraint on age of deposition. Furthermore, a majority of KPB studies that have absolute geochronology utilize the $^{40}Ar/^{39}Ar$ dating technique (e.g. Renne et al., 2013; Sprain et al., 2015; Renne et al., 2015), and in order to reduce systematic uncertainty and to increase the level of precision, it is important to use the same geochronometer.

Fluvial deposits in the Hell Creek region, NE Montana provide an opportunity to refine the ages of circum-KPB chrons using $^{40}Ar/^{39}Ar$ geochronology (C30n-C28n). The Hell Creek region is an ideal location for this study as it is one of the best-studied terrestrial KPB sites globally: it has a well-recorded succession of faunal change across the KPB (Wilson, 2014), its sediments contain reliable paleomagnetic recorders (Sprain et al., 2016), and tephra layers amenable to high-precision $^{40}Ar/^{39}Ar$ dating are interbedded throughout the stratigraphy (Sprain et al., 2015). Over 60 distinct sanidine-bearing tephra deposits have been identified, which have yielded $^{40}Ar/^{39}Ar$ ages with resolution as good as ± 11 ka and absolute accuracy in the range of ± 40 ka (Renne et al, 2013; Sprain et al., 2015). Further, it has been shown that these sediments

have relatively uniform sediment accumulation rates, which supports the use of linear interpolation to calculate reversal ages from bounding tephra layers (Sprain et al., 2015). Past magnetostratigraphic studies have been completed in the area (Archibald et al., 1982; Swisher et al., 1993; LeCain et al., 2014) but in order to constrain reversal ages, paleomagnetic and geochronologic samples need to be collected from the same sections. Further, using past magnetostratigraphy from the Hell Creek in combination with our new tephra ages in Sprain et al. (2015), yielded a duration for C29r of ~350 ka. This duration is not consistent with astronomically tuned chronologies (Thibault and Husson, 2016), constraints from Deccan stratigraphy (Schoene et al., 2015; Renne et al., 2015), or new results from Clyde et al. (2016). This result, in combination with new rock magnetic analysis, suggests that previous magnetostratigraphy of Hell Creek sediments likely has errors in reversal placement.

In this study, we present a revised Hell Creek chronostratigraphy based on 14 new magnetostratigraphic sections and 18 new $^{40}Ar/^{39}Ar$ ages, which in concert are used to provide a new calibration of the most important circum-KPB chron, C29r. Ultimately, this work allows for detailed analysis of the rates of terrestrial faunal change across the KPB, will aid comparison between terrestrial and marine KPB sites, provides an independent test of Paleocene astrochronology, and will ultimately provide the means for integration of faunal records with records of climate change and Deccan volcanism.

4.2 Geology/Previous magnetostratigraphy

The Hell Creek region is located within the northwestern portion of the Williston basin, south and east of the Fort Peck Reservoir (Figure 4.1). Within the Hell Creek, two formations are important to the study of the events surrounding the mass extinction at the end-Cretaceous: the Hell Creek Formation (mostly Cretaceous) and the Tullock Member of the Fort Union Formation (mostly Paleogene). Below the Hell Creek Formation, both the Fox Hills and the Bear Paw Formations, comprising marine-shallow marine and brackish deposits associated with the Late Cretaceous epicontinental Western Interior Seaway, are locally exposed. By the time of deposition of the Hell Creek Formation in the latest Maastrichtian, orogenic pulses loosely associated with the Laramide orogeny coupled with possible eustatic regression, resulted in the final regression of the seaway out of the Hell Creek region (Gill and Cobban, 1973), making way for terrestrial sedimentation. However, the seaway did persist in parts of the Western Interior through the end of the Cretaceous and had a period of transgression, marked by the marine sediments deposited from the Cannonball Sea in North and South Dakota, in the earliest Paleocene (Boyd and Lillegraven, 2011). The Hell Creek Formation and the Tullock Member consist of sediments associated with fluvial (*sensu lato*) deposition including siltstones, shales, lignites (hereafter referred to as coals) and fine sandstones, associated with low-energy deposition and coarser sandstones representative of higher-energy deposition, likely in channels. High energy deposits, such as conglomerates, have not been found. While many of the low energy deposits are often thought to only represent floodplain deposition, it is common to see these sediments in the Hell Creek region making up small channel deposits, evidenced by cross-bedding and ripple marks, and as channel infillings (up to ~20 m). Widespread lignite deposits and an abundance of variegated beds are more common in the Tullock Member and show evidence of extensive ponding (Fastovsky and Dott, 1986; Fastovksy, 1987). The contact between the Hell Creek Formation and the Tullock Member is marked by this transition to more ponded sediments and is defined by most workers as the first laterally persistent lignite (termed the Z coal) above the stratigraphically highest in-situ remains of non-avian dinosaurs (Calvert et

al., 1912; Brown, 1952; Clemens and Hartman, 2014; Moore et al., 2014; Hartman et al., 2014), but can also be seen by a color change from more somber gray colors of the Hell Creek, to more yellow and Fe-stained sediments with variegated bedding in the Tullock (Fastovsky and Bercovivi, 2015). Coals above the Z coal have traditionally received successive letter designations going in reverse alphabetical up through the U coal (Collier and Knechtel, 1939), which marks the contact between the Tullock and Lebo Members of the Fort Union Formation. Coal name designation is often used for relative stratigraphic correlation across the region, however it is known that this system is non-ideal and that similarly named coals are not everywhere time-correlative with the exception of the IrZ (see Sprain et al., 2015 and Ickert et al. 2015 for more details). The Hell Creek/Fort Union formational boundary, as defined by the first lateral continuous coal bed, is roughly coincident with the KPB but has been shown to be diachronous, varying in the Hell Creek region from coincident with the KPB (largely in the western region) to roughly 20 ka after the boundary (eastern region; Sprain et al., 2015). The KPB is recognized in this region above the highest appearance of in-situ non-avian dinosaur fossils, below the lowest occurrence of Paleocene pollen (Bercovici et al., 2009), locally by the impact claystone which contains an iridium anomaly, shocked quartz, and spherules, and by a -1.5 per mil to -2.8 per mil carbon isotope anomaly (Arens and Jahren, 2000; 2002; Arens et al., 2014). The only known occurrences of the impact claystone in the Hell Creek area are found within Garfield County within the Western part of the region. The impact claystone, where it has been identified, is preserved within a Z-complex coal, which has led some workers to change the coal's designation to the IrZ coal, to indicate its coincidence with the KPB (Swisher et al., 1993).

Within the lignite deposits, numerous thin (~1mm–10 cm) silicic tephras amenable to high-precision $^{40}Ar/^{39}Ar$ and U/Pb geochronology, and chemical analysis have been identified. We have identified over 60 distinct tephra deposits, ranging over 70 m of stratigraphy starting in the Upper Hell Creek through to the Lebo/Tullock contact. In Sprain et al. (2015), 15 of these tephras were dated using $^{40}Ar/^{39}Ar$ geochronology with ~ ±30 ka precision. Tephras are rarely preserved outside lignite beds and occur with higher frequency within the Tullock, however lignite deposits are also more abundant in the Tullock Member. The multitude of tephra deposits preserved throughout the stratigraphic section makes the Hell Creek region ideal for GPTS calibration in the time range of interest.

The Hell Creek region is arguably one of the most complete terrestrial KPB sites globally, preserving macroflora, pollen, and vertebrate faunas and is one of the best records of mammalian proliferation after the KPB, preserving mammalian fossil localities from late Cretaceous–early Paleogene in stratigraphic superposition (comprising Lancian [La], Puercan [Pu], and earliest Torrejonian [To] North American Land Mammal Ages [NALMA]; Clemens, 2002). Intensive sampling of vertebrate faunas over ~50 years has yielded over 150,000 vertebrate microfossils (over 12,000 of which are mammal), from > 500 localities (Wilson, 2014). These faunas are key to understanding the transition from disaster to recovery faunas after the KPB, in addition to providing constraints on Late Cretaceous ecologic instability. $^{40}Ar/^{39}Ar$ tephra ages (Swisher et al., 1993; Sprain et al., 2015), along with magnetostratigraphy (Archibald et al., 1982; Swisher et al., 1993; LeCain et al., 2014) form the geochronologic framework for these faunas.

Data from three paleomagnetic studies form the existing magnetostratigraphic framework for the Hell Creek region (Archibald et al., 1982; Swisher et al., 1993; LeCain et al., 2014). The focus of each study was to provide paleomagnetic constraints as a means to correlate paleontological sites across the region and to other basins. Archibald et al. (1982) measured four

magnetostratigraphic sections, two in Garfield County (Hell Hollow and Billy Creek) and two in McCone County (Bug Creek and Purgatory Hill), that identified three polarity zones (two normal and one reverse) from the top of the Hell Creek Formation to the middle of the Tullock Member. These zones were later assigned to C30n, C29r, and C29n (Archibald et al., 1987; Swisher et al., 1993). Swisher et al. (1993) further collected paleomagnetic samples for two additional magnetostratigraphic sections in Garfield County; Hauso Flats and Biscuit Butte. These sections extended magnetostratigraphy to the top of the Tullock Member and identified two more polarity zones that they associated with C28r and C28n. The study by LeCain et al. (2014) assessed magnetostratigraphy for four additional sections that covered the entire Hell Creek Formation and Tullock Member (Pearl Lake, Garbani Hill, Biscuit Butte, Flag Butte). Similar to Swisher et al. (1993) and Archibald et al. (1982), this study identified four polarity zones in the Tullock Member that they associated with C29r, C29n, C28r, and C28n. For the Hell Creek Formation, LeCain et al. (2014) identified two polarity zones which they associated with C30n and C29r, with the C30n/C29r transition in the top 30 m of the Hell Creek Formation consistent with results from Archibald et al. (1982). It should be noted that Lerbekmo (2014) identified a short period of normal polarity within C29r (~1–3 m thick) around the KPB within two sections in the Hell Creek region, which they ascribe to C29r.1n. Lerbekmo et al. (1996) also identified a short period of normal polarity near the KPB in western Canada. However, in other magnetostratigraphic studies that sampled around the KPB in the Hell Creek and North Dakota (Hicks et al., 2002; Lund et al, 2002; Swisher et al., 1993; Archibald et al., 1982, LeCain et al., 2014), a short normal polarity zone was not found. It is possibly an artifact of unremoved secondary overprints, however more study is needed to confirm the existence of C29r.1n. All studies resulted in similar placement of NALMA faunas into the magnetostratigraphic framework, with Lancian faunas within the C30n and the Cretaceous portion of C29r, with Pu1 within the Paleogene portion of C29r, Pu3 faunas occurring around the C29r/C29n transition, and the Pu3-To1 boundary near the top of C29n. These results are generally in agreement with results from other basins (Williamson, 1996; Lofgren et al., 2004; Hicks et al., 2003).

For GPTS calibration, new magnetostratigraphy is necessary for two reasons. First, field observations confirmed by lab analysis indicate that named coals are not laterally continuous, therefore requiring magnetic sampling to be completed only in sections where tephra ages can be determined for bounding coals. Because Swisher et al. (1993) and Archibald et al. (1982) were published before GPS was used in geologic studies, we cannot confidently relocate their exact original magnetostratigraphic sections. Second, using past magnetostratigraphy from the Hell Creek in combination with new tephra ages, Sprain et al. (2015) yielded a duration for C29r of ~350 ka. This result is not consistent with astronomically tuned chronologies (Thibault and Husson, 2016), constraints from Deccan stratigraphy (Schoene et al., 2015; Renne et al., 2015), or new results from Clyde et al. (2016) and raises the question of whether past magnetostratigraphies were correct. This question is further corroborated by new rock magnetic analysis of Hell Creek region sediments. All previous magnetostratigraphic studies used alternating field (AF) demagnetization techniques. AF techniques are useful in removing magnetizations held by magnetic minerals with low to moderate coercivities (i.e. magnetite, titanomagnetite, intermediate composition titanohematite) but cannot remove magnetizations held by phases with high-coercivity (e.g. goethite and hematite) which are often associated with secondary magnetizations. Unfortunately, new rock magnetic analysis of sediments from the Hell Creek region shows that goethite is abundant in these sediments (Sprain et al., 2016). Because signals from goethite cannot be removed using AF demagnetization, and because

cratonic North America has not moved much in the last 66 Ma, unremoved modern field secondary components held by goethite could easily be misinterpreted as late Cretaceous directions. Additionally, new rock magnetic analysis shows that one of the carriers of primary remanence in sediments from the Hell Creek Formation and Tullock Member is intermediate composition titanohematite ($Fe_{2-y}Ti_yO_3$; $0.5 \leq y \leq 0.7$; Sprain et al., 2016). Intermediate composition titanohematite when heated above its Curie temperature (~180ºC) self-reverses and acquires a remanence exactly 180º away from the applied field direction. If sediments are only slightly reheated (which could happen in coal fires during the Quaternary, e.g. Reiners et al., 2009) it is possible that the sediments could acquire a false reverse direction. It is for these reasons that we collected 14 new magnetostratigraphic sections in this study, while also reassessing past paleomagnetic determinations.

4.3 Methods

Paleomagnetism

From previous magnetostratigraphic studies in the Hell Creek region, the location of the C30n/C29r and C29r/C29n reversals are roughly known to be around the Null coal and Y coal complex, respectively (Archibald et al., 1982, Swisher et al., 1993; LeCain et al., 2014). Using this knowledge, fourteen sections were chosen for paleomagnetic and geochronologic sampling in an attempt to capture the reversals, and also to maximize relevance to paleontological work being conducted in the region. A few sections from previous magnetostratigraphic studies were resampled in effort to confirm previous paleomagnetic results and to tie geochronologic data more directly into the paleomagnetic framework. Due to complexities in the named coal stratigraphy outlined in Sprain et al. (2015), paleomagnetic samples were only collected in sections where tephra ages could be or have been determined for bounding coal layers. When possible, sections with obvious large channel deposits were avoided due to potential sedimentation complexities. Samples were collected during fieldwork in 2013–2016. At least three oriented block samples from siltstones, mudstones, and fine-grained sandstones were collected for each site. When possible, sediments with obvious iron staining, roots, and plant debris were avoided. One to three oriented 10 cm^3 specimen cubes were cut out of each block sample using a band-saw or dry tile-saw. Specimen cubes were subsequently sanded and blown with pressurized air to remove any extraneous material from the saw blades. Specimens with the largest volume, and least amount of surficial weathering and Fe-staining were chosen for demagnetization. Stratigraphic distance between samples was on average around 3 m with initial finer sampling (~1 m) conducted near suspected reversals. Once initial paleomagnetic results were obtained, finer sampling (<1 m) was conducted around identified reversals. With average age uncertainties of ~40 ka, and sediment accumulation rates of ~7 cm/ka (Sprain et al., 2015), this sampling resolution will be more than enough to calculate precise reversal ages. Sediments in the Hell Creek region have a trivial dip <0.5º so tilt corrections were not performed. Section-specific sampling details are outlined in the Appendix.

$^{40}Ar/^{39}Ar$ Geochronology

Thirty-six 1mm–8cm thick tephras were collected for $^{40}Ar/^{39}Ar$ or chemical analysis (e.g. Ickert et al., 2016) from coal layers bounding expected reversals within each section. Results for 21 new tephras are reported here and the other 15 are reported in Sprain et al. (2015). Roughly enough material to fill two, gallon size cloth bags was collected for each tephra layer (~1–5 kg). To separate sanidine grains for dating, tephras were disaggregated using crushing or water

suspension techniques, followed by washing and sieving. Feldspar grains were further concentrated using a combination of magnetic separation, ultrasonic cleaning in 7% hydrofluoric acid for ~5–10 min, and hydrogen peroxide treatment to remove excess coal. Selected grains were subsequently analyzed under clove oil to determine presence of plagioclase feldspar or quartz. If plagioclase or quartz was identified, the sample underwent a density separation to remove the unwanted minerals. Sanidine grains were finally handpicked from size fractions ranging from 125–400 microns. Clear, euhedral grains, without inclusions were picked preferentially.

4.4 Analysis

Paleomagnetic Analysis

Detailed rock magnetic analysis was performed on a subset of samples at the Institute for Rock Magnetism and the University of Minnesota. Results from this study are published in Sprain et al. (2016) and show that a majority of primary remanence in these sediments is held by (titano)magnetite ($Fe_{3-y}Ti_yO_4$) with some remanence held additionally by intermediate composition titanohematite ($Fe_{2-y}Ti_yO_3$; $0.5 \leq y \leq 0.7$). Goethite (FeOOH) was found as a common secondary mineral. There was no evidence for hematite. Demagnetization protocol was subsequently chosen to remove unwanted secondary components, and to best characterize the primary magnetic signal. Demagnetization experiments were conducted at the Berkeley Geochronology Center and a small subset of samples were demagnetized at the Institute for Rock Magnetism. At least three paleomagnetic specimens were demagnetized for each site. Samples were demagnetized using a combination of stepwise AF and thermal demagnetization techniques. Samples were heated to low-temperature steps varying from one thermal step at 150ºC to four thermal steps starting at 90ºC and ending at 210ºC, in a non-inductively wound ASC 48 specimen resistance furnace, housed within a shielded room at the BGC. Thermal demagnetization was performed to remove magnetization associated with goethite, which has a Curie T of ~120ºC. Goethite has a high coercivity (300–700 mT, upwards of 1 T; Roberts et al., 2006) and cannot be removed by AF demagnetization techniques at an achievable laboratory field. Past studies in the Hell Creek only utilized AF demagnetization and as such may be biased by unremoved secondary directions held by goethite. Thermal demagnetization could not be performed solely because the NRM of many samples becomes unstable during heating even to low temperatures (~300ºC), likely due to heat induced chemical changes associated with the formation of magnetite from clays (see Sprain et al., 2016 for details). Samples further underwent AF demagnetization using an in-line 2-axis static degausser associated with the 2G-755R cryogenic magnetometer, starting at fields of ~2 mT and going up to fields of 100 mT, in 2–10 mT steps, similar to demagnetization protocols used in LeCain et al. (2014) and Swisher et al. (1993). Based on the rock magnetic characterization of these sediments (Sprain et al., 2016), this demagnetization protocol should be adequate to reveal the magnetization held by the primary magnetic carriers (titanomagnetite and intermediate composition titanohematite). Progressive AF demagnetization was performed until the intensity of magnetization fell to levels around the noise level of the magnetometer (~1 x 10^{-12} Am^2), the measured directions became erratic, or up until a maximum AF field of 100 mT. All samples were measured using the 2G-755R cryogenic magnetometer.

Characteristic remanent magnetization directions for samples with quasi-linear trends toward the origin on Zjiderveld plots were determined using principal component analysis (Kirschvink, 1980). Best-fit lines were determined from a minimum of three consecutive

demagnetization steps trending toward the origin with maximum angles of deviation (MAD) < 20º. Best fit lines were not anchored to the origin as secondary components could not be considered 100% removed. For best fit lines with MAD > 20º, or for samples where the data clustered on Zijderveld plots and stopped trending, a Fisher (1953) mean was determined for at least three consecutive demagnetization steps that remained in the same direction. Data with $\alpha 95$'s > 35º were not used to calculate site means. For samples where demagnetization data lay in a plane between the characteristic remanence and a secondary unremoved overprint, directions were calculated by taking the Fisher mean of a minimum of three consecutive demagnetization steps that remained in the same direction and marked the end of trend. Data analysis was conducted using Demag GUI within the PmagPy software package (Tauxe et al., 2016)

Site means were characterized by two sets of criteria, one that was quantitative and one that was qualitative. The following criteria were used for quantitative analysis: 1) sites that passed Watson's test for randomness at the 95% confidence level (Watson, 1956) that had at least two specimens out of three with characteristic remanence directions determined by PCA were considered A sites, 2) sites where two or more specimen characteristic directions were determined by Fisher statistics and passed Watson's test for randomness were considered B sites, and 3) C sites were sites that did not pass Watson's test for randomness. Qualitative criteria in addition to the commonly used quantitative criteria were also used in final analysis of site level data. Qualitative criteria were used to help determine sites that had been completely remagnetized (whereby mean directions would cluster well and often be an A or B site using quantitative criteria) and to give credit to sites with samples with weak magnetizations and to sites where only one or two samples yielded characteristic directions consistent with Late Cretaceous and early Paleogene fields. The qualitative criteria used in this analysis are: 1) Sites where each specimen has a characteristic remanence that is distinct from secondary overprints and 3/3 specimens have an early Paleogene or late Cretaceous R or N direction or are trending toward an early Paleogene or late Cretaceous R or N direction, are considered alpha sites, 2) Sites where 1 to 2 specimens out of the three have an early Paleogene or late Cretaceous R or N direction or are trending toward an early Paleogene or late Cretaceous R or N direction, and have a distinct characteristic direction from secondary present local field (PLF) or antipodal PLF, are beta sites, and 3) gamma sites are those where all three specimens are not distinct from PLF or antipodal PLF.

$^{40}Ar/^{39}Ar$ Analysis

$^{40}Ar/^{39}Ar$ analyses were performed at the Berkeley Geochronology Center (BGC; California). Samples were irradiated in four separate 50 hour irradiations in the Cadmium-Lined In-Core Irradiation Tube (CLICIT) facility of the Oregon State University TRIGA reactor. Samples were loaded in 1-3 Al disks as figured in Renne et al. (2015) for each irradiation. Fast neutron fluence, monitored by the parameter J, was determined by analyzing single crystals of the standard Fish Canyon sanidine (FCs) for each of the six positions that span each disk. The value of J for each non-standard sample was determined by interpolation within a planar fit to J values determined from the FCs. For each interpolated J value the precision was better than 0.04%.

Mass spectrometry methods and facilities are described in Renne et al. (2015). In short, single sanidine crystals were analyzed by total fusion with a CO_2 laser on an extraction line coupled to a MAP 215C mass spectrometer with a Nier-type ion source and analog electron multiplier detector. Five argon isotopes (^{40}Ar, ^{39}Ar, ^{38}Ar, ^{37}Ar, and ^{36}Ar) were measured using

peak-hopping by magnetic field switching on a single detector in 15 cycles. Blanks were measured at least between every 1–3 total fusion analyses and air pipets were measured throughout each run, in order to properly determine mass discrimination values.

Final ages were calculated from blank-, discrimination-, and decay-corrected Ar isotope data after corrections for reactor interferences were made. Production ratios for interfering isotopes were determined from Fe-doped $KAlSiO_4$ glass reported in Renne et al. (2013) and from fluorite as reported in Renne et al. (2015). Ages are determined using the calibration of Renne et al. (2011). Single-crystal fusion results are shown in figures 4.8 and 4.9. All age uncertainties are reported at 1σ and are stated as ± X/Y, where X represents analytical uncertainty and Y includes systematic uncertainties arising from calibration. If one uncertainty is shown it always references the analytical uncertainty alone, which is appropriate for comparing $^{40}Ar/^{39}Ar$ dates based on the same calibration.

4.5 Section descriptions

See Appendix B.1. for section descriptions.

4.6 Paleomagnetic Results

285 specimens from 14 sections were demagnetized in this study using a combination of alternating field (AF) and thermal demagnetization. Secondary overprints were commonly removed in low AF demagnetization steps (between 2–15 mT) and in low thermal steps (<150ºC). A majority of specimens showed significant evidence of secondary remanence held by goethite, as evidenced by present local field directions being removed after heating through goethite's Curie T (Figure 4.2). In some samples, this component held a significant portion of the remanence. Characteristic remanent directions were often constrained by the 180ºC heating step (after removal of goethite) and by AF levels of 20 mT. These results are consistent with the rock magnetic results presented in Sprain et al. (2016) which showed that the primary carrier of remanence in sediments from the Hell Creek and Fort Union Formations is a combination of titanomagnetite and intermediate composition titanohematite, which both have intermediate Curie temperatures and coercivities (Figure 4.3). A majority of specimens were completely demagnetized by 70 mT, however a few specimens still had strong signals after demagnetization to those levels. This suggests the presence of a higher-coercivity phase, possibly hematite or maghemite. Because the samples are prone to alteration at low-T's (~300ºC), we could not isolate the signal from these higher coercivity phases. Due to this, we did not use anchored fits to the origin when performing PCA analysis.

By taking a Fisher mean of secondary components, which were dominantly removed below 20 mT and after the 150ºC heating step, it is clear that secondary overprints largely measure the present local field (Figure 4.2). Fisher means of normal and reverse directions also produce results that are consistent with expected late Cretaceous and Paleogene directions calculated using the program apwp.py in the in the PmagPy software package (Figure 4.4; available from http://earthref.org/PmagPy/cookbook of Tauxe [2010]). This program takes an input of plate ID (i.e. North America), age, and current latitude and longitude to calculate paleolatitude using the apparent polar wander paths of Besse and Courtillot (2002). Normal and reverse directions pass the Watson V reversal test and McFadden and McElhinny (1990) reversal test, showing that our combination of AF and thermal demagnetization properly removed secondary components while characterizing the primary signal. To assess the reliability of the selected criteria, we plotted site means that passed A and B criteria, just A criteria, alpha and

beta criteria, and just alpha criteria in four separate equal area plots (Figures 4.5). From these plots, it can be seen that A and alpha sites cluster further away the PLF and antipodal PLF than just AB or alpha and beta sites, and alpha sites even more than A sites. This result supports the use of these criteria to pick quality site directions. See Figure 4.6 and Figure 4.7 for section specific results.

McKeever Ranch

Five paleomagnetic sites were collected between the IrZ to just above the Y coal at the McKeever Ranch section. All sites yielded reverse polarities except for one that was excluded from analysis. Three of these sites (MK1, MK3, and MK3.5) yielded scattered directions between the three specimens analyzed and received a C rating based on our quantitative criteria. Of these C sites, two received a beta rating (MK3, MK3.5) based on qualitative criteria because one of the three specimens at each site had a final direction that looked like it was trending towards a Paleogene R direction. The remaining C site (MK1) also received a gamma rating based on qualitative criteria and was excluded from final analysis. All C sites had low susceptibilities and low magnetizations that reached the sensitivity of the magnetometer in early demagnetization steps. The remaining two sites (MK2, MK4), received B ratings and beta ratings using both sets of criteria. All directions determined were reverse in polarity. All but two specimens yielded secondary directions consistent with present local field.

Two paleomagnetic sites were collected at McKeever Ranch A, one ~ 5 meters below the Y coal and one only a meter above the Y coal. From this section, both sites were characterized as A sites and alpha sites using both qualitative and quantitative criteria. All specimens from site MKA1 had secondary directions that were not consistent with PLF, however because the characteristic direction is consistent in direction with Paleogene R, and because the secondary component represented a very small proportion of remanence, we do not think this sample was misoriented. Site MKA2 had secondary directions consistent with present local field. Both sites yielded reverse polarities.

Hell Hollow

Eight paleomagnetic sites were collected at Hell Hollow from just above the HFZ coal, to immediately below the upper Y coal. The lowermost five sites yielded directions of R polarity and the upper three sites yielded directions with N polarity, with the reversal between sites 15HH2 and HH4. All secondary directions are consistent with the present local field overprint (Figure 4.2). From the sites with reverse polarity, three were classified as A sites based on quantitative criteria (15HH1, HH1, HH2). Based on qualitative criteria, sites HH1 and 15HH2 were classified as beta sites, because in each site one specimen direction could not be easily constrained from the antipodal present local field direction. Site HH2 was classified as a gamma site based on qualitative criteria because all directions could not be readily distinguished from the antipodal present local field. The remaining two sites that yielded reverse polarity were classified as B sites using quantitative criteria (15HH2, HH3). Using qualitative criteria, HH3 was given a beta rating because only one out of the three directions was clearly distinguishable from antipodal present local field, and 15HH2 was given an alpha rating because all directions were distinct from antipodal PLF.

Of the sites with normal polarity, using quantitative criteria, two were classified as B sites (15HH3, HH4) and one was classified as an A site (HH5). From the B sites, both 15HH3 and HH4 were given gamma ratings using qualitative criteria. Directions from 15HH3 were scattered

and could not be easily distinguished from present local field or secondary overprints. Of the five specimens analyzed from site HH4 (HH4-4B by thermal only), three yielded directions that were distinct from present local field secondary overprints. However, specimen HH4-4B shows evidence of an unremoved reverse direction which is why this site is classified as a gamma. From site HH5, all characteristic directions are distinct from secondary present local field overprints so it was therefore classified as an alpha site using qualitative criteria.

For section Hell Hollow A, all five paleomagnetic sites yielded directions that were normal in polarity. From these five sites, three were classified as A sites (15HHA2, HHA2, HHA3), one a B site (15HHA1), and one a C site (HHA1) based on quantitative criteria. Of the A sites, 15HHA2 received a beta qualitative criteria rating, and HHA1 and HHA2 an alpha rating. Site 15HHA1 received a gamma qualitative rating because the data were so scattered that it was not clear whether the directions were distinct from their secondary overprints. HHA1 also received a gamma rating using qualitative criteria because one direction was not distinct from PLF, and the other two appeared to have unremoved reverse components.

Garbani Hill

Six sites were collected from just above the HFZ to about five meters above the Y coal doublet. From these six sites, two yielded reverse directions (15GB1, 15GB1A), three yielded normal directions (16GH2, 15GB2, 15GB3), and one was too scattered to be analyzed (16GH1), with the reversal occurring between sites 15GB1A and 15GB1. The lowermost reverse sample, site 15GB1, was classified as a C site, and 15GB1A as a B site using quantitative criteria. Using qualitative criteria, site 15GB1 was given a beta rating, because while the characteristic directions were neither present local field, Paleogene normal, or Paleogene Reverse, the data appear to trend towards a reverse direction before reaching intensity values that were below the sensitivity of the magnetometer. Site 15GB1A was given a gamma rating based on qualitative criteria because while the samples were clearly not normal polarity, the data were too scattered to tell if the characteristic directions were distinct from antipodal PLF. Site 16GH1, which was in between 15GB1A and 15GB1, yielded data that was too scattered to analyze by either quantitative or qualitative criteria. This sample was collected from the GC12-3 tephra and had a very low susceptibility and intensity.

Of the normal polarity sites, all received A ratings based on quantitative criteria. Site 15GB2 was classified as a beta site using qualitative criteria because while the normal direction was distinct from the PLF secondary overprint, it was not consistent with a Paleogene normal. This particular site was sampled from a fine sandstone that had clear cross-bedding, so directions may have been biased due to compaction or tilting along inclined bedding planes. Site 15GB3 likewise received a beta classification using qualitative criteria because only two out of the three specimens analyzed yielded normal directions that were distinct from the PLF secondary overprint. 16GH2 received an alpha rating based on qualitative criteria, as all three normal directions were consistent with Paleogene normal and distinct from secondary PLF. All sites had secondary overprints that were consistent in direction with the PLF.

These results are consistent with results presented in LeCain et al. (2014), however we find the reversal is more likely to be around the level of the Y coal doublet than multiple meters below it.

Pearl Lake

Five sites were collected at Pearl Lake between the HFZ to just above the Y coal stringer.

Four out of the five sites yielded characteristic directions that were reverse in polarity and one site yielded normal polarity. Of the four reverse sites, one was characterized as an A site based on quantitative criteria (15PL2), two as B sites (15PL1, 16PL1) and one as a C site. 15PL2 was further characterized as a gamma site using qualitative criteria. While the characteristic directions were distinguishable from antipodal PLF, the reverse directions were also distinguishable from Paleogene reverse. Only one specimen had a secondary direction that was consistent with PLF. It is possible there was an unidentified slump within this layer. Site 16PL1 was also classified as a gamma site using qualitative criteria because it was reverse but again not consistent with either antipodal PLF or Paleogene reverse. 15PL1 was given a beta rating using qualitative criteria because only two out of the three reverse directions look distinctly Paleogene reverse. Site 15PL1A was also given a beta rating using qualitative criteria. Two out of the three specimens had demagnetization trends that appeared to be trending towards a Paleogene reverse direction. The one normal site, 16PL2, was given an A rating based on quantitative criteria, while given a beta rating based on qualitative criteria. Of the three specimens, one looks clearly Paleogene normal with a distinct PLF overprint, while another specimen cannot be distinguished from PLF and the last specimen is close to Paleogene normal, but still not distinct from PLF.

Assuming the reverse direction that was characterized from site 16PL1 is indeed the result of a slumped Paleogene reverse direction, we place the reversal at this site between 16PL1 and 16PL2, at the level of the Y coal stringer (a thin coal bed). These results contrast with those presented in LeCain et al. (2014), where the reversal was placed ~3 m below the Y coal stringer. We can only assume the normal directions determined by LeCain et al. (2014) below the Y coal stringer were overprints.

Lerbekmo South

Six sites were collected at our Lerbekmo South locality between the MCZ to right above the upper Y coal. Sample direction determination at this section is difficult. Two sites near the base of the stratigraphic column yielded reverse directions (HC1, HC2), with HC1 receiving an A rating and HC2 receiving a B rating based on quantitative criteria. However, both sites were given C ratings using qualitative criteria as all R directions were not consistent with Paleogene R direction, and for HC2 they were was not distinct from an antipodal present local field. Moving up in stratigraphy, site HC3 yielded directions that were normal in polarity. Using quantitative criteria, this site received a B classification. Using qualitative criteria, this site received a gamma classification. While each specimen yielded a normal direction, there appears to be an unremoved R direction present. HC3-1A has a direction in the wrong quadrant, and all three continue to move toward shallower directions during demagnetization, consistent with removal of a N component with a R component being revealed. These results suggest that this site may have been entirely overprinted.

Above site HC3 is site HC4 (which was recollected in 2014 as 14HC1) and this site yields specimens with both reverse and normal polarity. HC4-1A yields a normal direction that overlaps with the secondary component and is consistent with the present local field. HC4-2A yields a very scattered direction that is consistent with Paleogene R, and HC4-3A yields a N direction that is distinct from the PLF secondary component and is roughly consistent with a Paleogene normal direction. 14HC1-1A yields a R direction, however it is more consistent with an antipodal present local field direction than a Paleogene R. 14HC1-2A looks like it might be trending towards Paleogene R, but reaches the sensitivity of the magnetometer before it makes it. 14HC1-3A yields a N direction that is very scattered and not too different from the present local

field. From the above data, we argue that this site should indeed be reverse in direction but it has been significantly remagnetized, as has site HC3 below it. Further, specimen HC4-2B, which was demagnetized by thermal techniques only, appears to be trending to a R Paleogene direction before altering.

Site 14HC2 is the highest stratigraphically and was collected just above the upper Y coal. A normal site mean determined from three Fisher mean directions gives this site a B quantitative classification. However, none of the normal directions are distinct from their secondary components, which is similar in direction to the present local field. Further, 14HC2-3B, which was demagnetized by thermal only, shows a demagnetization trend that is consistent with the presence of an unremoved R component. This evidence suggests that our samples from this site were also remagnetized and it therefore receives a gamma qualitative rating.

Isaac Ranch

Four paleomagnetic sites were collected at Isaac Ranch, from just above the MCZ to the Y coal. All sites yielded reverse directions roughly consistent with Paleogene R. Specimens from sites IS1, IS2, and IS4 behaved slightly erratically during demagnetization, so a Fisher mean was used for direction determination instead of PCA, resulting in a B quantitative classification. Of these B sites, two were classified as beta sites based on qualitative criteria (IS1, IS2), and one received an alpha rating (IS4). Site IS3 received an A rating based on quantitative criteria and an alpha rating based on qualitative criteria. All but one specimen yield distinct secondary directions that are consistent with the present local field.

Thomas Ranch

Thirteen paleomagnetic sites were collected at Thomas Ranch between ~ 5 meters below the Null coal to just above the MCZ. Of these thirteen sites, three were determined to be normal polarity and ten were determined to be reverse polarity. Most secondary directions are consistent with a secondary PLF overprint. Of the three normal polarity sites, two were given B ratings and one a C rating based on quantitative criteria. Of the two B sites, one received a gamma rating based on qualitative criteria (14TRA2), and one received an alpha rating (14TRA1). 14TRA2 was characterized as a gamma site because one of the samples looked to be trending to the R Cretaceous direction, making the normal polarity determination of the other specimens suspect. All directions determined from site 14TRA1 showed a clear distinction from PLF, and were consistent with the expected Cretaceous normal direction. Site 15TRA1 was characterized as a beta site using qualitative criteria as 2/3 directions looked like Cretaceous normal, but the third was not distinct from PLF.

Of the 10 reverse polarity sites, three received C ratings (14TR2, 14TR4, 14TRA2), four received B ratings (14TR1, 14TR5, 14TR7, 14TRA3) and three received A ratings (14TR3, 14TR6, 14TRA4), based on quantitative criteria. From these sites, 15TRA2, 14TRA3, 14TR5, 14TR6, 14TR7, 14TR2, 14TR1 were classified as beta sites based on qualitative criteria because one or more specimens had characteristic directions that were consistent with Cretaceous R, but one or more were also consistent with antipodal PLF. Of the remaining 5 sites, two sites (14TRA4, 14TR3) were characterized as alpha sites based on qualitative criteria. 14TR4 was classified as a gamma site based on qualitative criteria because while directions have reverse polarity, they are too scattered to tell if they are distinct from antipodal PLF.

Sandy Chicken

Seven sites were collected at Sandy Chicken from ~two meters below the Null coal to just below the MCZ. All sites yielded reverse polarities. Almost all sites had secondary directions consistent with PLF overprints. Three sites (14SC1, 14SC2, 14SC3) were assigned C criteria based on both quantitative and qualitative criteria. All directions for each site were very scattered, however all were plotting in the upper hemisphere. All of these samples have weak magnetizations, which may be why they scatter at low demagnetization steps because they have reached the sensitivity of the magnetometer. Due to this, we are assigning them reverse polarities. It is possible, based on information from other sections where the C30n/C29r reversal has been identified, that these sites represent magnetizations acquired in low field intensities shortly after the field reversed. The three subsequent sites (14SC4, 14SCA1, 14SCA2), were classified as B sites using quantitative criteria. 14SC4 and 14SCA2 were also classified as beta sites using qualitative criteria with 1/3 directions, and 2/3 directions looking Cretaceous reverse, respectively. 14SCA1 received a gamma classification using qualitative criteria because all characteristic directions were R, but were not consistent with antipodal PLF, or Cretaceous reverse. Site 14SCA3 received an A classification using quantitative criteria with a beta rating using qualitative criteria. Only one out of the three directions was distinct from antipodal PLF, and one specimen had a clear isothermal remanent magnetization overprint (likely from lightning) that could not be removed well enough to characterize the primary direction.

Bug Creek

Seven sites were sampled for paleomagnetic analysis from Bug Creek, starting ~ 10 m below the Null coal to about 10 m above it. The three lowest sites yielded characteristic directions that are normal in polarity, and the four highest sites yielded reverse polarity. From the normal polarity sites one received an A classification (14BC1), one a B (15BC1), and one a C (14BC2), based on quantitative criteria. Site 15BC1, the lowest in stratigraphy, was further classified as an alpha site using qualitative criteria. All results were normal in polarity and were distinct from PLF secondary overprints. Site 14BC1 was characterized as a beta site using qualitative criteria as only 1/3 directions was distinct from PLF and consistent with a Cretaceous normal direction. 14BC2 also received a beta classification as only 2/3 specimens yielded directions consistent with Cretaceous normal.

Of the reverse polarity sites, three out of the four are classified as C sites (14BC4, 14BC2A, 16BC2B) and one is classified as a B site using quantitative criteria. Out of the three C sites, two were further characterized as gamma sites based on qualitative criteria (14BC4, 14BC2A). For site 14BC2A, all sample yielded directions that are in the upper hemisphere, but the results are too scattered to say whether they are consistent with a Cretaceous reverse direction. Site 14BC4 also yields three specimens with directions that plot in the upper hemisphere, however it appears that this site was struck by lightning, based on a high initial NRM (~1 x 10^{-2} A/m) which quickly decayed with low (1–10 mT) AF steps, and the primary directions are obscured by an isothermal remanent magnetization. Site 16BC2B received a beta classification using the qualitative criteria because 2/6 directions are consistent with Cretaceous reverse and distinct from antipodal PLF. The one remaining B site, 14BC3 likewise received a beta classification using qualitative criteria as only 2/3 reverse directions are distinct from antipodal PLF.

All secondary directions are consistent with PLF. While the quality of data at Bug Creek are relatively low, based on results from both Sandy Chicken and Thomas Ranch, which are consistent with the results here, we place the reversal between 14BC2 and 14BC2A, ~ 3 meters

below the Null coal. This result is inconsistent with past paleomagnetic data presented in Archibald et al. (1982), where the reversal was identified 14 m above the Null Coal. Based on results from Thomas Ranch, where we also identified the reversal ~3 m below the Null coal, we believe the results from Archibald et al. (1982) to be in error, likely due to unremoved secondary overprints. Our new results are also consistent with the placement of the C30n/C29r reversal at Flag Butte (LeCain et al., 2014), both ~25 m below the formational boundary.

Purgatory Hill

At Purgatory hill, six sites were sampled for paleomagnetic analysis from a few meters above the Z coal to just below the upper Y coal. Four sites had reverse polarity and two sites had normal polarity. All specimens had secondary directions consistent with the PLF. Of the reverse sites, two were characterized as B sites and two as C sites based on quantitative criteria. Of the B sites, both 15PH1 and 15PH2 were given alpha classification using qualitative criteria, with each direction being distinct from antipodal PLF and similar to Paleogene reverse. Of the C sites, 15PH3 was given a gamma classification based on qualitative criteria. All specimens yielded normal directions but had trends that appeared to be moving towards reverse. These normal directions appear to be the result of secondary overprints as both samples above and below yielded reverse directions. Further, these specimens had low susceptibilities and magnetizations which made it so they reached the sensitivity of the magnetometer at low demagnetization steps. 15PH4 was classified as a beta site using qualitative criteria. One direction was entirely consistent with Paleogene reverse, while the others appeared to be trending there but their magnetizations reached the sensitivity of the magnetometer before they were completely demagnetized, resulting in scattered directions.

Of the normal polarity sites (15PH5, 16PH2), both received A ratings using quantitative criteria. Site 15PH5 additionally received an alpha rating using qualitative criteria, however site 16PH2 received a beta rating because one direction looked clearly Paleogene normal, while another appeared to have an unremoved reverse component. We place the reversal between sites 15PH4 and 15PH5.

McGuire Creek (Lofgren)

Eleven paleomagnetic sites were sampled at our Lofgren section ranging from immediately above the MCZ, to just above the X coal. The stratigraphically lower eight sites yielded characteristic directions that were of reverse polarity and three sites above yielded normal polarity. Of the eight sites with reverse polarity, six were classified as B sites using quantitative criteria (14LG3, 14LG4, 14LG5, 14LG6, 14LG7, 15LG1), one was classified as a C site (14LG1), and one was classified as an A site (14LG2). Of the B sites, five received beta ratings based on qualitative criteria (15LG1, 14LG7, 14LG6, 14LG5, 14LG3) whereby one or more directions could not be distinguished from antipodal PLF, when at least one clearly could. Site 14LG4 was classified as an alpha site using qualitative criteria as all characteristic directions were consistent with Paleogene reverse. 14LG1 received a beta rating using qualitative criteria because while the data were scattered, 2/3 specimens appeared to be trending towards Paleogene reverse directions. Site 14LG2 was characterized as a beta site because 1/3 specimens yielded a direction that was not distinct from antipodal PLF.

From the three sites where normal polarities were determined, two out of these received B ratings (15LG3, 15LG2) and one a C (14LG8) rating using quantitative criteria. Both B sites, 15LG3 and 15LG2, received beta ratings using qualitative criteria. Site 15LG2 only had one

specimen out of three yield a normal direction consistent with Paleogene Normal, and site 15LG3 had all three specimens yield characteristic directions which were distinct from PLF, but had an unremoved R component. Site 14LG8 was classified as a gamma site using qualitative criteria because the directions were too scattered to be able to tell if they were distinct from PLF, or if they were reverse samples that lost too much intensity before the R direction could be characterized.

While the results are not of the highest quality, we tentatively place the reversal between 14LG8 and 15LG2.

Jack's Channel

Six sites were collected at Jack's Channel, from a few meters below the 2380 Y coal to just below the 2440 Y coal. Two out of the six sites yielded reverse polarity (14JC1, 14JC2) and four out of the six sites yielded normal polarity (14JC3, JC1, JC2, JC3), with the reversal placed between sites 14JC2 and JC1. Of the reverse polarity sites, both were classified as A sites based on quantitative criteria. Using qualitative criteria, 14JC1 received a beta rating because two out of the three direction could not be distinguished from antipodal PLF. 14JC2 received a gamma rating using qualitative criteria because none of the directions were distinguishable from antipodal PLF. From the sites yielding normal directions, one out of the four received an A rating (JC3) based on quantitative criteria, and three received B ratings (JC2, 14JC3, JC1). Site JC3 was classified as a gamma site using qualitative criteria because a clear secondary component could not be identified and these directions were not distinct from the PLF. Of the B sites, 14JC3 and JC1 were classified as beta sites using qualitative criteria, and JC2 was classified as a gamma site. JC1 and 14JC3 were classified as beta sites because while their normal characteristic directions were distinct from PLF, an unremoved reverse component was observed for all specimens. Site JC2 was classified as a gamma site because the characteristic direction was not distinct from the direction removed during goethite demagnetization and was close to the PLF. Above the 2440 at Jack's channel is a clinker deposit (in situ burned coal seam). Because so many of these directions yielded non-ideal qualitative analysis, another site further away from the clinker covering the same stratigraphic interval was collected.

At the Jack's Channel 2015 section, 4 sites were collected. From these sites, two yielded reverse directions (15JC1, 15JC2) and two yielded normal directions (15JC3, 15JC4). Of the reverse sites, both were classified as B based on quantitative criteria. Using qualitative criteria, both were classified as beta. 15JC1 yielded on R direction that was distinct from antipodal PLF, and two of the specimens from 15JC2 had reverse directions that were distinct from antipodal PLF. The normal sites also received B ratings using quantitative criteria. 14JC3 was classified as a beta site using qualitative criteria because while directions were distinct from PLF, each specimen had an unremoved R component. Using qualitative criteria, 15JC4 received a gamma rating because the data were too scattered to tell if it was distinct from PLF.

At both our Jack's Channel and Jack's Channel 2015 sections, the first normal polarity site occurs in the same location, immediately above the 2380 coal. Thus, we believe the reversal to be the C29r/C30n reversal and not to be the result of secondary normal overprints.

4.7 $^{40}Ar/^{39}Ar$ Results

See Figures 4.8 and 4.9 for a summary of age spectra for all samples and Table 4.2 for summarized results.

McKeever Ranch

Seventy-nine grains of MK13-3 were analyzed from the IrZ coal at McKeever Ranch. Of these 79 grains, two were identified as plagioclase based on K/Ca ratios and were excluded from analysis. Of the remaining 77 grains, six were identified at xenocrysts and were also excluded. The remaining 71 grains yielded a weighted mean age of 66.096 ± 0.038/0.057 Ma, with an MSWD of 0.90.

From sample MK12-1, of the Y coal at McKeever ranch, 88 feldspar grains were analyzed. Of these 88 grains, five were identified as xenocrysts (ranging in age from 68.5 Ma to 1193 Ma) and were excluded from analysis. From the remaining 83 grains, a weighted mean age of 65.844 ± 0.033/0.054 Ma with an MSWD of 0.54, was determined.

Hell Hollow

From sample HH13-1, from the lowest collected Y coal at Hell Hollow, 70 grains were analyzed by total fusion individually. Of these 70 grains, five were identified at plagioclase based on K/Ca ratios and were excluded from final age determination. Of the remaining 65 grains, three were excluded as outliers, two identified as older xenocrysts and one identified as a younger outlier. From the remaining 62 grains, a weighted mean age of 65.774 ± 0.034/0.055 Ma with an MSWD of 1.32 was determined.

From HH13-2, of the uppermost Y coal sampled at Hell Hollow, 68 grains were analyzed. Of these grains, one grain was identified as a xenocryst and was excluded from final age determination. Of the remaining 67 grains, a weighted mean age of 65.692 ± 0.033/0.053 Ma was determined, with an MSWD of 0.87.

Seventy grains of HH13-3, the highest Y coal at Hell Hollow A, correlative with HH13-2 from Hell Hollow, were analyzed by single crystal total fusion. All 70 grains were identified at alkali feldspar based on K/Ca ratios and a weighted mean age of 65.710 ± 0.024/0.048 Ma with an MSWD of 1.12 was calculated.

Pearl Lake/MacDonald Locality

From sample PL14-1 of the Y coal stringer at Pearl Lake, 52 feldspar grains were analyzed by total fusion and yielded a weighted mean age of 65.709 ± 0.037/0.056 Ma, with an MSWD of 1.55.

From sample MD15-1 of the HFZ coal at the MacDonald locality, 41 feldspar grains were analyzed. Of these, seven were identified as plagioclase based on K/Ca ratios and were excluded from final analysis. The final weighted mean age of the remaining 36 analyses is 66.099 ± 0.076/0.088 Ma, with an MSWD of 1.08. While this age is older than the pooled age presented within Sprain et al. (2015) for the HFZ coal, their distributions do overlap within 2σ.

Lerbekmo South

From sample HC13-1 of the Y coal at Lerbekmo South, 73 grains were analyzed individually by total fusion. Of the 73 grains, four were identified as xenocrysts and were excluded. Seven additional grains were identified as plagioclase based on K/Ca ratios and were excluded from final analysis. Of the remaining 63 grains, a weighted mean age of 65.883 ± 0.032/0.053 Ma was calculated with an MSWD of 1.36.

Thomas Ranch

From TR13-2, of the Null coal at Thomas Ranch, 92 grains were analyzed. Like the Null

coal from Bug Creek, a majority of these analyses were xenocrysts, quartz, and some plagioclase. While a majority of grains were identified as outliers, a clear younger mode exists composed of 54 out of 92 analyses. From these 54 grains, a weighted mean age of 66.347 ± 0.151/0.159 Ma was calculated, with an MSWD of 0.779. This age is consistent with the age of the Null Coal obtained from Bug Creek.

From sample TR13-3 of the MCZ coal at Thomas Ranch, 66 grains were analyzed by total fusion. Of the 66 grains, seven were identified as plagioclase based on K/Ca ratios and were excluded from final age determination. An additional three grains were identified as xenocrysts and were excluded. Of the remaining 56 grains, a weighted mean age of 66.091 ± 0.038/0.056 Ma was determined, with an MSWD of 0.88.

TR14-1, a Y coal from Thomas Ranch, was analyzed in two aliquots, one in irradiation 456PR (37131) and one in irradiation 443PR (37005). 79 grains of 37005 were analyzed. Of these 79 grains, 11 were identified at plagioclase based on K/Ca ratios and were excluded from final age determination. From the remaining 68 grains, a weighted mean age of 66.164 ± 0.038/0.057 Ma was determined, with an MSWD of 1.29. 42 grains of sample 37131 were analyzed. Of these 42, 15 were excluded. Four grains were determined to be xenocrysts and were excluded, and 11 grains that were identified as plagioclase feldspar were excluded. Of the remaining 27, a weighted mean age of 66.118 ± 0.067/0.079 Ma was calculated, with an MSWD of 1.35. Based on this tephra's placement in stratigraphy and our dates for tephras collected below this sample, TR14-1 is likely a reworked tephra.

Purgatory Hill

From PH13-3, the lowest Y coal at Purgatory Hill, 69 grains were analyzed. From these grains, 55 grains were identified as xenocrysts and were not included in the final analysis. The remaining 14 grains have a skewed distribution with a younger tail and an MSWD ~ 1.8. To get a more representative population, grains were excluded from the younger side until an MSWD of ~ 1 was reached. The remaining 11 grains yielded a weighted mean age of 65.712 ± 0.086/0.096 Ma, with an MSWD of 0.931.

From sample PH13-1 of the middle Y coal at Purgatory Hill, 49 single crystals were analyzed, three of which were identified as plagioclase based on K/Ca ratios, and nine grains were identified as xenocrysts. These grains were excluded from final age analysis. The resulting 37 grains yielded a weighted mean age of 65.844 ± 0.051/0.066 Ma, with an MSWD of 0.71. Based on the age of PH13-3, which is stratigraphically lower than this sample, we believe that PH13-1 may be a reworked tephra.

From sample PH13-2, the highest Y coal at Purgatory Hill, two aliquots were analyzed in irradiation 456PR (37132) and irradiation 443PR (37006). From sample 37006, 73 grains were analyzed. All grains were determined to be alkali feldspar based on K/Ca ratios and a weighted mean age of 65.541 ± 0.048/0.064 Ma, with an MSWD of 1.72 was determined. Fifty-five grains of 37132 were analyzed. Of these 55 grains, 5 were identified as older xenocrysts, two were identified as plagioclase based on K/Ca ratios, and two were excluded because of low % radiogenic 40Ar. Once these grains were excluded from analysis, the population was still largely skewed to younger ages. Based on the age of the PH13-2 analyzed from sample 37006, which has a single uniform population, we know that these younger ages are anomalous and likely represent altered sanidines. As such, 15 analyses were excluded from the younger population sequentially until an MSWD close to 1 was reached. The final 30 grains yielded a weighted mean age of 65.537 ± 0.077/0.089 Ma with an MSWD of 1.08. Taking the weighted mean

(inverse variance) of these two samples yields an age for PH13-2 of 65.540 ± 0.041/0.059 Ma.

McGuire Creek (Lofgren)

LG13-1, the X coal at Lofgren (McGuire Creek), was analyzed in two irradiations: 456 PR (37133) and 443PR (37003). From sample 37133, 49 grains were analyzed by total fusion. Of these 49 grains, one was identified as plagioclase based on K/Ca ratios and one was identified as an older xenocryst. Both of these analyses were excluded. Two additional grains were excluded because they were young outliers, possibly reflecting alteration. Of the remaining 45 grains, a weighted mean age of 65.706 ± 0.068/0.080 Ma was determined with an MSWD of 0.89. From sample 37003, 78 grains were analyzed. Of these 78 grains, one was identified as plagioclase and was excluded from analysis. From the remaining 77 grains, a weighted mean age of 65.703 ± 0.043/0.059 Ma was calculated with an MSWD of 1.14. This age is indistinguishable from that calculated from the other irradiation and together they yield a weighted mean age of 65.704 ± 0.036/0.056 Ma. This result is ~200 ka older and distinct from the age of MC11-3, another tephra from this coal analyzed by step-heating analysis on multi-grain aliquots presented in Sprain et al. (2015). Based on the placement of the reversal in this section, we believe the MC11-3 age to be in error. Further, K/Ca ratios calculated during step-heating of MC11-3 suggest that the multi-grain aliquots analyzed contained a population of plagioclase. Statistically, plagioclase analyzed from Hell Creek tephras tend to be younger than the sanidine population, likely due to effects from alteration, which may be biasing the age for MC11-3.

Jack's Channel

Two aliquots of JC13-4, the lowest Y coal (2440 coal) collected from Jack's Channel, were analyzed from two different irradiations: 456PR (37130) and 430PR (36839). From sample 37130, 45 feldspar grains were analyzed. Of these, one was identified as plagioclase based on K/Ca ratio, and was also xenocrystic, and was excluded from analysis. Of the remaining 44 grains, five more were identified as xenocrystic based on the age determined for this samples from the other irradiation. From the remaining 39 grains, a weighted mean age of 65.868 ± 0.062/0.076 Ma was determined, with an MSWD of 0.532. For sample 36839, 71 feldspar grains were analyzed by single crystal total fusion. Of these, three were identified at plagioclase based on K/Ca ratios and were excluded from analysis. Two more grains were interpreted as xenocrysts and were excluded. Of the remaining 66 grains, a weighted mean age of 65.864 ± 0.041/0.059 was calculated with an MSWD of 1.57. Taking the weighted mean from both irradiations yields an age of 65.865 ± 0.035/0.054 Ma.

Fifty-six grains of JC13-3, of the middle Y coal at Jack's Channel, were analyzed by single crystal total fusion. Of these 56 grains, one grain was identified as a xenocryst and was excluded from analysis. Of the remaining 55 grains, a weighted mean age of 65.740 ± 0.042/0.059 Ma with an MSWD of 0.86 was determined.

Two aliquots of JC13-2, the highest Y coal from Jack's Channel (2440 coal), were analyzed, one from the 456PR (37129) irradiation and one from the 443PR irradiation (37002). 77 feldspar grains from 37002 were analyzed. Of these, two were identified as xenocrysts and were excluded. Of the remaining 75 grains, a weighted mean age of 65.851 ± 0.026/0.049 Ma was calculated, with an MSWD of 1.02. From sample 37129, 48 feldspar grains were analyzed. Of these, two were identified as xenocrysts and excluded from final age determination. The weighted mean age of the remaining 46 analyses is 65.998 ± 0.040/0.058 Ma with an MSWD of 0.64. Based on this tephra's stratigraphic position, and position relative to other dated tephras

and the magnetic reversal, we conclude that this is a reworked tephra and its age does not represent the age of deposition.

IrZ Coal

Two aliquots of HF15-1 (37108 and 37118) from the IrZ coal at Iridium Hill were analyzed in the same irradiation (456PR), but in separate irradiation disks. For sample 37108, ten feldspar grains were analyzed and all proved to alkali feldspars based on K/Ca ratios. No outliers were present and the ten grains yielded a weighted mean age of 66.039 ± 0.073/0.083 Ma with an MSWD of 1.38. For sample 37118, five grains were analyzed and K/Ca ratios showed that all were alkali feldspar. Again, this sample yielded no outliers and the five grains yielded a weighted mean age of 66.190 ± 0.113/0.124 Ma with an MSWD of 1.25. While this age is significantly older than the age for the IrZ coal presented in Sprain et al. (2015), it does overlap at 2 sigma and its older apparent age is most likely due to the small number of grains that were analyzed.

From sample HF-1PR, of the IrZ coal at Hauso Flats (see Renne et al. 2013 for more details), three aliquots were analyzed in irradiation 430PR in three separate irradiation disks: 36836, 36825, and 36847. From sample 36825, 49 grains were analyzed. Of these 49 grains, three were identified as plagioclase and were excluded from analysis. An additional two were identified at xenocrysts and were also excluded. Of the remaining 44 grains, one was excluded due to low % radiogenic 40Ar. Of the remaining 43 grains, a weighted mean age of 66.013 ± 0.032/0.053 Ma was calculated, with an MSWD of 1.57. From sample 36836, 39 grains were analyzed. From these 39 grains, one was identified as plagioclase based on K/Ca ratios and was excluded from analysis. Of the remaining 38 grains, a weighted mean age of 66.028 ± 0.033/0.053 Ma with an MSWD of 1.10 was determined. From sample 36847, 53 grains were analyzed. While these grains yield a unimodal population, and there are no clear outliers, the population has an MSWD ~ 1.74 and a very low probability (0.007). To obtain an age with a better probability, 8 grains were excluded from the older end until a probability >0.1 was reached. The resulting 45 grains yield a weighted mean age of 66.055 ± 0.036/0.056 Ma with an MSWD of 1.21. All three of these ages are indistinguishable from the pooled mean age for the IrZ coal presented in Sprain et al. (2015).

From sample HF14-1, of the IrZ coal at Snow Creek Road (see Ickert et al. 2015 for more details), two aliquots were analyzed from one irradiation from two separate disks (37004 and 37012). From sample 37004, 59 grains were analyzed. From these 59 grains, four were identified as plagioclase and were excluded from analysis. Of the remaining 55 grains a weighted mean age of 66.072 ± 0.028/0.051 Ma with an MSWD 1.45 was determined. From sample 37012, 20 grains were analyzed. All were identified at K-feldspar, and a weighted mean age of 66.052 ± 0.046/0.062 with an MSWD of 1.34 was calculated.

4.8 Pooled Results

In several cases in this study, we have dated the same tephra at multiple locations, as indicated based on stratigraphic position, mineralogy, and Pb-isotopic analysis of feldspars. In this section, we present pooled ages for these tephras and refer to them by the coal in which they occur. The pooled age is calculated by the inverse variance weighted mean of the individual sample mean ages. Each sample has a specific J values, so associated uncertainties are treated as random. Systematic uncertainties associated with decay constants and the $^{40}Ar^*/^{39}Ar$ of the standard are treated as they are in all other calculations. Pooled results are presented in Table 4.3.

Y Coal Hell Hollow

Based on stratigraphic position, placement of magnetic reversal, feldspar chemistry, and field observations we believe samples HH13-2 and HH13-3 are from the same tephra. Combining these results yields a weighted mean age of 65.704 ± 0.019/0.046 Ma. This weighted mean age will be the upper constraint for the reversal age at Hell Hollow.

IrZ Coal

Samples of HF14-1, HF-1PR, HF15-1, and MK13-3 may be combined with previous results of Sprain et al. (2015; NV12-1, HH12-1) and Renne et al. (2013; HF-1PR) for the Nirvana bentonite to yield a weighted mean age of 66.047 ± 0.008/0.043 Ma, with an MSWD of 0.953 (Figure 4.9). These tephras are correlatable based on stratigraphy, location with regard to the Ir-anomaly, field observations, and a distinct feldspar Pb-isotopic composition (Nirvana bentonite; Ickert et al., 2015). In all locations, the tephra collected was within ~1 cm of the impact claystone and we interpret this age to be the most reliable age available for the KPB.

MCZ/Z coal

Within the MCZ coal there are two tephras that have distinct feldspar Pb-isotopic compositions as described in Ickert et al. (2015). One of these tephras, the McGuire Creek bentonite, has been dated in multiple locations (Lofgren, LG11-1; Z-line, ZL12-2; Haxby Road, HX12-1; Lerbekmo; HC-2PR) yielding a pooled mean age presented in Sprain et al. (2015). Sample TR13-3 from Thomas Ranch has been identified as the McGuire Creek bentonite based on Pb isotopic analysis and as such may be combined with the results of Sprain et al. (2015) to yield a weighted mean age of 66.024 ± 0.014/0.044 Ma.

4.9 Geomagnetic Polarity Timescale calibration

Sprain et al. (2015) showed that between multiple stratigraphic sections in the Hell Creek, relatively uniform sediment accumulation rates exist. This study corroborates that conclusion, yielding sediment accumulation rates of ~ 3–12 cm/ka for all of our measured sections. These relatively uniform SARs support the validity of interpolating between dated tephras to constrain reversal ages. Using polarity sequences determined in the study, we calculate reversal ages using linear interpolation (and in two cases extrapolation) between dated tephras and chron boundaries. For this calculation, we placed the reversal halfway between bounding sites that define the reversal, using this half distance as the uncertainty in reversal placement. We further add an uncertainty of 5% on all stratigraphic height measurements. In this study, the uncertainty in resulting chron boundary ages is dominated by uncertainty in the $^{40}Ar/^{39}Ar$ tephra ages, as the reversals in all sections were determined within a 2-meter resolution. Results are presented within Table 4.4.

C30n/C29r reversal

To calculate an age for the C30n/C29r reversal we utilized magnetostratigraphic and geochronologic data from our Bug Creek and Thomas Ranch localities. At Bug Creek, we used the BC11-1/BC-1PR age calculated for the Null coal and the pooled Z coal age from this study for geochronologic constraints. Because we could not measure a section here from the Null to the Z coal, we used the mean distance between the MCZ and Null coal at Thomas Ranch and Sandy Chicken to calculate a sediment accumulation rate. The value was then used to extrapolate to the

reversal, yielding an age of 66.307 ± 0.055/0.070 Ma. Using a higher quality R site, we calculated a reversal age of 66.312 ± 0.066/0.079 Ma. At Thomas Ranch, we used our dates for the Null coal (TR13-2) and pooled MCZ age to calculate a sediment accumulation rate which was then used to extrapolate to the C30n/C29r boundary. Using linear extrapolation, we calculated an age of 66.373 ± 0.163/0.172 Ma for the reversal. Using a higher quality reverse polarity site, we calculate an age of 66.376 ± 0.166/0.174 Ma. Combining these results, we get a weighted mean age of 66.314 ± 0.052/0.068 Ma (or 66.321 ± 0.061/0.074 Ma) for the C30n/C29r reversal. Using our new pooled age for the IrZ coal, we calculate the Cretaceous duration of C29r to be 267 ± 53 ka (274 ± 61 ka based on higher quality sites).

It is further noted here that the stratigraphic distance between the C30n/C29r reversal and the formational boundary measured at Thomas Ranch is 26.2 m. This estimate is consistent with the thickness determined at the Flag Butte section in LeCain et al. (2014) of ~25 m and is not consistent with the estimate of 7 m determined in Lerbekmo (2009). Additionally, our revised placement of the boundary at Bug Creek shifts the reversal at least 10 m below its original placement (Archibald et al., 1982), which based on the published stratigraphic section would suggest a thickness of at least ~25 m for the Cretaceous portion of C29r. This result is further corroborated by our results from Sandy Chicken where we measured a distance of ~27 m between the formational boundary and the Null coal, which in our Bug Creek and Thomas Ranch localities is located ~ 3 meters above the C30n/C29r reversal. These new results suggest that the placement of the C30n/C29r reversal in Lerbekmo (2009) is incorrect, and that the duration of the Hell Creek Formation is closer to 1.8 Ma than 2.06 Ma, as calculated in Wilson (2014).

C29r/C29n reversal

To calculate an age for the C29r/C29n reversal, we utilized magnetostratigraphic and geochronologic data from our Purgatory Hill, Lofgren, Pearl Lake, Hell Hollow, Garbani Hill, and Jack's Channel localities. At Purgatory Hill, we calculated the reversal age in two ways, first utilizing our PH13-1 and PH13-2 age constraints, and second using our PH13-3 and PH13-2 ages. To calculate a reversal age using the PH13-1 age, we did not use the placement of the reversal based on half distance between bounding sites because this would place the reversal below PH13-1, yielding an age that would be too old based on analysis from other sections. Instead, we used the placement of the first normal polarity site as the placement of the boundary, using the whole distance between this site and the reverse site below as the stated uncertainty. Doing so yields an age of 65.738 ± 0.254/0.255 Ma for the reversal. Using instead our PH13-3 age as the lower bound, and using the placement of the reversal as the halfway point between the last R site and first N site, yields a reversal age of 65.607 ± 0.049/0.057 Ma. Because of the uncertainty in the reliability of the PH13-1 date, we prefer the latter date for the age of the reversal at Purgatory Hill. At our Lofgren locality, we use our pooled MCZ age as our lower dated bound, and our date for LG13-1 as our upper dated bound. Using these dates, we interpolate an age of 65.745 ± 0.032/0.049 Ma for the C29r/C29n reversal. As a conservative constraint, we also calculate the age for the reversal using a beta site instead of a gamma site for the first normal. Doing this yields an age of 65.720 ± 0.039/0.055 Ma. To calculate the reversal age at Pearl Lake, we use our MD15-1 date of the HFZ as the lower bound, and the PL14-1 date as the upper bound. Using linear interpolation, we calculate an age for the C29r/C29n reversal of 65.717 ± 0.042/0.059 Ma. At Hell Hollow, we calculate the age for the C29r/C29n reversal utilizing our pooled weighted mean age for the HH13-2/HH13-3 tephra as an upper bound, and our HH13-1 date as a lower bound, yielding a reversal age of 65.737 ± 0.019/0.036 Ma. As a

conservative estimate, we also calculate a reversal age using our HH5 alpha site as the first normal. Doing so yields and age of 65.728 ± 0.020/0.037 Ma. At Garbani Hill, we utilize our pooled mean age for the HFZ and our GC12-3 age for the lower tuff within the Y coal doublet (because it is more precise than our GC12-2 age) to calculate a sediment accumulation rate. The reversal was found to be near the Y coal, and including the GB1 gamma site as the last reverse sample, places the reversal just above the Y coal doublet. Using this placement, we calculate an age for the C29r/C29n reversal of 65.701 ± 0.031/0.060 Ma. If instead we utilize the GB1A beta site as the placement of the last reverse sample, we place the reversal just below the Y coal doublet and calculate an age of 65.773 ± 0.091/0.099 Ma. At Jack's Channel because of uncertainty in the accuracy of ages for samples JC13-4 and JC13-2, we use our age for JC13-3 and the pooled MCZ age to calculate the C29r/C30n reversal age. Using these constraints, we calculate an age of 65.770 ± 0.039/0.054 Ma for the reversal.

Combining these results, we calculate a weighted mean age for the C29r/C30n reversal of 65.726 ± 0.013/0.044 Ma (or 65.732 ± 0.015/0.045 Ma using more conservative constraints). Using our new pooled mean age for the IrZ tephra, we calculate the duration of the Paleogene portion of C29r to be 321 ± 15 ka (315 ± 17 ka).

4.10 Discussion

Combining our weighted mean ages for the C29r/C29n reversal and the C30n/C29r reversal, we calculate the total duration of C29r to be 588 ± 53 ka (589 ± 63 ka).

Comparison to Previous calibrations

Comparing our new results to those in GTS2012 (Ogg, 2012), our results are generally consistent (Figure 4.10). GTS2012 calculated an age for the C29r/C30n transition of 66.398 Ma (largely based on astronomical tuning results of Husson et al., 2011 and Thibault et al., 2012). Our new estimate of 66.314 ± 0.052/0.068 Ma is consistent with this result at 2σ. For the C29r/C29n reversal, GTS2012 provided an age of 65.688 Ma. Our new result of 65.726 ± 0.013/0.044 Ma overlaps with this estimate at 2σ, considering systematic uncertainty. It is important to note that GTS2012 did not cite uncertainty estimates for their chron boundaries.

Our new estimate for the duration of the Cretaceous portion of C29r, 267 ± 53 ka, is consistent with orbitally tuned marine sections which call for at least a minimum duration of 300 ka, representing between 15–19 precession cycles (Thibault and Husson, 2016). Our new data further support an age of 66.04 Ma for the KPB, and do not require an adjustment to the age of the KPB to obtain a Cretaceous duration of C29r close to 300 ka, as suggested in Thibault and Husson (2016). Our new duration estimate favors between 15–17 precessional cycles for the Cretaceous portion of C29r. Our new estimate for the duration of the Paleogene portion of C29r is also consistent with astronomical tuning results presented in Dinarés-Turrell et al. (2003, 2007) for Zumaia. Their results suggest a duration of 252 ka, which is reasonably consistent with our duration of 321 ± 15 ka.

Comparing our results to those from Clyde et al. (2016), our weighted mean age of the C29r/C29n reversal overlaps within 2σ of the estimate provided in Clyde et al. (2016; 65.726 ± 0.013/0.044 Ma vs. 65.806 ± 0.024 Ma using systematic uncertainty; Figure 4.10), with a difference of 80 ± 50 ka. Comparing our results for the C30n/C29r reversal (66.314 ± 0.052/0.068 vs. 66.436 ± 0.019 Ma), again our ages overlap within 2σ, with a difference of 122 ± 71 ka. Further comparing our results to recent estimates on the timing and duration of C29r from the Deccan (Schoene et al., 2015; Renne et al., 2015), our new date for the age of the C30n/C29r

reversal overlaps within 2σ of both a U/Pb zircon age for a segregation horizon within a lava flow of transitional polarity (66.228 ± 0.043 Ma, fully propagated uncertainty) and the $^{40}Ar/^{39}Ar$ date from the transitional lava flow itself (66.38 ± 0.05 Ma, analytic uncertainty). However, our new age for the C29r/C29n reversal does not overlap at 2σ with a U/Pb zircon age (65.552 ± 0.043 Ma, fully propagated uncertainty) calculated from zircons separated from a red bole that separates lava flows of R polarity below, and N polarity above. The C29r/C29n reversal age from Clyde et al. (2016) is also not consistent with Schoene et al.'s (2015) estimate, which suggests that the zircons present in the red bole were deposited 10's of ka after the eruption of the lower lava flow, in other words there is a hiatus present. Schoene et al. (2015) also did not perform their own paleomagnetic analysis and it is entirely possible that they misplaced their dated red bole within Chenet et al.'s (2008) magnetic stratigraphy considering Chenet et al. (2008) identified 8 red boles near the C29r/C29n transition.

Faunal implications

Results from this study support the placement of NALMA faunas within the Hell Creek region into the magnetostratigraphic framework as presented in Archibald et al. (1982), Swisher et al. (1993), and LeCain et al. (2014), despite the errors found in past reversal placement. Lancian faunas are constrained to the C30n and the Cretaceous portion of C29r. We find Pu1 faunas (Hell Hollow and Z-Line) constrained to the Paleogene portion of C29r, and the Pu3 faunas (Garbani Channel and Purgatory Hill; previously ascribed to Pu2/3, which was used to indicate initial uncertainty in correlation but adjusted in Clemens, 2013) constrained to C29n. These results are largely in agreement with results from other basins yielding Puercan faunas (San Juan Basin, Pu2 and Pu3 in C29n: Williamson, 1996; Lofgren et al., 2004; Denver Basin, Pu1 in C29r and Pu2 in C29n: Hicks et al., 2003, Eberle, 2003) and with the biochronologic scheme outlined in Lofgren et al. (2004; Pu1 – C29r, Pu2 – C30n, Pu3 – C30n). However, results from the Rav W-1 local fauna in southwestern Saskatchewan (Johnston and Fox, 1984; Fox, 1989; Fox and Scott, 2011), the Hiatt local fauna from Makoshika State Park in eastern Montana (Hunter et al., 1997), and the PITA Flats local fauna from western North Dakota (Hunter, 1999; Hunter and Archibald, 2002) are inconsistent with this biochronologic scheme. At each of these localities, local faunas that are assigned to Pu2 are found to occur within C29r. In context of the magnetostratigraphic analysis conducted at these three localities, it is important to note that only at the Rav W-1 and Hiatt localities were paleomagnetic samples collected, while at PITA Flats the placement into C29r is based on the estimated distance of this site above the KPB (which is not found in the PITA Flats section) compared to magnetostratigraphic results collected elsewhere (Hunter and Archibald, 2002). Furthermore, both paleomagnetic studies conducted at Rav W-1(Lerbekmo, 1985) and at Hiatt (Lund et al., 2002) dominantly used alternating field demagnetization techniques to characterize primary directions. However, the results from the San Juan basin placing Pu2 faunas into C29n are also based dominantly on alternating field demagnetization techniques (Butler and Lindsay, 1985). Considering the inconsistencies between basins, it may be best to reassess the paleomagnetic analyses performed at these sites in order to be confident in associated faunal conclusions. Unfortunately, the results presented here cannot test the placement of Pu2 faunas into a magnetostratigraphic framework as clear Pu2 faunas have yet to be identified in the Hell Creek region. However, considering the stratigraphic gap comprising ~ 300 ka between the highest Pu1 fauna (all within C29r) and the lowest Pu3 fauna in the Hell Creek area (all within C29n) it is entirely possible that Pu2 faunas do exist within C29r but have yet to be sampled.

Assuming the assignment of local faunas from Rav W-1, Hiatt, and PITA Flats to C29r is correct, Fox and Scott (2011) interpret these results to indicate that Pu1and Pu2 zones overlap, suggesting that potentially North American Puercan is diachronous and that more progressive mammal species evolved earlier at higher latitudes. Without better age control, this hypothesis is hard to test. However, using the Paleogene duration of C29r calculated here (~321 ka), and the estimate from Sprain et al. (2015) that Pu1 faunas from the Hell Creek region are constrained to at least the first 70 ka of the Cretaceous, it can be seen that roughly 250 ka of C29r may exist under which Pu2 faunas found at the Hiatt, PITA Flats, and Rav W-1 localities could occur without overlapping with the Pu1 zone. However, this won't be confirmed until a Pu2 fauna is identified in the Hell Creek region.

4.11 Conclusions

We calculate a duration of 588 ± 53 ka for C29r based on 14 new magnetostratigraphic sections and 18 new $^{40}Ar/^{39}Ar$ tephra ages from the Hell Creek region, MT. This result is consistent with past estimates for the age and duration of this chron based on cyclostratigraphy and U/Pb geochronology. A previous estimate for the duration of C29r of ~350 ka presented in Sprain et al. (2015), is shown to be incorrect due to errors in reversal placement in three different magnetostratigraphic sections presented in Archibald et al. (1982) and LeCain et al. (2014). These errors are probably due to unremoved normal overprints, likely held by goethite, which cannot be removed by only alternating field demagnetization techniques. This result calls for the reevaluation of magnetostratigraphic frameworks developed in central North American basins that were determined using only alternating field demagnetization techniques (e.g. the San Juan basin), especially in locations where inconsistencies in the placement of NALMA faunas occur.

Using our newly calibrated GPTS, we can begin to tie records of ecological and environmental change from both terrestrial and marine sections, together with records of Deccan volcanism at high-precision (Figure 4.11). Upon first analysis, it appears that records of pre-KPB ecological stress coincide with Maastrichtian climate changes and the start of Deccan volcanism within the Western Ghats. Using our new estimate for the duration of the Cretaceous portion of C29r, it shows that the 8ºC decrease in terrestrial temperature as observed in Tobin et al. (2014) and in Wilf et al. (2003), is at most constrained to the last ~267 ka of the Cretaceous and that Maastrichtian warming likely ended ~ 150 ka before the KPB (Figure 4.11; Thibault and Husson, 2016). These changes appear to coincide with the decline in mammal evenness observed within the last 200 ka of the Cretaceous in the Hell Creek region (Wilson, 2014; Sprain et al., 2015). Additionally, using our new estimate for the total duration of C29r, we further see that over 80% of the volume of the Deccan Traps within the Western Ghats erupted in ~600 ka (using volume estimates calculated in Richards et al., 2015). However, using the placement of the KPB as estimated in Renne et al. (2015), 70% of this volume erupted after the KPB. This result raises the question of whether the observed correlation between Late Maastrichtian climate change and Deccan volcanism is indeed a cause and effect scenario and if so, why larger climatic variations are not seen post-KPB during the eruption of the largest volume of Deccan lava.

We also provide a new pooled age for the IrZ tephra incorporating ~200 new analyses, of 66.047 ± 0.008/0.043 Ma, which we interpret as the most reliable age for the KPB available.

Figures

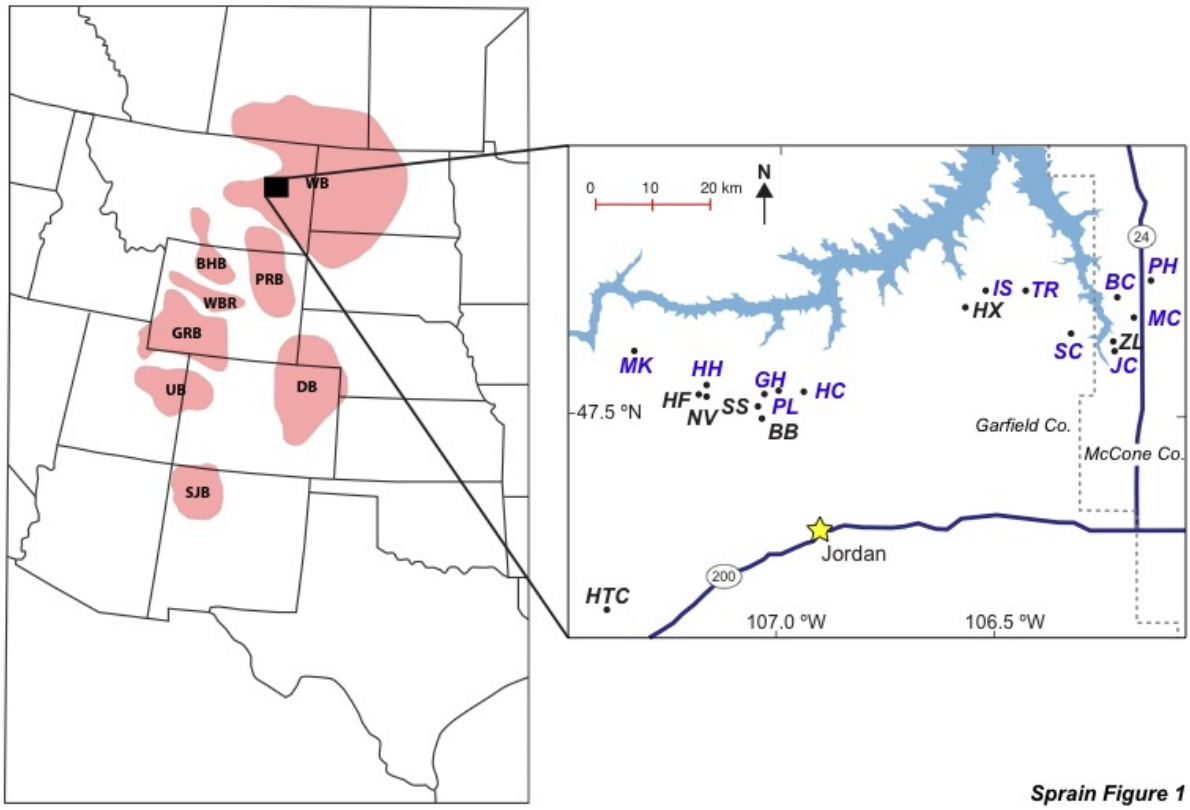

Figure 4.1. Major foreland basins systems of the western continental United States. WB: Williston basin, BHB: Big Horn basin, PRB: Powder River basin, WBR: Wind River basin, GRB: Green River basin, UB: Uinta basin, DB: Denver basin, SJB: San Juan basin. Inset shows a location map of our study area in the Hell Creek region of NE Montana around the Fort Peck Reservoir (blue) and near Jordan, Montana. Labeled dots indicate sampled localities from Sprain et al. (2015), Ickert et al. (2015), and this study (blue labels). MK: McKeever Ranch, HF: Hauso Flats, HH: Hell Hollow, NV: Nirvana, SS: Saddle Section, GH: Garbani Hill, BB: Biscuit Butte, PL: Pearl Lake, HC: Hell Creek Marina Road (Lerbekmo), HX: Haxby Road, IS: Isaac Ranch, TR: Thomas Ranch, SC: Sandy Chicken, BC: Bug Creek, PH: Purgatory Hill, MC: McGuire Creek (Lofgren, LG in Table 1), ZL: Z-Line, JC: Jack's Channel. Figure is modified from Sprain et al. (2016).

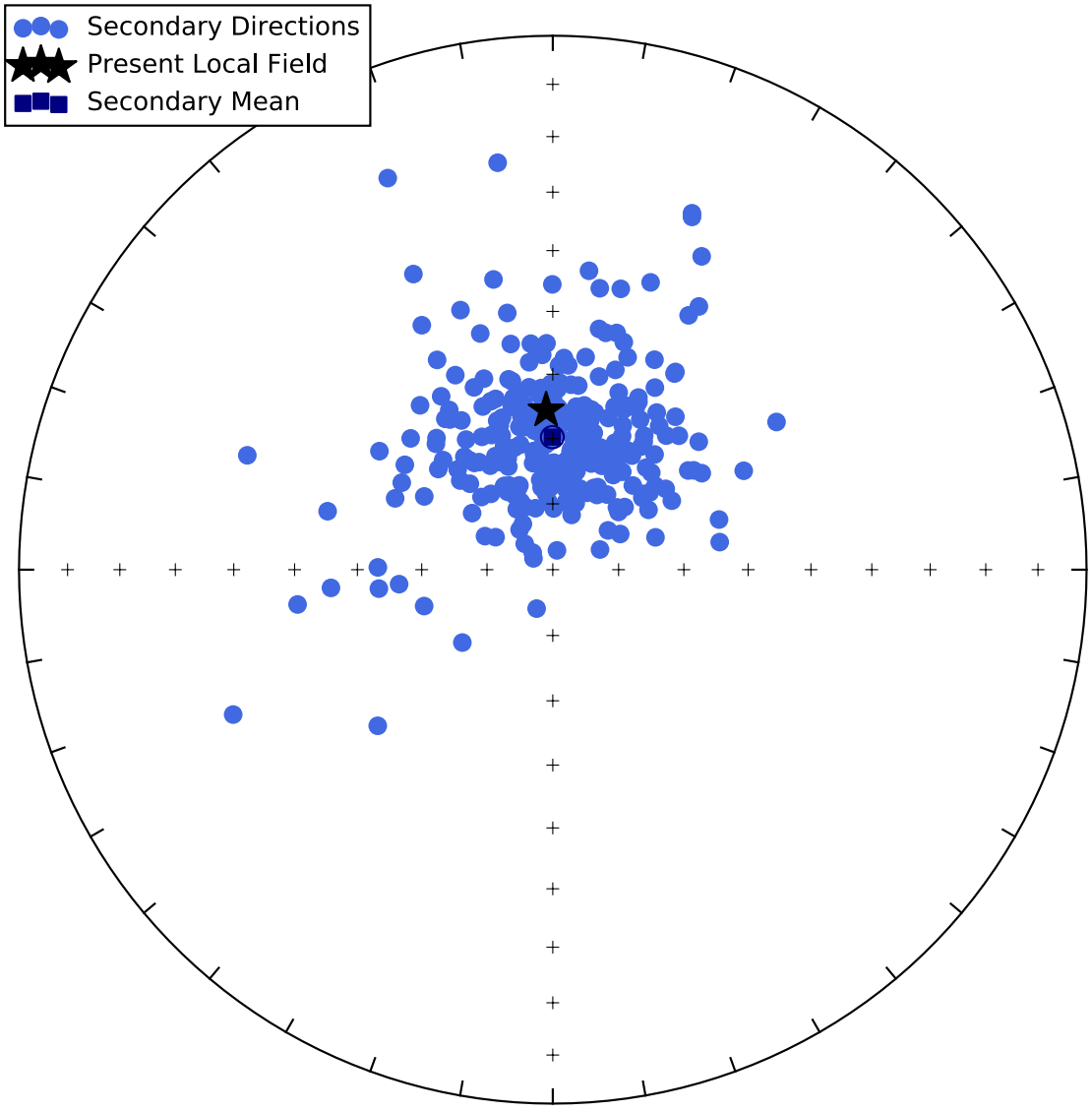

Figure 4.2. Equal Area plot showing all secondary directions determined in paleomagnetic analysis. The star indicates the present field direction in the Hell Creek region and the blue square shows the calculated Fisher mean and α95 (small circle around the blue square) calculated from all secondary directions.

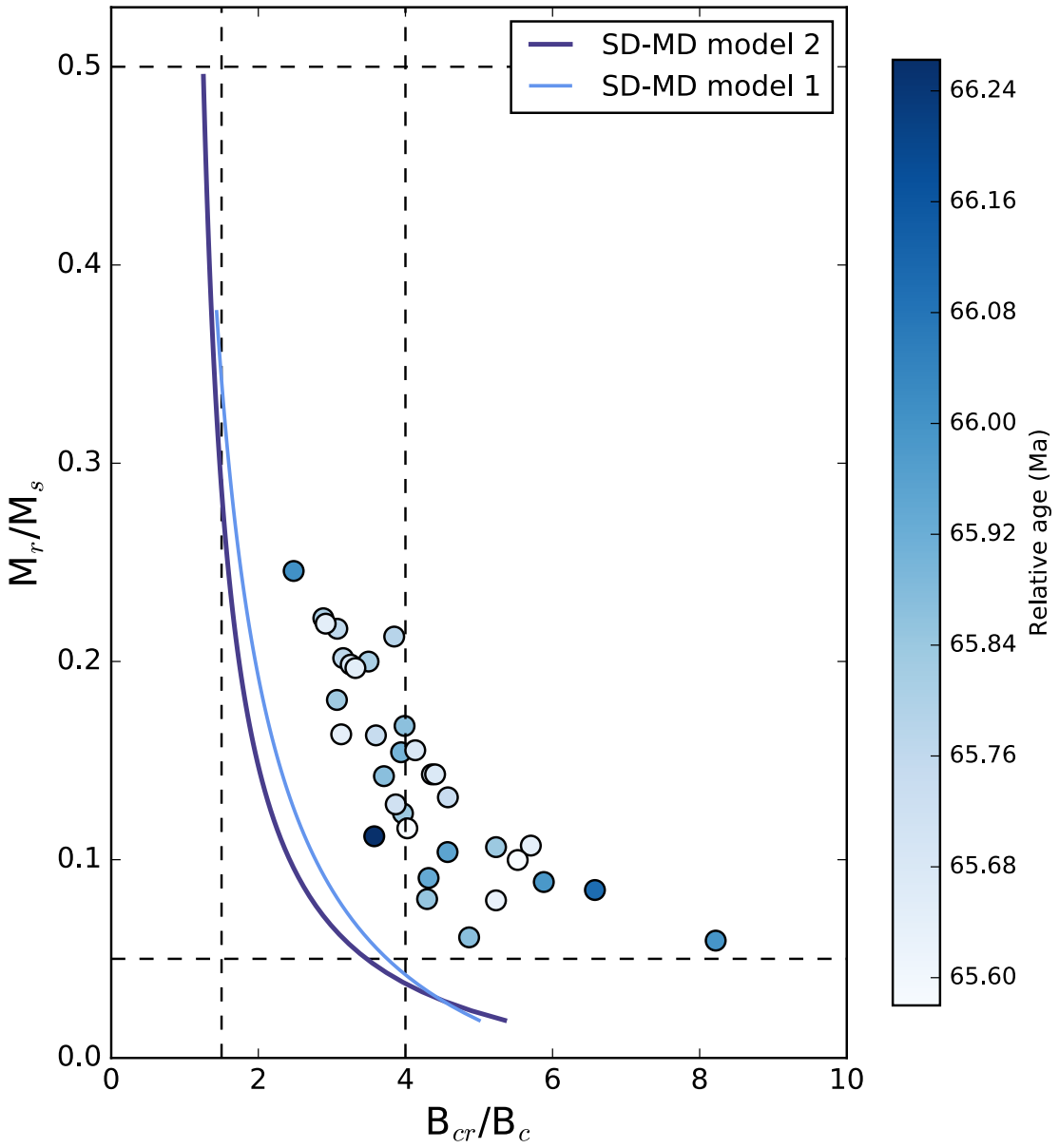

Figure 4.3. Day Plot (Day et al., 1977) of hysteresis ratios (Mr/Ms versus Bcr/Bc) for whole rock specimens from this study that were also analyzed in Sprain et al. (2016). Dark blue (light blue) curve indicate the theoretical mixing curve 2 (1) of single-domain and multidomain grains after Dunlop (2002). Data are colored based on relative age with lighter colors indicating younger samples. There is no observable trend in hysteresis ratios with age or stratigraphic position. This suggests that the source of magnetic material during the deposition of the upper Hell Creek Formation and Tullock Member was likely the same.

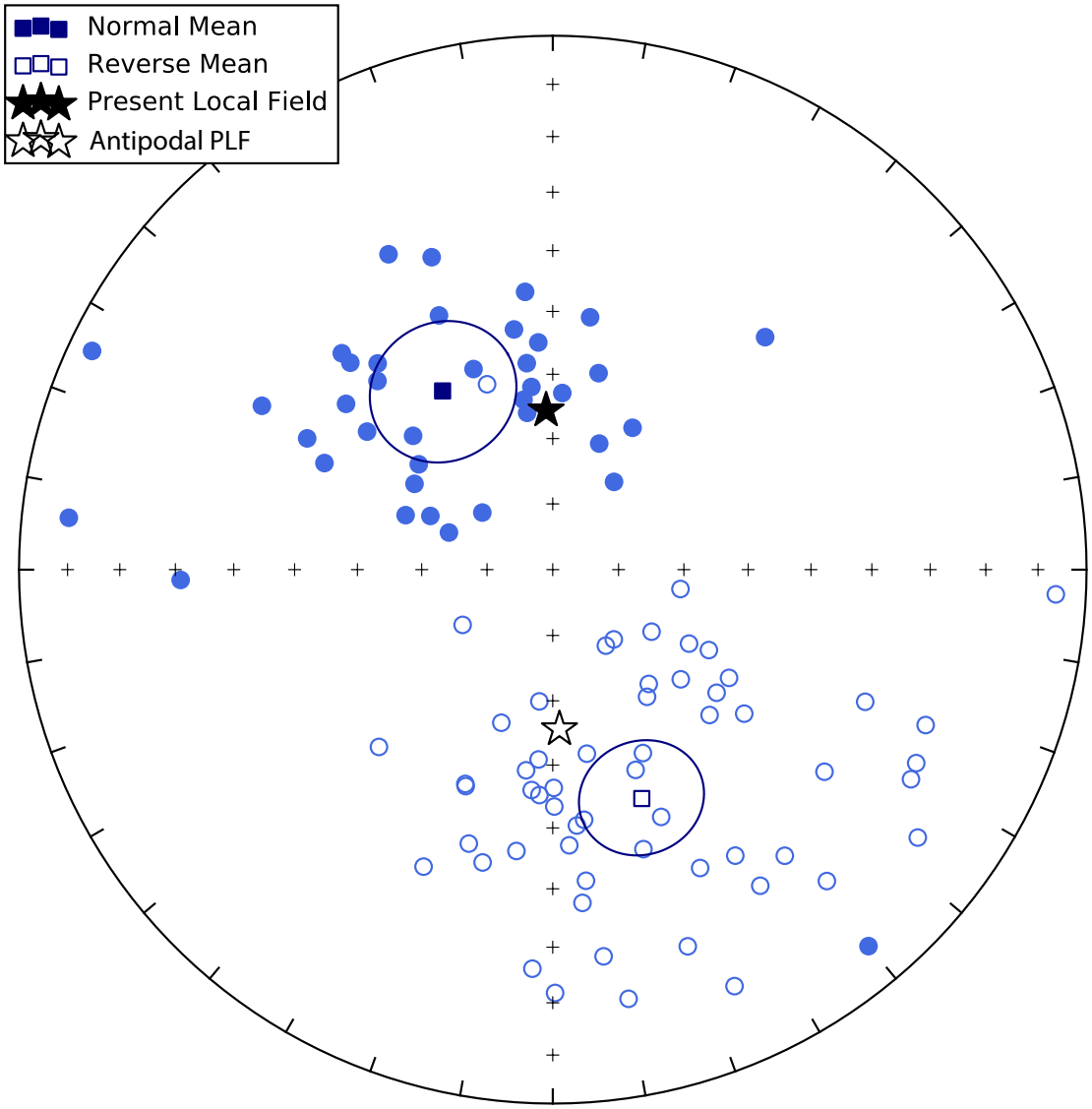

Figure 4.4. Equal Area plot showing all characteristic directions determined in paleomagnetic analysis. Closed (open) symbols indicate data plotting in the lower (upper) hemisphere. The black star indicates the present field direction in the Hell Creek region and the white star indicates the antipodal present field direction. The closed (open) blue square shows the Fisher mean and α95 (small circle around the blue square) calculated from all normal (reverse) directions.

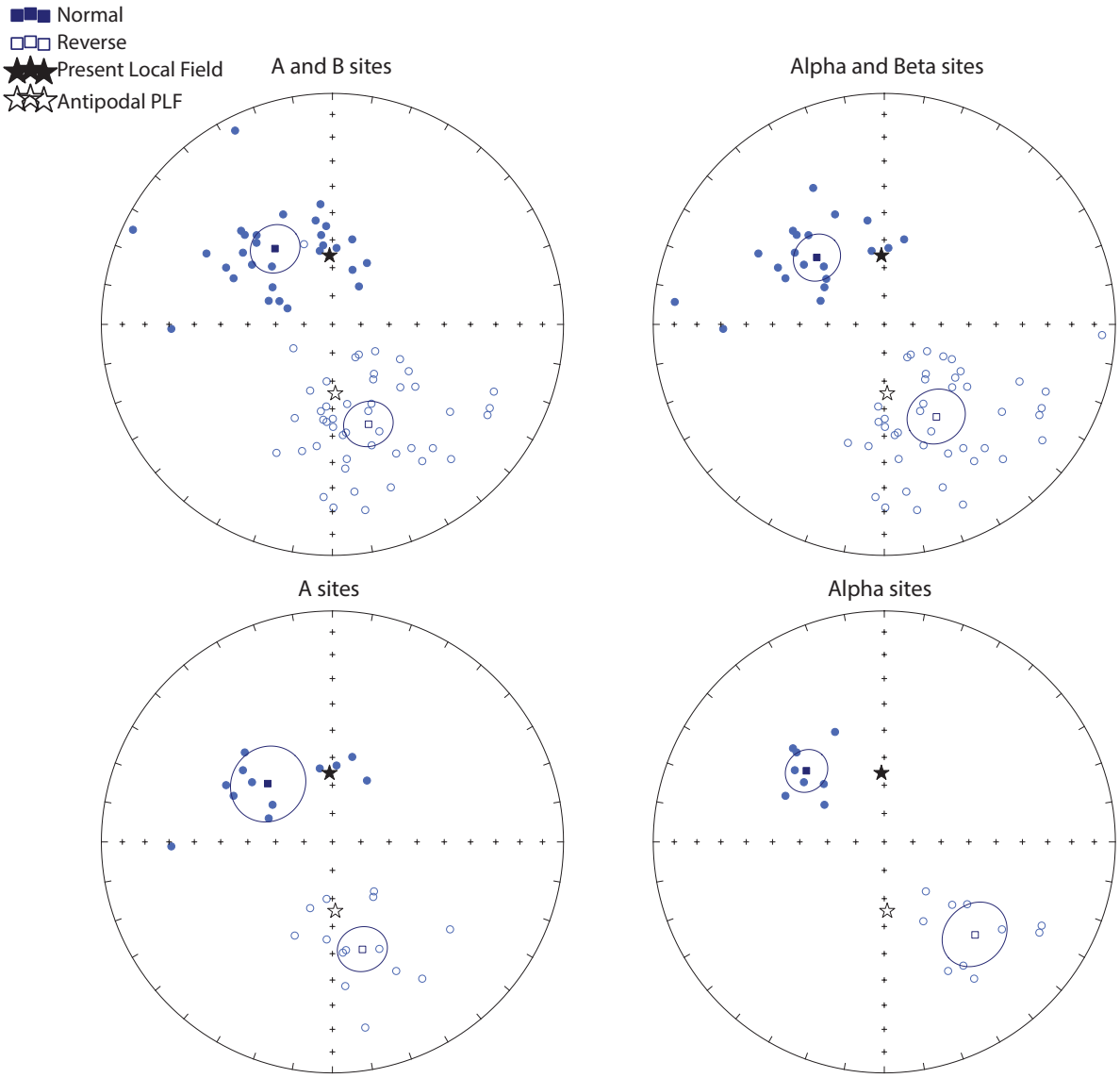

Figure 4.5. Equal area plots plotting sites that passed A and B criteria, just A criteria, alpha and beta criteria, and just alpha criteria. Closed (open) symbols indicate data plotting in the lower (upper) hemisphere. The black star indicates the present field direction in the Hell Creek region and the white star indicates the antipodal present field direction. The closed (open) blue square shows the Fisher mean and α95 (small circle around the blue square) calculated from normal (reverse) directions.

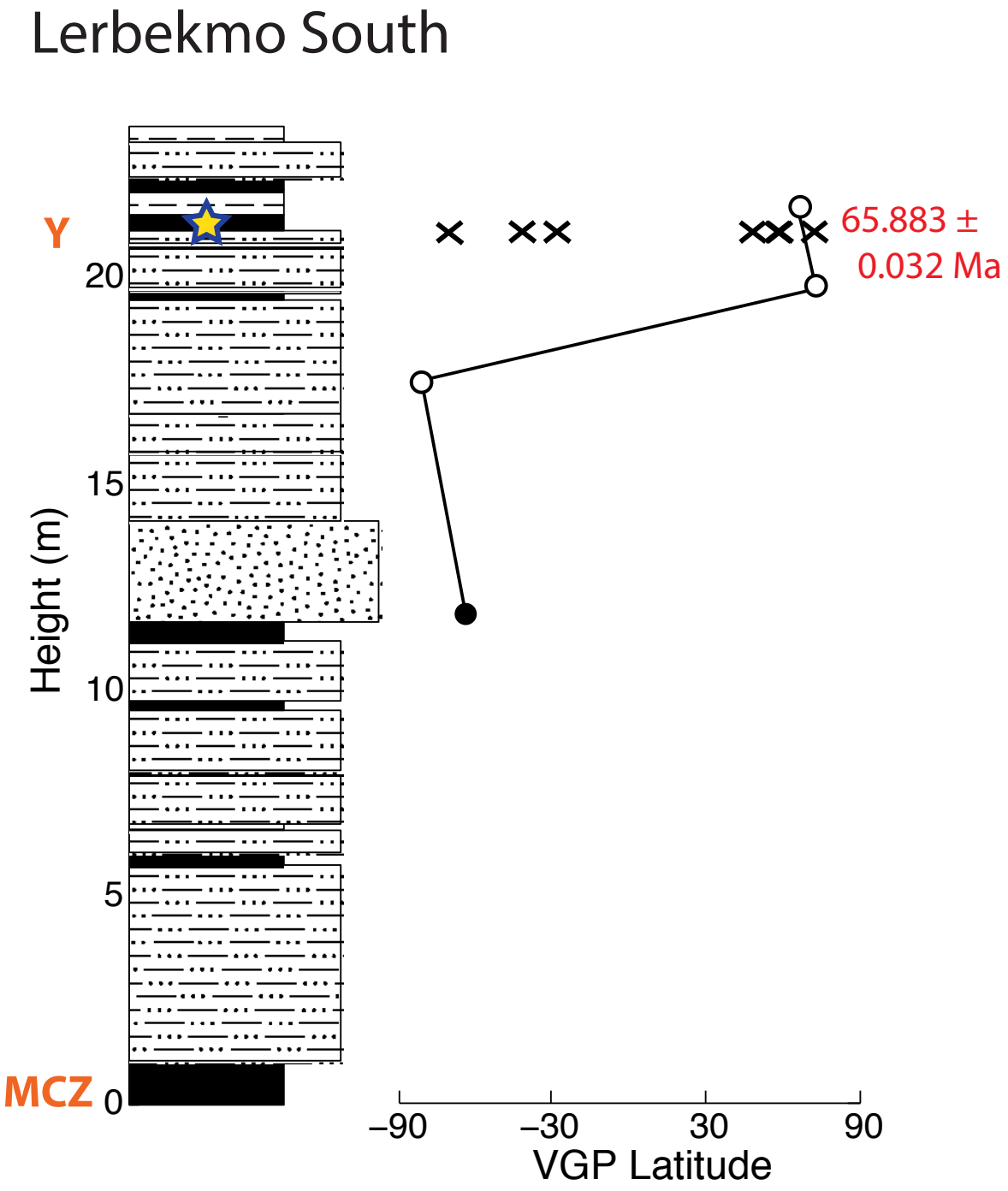

Figure 4.6. Stratigraphy, virtual geomagnetic pole (VGP) plots, and magnetostratigraphy of Lerbekmo South. Star indicates location of HC13-1 tephra, age shown in red. Stratigraphy was plotted using Matstrat (Lewis et al., 2011). Black (white) circles indicate A (B) sites and X's indicate C sites.

Figure 4.7A.

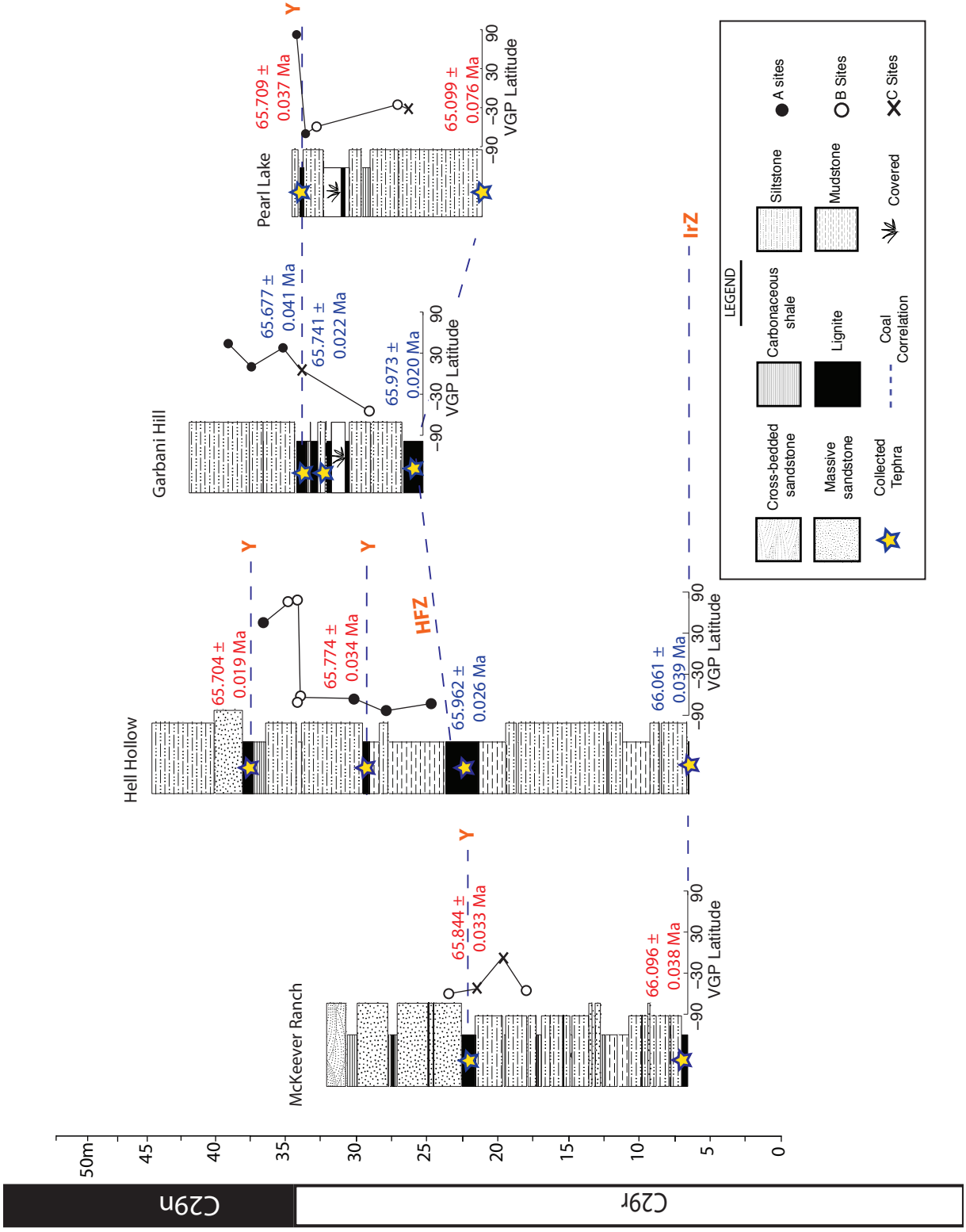
C29r
C29n
50m
45
40
35
30
25
20
15
10
5
0
McKeever Ranch
Hell Hollow
Garbani Hill
Pearl Lake
65.844 ± 0.033 Ma
66.096 ± 0.038 Ma
65.704 ± 0.019 Ma
65.774 ± 0.034 Ma
65.962 ± 0.026 Ma
66.061 ± 0.039 Ma
65.677 ± 0.041 Ma
65.741 ± 0.022 Ma
65.973 ± 0.020 Ma
65.709 ± 0.037 Ma
65.099 ± 0.076 Ma
VGP Latitude
–90
–30
30
90
Y
HFZ
IrZ
LEGEND
Cross-bedded sandstone
Massive sandstone
Collected Tephra
Carbonaceous shale
Lignite
Coal Correlation
Siltstone
Mudstone
Covered
A sites
B Sites
C Sites

Figure 4.7B.

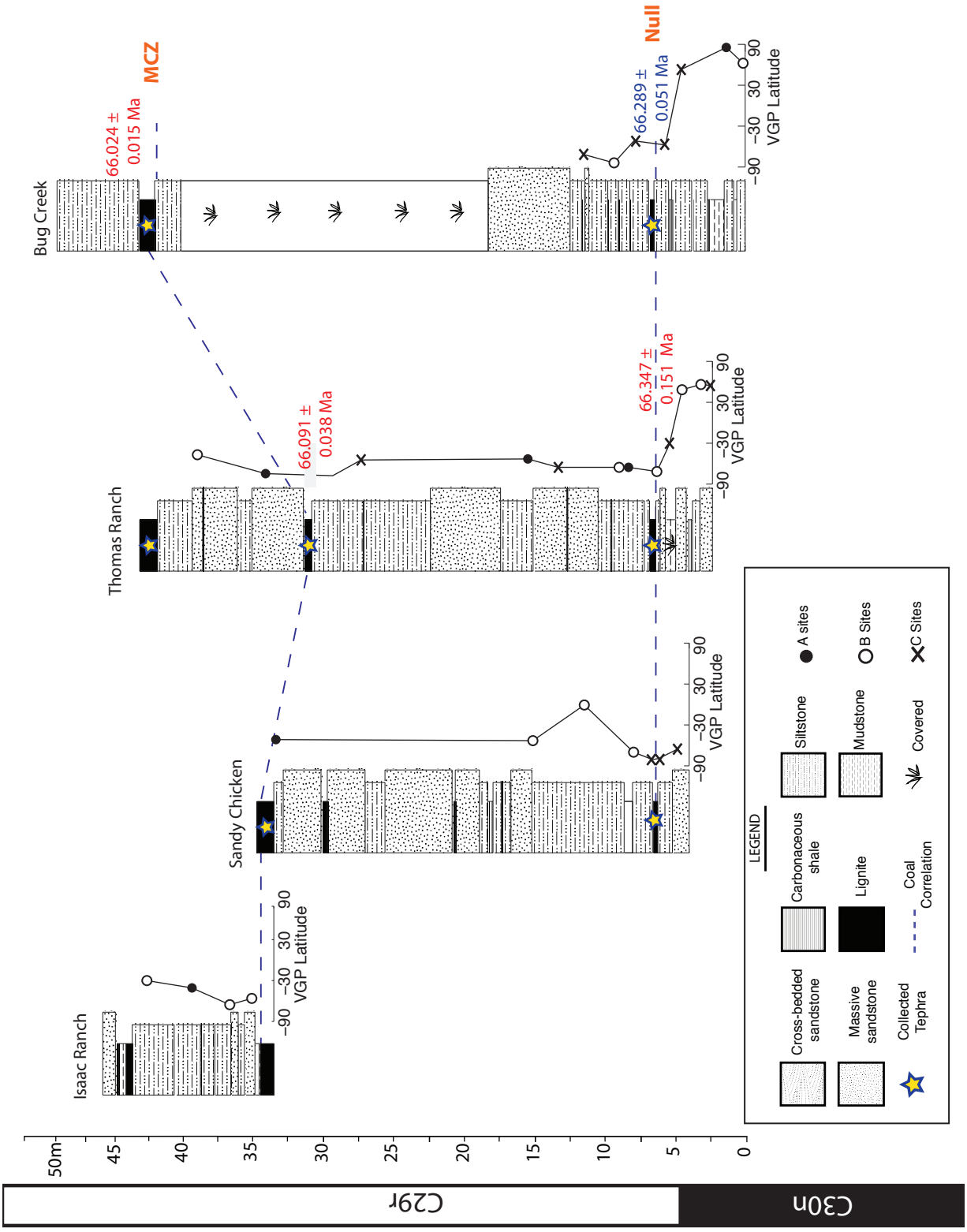
C30n
C29r
50m
45
40
35
30
25
20
15
10
5
0
Isaac Ranch
Sandy Chicken
Thomas Ranch
Bug Creek
MCZ
Null
66.024 ± 0.015 Ma
66.091 ± 0.038 Ma
66.347 ± 0.151 Ma
66.289 ± 0.051 Ma
VGP Latitude
–90
–30
30
90
LEGEND
Cross-bedded sandstone
Massive sandstone
Collected Tephra
Carbonaceous shale
Lignite
Coal Correlation
Siltstone
Mudstone
Covered
A sites
B Sites
C Sites

Figure 4.7C.

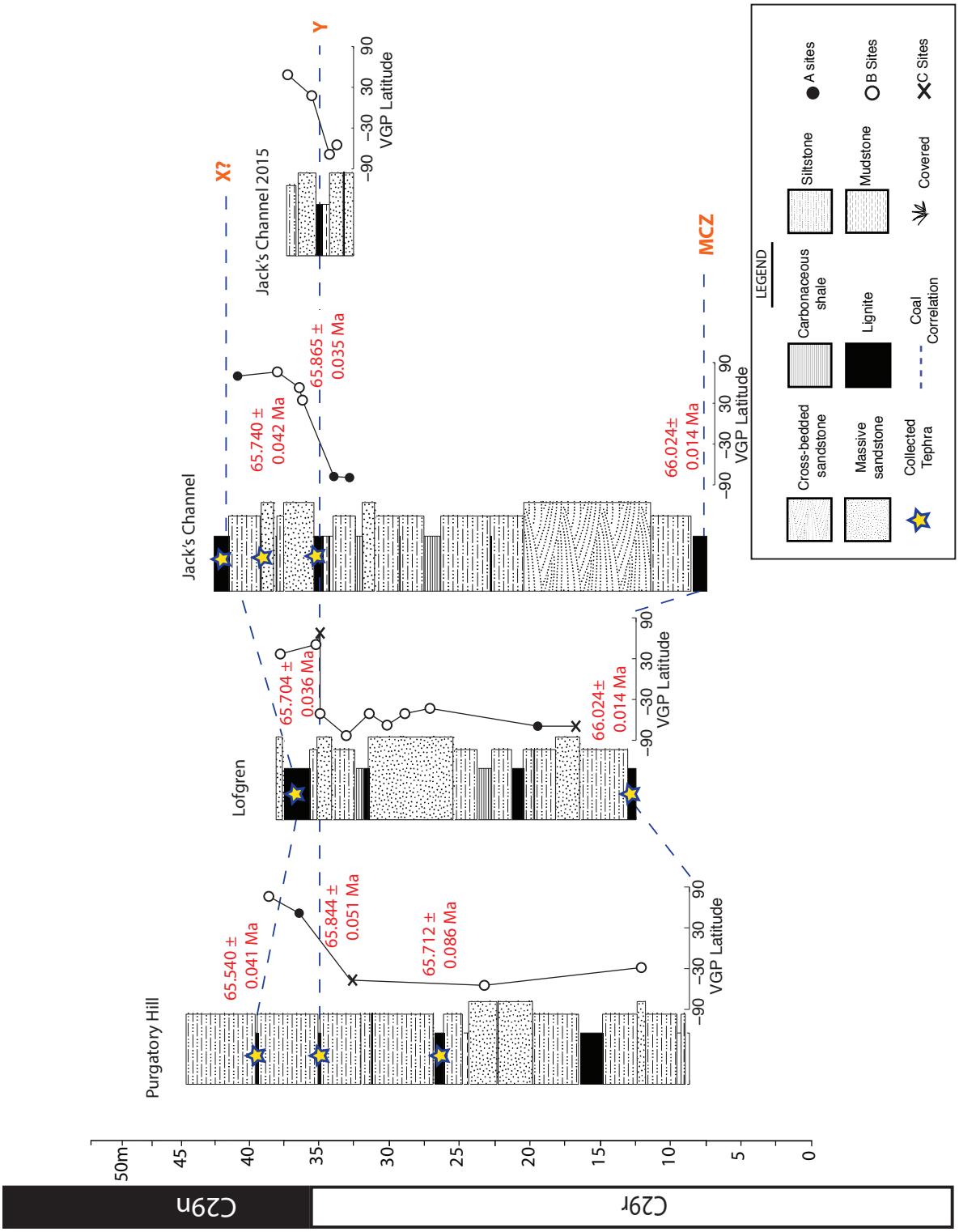

Figure 4.7. Stratigraphy, virtual geomagnetic pole (VGP) plots, and magnetostratigraphy of all sections. A. Western Garfield County. B. Eastern Garfield County. C. McCone County. Blue (red) dates are from Sprain et al. (2015) (this study). See legend for details. Stratigraphy was plotted using Matstrat (Lewis et al., 2011).

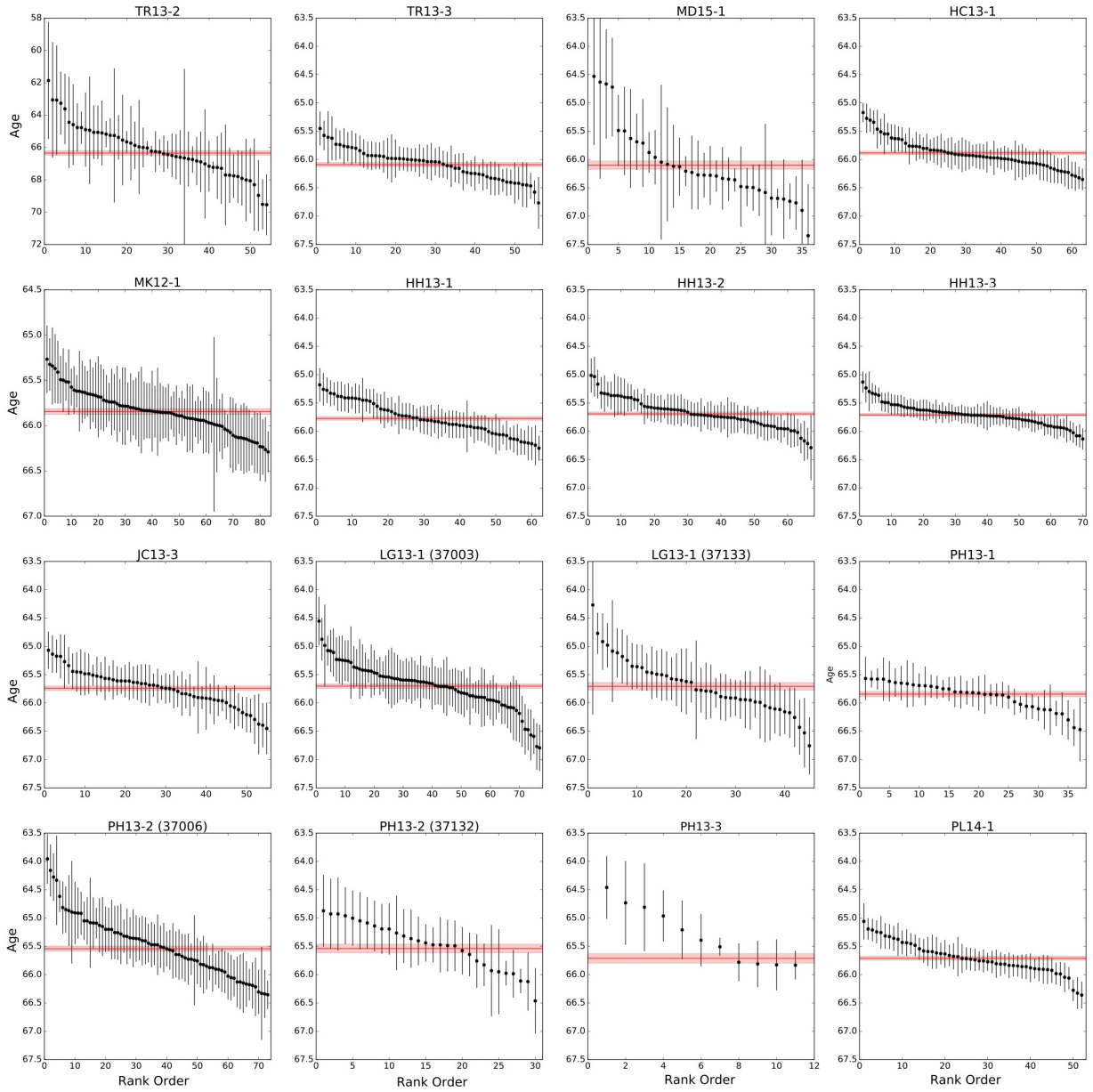

Figure 4.8. Summary of single crystal $^{40}Ar/^{39}Ar$ analyses for all non-IrZ tephras. Stratigraphic relationships are presented in Figure 4.7. Individual ages are presented in rank order with analytical uncertainty limits of 1σ. The red line indicates the weighted mean age and the red box shows the 1σ uncertainty on the weighted mean.

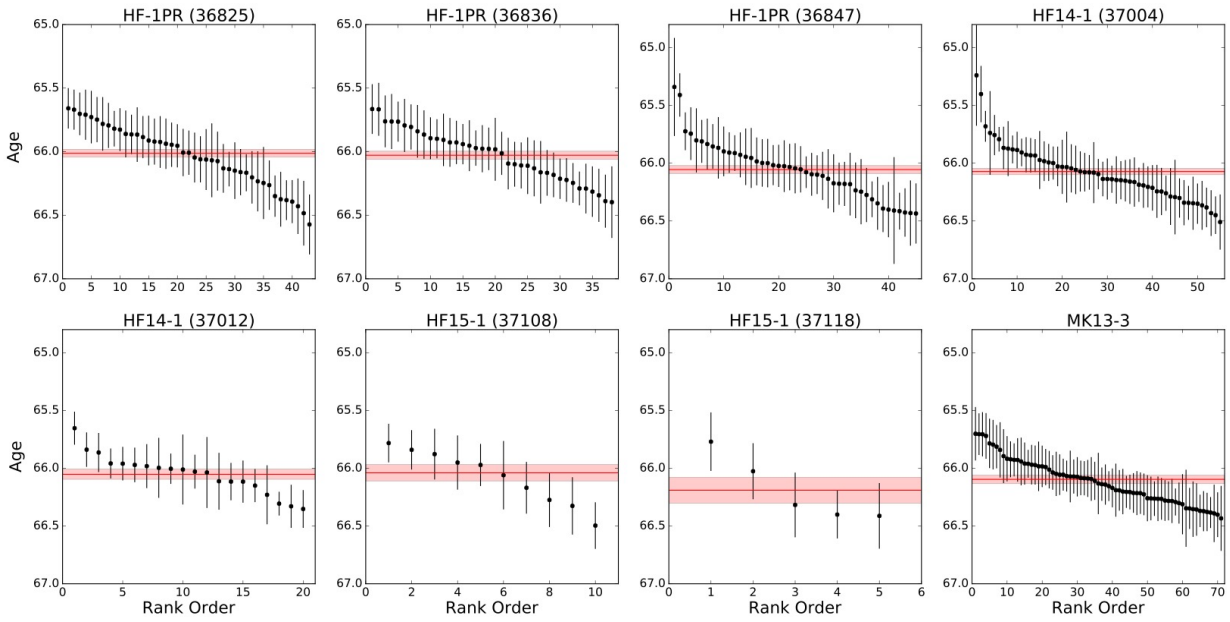

Figure 4.9. Summary of single crystal $^{40}Ar/^{39}Ar$ analyses for all new IrZ tephras. Individual ages are presented in rank order with analytical uncertainty limits of 1σ. The red line indicates the weighted mean age and the red box shows the 1σ uncertainty on the weighted mean.

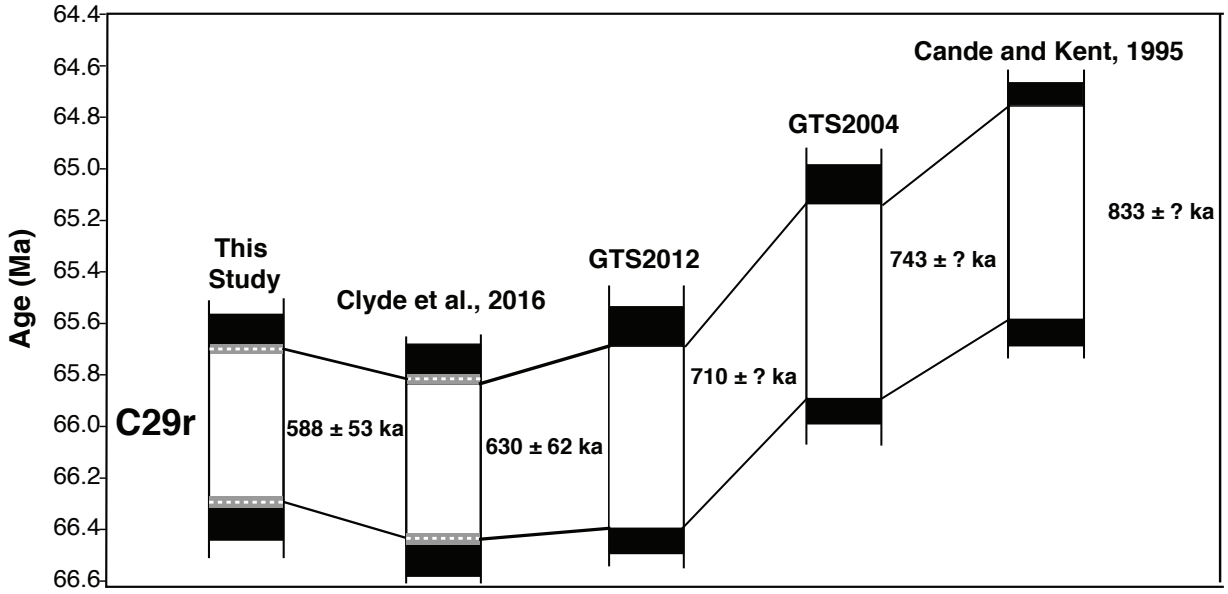

Figure 4.10. Duration of Chron 29r calculated in different calibrations. Cande and Kent (1995) calculated chron boundary ages using seafloor spreading models tied to dated calibration points. GTS2004 and GTS2012 utilized a similar spreading model, with the addition of new radioisotopic and orbitally tuned ages as calibration points. Dashed white lines denote weighted mean age and grey boxes indicate systematic uncertainty estimates at 1σ. Note, GTS2012 and GTS2004 did not provide uncertainty estimates.

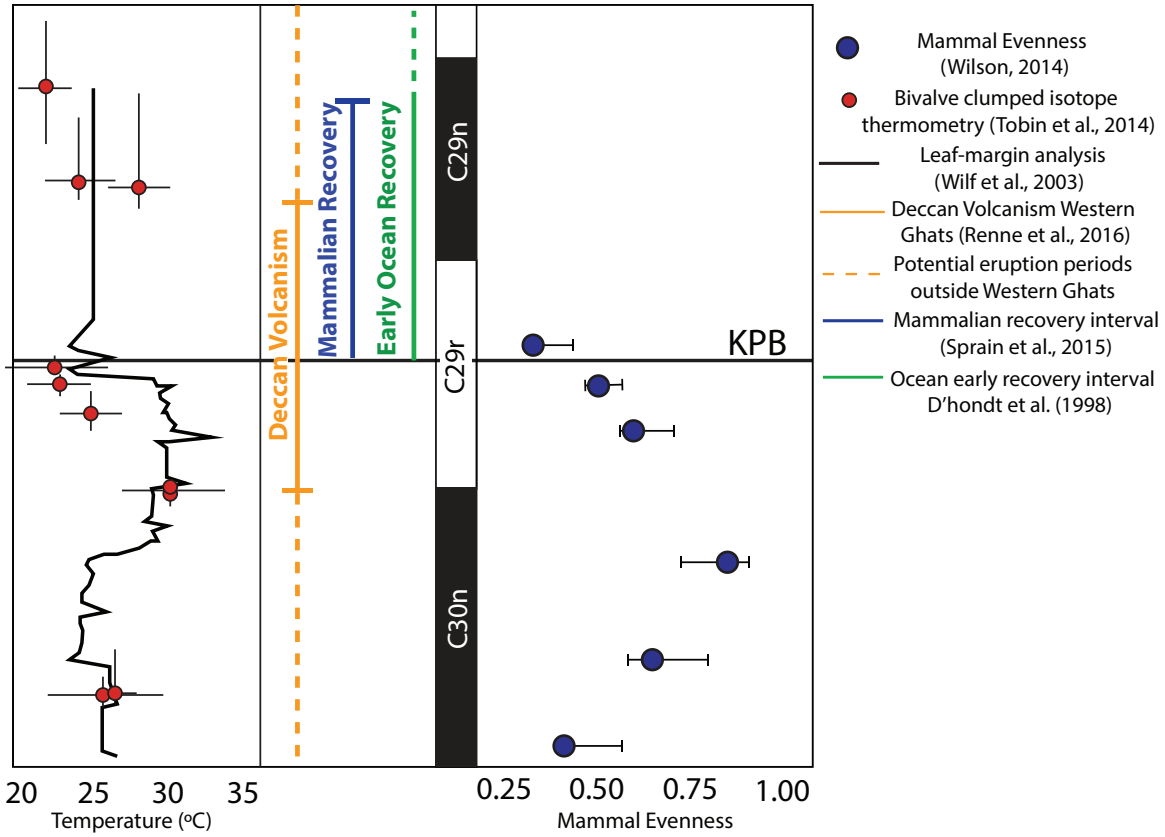

Figure 4.11. Circum-KPB environmental changes. Figure plots different environmental and ecological changes along with the timing of Deccan volcanism during C29r. Temperature and mammal evenness are from Tobin et al. (2014) and Wilson (2014), mammalian recovery is after Sprain et al. (2015), and ocean recovery interval is after D'Hondt et al. (1998). Figure after Tobin et al. (2014).

Table 4.1.

Site or Sample #	Section	Quant. Class.	Quali. Class.	Lat. (°)	Long. (°)	Strat Level (m)	Geo Dec (°)	Geo Inc (°)	α95	n	k	R	MAD (°)	VGP Lat (°)	Chron
15BC1	BC	B	α	47.680	-106.214	0.1	335.9	46.7	21.4	3	34	2.9415	N/A	62.79	C30n
14BC1	BC	A	β	47.680	-106.214	1.3	3.08	62.9	21.7	3	33	2.9397	N/A	86.03	C30n
14BC2-3A	BC	C	β	47.680	-106.214	4.6	332.5	33.8	5	1			N/A	53.22	C30n
14BC2A-1A	BC	C	γ	47.680	-106.214	5.7	130.6	-64.2	N/A	1	N/A	N/A	13	-56.72	C29r
14BC2B-2A	BC	C	β	47.680	-106.214	8.0	118.5	-66.3	9.5	1			N/A	-50.13	C29r
14BC3	BC	B	β	47.680	-106.214	9.4	184.3	-60.8	42.2	3	10	2.7914	N/A	-83.40	C29r
14BC4-1A	BC	C	γ	47.680	-106.214	11.6	176.6	-47.1	15.4	1			N/A	-70.42	C29r
15GB1A	GH	B	γ	47.515	-107.068	3.9	238.5	-73.9	48.1	3	8	2.738	N/A	-54.59	C29r
16GH1A	GH	C	γ	47.515	-107.068	7.9	N/A	N/A	N/A	N/A	N/A	N/A	N/A	N/A	N/A
15GB1-1A	GH	C	β	47.515	-107.068	8.9	276.1	9.7	19.6	1	N/A	N/A	N/A	7.73	C29r
16GH2	GH	A	α	47.515	-107.068	10.1	295	51	4.4	3	772	2.9974	N/A	39.09	C29n
15GB2	GH	A	β	47.515	-107.068	12.4	268.4	30.9	17.2	3	53	2.962	N/A	11.16	C29n
15GB3	GH	A	β	47.515	-107.068	14.1	290.3	66	37.6	3	12	2.8103	N/A	44.97	C29n
HH1	HH	A	β	47.535	-107.169	18.5	174.6	-50.2	20.6	3	37	2.9458	N/A	-72.93	C29r
HH2	HH	A	γ	47.535	-107.169	21.8	185.8	-69.8	24.2	3	27	2.9258	N/A	-82.86	C29r
15HH1	HH	A	β	47.535	-107.169	24.0	156.3	-48.1	28	3	21	2.9025	N/A	-64.05	C29r
HH3	HH	B	β	47.535	-107.169	27.6	138.8	-75.9	31.5	3	16	2.8782	N/A	-62.53	C29r
15HH2	HH	B	α	47.535	-107.169	27.8	153.8	-58.6	26.9	3	22	2.9092	N/A	-69.42	C29r
HH4	HH	B	γ	47.535	-107.169	27.9	352.8	58	29.1	5	8	4.4904	N/A	79.71	C29n
15HH3	HH	B	γ	47.535	-107.169	28.6	20.22	69.5	36.1	3	13	2.8431	N/A	75.97	C29n
HH5	HH	A	α	47.535	-107.169	30.2	315.6	44.9	5.6	4	267	3.9888	N/A	49.54	C29n
15HHA1	HHA	B	γ	47.535	-107.169	2.7	353.3	61.8	57.1	3	6	2.6512	N/A	83.48	C29n
1C	HHA	C	γ	47.535	-107.169	3.5	350.7	65.7	11.8	1	N/A	N/A	N/A	83.75	C29n
HHA2	HHA	A	α	47.535	-107.169	5.0	306.6	54.3	20.1	3	38	2.948	N/A	48.76	C29n
15HHA2	HHA	A	β	47.535	-107.169	5.1	298.1	46.7	35.3	3	13	2.8492	N/A	38.82	C29n
HHA3	HHA	A	α	47.535	-107.169	9.0	308.7	48.9	47.8	3	8	2.7409	N/A	47.16	C29n
IS1	IS	B	β	47.666	-106.502	1.6	182.9	-26.1	20	3	39	2.949	N/A	-56.01	C29r
IS2	IS	B	β	47.666	-106.502	3.1	162	-44.2	35.3	4	8	3.6132	N/A	-64.07	C29r
IS3	IS	A	α	47.666	-106.502	5.9	126.6	-36.7	9.6	3	167	2.988	N/A	-39.40	C29r
IS4	IS	B	α	47.666	-106.502	9.1	120.3	-23.3	26.1	3	23	2.9146	N/A	-29.21	C29r
14JC1	JC	A	β	47.606	-106.211	0.6	183.4	-55.2	14.4	3	74	2.9731	N/A	-77.86	C29r
14JC2	JC	A	γ	47.606	-106.211	1.7	198.6	-65.3	12.9	3	92	2.9783	N/A	-77.47	C29r
14JC3	JC	B	β	47.606	-106.211	4.0	299.4	37.5	19.7	6	13	5.6021	N/A	34.99	C29n
JC1	JC	B	β	47.605	-106.209	4.3	319.7	48	21.5	3	34	2.941	N/A	53.88	C29n
JC2	JC	B	γ	47.605	-106.209	5.8	356.4	54.9	12.8	4	52	3.9429	N/A	77.53	C29n
JC3	JC	A	γ	47.605	-106.209	8.7	29.35	65.1	6.2	3	390	2.9949	N/A	70.23	C29n
15JC1	JC	B	β	47.606	-106.207	1.2	179.7	-21.8	41.4	3	10	2.7984	N/A	-53.70	C29r
15JC2	JC	B	β	47.606	-106.207	1.7	179.7	-42.8	49.1	3	7	2.7171	N/A	-67.24	C29r

Table 4.1 cont.

15JC2	JC	B	β	47.606	-106.207	1.7	179.7	-42.8	49.1	3	7.0	2.7171	N/A	-67.24	C29r
15JC3	JC	B	β	47.606	-106.207	3.0	295.4	5	53.1	3	6.0	2.6902	N/A	18.73	C29n
15JC4	JC	B	γ	47.606	-106.207	4.7	293.7	69.6	55.2	3	6.0	2.6698	N/A	48.96	C29n
HC1	LBS	A	γ	47.516	-106.937	11.8	174.9	-37.4	9.1	3	185	2.9892	N/A	-63.09	C29r
HC2	LBS	B	γ	47.516	-106.937	17.5	169.5	-61.3	22.2	3	32.0	2.9373	N/A	-81.00	C29r
HC3	LBS	B	γ	47.516	-106.937	19.7	354.3	46.6	36.3	3	13.0	2.8413	N/A	69.86	C29r
HC4	LBS	C	γ	47.516	-106.937	N/A	N/A	N/A	N/A	N/A	N/A	N/A	N/A	N/A	N/A
14HC1	LBS	C	γ	47.516	-106.937	N/A	N/A	N/A	N/A	N/A	N/A	N/A	N/A	N/A	N/A
14HC2	LBS	B	γ	47.516	-106.937	21.7	34.91	73.7	23.9	3	28.0	2.9278	N/A	66.38	C29r
14LG1-3A	LG	C	β	47.630	-106.170	4.3	176.1	-42.4	8	1			N/A	-66.71	C29r
14LG2	LG	A	β	47.630	-106.170	7.0	143.4	-65.8	16.7	3	55.0	2.9639	N/A	-65.69	C29r
14LG3	LG	B	β	47.630	-106.170	14.8	138.64	-23.34	56.14	3.00	5.9	2.66	N/A	-40.56	C29r
14LG4	LG	B	α	47.630	-106.170	16.6	126.9	-53	22.5	3	31.0	2.9355	N/A	-48.24	C29r
14LG5	LG	B	β	47.630	-106.170	17.9	145	-75.9	31.2	3	17.0	2.8802	N/A	-65.25	C29r
15LG1	LG	B	β	47.630	-106.170	19.2	117.2	-63.1	37.8	3	12.0	2.8291	N/A	-47.59	C29r
14LG6	LG	B	β	47.630	-106.170	20.8	179.7	-56.4	21.7	3	33.0	2.94	N/A	-79.33	C29r
14LG7	LG	B	β	47.630	-106.170	22.7	121.5	-58.2	38	6	4.0	4.7683	N/A	-47.58	C29r
15LG2-1A	LG	C	β	47.630	-106.170	22.7	338.4	56.8	N/A	1	N/A	N/A	15.9	71.19	C29n
14LG8	LG	B	γ	47.630	-106.170	23.0	317.10	50.11	6.00	23.3	9.2	5.46	N/A	53.41	C29n
15LG3	LG	B	β	47.630	-106.170	25.6	333.35	6.81	42.57	3.00	9.5	2.79	N/A	40.18	C29n
MK1	MK	C	γ	47.594	-107.327	0.6	N/A	N/A	N/A	N/A	N/A	N/A	N/A	N/A	N/A
MK2	MK	B	β	47.594	-107.327	11.6	122.11	-72.23	23.31	3.00	29.0	2.93	N/A	-54.60	C29r
MK3-3A	MK	C	β	47.594	-107.327	13.2	92.81	-6.3	17.8	N/A	N/A	N/A	N/A	-4.23	C29r
MK3.5-2A	MK	C	β	47.594	-107.327	15.1	126.9	-58.5	5.7	N/A	N/A	N/A	N/A	-51.32	C29r
MK4	MK	B	β	47.594	-107.327	16.8	172.5	-27.8	32.9	4	9.0	3.6575	N/A	-56.59	C29r
MKA1	MKA	A	α	47.598	-107.340	0.2	153.7	-37.7	16.4	4	32.0	3.9076	N/A	-56.11	C29r
MKA2	MKA	A	α	47.598	-107.340	4.8	146.7	-29.9	12.4	4	56.0	3.946	N/A	-48.23	C29r
15PL1A-1A	PL	C	β	47.523	-107.057	5.9	112.9	-36.6	7.6	1	N/A	N/A	N/A	-30.22	C29r
15PL1	PL	B	β	47.523	-107.057	6.7	112.6	-25.3	52.7	3	7.0	2.6941	N/A	-24.99	C29r
15PL2	PL	A	γ	47.523	-107.057	12.2	201.9	-54	15.3	3	66.0	2.9695	N/A	-69.10	C29r
16PL1	PL	B	γ	47.523	-107.057	12.8	203.5	-39.2	35.1	3	13.0	2.8506	N/A	-58.41	C29r
16PL2	PL	A	β	47.523	-107.057	14.3	350.2	63.6	18.8	3	44.0	2.9546	N/A	82.87	C29n
15PH1	PH	B	α	47.703	-106.150	3.4	118	-23.9	19	3	43.0	2.9535	N/A	-27.95	C29r
15PH2	PH	B	α	47.703	-106.150	14.8	132.8	-57.1	26.2	3	23.0	2.9135	N/A	-54.51	C29r
15PH3	PH	C	γ	47.703	-106.150	23.1	N/A	N/A	N/A	N/A	N/A	N/A	N/A	N/A	N/A
15PH4-2A	PH	C	β	47.703	-106.150	24.4	156.4	-16	13.2	1	N/A	N/A	N/A	-45.69	C29r
15PH5	PH	A	α	47.703	-106.150	28.1	301.8	65.1	13	3	90.0	2.9779	N/A	51.58	C29n
16PH2	PH	A	β	47.703	-106.150	30.3	13.12	59	47.9	3	8.0	2.7395	N/A	77.66	C29n
3A	SC	C	γ	47.625	-106.353	0.8	193.5	-43	21.8	1	N/A	N/A	N/A	-64.99	C29r

Table 4.1 cont.

14SC2-3A	SC	C	γ	47.625	-106.353	2.1	185.5	-55.9	9.8	1	N/A	N/A	N/A	-78.11	C29r
1A	SC	C	γ	47.625	-106.353	2.6	187.6	-58.9	11.6	1	N/A	N/A	N/A	-80.33	C29r
14SC4	SC	B	β	47.625	-106.353	4.0	187.36	-45.87	20.00	3	39.0	2.95	N/A	-68.84	C29r
14SCA1	SC	B	γ	47.625	-106.353	7.5	340.48	-59.80	36.90	3	12.0	2.84	N/A	0.03	C29r
14SCA2	SC	B	β	47.625	-106.353	11.2	160.28	-26.00	35.70	3	13.0	2.85	N/A	-52.32	C29r
14SCA3	SC	A	β	47.625	-106.353	29.7	169.98	-19.50	32.60	3	15.0	2.87	N/A	-51.47	C29r
15TRA1-3A	TR	C	β	47.666	-106.422	0.1	308.17	63.90	4.20	1	N/A	N/A	N/A	55.01	C30n
14TRA1	TR	B	α	47.666	-106.422	0.8	313.77	60.30	9.40	6	51.0	5.90	N/A	56.89	C30n
14TRA2	TR	B	γ	47.666	-106.422	2.2	289.67	73.20	16.40	6	18.0	5.72	N/A	48.59	C29r?
15TRA2-1A	TR	C	β	47.666	-106.422	3.1	126.27	-16.30	16.50	1	N/A	N/A	N/A	-30.08	C29r
14TRA3	TR	B	β	47.666	-106.422	4.0	157.52	-56.64	27.20	3	21.6	2.91	N/A	-70.51	C29r
14TRA4	TR	A	α	47.666	-106.422	6.0	139.97	-67.20	20.50	3	37.0	2.95	N/A	-63.85	C29r
14TR1	TR	B	β	47.667	-106.426	6.7	173.91	-41.04	30.26	3	17.7	2.89	N/A	-65.37	C29r
2A	TR	C	β	47.667	-106.426	11.1	197.05	-45.40	14.10	1	N/A	N/A	N/A	-65.31	C29r
14TR3	TR	A	α	47.667	-106.426	13.2	147.45	-36.60	56.00	3	6.0	2.66	N/A	-52.14	C29r
2A	TR	C	γ	47.667	-106.426	25.2	224.45	-51.60	10.30	1	N/A	N/A	N/A	-53.23	C29r
14TR5	TR	B	β	47.667	-106.426	27.3	179.64	-53.43	26.44	3	22.8	2.91	N/A	-76.31	C29r
14TR6	TR	A	β	47.667	-106.426	32.1	172.85	-51.00	8.30	4	122	3.98	N/A	-73.12	C29r
14TR7	TR	B	β	47.667	-106.426	37.0	140.95	-31.60	32.00	3	16.0	2.87	N/A	-45.83	C29r

Table 4.1. Paleomagnetic site statistics. Note that names in column 1 ending in -#letter indicate single sample results that represent the best determined sample from C sites. BC: Bug Creek, GH: Garbani Hill, HH: Hell Hollow, HHA: Hell Hollow A, IS: Isaac Ranch, JC: Jack's Channel, LBS: Lerbekmo South, LG: Lofgren (McGuire Creek), MK: McKeever Ranch, MKA: McKeever Ranch A, PL: Pearl Lake, SC: Sandy Chicken, TR: Thomas Ranch. Latitude and Longitude are based in the WGS84 datum. Strat level marks the stratigraphic level as identified in each individual section. Geo dec/inc indicate declination/inclination of characteristic remanent directions in geographic coordinates; R is the resultant vector; k is kappa (precision parameter); α95 is the 95% confidence interval of Fisher mean; VGP lat is the latitude of the virtual geomagnetic pole calculated using the plate reconstruction model of Besse and Courtillot (1990).

Table 4.2. Summary of $^{40}Ar^*/^{39}Ar$ ages

Coal	Sample	Section	Age (Ma)	±σ (Ma)[1]	±σ (Ma)[2]	MSWD	N/N_0
X	LG13-1 (37003)	LG	65.703	0.043	0.059	1.144	77/78
X	LG13-1 (37133)	LG	65.706	0.068	0.080	0.888	45/49
X	**LG13-1***	**LG**	**65.704**	**0.036**	**0.056**		
Y	**PL14-1**	**PL**	**65.709**	**0.037**	**0.056**	**1.547**	**52/52**
Y	**HC13-1**	**HC**	**65.883**	**0.032**	**0.053**	**1.357**	**63/73**
Y	**MK12-1**	**MK**	**65.844**	**0.033**	**0.054**	**0.543**	**83/88**
Y	**HH13-1**	**HH**	**65.774**	**0.034**	**0.055**	**1.321**	**62/70**
Y	**HH13-2**	**HH**	**65.692**	**0.033**	**0.053**	**0.871**	**67/68**
Y	**HH13-3**	**HH**	**65.710**	**0.024**	**0.048**	**1.122**	**70/70**
Y	**JC13-3**	**JC**	**65.740**	**0.042**	**0.059**	**0.862**	**55/56**
Y	**PH13-3**	**PH**	**65.712**	**0.086**	**0.096**	**0.931**	**11/69**
Y	**PH13-1**	**PH**	**65.844**	**0.051**	**0.066**	**0.712**	**37/49**
Y	PH13-2 (37132)	PH	65.537	0.077	0.089	1.076	30/55
Y	PH13-2 (37006)	PH	65.541	0.048	0.064	1.722	73/73
Y	**PH13-2***	**PH**	**65.540**	**0.041**	**0.059**		
HFZ	**MD15-1**	**MD**	**66.099**	**0.076**	**0.088**	**1.075**	**36/41**
Z	**TR13-3**	**TR**	**66.091**	**0.038**	**0.056**	**0.882**	**56/66**
IrZ	MK13-3	MK	66.096	0.038	0.057	0.896	71/79
IrZ	HF-1PR (36825)	HF	66.013	0.032	0.053	1.571	43/49
IrZ	HF-1PR (36836)	HF	66.028	0.033	0.053	1.100	38/39
IrZ	HF-1PR (36847)	HF	66.055	0.036	0.056	1.206	45/53
IrZ	HF14-1 (37004)	HF	66.072	0.028	0.051	1.453	55/59
IrZ	HF14-1 (37012)	HF	66.052	0.046	0.062	1.340	20/20
IrZ	HF15-1 (37108)	HF	66.039	0.073	0.083	1.380	10/10
IrZ	HF15-1 (37118)	HF	66.190	0.113	0.124	1.247	5/5
IrZ	**All***	**MK, HF**	**66.047**	**0.014**	**0.044**		
Null Coal	TR13-2	TR	66.347	0.151	0.159	0.779	54/92

Notes: Coal designations are based on references cited in text. Ages are based on the calibration of Renne et al. (2011). Age uncertainties excluding[1] and including[2] systematic sources are shown. Samples with a * indicate the weighted mean age. N/N_0[3] refers to the the number of analyses (single crystal fusions or incremental heating steps) used for age calculation relative to the number of ages obtained.

Table 4.2. Summary of $^{40}Ar/^{39}Ar$ ages. Note, only ages that were determined to not be reworked are shown. Section name abbreviations are the same as in Figure 1.

Table 4.3. Summary of pooled $^{40}Ar^*/^{39}Ar$ ages

Coal	Samples	Sections	Age (Ma)	±σ (Ma)[3]	±σ (Ma)[4]
Y	HH13-2	HH	65.692	0.033	0.053
Y	HH13-3	HH	65.710	0.024	0.048
Y	**Pooled**		**65.704**	**0.019**	**0.046**
Z (MCZ)	LG11-1	LG[2]	66.022	0.038	0.057
Z	HX12-1	HX[2]	66.002	0.033	0.054
Z (MCZ)	ZL12-2	ZL[2]	65.998	0.044	0.061
Z	HC-2PR	LB[1]	66.019	0.021	0.046
Z	TR13-3	TR	66.091	0.038	0.056
Z	**Pooled**		**66.024**	**0.014**	**0.044**
IrZ	HF15-1 (37108)	HF	66.039	0.073	0.083
IrZ	HF15-1 (37118)	HF	66.190	0.113	0.124
IrZ	HF14-1 (37004)	HF	66.072	0.028	0.051
IrZ	HF14-1 (37012)	HF	66.052	0.046	0.062
IrZ	HF-1PR (36825)	HF	66.013	0.032	0.053
IrZ	HF-1PR (36836)	HF	66.028	0.033	0.053
IrZ	HF-1PR (36847)	HF	66.055	0.036	0.056
IrZ	MK13-3	MK	66.096	0.038	0.057
IrZ	HH12-1	HH[2]	66.061	0.039	0.059
IrZ	NV12-1	NV[2]	66.035	0.033	0.052
IrZ	HF-1PR	HF[1]	66.043	0.011	0.043
IrZ	**Pooled**		**66.047**	**0.008**	**0.043**

Notes: Ages pooled from multiple localities.[1]Denotes data from Renne et al. (2013), [2]denotes data from Sprain et al. (2015). Age uncertainties excluding[3] and including[4] systematic sources are shown.

Table 4.3. Summary of pooled $^{40}Ar/^{39}Ar$ ages. Section name abbreviations are the same as in Figure 1.

Table 4.4. Summary of reversal ages

Reversal	Section	Age (Ma)	±σ (Ma)[1]	±σ (Ma)[2]
C29r/C29n	PH	65.608	0.049	0.058
C29r/C29n	LG	65.745	0.032	0.049
C29r/C29n	PL	65.717	0.042	0.059
C29r/C29n	HH	65.737	0.019	0.036
C29r/C29n	GH	65.701	0.031	0.060
C29r/C29n	JC	65.770	0.039	0.054
C29r/C29n	**Pooled**	**65.726**	**0.013**	**0.044**
C30n/C29r	TR	66.373	0.163	0.172
C30n/C29r	BC	66.307	0.055	0.070
C30n/C29r	**Pooled**	**66.314**	**0.052**	**0.068**

Notes: Reversal ages pooled from multiple localities. Age uncertainties excluding[1] and including[2] systematic sources are shown.

Table 4.4. Summary of reversal ages. Section name abbreviations are the same as in Figure 1.

Chapter 5. Conclusion

In this dissertation, I develop a high-precision global chronologic framework for events around the Cretaceous-Paleogene boundary (KPB) using high-precision $^{40}Ar/^{39}Ar$ geochronology and paleomagnetism in the Hell Creek region of NE Montana focusing on two major areas of study: 1) refining the timing and tempo of terrestrial ecosystem change around the KPB, and 2) calibrating the geomagnetic polarity timescale (GPTS), and particularly the timing and duration of magnetic polarity chron C29r.

In chapter 2, I develop a chronostratigraphic framework for fluvial sediments within the Hell Creek region to help refine the timing and tempo of terrestrial ecological decline before the KPB and recovery after the mass extinction. Dates for 15 tephras are presented, with ± 30 ka precision, which range in time from 300 ka before the KPB to 1 Ma after. By tying these results to the well-defined paleontological framework already developed in the Hell Creek, this work is able to constrain the timing and tempo of terrestrial ecosystem change around the KPB. Application of the new ages to previous magnetostratigraphic data suggests an appreciably compressed duration for chron C29r (which spans the KPB), with a minimum estimate of 345 ± 38 ka compared to the 710 ka estimate from the Geologic Time Scale 2012 (Ogg, 2012). This result signifies potential errors in past placement of chron boundaries within sections in the Hell Creek region, and calls into question the reliability of Hell Creek sediments as paleomagnetic recorders, which has significant implications for the correlation of data from the Hell Creek to KPB sites worldwide.

To investigate the paleomagnetic recording fidelity of Hell Creek sediments, in chapter 3 I complete comprehensive rock magnetic analyses to determine magnetic mineralogy, what minerals are holding remanence, the grain size of magnetic particles, and the likelihood that Hell Creek sediments retain the direction of the magnetic field from the time of their deposition. To aid in rock magnetic characterization, in this chapter a new technique is developed to identify and characterize remanence held by compositionally intermediate titanohematite ($Fe_{2-y}Ti_yO_3$; $0.5 \leq y \leq 0.7$) in detrital sedimentary rocks. Results from rock magnetic analyses show that three main magnetic minerals contribute to the remanence of Hell Creek sediments: goethite, intermediate titanohematite, and magnetite/titanomagnetite ($Fe_{3-y}Ti_yO_4$). Both magnetite/titanomagnetite and intermediate titanohematite are likely to record primary remanence, whereas goethite most likely records a secondary overprint. In the last 66 Ma, cratonic North America has not moved significantly and therefore present field overprints, like those held by goethite, could easily be mistaken for primary late Cretaceous or early Paleogene normal directions. Because past magnetostratigraphic studies performed in the Hell Creek region relied upon demagnetization techniques that cannot sufficiently remove signals held by goethite (alternating field demagnetization), I conclude that the short duration calculated for C29r in chapter 2 is a result of misplaced reversals due to unremoved secondary overprints. This result necessitates new magnetostratigraphy for the Hell Creek region.

In chapter 4, I develop a new magnetostratigraphic framework for the Hell Creek region that, when coupled to new $^{40}Ar/^{39}Ar$ dates, allows for the calibration of the Geomagnetic Polarity Timescale (specifically C29r) at unprecedented precision. To mitigate problems found in past magnetostratigraphic studies, for this work I used both alternating field and thermal demagnetization techniques (in order to remove goethite), and developed a rigorous set of quality criteria, both quantitative and qualitative, to ensure that sites with unremoved secondary overprints were not used in the final interpretation. Presently, the GPTS is used for age control in numerous KPB studies including the timing of volcanism in the Deccan Traps, a majority of

studies based on marine sections, and studies on climate and ecological change across the KPB. By calibrating the GPTS at high-precision, this work allows for the correlation of our Hell Creek record to other KPB sites worldwide, provides high-precision age constraints for sections that lack the means for direct dating, aids correlation between marine and terrestrial KPB sections, and provides a means to compare records of biotic change to records of climatic change. In this chapter, I present results from 14 new magnetostratigraphic sections and 18 new high-precision $^{40}Ar/^{39}Ar$ ages, which together provide six independent constraints on the age of the C29r/C29n reversal and two constraints on the C30n/C29r reversal. Together, these results show that the duration of C29r is ~588 ka, consistent with past results calculated using astrochronology (showing that non-Milankovitch climate signals did significantly bias orbital records; Thibault and Husson, 2016) and U/Pb geochronology (suggesting that the zircons dated were within a few 10 ka of eruptive ages; Clyde et al., 2016). These results further add credence to chronologies already developed for marine sections, which are dominantly based on astronomical tuning. New magnetostratigraphy presented in this chapter further confirms that there were errors in reversal placement in past magnetostratigraphic studies. In this chapter I further provide new geochronologic data for the KPB, yielding the most precise age for the KPB yet of 66.047 ± 0.008/0043 Ma, consistent with the age of the Chicxulub crater (Renne et al., 2013).

The results from this dissertation help to clarify the temporal sequence of events around the KPB. In this dissertation, it is shown that the decline in terrestrial faunas (Wilson, 2014) began ~ 200 ka before the Cretaceous-Paleogene boundary. It is further shown that disaster faunas associated with Puercan 1 North American Land Ages (NALMA) are constrained to at least the first 70 ka of the Paleogene, that recovered faunas appear ~ 925 ka after the KPB, and that Torrejonian NALMA first appear in the Hell Creek ~ 1 Ma after the mass extinction. The period of ~925 ka for the recovery of terrestrial faunas calculated in this dissertation is significantly shorter than the 1–3 Ma period of recovery recorded in the oceans (D'hondt, 1998). This work additionally shows that Puercan 1 faunas are constrained to C29r in the Hell Creek, whereas Puercan 3 NALMA are solely found in C29n, suggesting they appeared at least ~270 ka after the KPB. These results are consistent with results from other North American basins and in general confirm past biochronologic frameworks. However, some inconsistencies, specifically in regard to the timing of Puercan 2, call for revaluation of past magnetostratigraphic frameworks particularly in the San Juan basin and parts of the Williston basin.

Using the chronologic framework developed in this dissertation, it appears that records of pre-KPB ecological stress recorded in the Hell Creek region coincide with Late Maastrichtian climate change and Deccan Traps volcanism, and that periods of protracted recovery additionally overlap with post-KPB Deccan volcanism (however, climate variations, like those observed in the Late Maastrichtian, are not recorded in the first 1 Ma of the Paleogene). New volume and geochronologic estimates from the Deccan Traps suggest that ~70% of the known volume (with an unknown component offshore) of Deccan lava erupted after the KPB (Richards et al., 2015; Renne et al., 2015). This result raises the question of whether observed trends between pre-KPB climate variations and Deccan volcanism are actually causally linked, and why larger climatic variations are not seen post-KPB during the eruption of the largest volume of Deccan lava. It further raises questions about how well we know the volume of the Deccan Traps, what amount and specific species of gas were emitted from the Deccan Traps and at what tempo, and overall what was the capacity of the Deccan Traps to affect global climate.

It is additionally important to note that KPB terrestrial sections are dominantly limited to central North America. This raises the question of whether records of terrestrial ecological

change around the KPB from North America (like the records presented here from the Hell Creek) are representative of a global signal or if they are biased by local environmental perturbations. This is especially important considering that the North American Western Interior Seaway was undergoing a major period of regression in the Late Maastrichtian. If we assume that the terrestrial records observed in North America are representative of global terrestrial environments, then questions regarding disparities between terrestrial and marine records, like why we don't see records of ecological stress in the marine realm before the KPB, still remain.

In conclusion, while many have claimed to know the cause of the KPB mass extinction during the last four decades of research, this topic is anything but closed. However, with ongoing research we are moving closer to understanding this remarkable event.

References

Alroy, J., 1999, Putting North America's End-Pleistocene Megafaunal Extinction in Context, in MacPhee, R.D.E. ed., Extinctions in Near Time, Springer US, Advances in Vertebrate Paleobiology 2, p. 105–143, doi: 10.1007/978-1-4757-5202-1_6.

Alvarez, L.W., Alvarez, W., Asaro, F., and Michel, H.V., 1980, Extraterrestrial cause for the Cretaceous–Tertiary extinction: Science, v. 208, p. 1095–1108.

Alvarez, L.W., 1983, Experimental evidence that an asteroid impact led to the extinction of many species 65 million years ago: National Academy of Sciences Proceedings, v. 80, p. 627–642.

Archibald, J.D., 1982, A study of Mammalia and geology across the Cretaceous-Tertiary boundary in Garfield County, Montana: University of California Publications in Geological Sciences, v. 122, 286 p.

Archibald, J.D., Butler, R.F., Lindsay, E.H., Clemens, W.A., and Dingus, L., 1982, Upper Cretaceous–Paleocene biostratigraphy and magnetostratigraphy, Hell Creek and Tullock Formations, northeastern Montana: Geology, v. 10, p. 153–159.

Archibald, J.D., Clemens, W.A., Padian, K., Rowe, T., Macleod, N., Barrett, P.M., Gale, A., Holroyd, P., Sues, H.-D., Arens, N.C., Horner, J.R., Wilson, G.P., Goodwin, M.B., Brochu, C.A., et al., 2010, Cretaceous Extinctions: Multiple Causes: Science, v. 328, p. 973–973, doi: 10.1126/science.328.5981.973-a.

Archibald, J.D., 2014, What the dinosaur record says about extinction scenarios: Geological Society of America Special Papers, v. 505, p. 213–224, doi: 10.1130/2014.2505(10).

Arens, N.C. and Jahren, A.H., 2000, Carbon isotopic excursion in atmospheric CO_2 at the Cretaceous-Tertiary boundary: Evidence from terrestrial sediments: Palaios, v. 15, p. 314–322, doi:10.1669/0883-1351(2000)015,0314:CIEIAC>2.0.CO;2

Arens, N.C., and Jahren, A.H., 2002, Chemostratigraphic correlation of four fossil-bearing sections in southwestern North Dakota, *in* Hartman, J.H., Johnson, K.R., and Nichols, D.J., eds., The Hell Creek Formation and the Cretaceous-Tertiary Boundary in the Northern Great Plains: An Integrated Continental Record of the End of the Cretaceous: Geological Society of America, Boulder, v. 361, p. 75–93.

Arens, N.C., and West, I.D., 2008, Press/pulse: A general theory of mass extinction?: Paleobiology, v. 34, p. 456–471, doi:10.1666/07034.1.

Arens, N.C., Thompson, A., and Jahren, A.H., 2014, A preliminary test of the press-pulse extinction hypothesis: Palynological indicators of vegetation change preceding the Cretaceous-Paleogene boundary, McCone County, Montana, USA, *in* Wilson, G.P., Clemens, W.A., Horner, J.R., and Hartman, J.H., eds., Through the End of the Cretaceous in the Type Locality of the Hell Creek Formation in Montana and Adjacent Areas: Geological Society of America Special Paper 503, p. 209–227.

Artemieva, N., and Morgan, J., 2009, Modeling the formation of the K–Pg boundary layer: Icarus, v. 201, p. 768–780, doi: 10.1016/j.icarus.2009.01.021.

Baadsgaard, H., and Lerbekmo, J.F. 1980. A Rb/Sr age for the Cretaceous - Tertiary boundary (Z coal), Hell Creek, Montana: Canadian Journal of Earth Sciences, v. 17, p. 671–673.

Baadsgaard, H., and Lerbekmo, J.F. 1983. Rb -Sr and U -Pb dating of bentonites. Canadian Journal of Earth Sciences, v. 20, p. 1282–1290.

Baadsgaard, H., Lerbekmo, J.F., and McDougall, I., 1988, A radiometric age for the Cretaceous-Tertiary boundary based on K-Ar, Rb-Sr, and U-Pb ages of bentonites from Alberta,

Saskatchewan and Montana: Canadian Journal of Earth Sciences, v. 25, p. 1088–1097.
Barrett, P.M., Benson, R.B.J., Rich, T.H., and Vickers-Rich, P., 2011, First spinosaurid dinosaur from Australia and the cosmopolitanism of Cretaceous dinosaur faunas: Biology Letters, v. 7, p. 933–936, doi: 10.1098/rsbl.2011.0466.
Bercovici, A., Pearson, D.A., Nichols, D.J., and Wood, J., 2009, Biostratigraphy of selected K/T boundary sections in southwestern North Dakota, USA: Toward a refinement of palynological identification criteria: Cretaceous Research, v. 30, p. 632–658, doi:10.1016/j.cretres.2008.12.007.6
Besse, J., and Courtillot, V., 2002, Apparent and true polar wander and the geometry of the geomagnetic field over the last 200 Myr: Journal of Geophysical Research: Solid Earth, v. 107, p. 2300, doi: 10.1029/2000JB000050.
Bilardello, D. and Jackson, M., 2013, What do the Mumpsies do?, IRM Quarterly, v. 23(3), no. 1, p. 11–15.
Bina, M., Tanguy, J.C., Hoffmann, Prévot, V. M., Listanco, E.L., Keller, R., Fehr, K. Th, Goguitchaichvili, A.T. and Punongbayan, R.S., 1999, A detailed magnetic and mineralogical study of self-reversed dacitic pumices from the 1991 Pinatubo eruption (Philippines): Geophysical Journal International, v. 138, p. 159–178
Bohor, B.F., 1990, Shocked quartz and more; Impact signatures in Cretaceous/Tertiary boundary clays: Geological Society of America Special Papers, v. 247, p. 335–342, doi: 10.1130/SPE247-p335.
Bown, P., 2005, Selective calcareous nannoplankton survivorship at the Cretaceous-Tertiary boundary: Geology, v. 33, p. 653–656, doi: 10.1130/G21566AR.1.
Boyd, D.W., and Lillegraven, J.A., 2011, Persistence of the Western Interior Seaway Historical background and significance of ichnogenus Rhizocorallium in Paleocene strata, south-central Wyoming: Rocky Mountain Geology, v. 46, p. 43–69, doi: 10.2113/gsrocky.46.1.43.
Brown, R.W., 1952, Tertiary strata in eastern Montana and western North and South Dakota, in Sonnenberg, F.P., ed., Billings Geological Society guidebook, Third Annual Field Conference Billings, Montana: Billings Geological Society, p. 89–92.
Burton, B.P., Robinson, P., McEnroe, S.A., Fabian, K., and Ballaran, T.B., 2008, A low-temperature phase diagram for ilmenite-rich compositions in the system Fe2O3-FeTiO3: American Mineralogist, v. 93(8-9), p. 1260–1272.
Butler, R., 1982, Magnetic Mineralogy of Continental Deposits, San Juan Basin, New Mexico, and Clark's Fork Basin, Wyoming: Journal of Geophysical Research, v. 87(B9), p. 7843–7852, doi: 10.1029/JB087iB09p07843.
Butler, R.F., Gingerich, P.D., and Lindsay, E.H., 1981, Magnetic Polarity Stratigraphy and Biostratigraphy of Paleocene and Lower Eocene Continental Deposits, Clark's Fork Basin, Wyoming: The Journal of Geology, v. 89, p. 299–316.
Butler, R.F., and Lindsay, E.H., 1985, Mineralogy of Magnetic Minerals and Revised Magnetic Polarity Stratigraphy of Continental Sediments, San Juan Basin, New Mexico: The Journal of Geology, v. 93, p. 535–554.
Butler, R.F., Krause, D.W., and Gingerich, P.D., 1987, Magnetic Polarity Stratigraphy and Biostratigraphy of Middle-Late Paleocene Continental Deposits of South-Central Montana: The Journal of Geology, v. 95, p. 647–657.
Calvert, W.R., 1912, Geology of certain lignite fields in eastern Montana: U.S. Geological Survey Bulletin 471, p. 187–201.

Calvert, W.R., Bowen, C.F., Herald, F.A., Hance, J.H., Stebinger, E., and Beekly, A.L., 1912, Geology of certain lignite fields in eastern Montana: US Government Printing Office.
Cande, S.C., and Kent, D.V., 1995, Revised calibration of the geomagnetic polarity timescale for the Late Cretaceous and Cenozoic: Journal of Geophysical Research: Solid Earth, v. 100, p. 6093–6095, doi: 10.1029/94JB03098.
Chenet, A.L., Quidelleur, X., Fluteau, F., Courtillot, V., and Bajpai, S., 2007, K-40-Ar-40 dating of the Main Deccan large igneous province: Further evidence of KTB age and short duration: Earth and Planetary Science Letters, v. 263, p. 1–15, doi: 10.1016/j.epsl.2007.07.011.
Chenet, A.L., Fluteau, F., Courtillot, V., Gerard, M., and Subbarao, K.V., 2008, Determination of rapid Deccan eruptions across the Cretaceous-Tertiary boundary using paleomagnetic secular variation: Results from a 1200-m-thick section in the Mahabaleshwar escarpment: Journal of Geophysical Research-Solid Earth, v. 113, doi: 10.1029/2006jb004635.
Chenet, A.L., Courtillot, V., Fluteau, F., Gerard, M., Quidelleur, X., Khadri, S.F.R., Subbarao, K.V., and Thordarson, T., 2009, Determination of rapid Deccan eruptions across the Cretaceous-Tertiary boundary using paleomagnetic secular variation: 2. Constraints from analysis of eight new sections and synthesis for a 3500-m-thick composite section: Journal of Geophysical Research-Solid Earth, v. 114, doi: 10.1029/2008jb005644.
Cherven, V.B., and Jacob, A.R., 1985, Evolution of Paleogene depositional systems, Williston Basin, in response to global sea level changes, *in* Flores, M.R., and Kaplan, S.S., eds., Cenozoic paleogeography of the west-central United States: Society of Economic Paleontologists and Mineralogists, Rocky Mountain Section, p. 127–170.
Church, N., Feinberg J., and Harrison, R., 2011, Low-temperature domain wall pinning in titanomagnetite: Quantitative modeling of multidomain first-order reversal curve diagrams and AC susceptibility: Geochem. Geophys. Geosyst., v.12, Q07Z27, DOI: 10.1029/2011GC003538.
Chin, K., Pearson, D, and Ekdale, A.A., 2013, Fossil Worm Burrows Reveal Very Early Terrestrial Animal Activity and Shed Light on Trophic Resources after the End-Cretaceous Mass Extinction: PLOS ONE, v. 8, e70920.
Clemens, W.A., 2002, Evolution of the mammalian fauna across the Cretaceous-Tertiary boundary in northeastern Montana and other areas of the Western Interior, *in* Hartman, J.H., Johnson, K.R., and Nichols, D.J., eds., The Hell Creek Formation and the Cretaceous-Tertiary Boundary in the Northern Great Plains: An Integrated Continental Record of the End of the Cretaceous: Geological Society of America, Boulder, v. 361, p. 217–245.
Clemens, W.A., 2010, Were immigrants a significant part of the earliest Paleocene mammalian fauna of the North American Western Interior?: Vertebrata PalAsiatica, v. 48, p. 285–307.
Clemens, W.A., 2011, *Eoconodon* ("Triisodontidae," Mammalia) from the early Paleocene (Puercan) of northeastern Montana, U.S.A.: Palaeontologica Electronica, v. 14: 22A, 22p; palaeo-electronica.org/2011_3/3clemens/index.html.
Clemens, W.A., 2013, Cf. Wortmania from the Early Paleocene of Montana and an evaluation of the fossil record of the initial diversification of the Taeniodonta (Mammalia): Canadian Journal of Earth Sciences, v. 50, p. 341-354.
Clemens, W.A., and Wilson, G.P., 2009, Early Torrejonian local faunas from northeastern Montana, U.S.A.: Museum of Northern Arizona Bulletin, v. 65, p. 111–157.

Clemens, W.A., and Hartman, J.H., 2014, From Tyrannosaurus rex to asteroid impact: Early studies (1901–1980) of the Hell Creek Formation in its type area, *in* Wilson, G.P., Clemens, W.A., Horner, J.R., and Hartman, J.H., eds., Through the End of the Cretaceous in the Type Locality of the Hell Creek Formation in Montana and Adjacent Areas: Geological Society of America Special Paper 503, p. 1–87.

Clyde, W.C., Ramezani, J., Johnson, K.R., Bowring, S.A., and Jones, M.M., 2016, Direct high-precision U–Pb geochronology of the end-Cretaceous extinction and calibration of Paleocene astronomical timescales: Earth and Planetary Science Letters, v. 452, p. 272–280, doi: 10.1016/j.epsl.2016.07.041.

Collier, A.J., and Knechtel, M., 1939, The coal resources of McCone County, Montana: U.S. Geological Survey Bulletin 905, 80 p.

Courtillot, V., Besse, J., Vandamme, D., Jaeger, J.J., and Montigny, R., 1986, Deccan Trap volcanism as a cause of biologic extinctions at the Cretaceous-Tertiary boundary: Comptes Rendus De L Academie Des Sciences Serie Ii, v. 303, p. 863-.

Courtillot, V., Vandamme, D., Besse, J., and Jaeger, J.J., 1988, Deccan Volcanism at the Cretaceous-Tertiary Boundary: Chemical Geology, v. 70, p. 118–118.

Courtillot, V., and Fluteau, F., 2010, Cretaceous Extinctions: The Volcanic Hypothesis: Science, v. 328, p. 973–974, doi: 10.1126/science.328.5981.973-b.

Cox, A., Doell, R.R., and Dalrymple, G.B., 1963, Geomagnetic polarity epochs and Pleistocene geochronometry: Nature, v. 198, p. 1049–1051, doi:10.1038/1981049a0.

D'Hondt, S., Donaghay, P., Zachos, J.C., Luttenberg, D., and Lindinger, M., 1998, Organic Carbon Fluxes and Ecological Recovery from the Cretaceous-Tertiary Mass Extinction: Science, v. 282, p. 276–279, doi: 10.1126/science.282.5387.276.

D'Hondt, S., 2005, Consequences of the Cretaceous/Paleogene mass extinction for marine ecosystems: Annual Review of Ecology, Evolution, and Systematics, v. 36, p. 295–317.

Day, R., Fuller, M., and Schmidt, V.A., 1977, Hysteresis properties of titanomagnetites: Grain-size and compositional dependence: Physics of the Earth and Planetary Interiors, v. 13, p. 260–267.

Dekkers, M. J., 1989, Magnetic properties of natural goethite—II. TRM behaviour during thermal and alternating field demagnetization and low-temperature treatment: Geophysical Journal, v. 97, p. 341–355.

Diehl, J.F., 1991, The Elkhorn Mountains revisited: New data for the Late Cretaceous paleomagnetic field of North America: Journal of Geophysical Research: Solid Earth, v. 96, p. 9887–9894, doi: 10.1029/91JB00959.

Dinarès-Turell, J., Baceta, J.I., Pujalte, V., Orue-Etxebarria, X., Bernaola, G., and Lorito, S., 2003, Untangling the Palaeocene climatic rhythm: an astronomically calibrated Early Palaeocene magnetostratigraphy and biostratigraphy at Zumaia (Basque basin, northern Spain): Earth and Planetary Science Letters, v. 216, p. 483–500, doi: 10.1016/S0012-821X(03)00557-0.

Dinarès-Turell, J., Baceta, J.I., Bernaola, G., Orue-Etxebarria, X., and Pujalte, V., 2007, Closing the Mid-Palaeocene gap: Toward a complete astronomically tuned Palaeocene Epoch and Selandian and Thanetian GSSPs at Zumaia (Basque Basin, W Pyrenees): Earth and Planetary Science Letters, v. 262, p. 450–467, doi: 10.1016/j.epsl.2007.08.008.

Duncan, R.A., and Pyle, D.G., 1988, Rapid eruption of the Deccan flood basalts at the Cretaceous/Tertiary boundary: Nature, v. 333, p. 841–843.

Dunlop, D.J., 2002, Theory and application of the Day plot (Mrs/Ms versus Hcr/Hc) 1.

Theoretical curves and tests using titanomagnetite data: Journal of Geophysical Research: Solid Earth, v. 107(B3), p. 1–22, doi: 10.1029/2001JB000486.
Dunlop, D.J., and Özdemir, Ö., 1997, Rock Magnetism: Fundamentals and Frontiers, pp. 573, Cambridge University Press, Cambridge.
Eberle, J.J., 2003, Puercan mammalian systematics and biostratigraphy in the Denver Formation, Denver Basin, Colorado: Rocky Mountain Geology, v. 38, p. 143–169, doi: 10.2113/gsrocky.38.1.143.
Egli, R., 2013, VARIFORC: An optimized protocol for calculating non-regular first-order reversal curve (FORC) diagrams: Global and Planetary Change, v. 110, p. 302–320.
Ernst, R.E., and Youbi, N. How Large Igneous Provinces affect global climate, sometimes cause mass extinctions, and represent natural markers in the geological record: Palaeogeography, Palaeoclimatology, Palaeoecology, doi: 10.1016/j.palaeo.2017.03.014.
Fabian, K., Miyajima, N., Robinson, P., McEnroe, S.A., Ballaran, T.B., and Burton, B.P., 2011, Chemical and magnetic properties of rapidly cooled metastable ferri-ilmenite solid solutions: implications for magnetic self-reversal and exchange bias—I. Fe-Ti order transition in quenched synthetic ilmenite 61: Geophysical Journal International, v. 186, p. 997–1014, doi: 10.1111/j.1365-246X.2011.05109.x.
Fabian, K., Shcherbakov, V.P. and McEnroe, S.A., 2013, Measuring the Curie temperature: Geochem., Geophys., Geosyst., v. 14(4), p. 947–961, doi: 10.1029/2012gc004440.
Fastovsky, D.E., 1987, Paleoenvironments of vertebrate-bearing strata during the Cretaceous–Paleogene transition, eastern Montana and western North Dakota: Palaios, v. 2, p. 282–295, doi: 10 .2307 /3514678.
Fastovsky, D.E., and Dott, R. H. Jr., 1986, Sedimentology, stratigraphy, and extinctions during the Cretaceous-Paleogene transition at Bug Creek, Montana: Geology, v. 14, p. 279–282.
Fastovsky, D.E., and Sheehan, P.M., 2005, The extinction of the dinosaurs in North America: GSA Today, v. 15, p. 4–10.
Fastovsky, D.E., and Bercovici, A., 2016, The Hell Creek Formation and its contribution to the Cretaceous–Paleogene extinction: A short primer: Cretaceous Research, v. 57, p. 368–390, doi: 10.1016/j.cretres.2015.07.007.
Folinsbee, R.E., Baadsgaard, H., and Cumming, G.L. 1963. Dating of volcanic ash beds (bentonites) by the K-Ar method: Nuclear Geophysics, v. 1075, p. 70–82.
Force, E.R., 2000, Titanium-mineral resources of the western U.S.-an update: U.S. Geological Survey Open-file Report OF 00-442.
Force, E.R., Butler, R.F., Reynolds, R.L., and Houston, R.S., 2001, Magnetic Ilmenite-Hematite Detritus in Mesozoic-Tertiary Placer and Sandstone-Hosted Uranium Deposits of the Rocky Mountains: Economic Geology, v. 96, p. 1445–1453, doi: 10.2113/gsecongeo.96.6.1445.
Fox, R.C., 2011, An Unusual Early Primate from the Paleocene Paskapoo Formation, Alberta, Canada: Acta Palaeontologica Polonica, v. 56, p. 1–10, doi: 10.4202/app.2009.0079.
Fox, R.C., 1989, The Wounded Knee local fauna and mammalian evolution near the Cretaceous-Tertiary boundary, Saskatchewan, Canada: Palaeontographica Abteilung A, p. 11–59.
Fox, R.C., and Scott, C.S., 2011, A New, Early Puercan (Earliest Paleocene) Species of Purgatorius (Plesiadapiformes, Primates) from Saskatchewan, Canada: Journal of Paleontology, v. 85, p. 537–548, doi: 10.1666/10-059.1.
France, D.E. and Oldfield, F., 2000, Identifying goethite and hematite from rock magnetic measurements of soils and sediments: Journal of Geophysical Research, v. 105(B2), p.

2781–2795.
Gill, J.R., and Cobban, W.A., 1973, Stratigraphy and geologic history of the Montana Group and equivalent rocks, Montana, Wyoming, and North and South Dakota: U.S. Geological Survey Professional Paper 776, 36 p.
Goguitchaichvili, A., and Prévot, M., 2000, Magnetism of oriented single crystals of hemolilmenite with self-reversed thermoremanent magnetization: Journal of Geophysical Research, v. 105(B2), p. 2761–2780.
Goldin, T.J., and Melosh, H.J., 2009, Self-shielding of thermal radiation by Chicxulub impact ejecta: Firestorm or fizzle? Geology, v. 37, p. 1135–1138, doi: 10.1130/G30433A.1.
Haag, M., Heller, F., Carracedo, J.C., and Soler, V., 1990a, Remanent magnetization of andesitic and dacitic pumice from the 1985 eruption of Nevado del Ruiz (Colombia) reversed due to self-reversal: Journal of Volcanology and Geothermal Research, v. 41, p. 369–377, doi: 10.1016/0377-0273(90)90097-Y.
Haag, M., Heller, F., Allenspach, R., and Roch, K., 1990b, Self-reversal of natural remanent magnetization n andesitic pumic: Physics of the Earth and Planetary Interiors, v. 65(1), p. 104–108.
Haag, M., Heller, F., Lutz, M., and Reusser, E., 1993, Domain observations of the magnetic phases in volcanics with self-reversed magnetization: Geophysical research letters, v. 20, p. 675–678.
Halliday, T.J.D., and Goswami, A., 2016, Eutherian morphological disparity across the end-Cretaceous mass extinction: Biological Journal of the Linnean Society, v. 118, p. 152–168, doi: 10.1111/bij.12731.
Harrison, R.J., and Feinberg, J.M., 2008, FORCinel: An improved algorithm for calculating first-order reversal curve distributions using locally weighted regression smoothing: Geochem., Geophys., Geosyst., v. 9, Q05016, doi: 10.1029/2008GC001987.
Hartman, J.H., 2002, Hell Creek Formation and the early picking of the Cretaceous-Tertiary boundary in the Williston Basin, *in* Hartman, J.H., Johnson, K.R., and Nichols, D.J., eds., The Hell Creek Formation and the Cretaceous-Tertiary Boundary in the Northern Great Plains: An Integrated Continental Record of the End of the Cretaceous: Geological Society of America, Boulder, v. 361, p. 1–7.
Hartman, J.H., Johnson, K.R., and Nichols, D.J., eds., 2002, The Hell Creek Formation and the Cretaceous-Tertiary boundary in the northern Great Plains: An integrated continental record of the end of the Cretaceous: Boulder, Colorado, Geological Society of America Special Paper 361
Hartman, J.H., Butler, R.D., Weiler, M.W., and Schumaker, K.K., 2014, Context, naming, and formal designation of the Cretaceous Hell Creek Formation lectostratotype, Garfield County, Montana, *in* Wilson, G.P., Clemens, W.A., Horner, J.R., and Hartman, J.H., eds., Through the End of the Cretaceous in the Type Locality of the Hell Creek Formation in Montana and Adjacent Areas: Geological Society of America Special Paper 503, p. 89–121.
Harvey, M.C., Brassell, S.C., Belcher, C.M., and Montanari, A., 2008, Combustion of fossil organic matter at the Cretaceous-Paleogene (K-P) boundary: Geology, v. 36, p. 355–358, doi: 10.1130/G24646A.1.
Heller, F., Carracedo, J.C., and Solert, V., 1986, Reversed magnetization in pyroclastics from the 1985 eruption of Nevado del Ruiz, Colombia: Nature, v. 324, p. 241–242, doi: 10.1038/324241a0.

Hicks, J.F., Johnson, K.R., Obradovich, J.D., Tauxe, L., and Clark, D., 2002, Magnetostratigraphy and geochronology of the Hell Creek and basal Fort Union Formations of southwestern North Dakota and a recalibration of the age of the Cretaceous-Tertiary boundary: Geological Society of America Special Papers, v. 361, p. 35–55, doi: 10.1130/0-8137-2361-2.35.
Hicks, J.F., Johnson, K.R., Obradovich, J.D., Miggins, D.P., and Tauxe, L., 2003, Magnetostratigraphy of Upper Cretaceous (Maastrichtian) to lower Eocene strata of the Denver Basin, Colorado: Rocky Mountain Geology, v. 38, p. 1–27, doi: 10.2113/gsrocky.38.1.1.
Hildebrand, A.R., and Boynton, W.V., 1990, Proximal Cretaceous-Tertiary boundary impact deposits in the Caribbean: Science, v. 248, p. 843–847, doi: 10.1126/science.248.4957.843.
Hoffman, K.A., 1975, Cation Diffusion Processes and Self-reversal of Thermoremanent Magnetization in the Ilmenite-Haematite Solid Solution Series: Geophysical Journal International, v. 41, p. 65–80, doi: 10.1111/j.1365-246X.1975.tb05485.x.
Hoffman, K., 1992, Self-reversal of thermoremanent magnetization in the ilmenite-hematite system- Order-disorder, symmetry, and spin alignment: Journal of Geophysical Research, v. 97, p. 10,833–10,895.
Hoffmann, V., and Fehr, K.T., 1996, Micromagnetic, rock magnetic and mineralogical studies on Dacitic Pumice from the Pinatubo Eruption (1991, Phillipines) Showing self-reversed TRM: Geophysical Research Letters, v. 23, p. 2835–2838, doi: 10.1029/96GL01317.
Horner, J.R., Goodwin, M.B., and Myhrvold, N., 2011, Dinosaur Census Reveals Abundant Tyrannosaurus and Rare Ontogenetic Stages in the Upper Cretaceous Hell Creek Formation (Maastrichtian), Montana, USA: PLOS ONE, v. 6, p. e16574, doi: 10.1371/journal.pone.0016574.
Houston, R.S., and Murphy, J.F., 1962, Titaniferous black sandstone deposits of Wyoming: Geological Society of Wyoming Bulletin, v. 49, p. 120.
Houston, R.S., and Murphy, J.F., 1965, Age and distribution of sedimentary zircon as a guide to provenance: U.S. Geological Survey Professional Paper, 525D, p. 22–25.
Huggett, A.J., 2005, The concept and utility of "ecological thresholds" in biodiversity conservation: Biological Conservation, v. 124, p. 301–310, doi: 10.1016/j.biocon.2005.01.037.
Hunter, J.P., 1999, Evolution at all scales in the vertebrate fossil record, Evolution: investigating the evidence, p. 203.
Hunter, J.P., Hartman, J.H., and Krause, D.W., 1997, Mammals and mollusks across the Cretaceous-Tertiary boundary from Makoshika State Park and vicinity (Williston Basin), Montana: Rocky Mountain Geology, v. 32, p. 61–114.
Hunter, J.P., and Archibald, J.D., 2002, Mammals from the end of the age of dinosaurs in North Dakota and southeastern Montana, with a reappraisal of geographic differentiation among Lancian mammals: Geological Society of America Special Papers, v. 361, p. 191–216, doi: 10.1130/0-8137-2361-2.191.
Husson, D., Galbrun, B., Laskar, J., Hinnov, L.A., Thibault, N., Gardin, S., and Locklair, R.E., 2011, Astronomical calibration of the Maastrichtian (Late Cretaceous): Earth and Planetary Science Letters, v. 305, p. 328–340.
Ickert, R.B., Mulcahy, S.R., Sprain, C.J., Banaszak, J.F., and Renne, P.R., 2015, Chemical and Pb isotope composition of phenocrysts from bentonites constrains the chronostratigraphy

around the Cretaceous-Paleogene boundary in the Hell Creek region, Montana: Geochemistry, Geophysics, Geosystems, v. 16, p. 2743–2761, doi: 10.1002/2015GC005898.
Ishikawa, Y., 1962, Magnetic Properties of Ilmenite-Hematite System at Low Temperature: Journal of the Physical Society of Japan, v. 17, p. 1835–1843, doi: 10.1143/JPSJ.17.1835.
Ishikawa, Y., and Akimoto, S., 1957, Magnetic Properties of the FeTiO3-Fe2O3 Solid Solution Series: Journal of the Physical Society of Japan, v. 12, p. 1083–1098, doi: 10.1143/JPSJ.12.1083.
Ishikawa, Y., and Syono, Y., 1962, Reverse thermo-remanent magnetism in $FeTiO_3$-Fe_2O_3 System: Journal of the Physical Society of Japan, v. 17, p. 714.
Ishikawa, Y., and Syono, Y., 1963, Order-disorder transformation and reverse thermo-remanent magnetism in the FeTiO3Fe2O3 system: Journal of Physics and Chemistry of Solids, v. 24, p. 517–528.
Ivanov, B.A., 2005, Numerical Modeling of the Largest Terrestrial Meteorite Craters: Solar System Research, v. 39, p. 381–409, doi: 10.1007/s11208-005-0051-0.
Johnson, K.R., 1992, Leaf-fossil evidence for extensive floral extinction at the Cretaceous-Tertiary boundary, North Dakota, USA: Cretaceous Research, v. 13, p. 91–117.
Johnston, P.A., and Fox, R.C., 1984, Paleocene and late Cretaceous mammals from Saskatchewan, Canada: Palaeontographica Abteilung A, p. 163–222.
Keller, G., 2008, Cretaceous climate, volcanism, impacts, and biotic effects: Cretaceous Research, v. 29, p. 754–771.
Keller, G., Adatte, T., Gardin, S., Bartolini, A., and Bajpai, S., 2008, Main Deccan volcanism phase ends near the K–T boundary: Evidence from the Krishna–Godavari Basin, SE India: Earth and Planetary Science Letters, v. 268, p. 293–311, doi: 10.1016/j.epsl.2008.01.015.
Keller, G., Adatte, T., Pardo, A., Bajpai, S., Khosla, A., and Samant, B., 2010, Cretaceous Extinctions: Evidence Overlooked: Science, v. 328, p. 974-975, author reply p. 975, doi: 10.1126/science.328.5981.974-a.
Keller, G., Punekar, J., and Mateo, P., 2016, Upheavals during the Late Maastrichtian: Volcanism, climate and faunal events preceding the end-Cretaceous mass extinction: Palaeogeography, Palaeoclimatology, Palaeoecology, v. 441, Part 1, p. 137–151, doi: 10.1016/j.palaeo.2015.06.034.
Kennedy, L.P., 1981, Self Reversed Thermoremanent Magnetization in a Late Brunhes Dacite Pumice: Journal of geomagnetism and geoelectricity, v. 33, p. 429–448, doi: 10.5636/jgg.33.429.
Kennedy, L.P., and Osborne, M.D., 1987, Composite titanomagnetite-ferrian ilmenite grains and correlative magnetic components in a dacite with self-reversed TRM: Earth and Planetary Science Letters, v. 84, p. 479–486, doi: 10.1016/0012-821X(87)90012-4.
Kidwell, S.M., and Holland, S.M., 2002, The Quality of the Fossil Record: Implications for Evolutionary Analyses: Annual Review of Ecology and Systematics, v. 33, p. 561–588, doi: 10.1146/annurev.ecolsys.33.030602.152151.
Kirschvink, J.L., 1980, The least-squares line and plane and the analysis of palaeomagnetic data: Geophysical Journal International, v. 62, p. 699–718, doi: 10.1111/j.1365-246X.1980.tb02601.x.
Krasa, D., Shcherbakov, V.P., Kunzmann, T., and Petersen, N., 2005, Self-reversal of remanent magnetization in basalts due to partially oxidized titanomagnetites: Geophysical Journal

International, v. 162(1), p. 115–136.
Kring, D.A., 2007, The Chicxulub impact event and its environmental consequences at the Cretaceous–Tertiary boundary: Palaeogeography, Palaeoclimatology, Palaeoecology, v. 255, p. 4–21, doi: 10.1016/j.palaeo.2007.02.037.
Kucera, M., and Malmgren, B.A., 1998, Terminal Cretaceous warming event in the mid-latitude South Atlantic Ocean: evidence from poleward migration of Contusotruncana contusa (planktonic foraminifera) morphotypes: Palaeogeography, Palaeoclimatology, Palaeoecology, v. 138, p. 1–15, doi: 10.1016/S0031-0182(97)00124-7.
Kuiper, K.F., Deino, A., Hilgen, F.J., Krijgsman, W., Renne, P.R., and Wijbrans, J.R., 2008, Synchronizing Rock Clocks of Earth History: Science, v. 320, p. 500–504.
Lagroix, F., Banerjee, S.K., and Moskowitz, B.M., 2004, Revisiting the mechanism of reversed thermoremanent magnetization (rTRM) based on observations from synthetic titanohematite (y = 0.7): Journal of Geophysical Research B: Solid Earth, v. 109, B12108, doi:10.1029/B01104.
Laskar, J., Robutel, P., Joutel, F., Gastineau, M., Correia, A.C.M., and Levrard, B., 2004, A long-term numerical solution for the insolation quantities of the Earth: Astronomy & Astrophysics, v. 428, p. 261–285, doi: 10.1051/0004-6361:20041335.
Lawson, C.A., Nord Jr., G.L., and Champion, D.E., 1987, Fe-Ti oxide mineralogy and the origin of normal and reverse remanent magnetization in dacitic pumice blocks from Mt. Shasta, California: Physics of the Earth and Planetary Interiors, v. 46, p. 270–288, doi: 10.1016/0031-9201(87)90190-7.
LeCain, R., Clyde, W.C., Wilson, G.P., and Riedel, J., 2014, Magnetostratigraphy of the Hell Creek and Lower Fort Union Formations in northeastern Montana, *in* Wilson, G.P., Clemens, W.A., Horner, J.R., and Hartman, J.H., eds., Through the End of the Cretaceous in the Type Locality of the Hell Creek Formation in Montana and Adjacent Areas: Geological Society of America Special Paper 503, p. 137–147, doi: 10.1130/2014.2503(04).
Lerbekmo, J.F., 1999, Magnetostratigraphy of the Canadian Continental Drilling Program Cretaceous-Tertiary (K-T) Boundary Project core holes, western Canada: Canadian Journal of Earth Sciences, v. 36, p. 705–715, doi: 10.1139/e98-066.
Lerbekmo, J.F., 2009, Glacioeustatic sea level fall marking the base of supercycle TA-1 at 66.5 Ma recorded by the kaolinization of the Whitemud Formation and the Colgate Member of the Fox Hills Formation: Marine and Petroleum Geology, v. 26, p. 1299–1303, doi: 10.1016/j.marpetgeo.2008.08.001.
Lerbekmo, J.F., 2014, Chicxulub-Shiva extraterrestrial one-two killer punches to Earth 65 million years ago: Marine and Petroleum Geology, v. 49, p. 203–207.
Lerbekmo, J.F., and Coulter, K.C., 1984, Magnetostratigraphic and Biostratigraphic Correlations of Late Cretaceous to Early Paleocene Strata Between Alberta and North Dakota, in The Mesozoic of middle North America, edited by D.F. Stott and D.J. Glass, Canadian Society of Petroleum Geologists, Memoir 9, pp. 313–317.
Lerbekmo, J.F., and Coulter, K.C., 1985, Magnetostratigraphic and Lithostratigraphic Correlation of Coal Seams and Contiguous Strata, Upper Horseshoe Canyon and Scollard Formations (Maastrichtian to Paleocene), Red Deer Valley, Alberta: Bulletin of Canadian Petroleum Geology, v. 33, p. 295–305.
Lerbekmo, J.F., Sweet, A.R., Duke, M.J.M., 1996, A normal polarity subchron that embraces the K/T boundary: a measure of sedimentary continuity across the boundary and synchoneity

of boundary events: Geological Society of America Special Paper 307, p. 465–476.
Lewis, K.W., Keeler, T.L., and Maloof, A.C., 2011, New software for plotting and analyzing stratigraphic data: Eos, Transactions American Geophysical Union v. 92.5, p. 37–38.
Li, L., and Keller, G., 1998, Abrupt deep-sea warming at the end of the Cretaceous: Geology, v. 26, p. 995–998, doi: 10.1130/0091-7613(1998)026<0995:ADSWAT>2.3.CO;2.
Li, L., and Keller, G., 1999, Variability in Late Cretaceous climate and deep waters: evidence from stable isotopes: Marine Geology, v. 161, p. 171–190, doi: 10.1016/S0025-3227(99)00078-X.
Lindsay, E.H., Butler, R.F., and Johnson, N.M., 1981, Magnetic polarity zonation and biostratigraphy of late Cretaceous and Paleocene continental deposits, San Juan Basin, New Mexico: American Journal of Science, v. 281, p. 390–435.
Lofgren, D.L., 1995, The Bug Creek Problem and the Cretaceous–Tertiary transition at McGuire Creek, Montana: University of California Publications in Geological Sciences, v. 140, 185 p.
Lofgren, D.L., Lillegraven, J.A., Clemens, W.A., Gingerich, P.D., Williamson, T.E., and Woodburne, M.O., 2004, Paleocene biochronology: the Puercan through Clarkforkian land mammal ages: Late Cretaceous and Cenozoic Mammals of North America: Biostratigraphy and Geochronology. Columbia University Press, New York, p. 43–105.
Lowrie, W., 1990, Identification of ferromagnetic minerals in a rock by coercivity and unblocking temperature properties: Geophysical Research Letters, v. 17, p. 159–162, doi: 10.1029/GL017i002p00159.
Lowrie, W. and Heller, F., 1982, Magnetic properties of marine limestones, Reviews of Geophysics and Space Physics, v. 20, p. 171–192.
Lund, S.P., Hartman, J.H., and Banerjee, S.K., 2002, Magnetostratigraphy of interfingering Upper Cretaceous–Paleocene marine and continental strata of the Williston Basin, North Dakota and Montana: The Hell Creek Formation and the Cretaceous-Tertiary Boundary in the northern Great Plains: Geological Society of America Special Paper, v. 361, p. 57–74.
MacLeod, K.G., Huber, B.T., and Isaza-Londoño, C., 2005, North Atlantic warming during global cooling at the end of the Cretaceous: Geology, v. 33, p. 437–440, doi: 10.1130/G21466.1.
MacLeod, K.G., Whitney, D.L., Huber, B.T., and Koeberl, C., 2007, Impact and extinction in remarkably complete Cretaceous-Tertiary boundary sections from Demerara Rise, tropical western North Atlantic: Geological Society of America Bulletin, v. 119, p. 101–115, doi: 10.1130/B25955.1.
McDougall, I., and Tarling, D.H., 1963, Dating of reversals of the earth's magnetic field: Nature, v. 198, p. 1012–1013.
McFadden, P.L., and McElhinny, M.W., 1990, Classification of the reversal test in palaeomagnetism: Geophysical Journal International, v. 103, p. 725–729, doi: 10.1111/j.1365-246X.1990.tb05683.x.
McGhee Jr., G.R., Sheehan, P.M., Bottjer, D.J., and Droser, M.L., 2004, Ecological ranking of Phanerozoic biodiversity crises: ecological and taxonomic severities are decoupled: Palaeogeography, Palaeoclimatology, Palaeoecology, v. 211, p. 289–297, doi: 10.1016/j.palaeo.2004.05.010.
McLean, D.M., 1979, Global warming and late Pleistocene mammalian extinctions: Geological Society of American, Southeastern Section, in Abstracts, 28th Annual Meeting,

Blacksburg, VA, v. 205.
McLean, D.M., 1980, Terminal Cretaceous Castastrophe: Nature, v. 287, p. 760–760, doi: 10.1038/287760a0.
McLean, D.M., 1985, Deccan Traps mantle degassing in the terminal Cretaceous marine extinctions: Cretaceous Research, v. 6, p. 235–259, doi: 10.1016/0195-6671(85)90048-5.
Meredith, R.W., Janečka, J.E., Gatesy, J., Ryder, O.A., Fisher, C.A., Teeling, E.C., Goodbla, A., Eizirik, E., Simão, T.L.L., Stadler, T., Rabosky, D.L., Honeycutt, R.L., Flynn, J.J., Ingram, C.M., et al., 2011, Impacts of the Cretaceous Terrestrial Revolution and KPg Extinction on Mammal Diversification: Science, v. 334, p. 521–524, doi: 10.1126/science.1211028.
Mitchell III, W.S, 2014, High-resolution U-Pb Geochronology of Terrestrial Cretaceous-Paleogene and Permo-Triassic Boundary Sequences in North America: Ph.D. Dissertation, University of California, Berkeley, Berkeley, California.
Montanari, A., Hay, R.L., Alvarez, W., Asaro, F., Michel, H.V., Alvarez, L.W., and Smit, J., 1983, Spheroids at the Cretaceous-Tertiary boundary are altered impact droplets of basaltic composition: Geology, v. 11, p. 668–671, doi: 10.1130/0091-7613(1983)11<668:SATCBA>2.0.CO;2.
Moore, J.R., Wilson, G.P., Sharma, M., Hallock, H.R., Braman, D.R., and Renne, P.R., 2014, Assessing the relationships of the Hell Creek–Fort Union contact, Cretaceous-Paleogene boundary, and Chicxulub impact ejecta horizon at the Hell Creek Formation lectostratotype, Montana, USA, *in* Wilson, G.P., Clemens, W.A., Horner, J.R., and Hartman, J.H., eds., Through the End of the Cretaceous in the Type Locality of the Hell Creek Formation in Montana and Adjacent Areas: Geological Society of America Special Paper 503, p. 123–135.
Moskowitz, B.M., Jackson, M., and Kissel, C., 1998, Low-temperature magnetic behavior of titanomagnetites: Earth and Planetary Science Letters, v. 157(3–4), p. 141–149.
Moskowitz, B.M., Jackson M., and Chandler, V., 2015, 11.05 - Geophysical Properties of the Near-Surface Earth: Magnetic Properties, in *Treatise on Geophysics (Second Edition),* edited by Gerald Schubert, pp. 139–174, Elsevier, Oxford, http://dx.doi.org/10.1016/B978-0-444-53802-4.00191-3.
Nagata, T., 1961, Rock magnetism, 366 pp., Maruzen Co., Tokyo
Nagata, T., Akimoto, S., and Uyeda, S., 1951, Reverse Thermo-Remanent Magnetism: Proceedings of the Japan Academy, v. 27, p. 643–645, doi: 10.2183/pjab1945.27.643.
Nagata, T., and Akimoto, S., 1956, Magnetic properties of ferromagnetic ilmenites: Geofisica pura e applicata, v. 34, p. 36–50, doi: 10.1007/BF02122815.
Nagata, T., and Uyeda, S., 1959, Exchange Interaction as a Cause of Reverse Thermo-Remanent Magnetism: Nature, v. 184, 890–891, doi: 10.1038/184890a0.
Nichols, D.J. and Johnson, K.R., 2002, Palynology and microstratigraphy of the Cretaceous-Tertiary boundary sections in southwestern North Dakota, *in* Hartman, J.H., Johnson, K.R., and Nichols, D.J., eds., The Hell Creek Formation and the Cretaceous-Tertiary Boundary in the Northern Great Plains: An Integrated Continental Record of the End of the Cretaceous: Geological Society of America, Boulder, v. 361, p. 95–143.
Nichols, D.J., and Johnson, K.R., 2008, Plants and the K-T Boundary: Cambridge University Press, 291 p.
Nord, G.L., and Lawson, C.A., 1989, Order-disorder transition-induced twin domains and magnetic properties in ilmenite-hematite: American Mineralogist, v. 74, p. 160–176.

Nordt, L., Atchley, S., and Dworkin, S., 2003, Terrestrial evidence for two greenhouse events in the latest Cretaceous: GSA today, v. 13, p. 4–9.
O'Leary, M.A., Bloch, J.I., Flynn, J.J., Gaudin, T.J., Giallombardo, A., Giannini, N.P., Goldberg, S.L., Kraatz, B.P., Luo, Z.-X., Meng, J., Ni, X., Novacek, M.J., Perini, F.A., Randall, Z.S., et al., 2013, The Placental Mammal Ancestor and the Post–K-Pg Radiation of Placentals: Science, v. 339, p. 662–667, doi: 10.1126/science.1229237.
Ogg, J.G., 2012, Chapter 5 - Geomagnetic Polarity Time Scale, in The Geologic Time Scale, Boston, Elsevier, p. 85–113, doi: 10.1016/B978-0-444-59425-9.00005-6.
Ozima, M., Funaki, M., Hamada, N., Aramaki, S., and Fujii, T., 1992, Self-Reversal of Thermo-Remanent Magnetization in Pyroclastics from the 1991 Eruption of Mt. Pinatubo, Philippines: Journal of geomagnetism and geoelectricity, v. 44, p. 979–984, doi: 10.5636/jgg.44.979.
Ozima, M., and Funaki, M., 2001, Magnetic properties of hemoilmenite single crystals in Haruna dacite pumice revealed by the Bitter technique, with special reference to self-reversal of thermoremanent magnetization: Earth, Planets and Space, v. 53, p. 111–119, doi: 10.1186/BF03352368.
Ozima, M., Oshima, O., and Funaki, M., 2003, Magnetic properties of pyroclastic rocks from the later stage of the eruptive activity of Haruna Volcano in relation to the self-reversal of thermo-remanent magnetization: Earth, Planets and Space, v. 55, p. 183–188, doi: 10.1186/BF03351747.
Pearson, M.J., and Obaje, N.G., 1999, Onocerane and other triterpenoids in Late Cretaceous sediments from the Upper Benue Trough, Nigeria: tectonic and palaeoenvironmental implications: Organic Geochemistry, v. 30, p. 583–592, doi: 10.1016/S0146-6380(99)00069-8.
Pearson, D.A., Schaefer, T., Johnson, K.R., and Nichols, D.J., 2001, Palynological calibrated vertebrate record from North Dakota consistent with abrupt dinosaur extinction at the Cretaceous-Tertiary boundary: Geology, v. 29, p. 39–42.
Peppe, D.J., Evans, D.A.D., and Smirnov, A.V., 2009, Magnetostratigraphy of the Ludlow Member of the Fort Union Formation (Lower Paleocene) in the Williston Basin, North Dakota: Geological Society of America Bulletin, v. 121, p. 65–79, doi: 10.1130/B26353.1.
Peppe, D.J., Johnson, K.R., and Evans, D.A.D., 2011, Magnetostratigraphy of the Lebo and Tongue River Members of the Fort Union Formation (Paleocene) in the northeastern Powder River Basin, Montana: American Journal of Science, v. 311, p. 813–850, doi: 10.2475/10.2011.01.
Petersen, S.V., Dutton, A., and Lohmann, K.C., 2016, End-Cretaceous extinction in Antarctica linked to both Deccan volcanism and meteorite impact via climate change: Nature Communications, v. 7, p. 12079, doi: 10.1038/ncomms12079.
Pierazzo, E., Hahmann, A.N., and Sloan, L.C., 2003, Chicxulub and Climate: Radiative Perturbations of Impact-Produced S-Bearing Gases: Astrobiology, v. 3, p. 99–118, doi: 10.1089/153110703321632453.
Renne P. R., Balco G., Ludwig K. R., Mundil R. and Min K., 2011, Response to the comment by W.H. Schwarz et al. on Joint determination of ^{40}K decay constants and $^{40}Ar^{*}/^{40}K$ for the Fish Canyon sanidine standard, and improved accuracy for $^{40}Ar/^{39}Ar$ geochronology by P.R. Renne et al. (2010): Geochimica et Cosmochimica Acta, v. 75, p. 5097–5100.
Renne, P.R., Deino, A.L., Hilgen, F.J., Kuiper, K.F., Mark, D.F., Mitchell, W.S., Morgan, L.E.,

Mundil, R., and Smit, J., 2013, Time Scales of Critical Events Around the Cretaceous-Paleogene Boundary: Science, v. 339, p. 684–687, doi: 10.1126/science.1230492.
Renne, P.R., Sprain, C.J., Richards, M.A., Self, S., Vanderkluysen, L., and Pande, K., 2015, State shift in Deccan volcanism at the Cretaceous-Paleogene boundary, possibly induced by impact: Science, v. 350, p. 76–78, doi: 10.1126/science.aac7549.
Retallack, G.J., 1994, A pedotype approach to latest Cretaceous and earliest Tertiary paleosols in eastern Montana: Geological Society of America Bulletin, v. 106, p. 1377–1397.
Richards, M.A., Alvarez, W., Self, S., Karlstrom, L., Renne, P.R., Manga, M., Sprain, C.J., Smit, J., Vanderkluysen, L., and Gibson, S.A., 2015, Triggering of the largest Deccan eruptions by the Chicxulub impact: Geological Society of America Bulletin, v. 127, p. 1507–1520, doi: 10.1130/B31167.1.
Rigby, J. K. Jr, Newman, K. R., Smit, J., Van der Kaars, S., Sloan, and R. E., Rigby, J. K., 1987, Dinosaurs from the Paleocene part of the Hell Creek Formation, McCone County, Montana. Palaios, v. 2, p. 296–302.
Rigby, J.K., and Rigby, J.K., Jr., 1990, Geology of the Sand Arroyo and Bug Creek Quadrangles, McCone County, Montana: Brigham Young University, Geology Studies, v. 36, p. 69–134.
Riihimaki, C.A., Reiners, P.W., and Heffern, E.L., 2009, Climate control on Quaternary coal fires and landscape evolution, Powder River basin, Wyoming and Montana: Geology, v. 37, p. 255–258, doi: 10.1130/G25195A.1.
Roberts, A.P., Liu, Q., Rowan, C.J., Chang, L., Carvallo, C., Torrent, J., and Horng, C.-S., 2006, Characterization of hematite (α-Fe2O3), goethite (α-FeOOH), greigite (Fe3S4), and pyrrhotite (Fe7S8) using first-order reversal curve diagrams: Journal of Geophysical Research: Solid Earth, v. 111, p. B12S35, doi: 10.1029/2006JB004715.
Robertson, D.S., McKenna, M.C., Toon, O.B., Hope, S., and Lillegraven, J.A., 2004, Survival in the first hours of the Cenozoic: Geological Society of America Bulletin, v. 116, p. 760–768, doi: 10.1130/B25402.1.
Robinson, P., Harrison, R.J., Miyajima, N., McEnroe, S.A., and Fabian, K., 2012a, Chemical and magnetic properties of rapidly cooled metastable ferri-ilmenite solid solutions: implications for magnetic self-reversal and exchange bias-II. Chemical changes during quench and annealing: Geophysical Journal International, v. 188, p. 447–472, doi: 10.1111/j.1365-246X.2011.05277.x.
Robinson, P., Harrison, R.J., Fabian, K., and McEnroe, S.A., 2012b, Chemical and magnetic properties of rapidly cooled metastable ferri-ilmenite solid solutions: implications for magnetic self-reversal and exchange bias—III. Magnetic interactions in samples produced by Fe–Ti ordering: Geophysical Journal International, v. 191, p. 1025–1047, doi: 10.1111/j.1365-246X.2012.05692.x.
Robinson, P., McEnroe, S.A., Fabian, K., Harrison, R.J., Thomas, C.I., and Mukai, H., 2014, Chemical and magnetic properties of rapidly cooled metastable ferri-ilmenite solid solutions – IV: the fine structure of self-reversed thermoremanent magnetization: Geophysical Journal International, v. 196, p. 1375–1396, doi: 10.1093/gji/ggt486.
Scheffer, M., Carpenter, S., Foley, J.A., Folke, C., and Walker, B., 2001, Catastrophic shifts in ecosystems: Nature, v. 413, p. 591–596, doi: 10.1038/35098000.
Scheffer, M., and Carpenter, S.R., 2003, Catastrophic regime shifts in ecosystems: linking theory to observation: Trends in Ecology & Evolution, v. 18, p. 648–656, doi: 10.1016/j.tree.2003.09.002.

Schoene, B., Samperton, K.M., Eddy, M.P., Keller, G., Adatte, T., Bowring, S.A., Khadri, S.F.R., and Gertsch, B., 2015, U-Pb geochronology of the Deccan Traps and relation to the end-Cretaceous mass extinction: Science, v. 347, p. 182–184, doi: 10.1126/science.aaa0118.

Schulte, P., Alegret, L., Arenillas, I., Arz, J.A., Barton, P.J., Bown, P.R., Bralower, T.J., Christeson, G.L., Claeys, P., Cockell, C.S., Collins, G.S., Deutsch, A., Goldin, T.J., Goto, K., et al., 2010, The Chicxulub Asteroid Impact and Mass Extinction at the Cretaceous-Paleogene Boundary: Science, v. 327, p. 1214–1218, doi: 10.1126/science.1177265.

Self, S., Schmidt, A., and Mather, T.A., 2014, Emplacement characteristics, time scales, and volcanic gas release rates of continental flood basalt eruptions on Earth: Geological Society of America Special Papers, v. 505, p. SPE505-16, doi: 10.1130/2014.2505(16).

Sereno, P.C., 1999, The Evolution of Dinosaurs: Science, v. 284, p. 2137–2147, doi: 10.1126/science.284.5423.2137.

Shafiqullah, M., Follinsbee, R.E., Baadsgaard, H., Curnming, G.L., and Lerbekmo, J.F. 1964. Geochronology of the Cretaceous-Tertiary boundary, Alberta, Canada. 22nd International Geological Congress, New Delhi, 1963, Part 111, Section 3.

Simon, J.I., Renne, P.R., and Mundil, R., 2008, Implications of pre-eruptive magmatic histories of zircons for U–Pb geochronology of silicic extrusions: Earth and Planetary Science Letters, v. 266, p. 182–194, doi: 10.1016/j.epsl.2007.11.014.

Sloan, R.E., and Van Valen, L., 1965, Cretaceous mammals from Montana: Science, v. 148, p. 220–227.

Smit, J., and van der Kaars, S., 1984, Terminal Cretaceous extinctions in the Hell Creek area, Montana: Compatible with catastrophic extinction: Science, v. 223, p. 1177–1179.

Smit, J., van der Kaars, W. A., and Rigby, J. K. Jr., 1987, Stratigraphic aspects of the Cretaceous-Tertiary boundary in the Bug Creek area of eastern Montana, U.S.A., *in* Mesozoic Ecological Proceedings: Paris, Mémoirs Société Géologique France, N. S., v. 150, p. 53–73.

Smit, J., 1990, Meteorite impact, Extinction and the Cretaceous-Tertiary Boundary: Geologie En Mijnbouw, v. 69, p. 187–204.

Smit, J., and Hertogen, J., 1980, An extraterrestrial event at the Cretaceous–Tertiary boundary: Nature, v. 285, p. 198–200.

Sprain, C.J., Renne, P.R., Wilson, G.P., and Clemens, W.A., 2015, High-resolution chronostratigraphy of the terrestrial Cretaceous-Paleogene transition and recovery interval in the Hell Creek region, Montana: Geological Society of America Bulletin, v. 127, p. 393–409, doi: 10.1130/B31076.1.

Sprain, C.J., Feinberg, J.M., Renne, P.R., and Jackson, M., 2016, Importance of titanohematite in detrital remanent magnetizations of strata spanning the Cretaceous-Paleogene boundary, Hell Creek region, Montana: Geochemistry, Geophysics, Geosystems, , v. 17, p. 660–678

Strehlau, J.H., Hegner, L.A., Strauss, B.E., Feinberg, J.M., and Penn, R.L., 2014, Simple and Efficient Separation of Magnetic Minerals From Speleothems and Other Carbonates: Journal of Sedimentary Research, v. 84, p. 1096–1106.

Stüben, D., Kramar, U., Berner, Z. A., Meudt, M., Keller, G., Abramovich, S., Adatte, T., Hambach, U., and Stinnesbeck, W., 2003, Late Maastrichtian paleoclimatic and paleoceanographic changes inferred from Sr/Ca ratio and stable isotopes: Palaeogeography Palaeoclimatology Palaeoecology, v. 199, p. 107–127.

Sweet, A.R., 2001, Plants, a Yardstick for Measuring the Environmental Consequences of the

Cretaceous-Tertiary Boundary Event: Geoscience Canada, v. 28, https://journals.lib.unb.ca/index.php/GC/article/view/4087 (accessed April 2017).
Sweet, A.R., and Braman, D.R., 2001, Cretaceous-Tertiary palynofloral perturbations and extinctions within the Aquilapollenites Phytogeographic Province: Canadian Journal of Earth Sciences, v. 38, p. 249–269, doi: 10.1139/e00-024.
Swisher, C.C., Grajales-Nishimura, J.M., Montanari, A., Margolis, S.V., Claeys, P., Alvarez, W., Renne, P., Cedillo-Pardo, E., Maurrasse, F.J.-M.R., and Curtis, G.H., 1992, Coeval Ar-40/Ar-39 ages of 65.0 million years ago from Chicxulub crater melt rock and Cretaceous-Tertiary boundary tektites: Science, v. 257, p. 954–958, doi: 10.1126/science.257.5072.954.
Swisher III, C.C., Dingus, L., and Butler, R.F., 1993, 40Ar/39Ar dating and magnetostratigraphic correlation of the terrestrial Cretaceous–Paleogene boundary and Puercan Mammal Age, Hell Creek – Tullock formations, eastern Montana: Canadian Journal of Earth Sciences, v. 30, p. 1981–1996, doi: 10.1139/e93-174.
Tauxe, L., 2010, Essentials of paleomagnetism: CERN Document Server, http://cds.cern.ch/record/1604091 (accessed November 2014).
Tauxe, L., Shaar, R., Jonestrask, L., Swanson-Hysell, N.L., Minnett, R., Koppers, A. a. P., Constable, C.G., Jarboe, N., Gaastra, K., and Fairchild, L., 2016, PmagPy: Software package for paleomagnetic data analysis and a bridge to the Magnetics Information Consortium (MagIC) Database: Geochemistry, Geophysics, Geosystems, v. 17, p. 2450–2463, doi: 10.1002/2016GC006307.
Taylor, L.H., and Butler, R.F., 1980, Magnetic-polarity stratigraphy of Torrejonian sediments, Nacimiento Formation, San Juan Basin, New Mexico, American Journal of Science, v. 280, p. 97–115, doi: 10.2475/ajs.280.2.97.
Thibault, N., Husson, D., Harlou, R., Gardin, S., Galbrun, B., Huret, E., and Minoletti, F., 2012, Astronomical calibration of upper Campanian-Maastrichtian carbon isotope events and calcareous plankton biostratigraphy in the Indian Ocean (ODP Hole 762C): Implications for the age of Campanian-Maastrichtian boundary: Palaeogeography, Palaeoclimatology, Palaeoecology, v. 337–338, p. 52–71.
Thibault, N., Harlou, R., Schovsbo, N.H., Stemmerik, L., and Surlyk, F., 2016, Late Cretaceous (late Campanian–Maastrichtian) sea-surface temperature record of the Boreal Chalk Sea: Clim. Past, v. 12, p. 429–438, doi: 10.5194/cp-12-429-2016.
Thibault, N., and Husson, D., 2016, Climatic fluctuations and sea-surface water circulation patterns at the end of the Cretaceous era: Calcareous nannofossil evidence: Palaeogeography, Palaeoclimatology, Palaeoecology, v. 441, Part 1, p. 152–164, doi: 10.1016/j.palaeo.2015.07.049.
Tobin, T.S., Ward, P.D., Steig, E.J., Olivero, E.B., Hilburn, I.A., Mitchell, R.N., Diamond, M.R., Raub, T.D., and Kirschvink, J.L., 2012, Extinction patterns, delta 18 O trends, and magnetostratigraphy from a southern high-latitude Cretaceous-Paleogene section: Links with Deccan volcanism: Palaeogeography, Palaeoclimatology, Palaeoecology, v. 350/352, p. 180–188, doi: 10.1016/j.palaeo.2012.06.029.
Tobin, T.S., Wilson, G.P., Eiler, J.M., and Hartman, J.H., 2014, Environmental change across a terrestrial Cretaceous-Paleogene boundary section in eastern Montana, USA, constrained by carbonate clumped isotope paleothermometry: Geology, doi: 10.1130/G35262.1.
Toon, O.B., Zahnle, K., Morrison, D., Turco, R.P., and Covey, C., 1997, Environmental perturbations caused by the impacts of asteroids and comets: Reviews of Geophysics, v.

35, p. 41–78, doi: 10.1029/96RG03038.
Turner, B.W., 2010, Testing the local diachroneity of the terrestrial lithostratigraphic KPg boundary, Northern Montana: M.S. Thesis, Montana State University, Bozeman, Montana.
Uyeda, S., 1957, Thermo-Remanent Magnetism and Coercive Force of the Ilmenite-Hematite Series: Journal of geomagnetism and geoelectricity, v. 9, p. 61–78, doi: 10.5636/jgg.9.61.
Uyeda, S., 1958, Thermo-remanent magnetism as a medium of paleomagnetism, with special reference to reverse thermo-remanent magnetism: Jap. J. Geophys., v. 2, p. 1–123.
Vajda, V., Raine, J.I., and Hollis, C.J., 2001, Indication of Global Deforestation at the Cretaceous-Tertiary Boundary by New Zealand Fern Spike: Science, v. 294, p. 1700–1702, doi: 10.1126/science.1064706.
Vandamme, D., and Courtillot, V., 1992, Paleomagnetic constraints on the structure of the Deccan traps: Physics of the Earth and Planetary Interiors, v. 74, p. 241–261, doi: 10.1016/0031-9201(92)90013-L.
Vellekoop, J., Sluijs, A., Smit, J., Schouten, S., Weijers, J.W.H., Damsté, J.S.S., and Brinkhuis, H., 2014, Rapid short-term cooling following the Chicxulub impact at the Cretaceous–Paleogene boundary: Proceedings of the National Academy of Sciences, v. 111, p. 7537–7541, doi: 10.1073/pnas.1319253111.
Vellekoop, J., Esmeray-Senlet, S., Miller, K.G., Browning, J.V., Sluijs, A., Schootbrugge, B. van de, Damsté, J.S.S., and Brinkhuis, H., 2016, Evidence for Cretaceous-Paleogene boundary bolide "impact winter" conditions from New Jersey, USA: Geology, v. 44, p. 619–622, doi: 10.1130/G37961.1.
Wang, D., and Van der Voo, R., 2004, The hysteresis properties of multidomain magnetite and titanomagnetite/titanomaghemite in mid-ocean ridge basalts: Earth and Planetary Science Letters, v. 220, p. 175–184.
Watson, G.S., 1956, A Test for Randomness of Directions: Geophysical Supplements to the Monthly Notices of the Royal Astronomical Society, v. 7, p. 160–161, doi: 10.1111/j.1365-246X.1956.tb05561.x.
Westerhold, T., Rohl, U., Raffi, I., Fornaciari, E., Monechi, S., Reale, V., Bowles, J., and Evans, H.F., 2008, Astronomical calibration of the Paleocene time: Palaeogeography Palaeoclimatology Palaeoecology, v. 257, p. 377–403, doi: 10.1016/j.palaeo.2007.09.016.
White, R.V., and Saunders, A.D., 2005, Volcanism, impact and mass extinctions: incredible or credible coincidences? Lithos, v. 79, p. 299–316, doi: 10.1016/j.lithos.2004.09.016.
Wignall, P.B., 2001, Large igneous provinces and mass extinctions: Earth-Science Reviews, v. 53, p. 1–33.
Wilf, P., Johnson, K.R., and Huber, B.T., 2003, Correlated terrestrial and marine evidence for global climate changes before mass extinction at the Cretaceous–Paleogene boundary: Proceedings of the National Academy of Sciences, v. 100, p. 599–604, doi: 10.1073/pnas.0234701100.
Wilf, P., and Johnson, K.R., 2004, Land plant extinction at the end of the Cretaceous: a quantitative analysis of the North Dakota megafloral record: Paleobiology, v. 30, p. 347–368.
Williamson, T.E., 1996, The Beginning of the Age of Mammals in the San Juan Basin, New Mexico: Biostratigraphy and Evolution of Paleocene Mammals of the Nacimiento Formation: Bulletin 8: New Mexico Museum of Natural History and Science, 147 p.
Wilson, G.P., 2005, Mammalian Faunal Dynamics During the Last 1.8 Million Years of the

Cretaceous in Garfield County, Montana: Journal of Mammalian Evolution, v. 12, p. 53–76, doi: 10.1007/s10914-005-6943-4.
Wilson, G.P., 2013, Mammals across the K/Pg boundary in northeastern Montana, U.S.A: Dental morphology and body-size patterns reveal extinction selectivity and immigrant-fueled ecospace filling: Paleobiology, v. 39, p. 429–469, doi: 10.1666/12041.
Wilson, G.P., 2014, Mammalian extinction, survival, and recovery dynamics across the Cretaceous-Paleogene boundary in northeastern Montana, in Wilson, G.P., Clemens, W.A., Horner, J.R., and Hartman, J.H. eds., Through the End of the Cretaceous in the Type Locality of the Hell Creek Formation in Montana and Adjacent Areas: Geological Society of America Special Paper 503, p. 1–28, 10.1130/2014.2503(15).
Wilson, G.P., Clemens, W.A., Horner, J.R., and Hartman, J.H., eds., 2014a, Through the End of the Cretaceous in the Type Locality of the Hell Creek Formation in Montana and Adjacent Areas: Geological Society of America Special Paper 503.
Wilson, G.P., DeMar, D.G., and Carter, G., 2014, Extinction and survival of salamander and salamander-like amphibians across the Cretaceous-Paleogene boundary in northeastern Montana, USA: Geological Society of America Special Papers, v. 503, p. 271–297, doi: 10.1130/2014.2503(10).
Witts, J.D., Whittle, R.J., Wignall, P.B., Crame, J.A., Francis, J.E., Newton, R.J., and Bowman, V.C., 2016, Macrofossil evidence for a rapid and severe Cretaceous–Paleogene mass extinction in Antarctica: Nature Communications, v. 7, p. 11738, doi: 10.1038/ncomms11738.
Wotzlaw, J.-F., Hüsing, S.K., Hilgen, F.J., and Schaltegger, U., 2014, High-precision zircon U–Pb geochronology of astronomically dated volcanic ash beds from the Mediterranean Miocene: Earth and Planetary Science Letters, v. 407, p. 19–34, doi: 10.1016/j.epsl.2014.09.025.

Appendix A. High-resolution chronostratigraphy of the terrestrial Cretaceous-Paleogene transition and recovery interval in the Hell Creek region, Montana

A.1. Methods $^{40}Ar/^{39}Ar$ Geochronology

Feldspars for dating were separated from 1–5 kg samples of tephra that were collected from thin interbeds within lignite deposits. Samples were disaggregated using crushing and/or water suspension techniques, followed by washing and sieving. The feldspars were concentrated using a combination of magnetic and density separations followed by ultrasonic cleaning in 7% hydrofluoric acid for approximately 5 minutes. Some samples required an additional treatment of hydrogen peroxide to remove excess coal prior to density separation. Feldspars were then handpicked from size fractions ranging from 177 to 595 microns. Large, clear grains were picked preferentially.

$^{40}Ar/^{39}Ar$ analyses were conducted at the Berkeley Geochronology Center (BGC). Samples were irradiated in the Cadmium-Lined In-Core Irradiation Tube (CLICIT) facility of the Oregon State University TRIGA reactor, in three separate 50-hour irradiations. Samples were loaded into 1–3 Al disks as figured by Renne et al. (2013) for each irradiation. Fast neutron fluence represented by the parameter *J* was determined for each of six positions spanning each disk using analysis of single crystals of the Fish Canyon sanidine (FCs) standard. The value of *J* for each unknown sample was determined by interpolation within a planar fit to the *J*-values determined by the standards. The relative precision of these interpolated *J*-values was better than 0.1% in all cases.

For mass spectrometry, we used the methods and facilities described in Renne et al. (2013). In brief, samples were analyzed mainly by total fusion, augmented in some cases by incremental heating, with CO_2 lasers on two different extraction systems coupled to MAP 215 mass spectrometers (MAP1 and Nexus). MAP1 is a 215C and Nexus is a MAP 215-50. Both have Nier-type ion sources and analog electron multiplier detectors. The mass spectrometry applied peak-hopping by magnetic field switching on a single detector in 15 cycles. Blanks were measured between every 1–3 unknowns.

Ages were computed from blank-, discrimination-, and decay-corrected Ar isotope data after correcting data for interfering isotopes based on production ratios determined from fluorite and Fe-doped $KAlSiO_4$ glass as reported by Renne et al. (2013). Ages are based on the calibration of Renne et al. (2011). Ar isotope data are shown in Table DR1. Results of single crystal laser fusion analyses are shown in Figure 2. Age spectra (Fig. 3) were obtained from incremental heating experiments on multigrain aliquots of a few samples in which no xenocrysts were evident from the single crystal analyses. Age uncertainties are given at one standard deviation and are stated as ±X/Y, where X is the analytical uncertainty and Y includes systematic uncertainties arising from the calibration. In cases where only one uncertainty value is given, as in calculating interval durations, it refers to analytical sources alone.

Plateau ages (i.e., for samples depicted in Fig. 3) are defined here by having more than three contiguous steps releasing more than 50% of the ^{39}Ar, with all steps having mutually indistinguishable ages at the 95% confidence level considering only experimental uncertainties.

A.2. Details of $^{40}Ar/^{39}Ar$ Results for Individual Samples

From samples BC-1PR and BC11-1 in the Null coal at Bug Creek, 174 feldspar crystals (both 149–177 microns) were analyzed. The two samples were collected at precisely the same locality in successive years, but were prepared and irradiated separately. Both samples yielded a broad spectrum of single crystal ages ranging from 218.590 ± 0.630 to 65.532 ± 0.483 Ma, with a well-defined younger mode. Despite the preponderance of xenocrysts, the identification of this unit as a tephra is supported by the presence of beta quartz pseudomorphs, which indicate a volcanic origin. Seventy crystals of BC-1PR were run on MAP 1 and 29 on Nexus. Of these 99 crystals 21 yielded ages defining this younger mode; with the remainder interpreted as xenocrysts. In an effort to concentrate the younger mode, sample BC11-1 was subjected to a more restricted density separation based on the observation that the xenocrysts tended to have higher K/Ca values. Crystals from BC11-1 were also selected with higher standards of optical clarity than those of BC-1PR. Accordingly, 33 of 75 (44%) grains of sample BC11-1 (all run on MAP 1) yielded ages defining a younger mode. The 54 grains from both samples defining the younger mode yield a weighted mean age of 66.289 ± 0.051/0.065 Ma.

From sample HH12-1 of the IrZ coal at Hell Hollow, 74 feldspar crystals (210-297 microns) were analyzed individually by total fusion followed by argon isotope analysis with the MAP 1 mass spectrometer. Of the 74 grains, three were identified as plagioclase on the basis of K/Ca ratios. Of the remaining 71 grains, one grain showed a parabolic evolution of ^{40}Ar and was excluded from age analysis. The resulting 70 grains yielded a weighted mean age of 66.061 ± 0.039/0.059 Ma.

From sample NV12-1 in the IrZ coal at the Nirvana site, 56 feldspar crystals (250–297 microns) were analyzed as single crystals; 31 on MAP 1 and 25 on Nexus. All were sanidine based on K/Ca. Excluding one obvious xenocryst at 67.55 ± 0.32, the remainder yielded a unimodal distribution with a well-defined weighted mean age of 66.035 ± 0.033/0.052 Ma, indistinguishable from the age reported by Renne et al. (2013) for the tephra in the IrZ coal at nearby Hauso Flats or from that (HH12-1) at Hell Hollow reported herein.

From sample ZL12-2, the MCZ coal at the Z-line quarry, 90 feldspar crystals (177–210 microns) were analyzed individually by total fusion; 61 on MAP 1 and 29 on Nexus. All but one were alkali feldspars based on K/Ca. Excluding one obvious xenocryst at 87.74 ± 2.34 Ma, the remaining samples yielded a unimodal age distribution with a weighted mean age of 65.998 ± 0.044/0.061 Ma.

From sample LG11-1, in the MCZ coal at McGuire Creek, 150 feldspar crystals (177–210 microns) were analyzed by total fusion; 109 on MAP 1 and 41 on Nexus. 72 of these were alkali feldspar based on K/Ca. The alkali feldspars yielded a unimodal and symmetric age distribution with a weighted mean age of 66.015 ± 0.052/0.066 Ma. The remaining 78 feldspar grains also yielded a unimodal age distribution, but with a distinct skew towards younger ages suspected to be due to subtle alteration. Although the weighted mean of plagioclase ages (65.69 ± 0.15 Ma) is indistinguishable at 95% confidence from the sanidine results, we exclude them as being likely biased. This sample is noteworthy in yielding a much larger proportion of plagioclase than any other sample. This may result from unusual preservation, as plagioclase is typically altered in the samples of this study, or it may reflect a relatively poor mineral separation. In addition to the single crystal analyses, 4 aliquots comprising 10–15 grains each were analyzed by incremental heating on Nexus. Two of these yielded well-defined plateau ages of 66.016 ± 0.069 and 66.039 ± 0.065 Ma. The two aliquots failing to define plateaux are clearly

suspect of containing xenocrysts, particularly apparent in aliquot 36619-101 (Fig. 3C). The weighted mean of the two well-defined plateau ages is 66.028 ±0.050/0.065 Ma. Data pooled from the two experiments yielding plateaux and the single crystal sanidine analyses yield a weighted mean age of 66.022 ± 0.038/0.057 Ma.

From sample HX12-1 of the Z coal at a site near the Haxby Road, 94 feldspar crystals (177–210 microns) were analyzed individually by total fusion on MAP 1. All proved to be alkali feldspars based on K/Ca ratios. One distinctly older (68.38 ± 0.33 Ma) grain interpreted as a xenocryst was excluded. The remaining grains yielded a unimodal age distribution with a weighted mean age of 66.002 ± 0.033/0.054 Ma.

From HH12-2 of the HFZ coal at Hell Hollow, 79 feldspar crystals (297–420 microns) were analyzed individually by total fusion followed by argon isotope analysis with the MAP 1 mass spectrometer. Of the 79 crystals one was identified as plagioclase based on K/Ca ratios with an anomalous value of 39.55 ± 35.84 Ma. An additional outlier was excluded on the basis of low percent radiogenic argon. From the remaining 77 grains, a weighted mean age of 65.962 ± 0.026/0.050 Ma was computed.

From sample GC12-3, in the lower Y coal at Garbani Hill, 106 feldspar crystals (250–297 microns) were analyzed by total fusion; 86 on MAP 1 and 25 on Nexus. All were alkali feldspars based on K/Ca. Excluding two apparent xenocrysts at 66.55 ± 0.20 and 66.61 ± 0.15 Ma, the remaining crystals defined a unimodal age distribution with a weighted mean age of 65.741 ± 0.022/0.048 Ma.

From sample GC12-2 of the upper Y coal at Garbani Hill, 243 feldspar crystals (177–210 microns) were analyzed individually by total fusion followed by argon isotope analysis with the MAP 1 mass spectrometer. Of the 243 crystals, 125 crystals proved to be either plagioclase (on the basis of K/Ca ratios) or were distinctly xenocrystic, yielding ages ranging from 67 Ma to 3.0 Ga. The remaining 118 grains yielded a weighted mean age of 65.677 ± 0.041/0.059 Ma.

From sample MC11-3, in the X coal at McGuire Creek, 52 aliquots of 5 grains (177–210 microns) each were analyzed by total fusion on MAP 1. K/Ca ratios were consistent with all grains being alkali feldspar. All analyses defined a unimodal age distribution with a weighted mean age of 65.494 ± 0.038/0.056 Ma. In addition, four aliquots comprising 10–15 grains each were analyzed by incremental heating on Nexus, yielding plateau ages of 65.467 ± 0.075 to 65.510 ± 0.065 Ma (Fig. 3B). The weighted mean plateau age is 65.488 ± 0.039/0.057 Ma. Data pooled from all experiments yield a weighted mean age of 65.491 ± 0.032/0.053 Ma.

From sample SS11-3 of the upper W coal near Garbani Hill, 68 feldspar crystals (595–841 microns) were analyzed individually by total fusion on MAP 1. All proved to be alkali feldspars based on K/Ca ratios, but these ratios are distinctly higher than in most other samples and they may properly be termed anorthoclase. A unimodal age distribution yielded a weighted mean age of 65.118 ± 0.024/0.048 Ma.

From sample HTC12-1 of the W coal at Horsethief Canyon, 93 feldspar crystals (420-595 microns) were analyzed individually by total fusion of 73 grains on the MAP 1 mass spectrometer and 20 grains on the Nexus mass spectrometer. Of these crystals all but six grains were identified as alkali feldspars on the basis of K/Ca ratios. Plagioclase ages were all distinguishably younger than alkali feldspar ages, presumably due to subtle alteration, and were excluded from age calculations. In addition to plagioclase, one sanidine crystal was excluded due to incorrigible mass spectrometry data and one was a clear xenocryst. From the remaining 85 crystals, a weighted mean age of 65.197 ± 0.024/0.048 Ma was calculated.

From sample BB12-1 of the Biscuit Butte V coal tephra, 179 feldspar crystals (297–420

microns) were analyzed individually using total fusion and argon isotope analysis. 159 of these grains were analyzed on the MAP 1 mass spectrometer and 20 grains were analyzed on the Nexus mass spectrometer. All crystals yielding measurable Ar were identified to be alkali feldspars on the basis of K/Ca ratios. Two compositionally distinct populations are present: one with K/Ca = 60 ± 24 (N=112) and one with K/Ca = 357 ± 127 (N=63). Both phases appear cognate, as there is no statistically significant age difference between them. Excluding one anomalously young outlier at 64.11 ± 0.26 Ma and three due to incorrigible mass spectrometry data, the remaining 175 grains yielded a weighted mean age of 65.041 ± 0.023/0.048 Ma.

From sample HTC12-3 of the U coal at Horsethief Canyon, 73 feldspar crystals (297–420 microns) were analyzed individually by total fusion followed by argon isotope analysis with the MAP 1 mass spectrometer. All crystals analyzed proved to be alkali feldspar on the basis of K/Ca ratios. Excluding one outlier at 66.91 ± 0.19 Ma, interpreted to be a xenocryst, and one due to incorrigible mass spectrometry data, the remaining 71 grains yielded a unimodal age distribution with a weighted mean age of 64.904 ± 0.026/0.049 Ma.

From sample BB11-1 in the U coal at Biscuit Butte, 119 feldspar crystals (250–297 microns) were analyzed as single crystals, all on MAP 1. All were sanidine based on K/Ca, and all defined a unimodal age distribution with a weighted mean age of 64.865 ± 0.024/0.047 Ma. Four aliquots, each of 10–20 grains, were analyzed by incremental heating on Nexus. Each aliquot yielded a plateau comprising >99% of the ^{39}Ar released with plateau ages ranging from 64.848 ± 0.051 to 64.890 ± 0.068 Ma (Fig. 3A), indistinguishable from the single crystal fusion results. The weighted mean plateau age is 64.867 ± 0.031/0.052 Ma. A pooled weighted mean of results from both types of experiment yields 64.866 ± 0.023/0.047 Ma.

Pooled results

In several cases, we have dated the same tephra at multiple locations, as indicated by correlations based on physical continuity, stratigraphic position, mineralogy and mineral chemistry. These are referred to here by the coals in which they occur. The pooled age is calculated from the weighted (by inverse variance) mean of the individual sample mean ages. Because each sample has a specific *J*-value, associated uncertainties are treated as random. Uncertainties associated with decay constants and the ^{40}Ar*/^{40}K of the standard are treated as systematic, as in all other computations. Pooled ages are shown in Table 2.2.

IrZ coal. Samples NV12-1 and HH12-1 may be combined with results of Renne et al. (2013) from Hauso Flats to yield a weighted mean age of 66.043 ± 0.010/0.043 (non-systematic/systematic) Ma. Given the occurrence of this tephra within ~1 cm of an impact claystone containing an iridium anomaly and shocked quartz (Alvarez, 1983), we consider this to be the most reliable age available for the KPB.

MCZ coal, Z coal on Haxby Road and Z coal in the Lerbekmo Section. Three of the samples reported here (LG11-1, ZL12-2, HX12-1) are correlative with the lower tephra (sample HC-2PR) at the Hell Creek Marina Road section (same as our Lerbekmo section) shown in figure 1 of Renne et al. (2013). In all four of these occurrences, the dated tephra lies 10–30 cm below a distinctively thick (5–10 cm) biotite-bearing tephra that serves as a unique marker. The weighted mean age for the dated unit is 66.013 ± 0.015/0.044 Ma. We note that correlation of this distinctive tephra over a relatively large area does not necessarily imply that the hosting coals are laterally continuous throughout the intervening area. The pooled age for the this tephra is

indistinguishable from that (66.024 ± 0.040/0.059 Ma) reported by Moore et al. (2014) for a tephra ~3 m above an impact clay layer identified as the KPB at Flag Butte, approximately 7 km NE of our LB locality (Fig. 1).

HFZ coal. Our sample HH12-2 is a tephra ~12 cm above one correlated with sample HF-3PR of Renne et al. (2013) from Hauso Flats. The correlated tephra is unique in the region in that it is a deep red-brown color and contains remarkably well-preserved pseudomorphs of cuspate glass shards easily visible with a hand lens. Because the 12 cm stratigraphic separation between the two tephras at Hell Hollow represents a time difference that is below age resolution, it is valid to attribute the combined results to the age of the HFZ coal. The weighted mean age for these two samples is 65.973 ± 0.020/0.047 Ma.

A.3. Gazetteer

Sample location coordinates based on GPS measurements (WGS84) are listed in the text. The locations of several other places mentioned in the text are given below. Where a specific point location is designated, GPS coordinates are given; where a broader area is intended, the cadastral survey coordinates are given.

Brownie Butte summit: 47°31’49.78”N/107°01’01.25” W

Hauso Flats: Sec. 1, T20N, R35E. This area includes the informally named Iridium Hill.

Haxby Road: Montana State Highway 341. Prior to the flooding of the Fort Peck Reservoir, which began in 1937, this road extended from Jordan, Montana, to the settlement at Lismas. A ferry across the Missouri River connected Lismas with Fort Peck (Clemens and Hartman, 2014).

Hell Hollow: Secs. 25 and 36, T21N, R35E.

Iridium Hill summit: 47°31’36.69” N/107°12’38.6” W

Pearl Lake: Bureau of Land Management reservoir, dam 47°31’30.94”N/107°03’42.52” W

Russell Basin: SE ¼, Sec 10 and NE ¼, Sec 15, T 22 N, R 43 E. The basin is delimited on maps in Fastovsky and Dott (1986) and Smit et al. (1987).

Appendix B. Calibration of Chron 29r: New high-precision geochronologic and paleomagnetic constraints from the Hell Creek region, Montana and their implications for the Cretaceous-Paleogene boundary mass extinction

B.1. Section Descriptions

McKeever Ranch

The McKeever Ranch locality (N47.59407º, W107.3267º; All latitude and longitude measurements are based on the WGS84 datum) is located roughly 44 km NW of the town of Jordan, MT. At this locality two lignites crop out. Both coals contain tephra deposits and detailed microstratigraphy for each coal is described in detail in Ickert et al. (2015). The lowermost coal (~35 cm thick) marks the base of the section and has been recognized as the IrZ coal, based on the identification of the Nirvana bentonite, using Pb-isotopes (per Ickert et al. 2015), that crops out 4 cm below the top of the coal. The Nirvana bentonite was collected for dating (MK13-3).

Roughly 14 m above the IrZ coal, a Y coal (~1 m thick) is identified. This coal contains 7 tephra deposits. One tephra layer ~ 80 cm from the base of the coal was collected for chemical analysis (MK13-1). Pb-isotopic analysis of this tephra conducted by Ickert et al. (2015) reveals that it falls into the Unnamed assorted bentonites category, and while it has similar compositions to Y coals from Lerbekmo, Hell Hollow, Jack's Channel, and Isaac Ranch, these tephras can't be correlated because some tephras in this category clearly represent different stratigraphic horizons. Roughly 1 km NW of the MK13-1 location, the Y coal is again recognized (this site is termed McKeever Ranch A). This coal is similarly ~ 1m thick and contains at least 6 tephras. A tephra located 78 cm from the base of the coal (MK12-1) was collected for dating, reported in this study, and chemical analysis conducted by Ickert et al. (2015). It similarly falls into the Unnamed assorted bentonites category (Ickert et al., 2015).

Paleomagnetic sampling was conducted at both sites in the summer of 2013. Sampling at McKeever Ranch ranged stratigraphically from immediately above the IrZ coal, to 65 cm above the Y coal, with the lower three samples collected in siltstone or claystone, and the highest sample collected from a fine sandstone deposit that displayed fine cross-bedding. Below the Y coal, this section is dominated by siltstones and claystones, which are representative of a low-energy flood plain environment, ideal for paleomagnetic sampling. A channel deposit is identified at the top of our section and as such paleomagentic sampling was mostly limited to collection below this unit.

Paleomagnetic samples were also collected at our McKeever Ranch A site (N47.59773º, W107.3402º). Sampling at this locality was focused in an interval from Y coal down 5.5 m to the top of a large (~10 m thick) channel deposit. Two samples were collected, one right on top of the channel and one right below the Y coal. Both samples were collected in sandy siltstones. Again, this locality is dominated by floodplain deposits composed of siltstones and claystones. While the IrZ coal does appear to crop out at the base of this section, intervening rocks were not collected due to the large channel deposit that cuts through the top of the IrZ coal, and ends ~5.5 m below the Y coal.

Hell Hollow

Approximately 13 km SE of McKeever Ranch is the Hell Hollow locality (N47.53472º, W107.1687º). At this locality, four coals have been identified: the IrZ, HFZ, and two Y coals. All coals contain tephra deposits that are amenable to high-precision geochronology, and dates

for tephras from the IrZ (HH12-1) and HFZ (HH12-2) are reported in Sprain et al. (2015). Tephra deposits from each coal were chemically analyzed using electron microprobe analysis and Pb-isotopic analysis in Ickert et al. (2015). Chemical analysis corroborates mapping done in this area by Archibald (1982), and confirms the identity of the IrZ coal (based on the identification of the Nirvana bentonite) and the HFZ and Y coals.

The two Y coals crop out 5 and 13 m (respectively), above the HFZ coal. The first Y coal (~20 cm thick) contains three tephras described in Ickert et al., (2015). The tephra 16 cm from the base of the coal (HH13-1) was collected for dating and results are reported in this study. Four tephra layers are identified within the second Y coal (1.5-m-thick), and are likewise described in Ickert et al. (2015). A tephra (HH13-2), 126 cm from the base of the coal, was collected for geochronology and is reported here.

Roughly 1.5 km SW from the HH13-2 collection site, is another outcrop of the second Y coal recognized by its distinctive thickness, elevation, and by the appearance of a similar distinctive capping unit, a tan/yellow sandstone, that similarly caps the HH13-2 coal. This site, named the Hell Hollow A locality, is along the side of the road and has limited stratigraphic range, encompassing around 2 meters below and 4 m above the Y coal. The Y coal at this locality contains two tephras layers, and the first layer (80 cm from the coal base: HH13-3) was collected for dating. Both tephra samples from the second Y coal, HH13-2 and HH13-3, share similar distinctive Pb isotope compositions, further supporting their field-based correlation (Ickert et al., 2015). Microstratigraphy for the HH13-3 coal is described in Ickert et al. (2015).

Samples for paleomagnetic analysis were collected between the HFZ and second Y coal, to best locate the C29r/C29n reversal. Lithology at the collection site is dominated by thin layers of siltstone, claystone, and lignites, representative of low energy flood-plain deposition. Paleomagnetic samples were collected either from siltstone or claystone layers, with ~ 4 m resolution towards the base of the section and less than 1 m resolution near the reversal.

Paleomagnetic samples were also collected from the Hell Hollow A locality (N47.52228º, W107.1775º), focused around the Y coal to fill in gaps that were unavoidable due to plant cover at the Hell Hollow locality. Site lithologies agree with flood plain deposition.

Garbani Hill/Pearl Lake

The Garbani Hill locality (N47.5151º, W107.0683º) is located 8 km SE of Hell Hollow. Previous descriptions of this section describe two coals, a Y coal doublet and the X coal, outcropping at this locality (see Sprain et al. 2015 for details). However, upon closer inspection, three additional coals are exposed roughly 0.5, 2, and 6 m, below the Y coal doublet. While areas beneath the Y coal doublet are certainly influenced by slumping, we believe these coals are in place based on identification of distinctive tephras, and the fact that similar stratigraphy is found just north of Garbani Hill at the MacDonald locality.

The basal coal in this section, 6.13 meters below the base of the Y doublet, is 1.46 m thick and three tephra layers are identified. The first layer is ~0.5-cm-thick, and is located 50 cm from the base of the coal. It is red in color (Munsell color 10 R 3/4), and not well consolidated, but appears to contain euhedral sanidine crystals. A second tephra is found 58 cm from the base of the coal. This layer varies from a few mm to 1 cm thick, it is pink/red in color (10 R 5/4), and also has apparent euhedral crystals. The third tephra (0.5–1 cm thick), is located 64 cm from the base, and is light pink in color (10 R 8/2). The next coal in stratigraphic sequence is located 3.85 m above the basal coal, and 1.98 m below the Y doublet. This coal is 30 cm thick and no tephra layers were identified. Approximately 0.55 cm below the Y doublet, the third coal (43 cm thick)

in stratigraphic sequence is exposed. Three to four tephra layers were identified in this unit, starting at 30 cm from the base of the coal. Tephras are ~1 cm thick, pink in color (5 R 8/2), are exposed every 3–5 cm.

Using traditional nomenclature, these coals would be classified as variants of Z coals. However, we believe the basal coal in this section is the HFZ based on thickness, distinctive red tephras, and the fact that the HFZ was mapped at the same stratigraphic level to the North at the MacDonald locality and the Pearl Lake locality (LeCain et al., 2014). Therefore, the other two coals are best classified as part of the Y coal complex. LeCain et al. (2014) conducted a paleomagnetic study to the North of this area at Pearl Lake and identified the C29r/C29n reversal a few meters below what they call a Y coal stringer (a thin, <30 cm thick, coal bed). This study further attempts to correlate their findings at Pearl Lake to Garbani Hill, which contains important vertebrate fauna localities within the Garbani Quarry, by tying their Y coal stringer at Pearl Lake to the Y coal doublet at Garbani Hill. Paleomagnetic sampling was only conducted above the Y coal doublet at Garbani Hill, and all samples were of normal polarity, leading LeCain et al. (2014) to conclude the C29r/C29n reversal must likewise fall below the Y coal doublet. This conclusion is suspect in light of our new stratigraphy at Garbani Hill, as the Pearl Lake section reports the reversal to be below the first coal outcropping above the HFZ. This correlation is further suspect because the distinctive tephras in the Y coal doublet at Garbani Hill, identified and dated by Sprain et al. (2015), are not identified within the Y coal stringer at Pearl Lake.

To mediate this problem, paleomagnetic sampling was collected at Garbani Hill and Pearl Lake in this study. At Garbani Hill, sampling started 2.28 m below the Y coal doublet and continued to the base of the X coal. All samples were collected in siltstone to fine sandstone deposits, except two samples that were collected from the GC12-2 and GC12-3 tephras (described and dated in Sprain et al., 2015). Paleomagnetic sampling was conducted adjacent to the Garbani channel, however our site was specifically chosen so that the section was not affected by channel scouring and was dominated by flood plain deposition.

At Pearl Lake (N47.52343º, W107.0569º), paleomagnetic samples were collected starting 5.92 m above the HFZ coal and extended to 0.47 m above the Y coal stringer. All paleomagnetic samples were collected from siltstone deposits. Sampling was conducted along the same profile as in LeCain et al. (2014). The Y coal stringer at this locality is 22 cm thick and two thin (1–3 mm) light pink (5 R 8/2) tephra layers were identified ~7.5 cm and ~8.5 cm from the base of the coal. Both tephras pinch and swell and in some areas, pinch out completely. Both tephras have apparent euhedral feldspars. The first tephra was collected for $^{40}Ar/^{39}Ar$ analysis (PL14-1). Near the MacDonald locality, a tephra was also collected from the HFZ. The HFZ at this locality can be visually traced to the HFZ below our paleomagnetic section at Pearl Lake. The HFZ coal at the MacDonald locality is 1.2-m-thick and contains 4 tephra deposits. The first tephra is 37 cm from the top of the coal and is 4 mm thick. It is pink/brown (10 R 6/2) in color and has apparent feldspar crystals. The next tephra is 2 cm below the first layer, and is 2-mm-thick and pink-white (10 R 8/2) in color. The third tephra (MD15-1) appears 45 cm from the top of the coal and is 1–2 cm thick (10 R 8/2). This layer is red (10 R 3/4) in color and has euhedral feldspar crystals. We collected this tephra for geochronologic analysis. The highest tephra deposit is 86 cm from the top of the coal, is 1.5 cm thick, and is orange/brown (10 R4/6) in color.

Lerbekmo South (Hell Creek Marina Road)

Roughly 10 km E of Garbani Hill is our Lerbekmo South locality (N47.51602º,

W106.9366º). This locality is roughly 1 km south, along County Road 543, from the Lerbekmo (Hell Creek Marina Road) locality, which contains one of the first recognized iridium anomalies, and is the location of the first radioisotopically dated bentonite layer (Folinsbee et al., 1963). The Lerbekmo locality has only one coal outcrop, and it is the Z coal. This Z coal is unique in that it is one of the few Z coals to contain both the Ir-anomaly, identified in an impact clay layer at the base of the coal, and the Lerbekmo and McGuire Creek bentonites (Ickert et al., 2015). These bentonites are characteristic of Z and MCZ coals that define the formational boundary in eastern Garfield County and McCone County, where the Ir-anomaly has yet to be identified.

One kilometer south at our Lerbekmo South locality, the section extends higher and the Z coal, identified by its thickness and unique bentonites, crops out at the base of a section with five additional coals above it. Of these five coals, which can best be described as a part of the Y coal complex, only one coal at the top of the section contains tephra deposits. The microstratigraphy of this coal is described in detail in Ickert et al. (2015). One tephra (HC13-1), located 20 cm from the base of the coal, was collected for dating (reported in this study) and chemical analysis (reported in Ickert et al., 2015). This tephra falls into the Unnamed assorted bentonites category, and therefore cannot be used to correlate this section to other parts of the region (Ickert et al., 2-15).

Paleomagnetic sampling was conducted ranging from ~10 m above the Z coal to right above the uppermost Y coal. Samples were collected from siltstone or claystone deposits. While channel deposits can be seen around this locality, sampling was concentrated in a section that was not affected by channel deposition, and was dominated by lithologies representative of flood plain deposits.

Isaac Ranch

The Isaac Ranch locality (N47.66572º, W106.502º) is located roughly 37 km NE of Lerbekmo South. Three coals have been identified at this locality. The lowermost coal has been tentatively identified as the MCZ coal, based on the appearance of a thick bentonite layer similar to the Lerbekmo bentonite described in Ickert et al. (2015). The two upper coals, ~ 9 and 11 m above the MCZ, are assigned to the Y coal suite. The first of these coals (~50 cm thick) contains two tephra layers, one of which (IS13-2, 40 cm from base of coal) underwent chemical analysis conducted in Ickert et al. (2015) and falls into the Unnamed assorted bentonite category. Detailed microstratigraphy for this coal can be found in Ickert et al. (2015).

Samples for paleomagnetic analysis were collected between the MCZ and first Y coal. All but one sample were collected from siltstone deposits, and the other sample was collected from a horizontally bedded fine sandstone. All lithologies within the sampling interval are associated with low energy deposition.

Thomas Ranch

Seven km roughly East of Isaac Ranch is the Thomas Ranch locality (N47.66675º, W106.4258º). Three coals crop out here and have been identified as the Null, MCZ, and Y coals. Detailed coal stratigraphy is reported in Ickert et al. (2015). The Null coal (~42 cm thick) was first noted at this locality by Lofgren (1995), and has since been corroborated by field analysis to other Null coal localities (i.e. Bug Creek) based on abundance of amber within the coal and identification of a distinctive fine-grain bentonite (1–2.5 cm thick, located ~ 35 cm from coal base) which has been collected at this locality (TR13-2) for dating (reported in this study) and chemical analysis (Ickert et al., 2015). Another tephra appears within the Null coal at Thomas

Ranch that was collected for chemical analysis, but it is laterally discontinuous, similar to other Null coal outcrops. Due to an abundance of detrital grains within the Null coal tephra, chemical fingerprinting proved difficult and cannot be used to correlate the Null coal tephras.

Roughly 25 m above the Null coal, the MCZ is exposed. At this locality, the MCZ is 80–90 cm thick and contains at least three tephras. The lowest tephra layer (2–4 cm thick), ~ 16 cm from the top of the coal, was collected for geochronology (TR13-3) and chemical analysis. Pb-isotopic analysis of this tephra reveals that it falls into the McGuire Creek bentonite category, and thus the coal is confirmed to be the MCZ (Ickert et al., 2015). About 10.5 m above the MCZ another coal ~1.3 m thick crops out, and is nominally a Y coal. Three apparent tephra deposits are identified within the coal, and the lowermost tephra (20 cm from the base of the unit) was collected for dating (TR14-1).

Paleomagnetic sampling ranged from 4 m below the Null coal to 2.5 m below the Y coal. A channel sandstone cuts through the section about 8 m below the MCZ, and is ~5 m thick in our section. This unit was unavoidable due to its large lateral extent. The lithologies selected for paleomagnetic sampling were representative of low-energy deposition, including both fine-grained horizontally bedded sandstones, and siltstones.

Sandy Chicken

The Sandy Chicken locality (N47.62519º, W106.3527º) is located roughly 7 km SE of Thomas Ranch. Two coals are exposed in this section, nominally assigned to the Null and MCZ coals based initially upon stratigraphic position. The Null coal at this location is 27 cm thick and contains one tephra horizon (SC14-1) approximately 2 cm from the base of the coal. This layer is 2-cm-thick, pink in color (5 R 8/2), and is fine-grained. The coal here has notably less amber compared to other Null coal deposits. Roughly 27 m above the Null coal, the MCZ is identified. The MCZ is ~1.2 m thick, however contains three shale partings at 29, 46, and 78 cm from coal base and are roughly 8-, 13-, and 31- cm thick, respectively. A thick 8–10 cm bentonite occurs 3 cm from the base of this coal. This layer is brown-pink (10 R 4/2) in color, is waxy in appearance, and contains altered biotite and fine euhedral sanidine crystals, similar in character to the Lerbekmo bentonite described from other MCZ sections. No other tephra layers are apparent.

Paleomagnetic samples were collected from approximately 2.3 m below the Null coal, to 70 cm below the MCZ. All sampling sites were within low energy deposits, 6 collected from siltstone deposits and 1 collected from a fine-grained silty-sandstone. No channel deposits outcrop in the paleomagnetic section.

Bug Creek

Thirteen km NE of Sandy Chicken, in McCone County across the Big Dry arm of the Fort Peck Reservoir, is the Bug Creek locality (N47.68017º, W106.2138º). At this locality both the Null coal and the MCZ crop out, as originally mapped by Rigby and Rigby (1990) and are described in detail in Sprain et al. (2015) and Ickert et al. (2015), respectively. Both the MCZ and Null coal have been chemically analyzed (Ickert et al., 2015) and the tephra within the Null coal has been dated (BC1-PR/BC11-1; Sprain et al., 2015). Chemical analysis confirms identification of the MCZ.

Nowhere in the Bug Creek locality do the MCZ and Null coal crop out in a continuously exposed section. Previous magnetostratigraphy completed in the locality shows a section that ranges from the below the Null coal up through the MCZ. Based on our own field observations,

this section was likely made by siting across large lateral distances, which becomes uncertain due to broad areas that are covered in vegetation. This type of correlation is unsuitable for a high-resolution geochronologic study, and therefore we collected paleomagnetic samples only from one hill, which ranges from 6.55 m below the Null coal, to 5.47 m above it. This section is composed solely of horizontally deposited flood plain sediments, and all samples were collected from siltstones.

Purgatory Hill

Five km NE of Bug Creek is our Purgatory Hill locality (N47.7033º, W106.1501º). At this locality, at least 5 coals are present. The lowermost coal is less than 1 m thick and contains no tephra deposits. However, if this coal is walked out to the north it thickens and tephras similar in appearance to the Lerbekmo and McGuire Creek bentonites appear, suggesting that this coal is the MCZ. The next four coals can best be described are part of the Y suite. The first of these is 1.75 m thick, and contains no tephras. Approximately 10 m above this coal another coal, ~75 cm thick, crops out. Within this layer both a shale parting and a tephra are identified. The shale parting is ~8 cm thick, and pink in color (5 R 8/2), and it is within the top 40 cm of the coal. Towards the base of the coal, at around 10 cm, the tephra layer is identified. It is pink/salmon (10 R 7/4) in color, and is up to 2 cm thick. This tephra (PH13-3) was collected for dating. A third coal is exposed roughly 8 m above. This coal is much thinner, only around 20-cm-thick, but within these 20 cm two tephras are exposed. Seven cm from the base of the coal a thin, <0.5 cm tephra is found. It is pink in color (5 R 8/2) and contains visible euhedral crystals. Eleven cm above this layer, another tephra is identified. The tephra is peach in color (10 R 7/4), ~1.5 cm thick but pinches and swells laterally, and also contains visible euhedral crystals. This tephra (PH13-1) was collected for dating. Roughly 4 m above this section another thin coal crops out. It is only 15-cm-thick, but contains one tephra deposit. This tephra varies from 2–7 cm from the top of the coal. It is white-pink (10 R 8/2) in color, has apparent euhedral crystals, and is 1–3 mm thick. Occasionally, a second 1-mm-thick tephra is exposed below.

Paleomagnetic sampling was conducted from about 3 m below the first Y coal to one meter below the top Y coal in our section. Large channel deposits were not identified in our section and paleomagnetic samples were collected from low energy deposits comprising siltstones and fine-grained horizontally laminated sandstones.

McGuire Creek (Lofgren)

Approximately 8.5 km south of Purgatory Hill is our McGuire Creek locality (also known as our Lofgren locality; N47.62985º, W106.1701º). At this locality three coals are identified: the MCZ, a Y coal, and an X coal per Rigby and Rigby (1990). Coal microstratigraphy is described in detail for the MCZ and X coal in Sprain et al. (2015), and for the Y coal in Ickert et al. (2015). Two tephras were dated from this locality in Sprain et al. (2015), one from the MCZ (LG11-1) and another from the X coal (MC11-3). The tephra dated in Sprain et al. (2015) from the MCZ coal, LG11-1, has been designated the type locality for the McGuire Creek bentonite characterized in Ickert et al. (2015). Due to the low precision of the MC11-3 date, and K/Ca ratios during step-heating analysis that are suggestive of plagioclase contamination, more tephra from the X coal was collected for dating. The second tephra layer in the X coal, ~90 cm from the base, was collected (LG13-1). This sample is pink (5 R 8/2), 0.5 cm–2 mm thick, and has apparent euhedral crystals.

Samples for paleomagnetic analysis were collected starting roughly 3.5 m above the

MCZ and extending to 10 cm above the X coal. Sampled lithologies ranged from siltstone to fine-sandstone. All sandstone deposits in the section appear fine-grained, and horizontally laminated, with non-erosive features.

Jack's Channel

The Jack's Channel locality is 4 km SW of the McGuire Creek section. At this locality two coals, and one tephra bearing carbonaceous shale, are present. The coals at this locality have been informally named based on elevation (the 2380 and 2440 coals, respectively) and were mapped by D. Lofgren (personal communication). Around twenty-five meters below the 2380 coal, the MCZ crops out and can be walked out laterally to our Z-line locality presented in Sprain et al. (2015). The tephra-bearing carbonaceous shale layer crops out in between the 2380 and 2440 coals. Each carbonaceous unit contains tephra deposits that have been chemically analyzed (Ickert et al., 2015). Chemical analysis confirms that these coals fall into the Y/X suite. $^{40}Ar/^{39}Ar$ ages for sanidine from tephras JC13-4 (2380), JC13-3 (carb shale), and JC13-2 (2440) are presented here.

Paleomagnetic sampling was conducted at Jack's Channel at three different locations. The first location is by the JC13-1 tephra, described in Ickert et al. (2015), and ranges from 2.65 m below the 2380 coal to 10 cm above it (N47.60567º, W106.2105º). The 2380 coal can be visually traced to our second sampling locality (N47.6047º, W106.2086º). This correlation is confirmed by Pb-isotopic analysis showing that Pb-isotopes from the JC13-1 tephra and JC13-4 tephra (collected from the same horizon within the 2380 coal at these two localities) are identical in composition. Sampling here starts 1 m above the 2380 and continues to 25 cm below the 2440. Another sampling locality was chosen in order to confirm previous magnetostratigraphic results (N47.60596º, W106.20665º). This site is roughly 0.5 km away and contains only the 2380 coal, identified by unique capping unit and thin tephra layer exposed near the top of the coal. Paleomagnetic sample collection was focused around the 2380 coal and extends 2 m above and 2 m below the coal. Sampled lithologies range from silty fine-grained sandstone to siltstone. No channel deposits are apparent in any of the sampling sections, however Jack's Channel, a 10-m thick channel deposit, crops out ~15 m below the 2380.

Appendix References

Alvarez, L.W., 1983, Experimental evidence that an asteroid impact led to the extinction of many species 65 million years ago: National Academy of Sciences Proceedings, v. 80, p. 627–642.

Clemens, W.A., and Hartman, J.H., 2014, From Tyrannosaurus rex to asteroid impact: Early studies (1901–1980) of the Hell Creek Formation in its type area, *in* Wilson, G.P., Clemens, W.A., Horner, J.R., and Hartman, J.H., eds., Through the End of the Cretaceous in the Type Locality of the Hell Creek Formation in Montana and Adjacent Areas: Geological Society of America Special Paper 503, p. 1–87.

Fastovsky, D.E., and Dott, R. H. Jr., 1986, Sedimentology, stratigraphy, and extinctions during the Cretaceous-Paleogene transition at Bug Creek, Montana: Geology, v. 14, p. 279–282.

Folinsbee, R.E., Baadsgaard, H., and Cumming, G.L., 1963, Dating of volcanic ash beds (bentonites) by the K-Ar method: Nat. Acad. Sci.-Nat. Res. Counc. Nuclear Science Series, Rept, p. 70–82.

Ickert, R.B., Mulcahy, S.R., Sprain, C.J., Banaszak, J.F., and Renne, P.R., 2015, Chemical and Pb isotope composition of phenocrysts from bentonites constrains the chronostratigraphy around the Cretaceous-Paleogene boundary in the Hell Creek region, Montana: Geochemistry, Geophysics, Geosystems, v. 16, p. 2743–2761, doi: 10.1002/2015GC005898.

LeCain, R., Clyde, W.C., Wilson, G.P., and Riedel, J., 2014, Magnetostratigraphy of the Hell Creek and lower Fort Union Formations in northeastern Montana: Geological Society of America Special Papers, v. 503, p. 137–147, doi: 10.1130/2014.2503(04).

Lofgren, D.L., 1995, The Bug Creek Problem and the Cretaceous-Tertiary Transition at McGuire Creek, Montana: University of California Press, 204 p.

Moore, J.R., Wilson, G.P., Sharma, M., Hallock, H.R., Braman, D.R., and Renne, P.R., 2014, Assessing the relationships of the Hell Creek–Fort Union contact, Cretaceous-Paleogene boundary, and Chicxulub impact ejecta horizon at the Hell Creek Formation lectostratotype, Montana, USA, *in* Wilson, G.P., Clemens, W.A., Horner, J.R., and Hartman, J.H., eds., Through the End of the Cretaceous in the Type Locality of the Hell Creek Formation in Montana and Adjacent Areas: Geological Society of America Special Paper 503, p. 123–135.

Renne, P.R., Deino, A.L., Hilgen, F.J., Kuiper, K.F., Mark, D.F., Mitchell, W.S., III, Morgan, L.E., Mundil, R., and Smit, J., 2013, Time Scales of critical events around the Cretaceous-Paleogene boundary: Science, v. 339, p. 684–687.

Renne P. R., Balco G., Ludwig K. R., Mundil R. and Min K., 2011, Response to the comment by W.H. Schwarz et al. on Joint determination of ^{40}K decay constants and $^{40}Ar^{*}/^{40}K$ for the Fish Canyon sanidine standard, and improved accuracy for $^{40}Ar/^{39}Ar$ geochronology by P.R. Renne et al. (2010): Geochimica et Cosmochimica Acta, v. 75, p. 5097–5100.

Rigby, J.K., and Rigby Jr, J.K., 1990, Geology of the Sand Arroyo and Bug Creek quadrangles: McCone County, Montana: Brigham Young University Geology Studies, p. 69–134.

Smit, J., Van der Kaars, W. A., and Rigby, J. K. Jr., 1987, Stratigraphic aspects of the Cretaceous-Tertiary boundary in the Bug Creek area of eastern Montana, U.S.A., *in* Mesozoic Ecological Proceedings: Paris, Mémoirs Société Géologique France, N. S., v. 150, p. 53–73.

Sprain, C.J., Renne, P.R., Wilson, G.P., and Clemens, W.A., 2015, High-resolution chronostratigraphy of the terrestrial Cretaceous-Paleogene transition and recovery

interval in the Hell Creek region, Montana: Geological Society of America Bulletin, v. 127, p. 393–409, doi: 10.1130/B31076.1.